

**Shared Wideband Transmit Antenna Arrays:
Optimal Pattern Synthesis and
Spatio-Temporal Delta-Sigma Modulation**

by
Dan P. Scholnik

Dissertation submitted to the Faculty of the Graduate School
of the University of Maryland in partial fulfillment
of the requirements for the degree of
Doctor of Philosophy
2006

© Copyright by

Dan P. Scholnik

2006

APPROVAL SHEET

Title of Dissertation: Shared Wideband Transmit Antenna Arrays:
Optimal Pattern Synthesis and
Spatio-Temporal Delta-Sigma Modulation

Student's Name: Dan P. Scholnik
Doctor of Philosophy, 2005

Dissertation and Abstract Approved: _____
Dr. Tülay Adalı, Professor
Computer Science and Electrical Engineering

Date Approved: _____

Dissertation and Abstract Approved: _____
Dr. Jeffrey O. Coleman
Naval Research Laboratory

Date Approved: _____

Curriculum Vitae

Dan P. Scholnik

1412 Woodman Ave.
Silver Spring, MD 20902
scholnik@nrl.navy.mil

EDUCATION

Ph.D. in Electrical Engineering, May 2006

University of Maryland, Baltimore County

M.S. in Electrical Engineering, August 1997

Michigan Technological University

B.S. in Electrical Engineering, May 1995

Michigan Technological University

EMPLOYMENT

Electronics Engineer, May 1995–Present

Radar Division, Signal Processing Theory and Methods section (Code 5328)

Naval Research Laboratory

4555 Overlook Ave. SW, Washington, DC 20375

PUBLICATIONS

- D. P. Scholnik, J. O. Coleman, J. Brandriss, D. Bowling, M. Neel, S. Rogala, and F. Schiavone, “Results of July 2003 space-time delta-sigma hardware experiments at China Lake,” Naval Research Laboratory, Memo Report MR8877, Sept. 2005.

- J. O. Coleman, D. P. Scholnik, and P. E. Cahill, “Synthesis of a polarization-controlled pattern for a wideband array by solving a second-order cone program,” in *Proc. 2005 IEEE AP-S Int’l Symp.*, Washington, DC, July 2005.
- J. O. Coleman and D. P. Scholnik, “Beam Design for a Ping-Pong-Sampled Linear Receive Array,” in *12th European Signal Processing Conference*, Vienna, Austria, Sept. 2004.
- D. P. Scholnik, “Optimization of the composite ambiguity function of synthetic wideband waveforms (U),” in *Proc. of the Tri-Service Radar Symposium*, Albuquerque, NM, June 2004.
- D. P. Scholnik, J. O. Coleman, D. Bowling, and M. Neel, “Spatio-temporal delta-sigma modulation for shared wideband transmit arrays,” in *Proc. IEEE Radar Conference*, Philadelphia, PA, Apr. 2004.
- J. O. Coleman, D. P. Scholnik, and J. J. Brandriss, “A specification language for the optimal design of exotic FIR filters with second-order cone programs,” in *Proc. Asilomar Conf. on Signals, Systems, and Computers*, Pacific Grove, CA, Nov. 2002.
- D. P. Scholnik, “Mixed-norm FIR filter optimization using second-order cone programming,” in *Proc. IEEE Int. Conf. Acoustic, Speech, and Signal Processing*, Orlando, FL, May 2002.
- ———, “A Parallel Digital Architecture for Delta-Sigma Modulation,” in *Proc. 2002 Midwest Symp. on Circuits and Systems (MWSCAS 2002)*, Tulsa, OK, Aug. 2002.
- D. P. Scholnik and J. O. Coleman, “Space-Time Vector Delta-Sigma Modulation,” in *Proc. 2002 Int’l Symp. on Circuits and Systems (ISCAS 2002)*, Scottsdale, AZ, May 2002.

- ———, “Computability Constraints in Space-Time Delta-Sigma Arrays,” in *Proc. Asilomar Conf. on Signals, Systems, and Computers*, Pacific Grove, CA, Nov. 2001.
- ———, “Joint Spatial and Temporal Delta-Sigma Modulation for Wideband Antenna Arrays and Video Halftoning,” in *Proc. IEEE Int. Conf. Acoustic, Speech, and Signal Processing (ICASSP 2001)*, Salt Lake City, UT, May 2001.
- ———, “Superdirectivity and SNR constraints in wideband array-pattern design,” in *IEEE Int’l Radar Conference*, Atlanta, GA, May 2001.
- J. O. Coleman, J. J. Alter, and D. P. Scholnik, “FPGA architecture for gigahertz-sampling wideband IF-to-baseband conversion,” in *International Conference on Signal Processing Applications and Technology (ICSPAT 2000)*, Dallas, TX, Oct. 2000.
- M. G. Parent, J. J. Alter, R. Pickles, J. Rao, J. O. Coleman, and D. P. Scholnik, “Wideband digital subarray beamforming using true time delay steering at the element level,” in *Proc. 2000 Antenna Applications Symp.*, Monticello IL, Sept. 2000.
- D. P. Scholnik, “Optimal filters for range-time sidelobe suppression,” in *European Signal Processing Conference (EUSIPCO 2000)*, Tampere, Finland, Sept. 2000.
- D. P. Scholnik and J. O. Coleman, “Joint Shaping of Quantization and Hardware-Mismatch Errors in a Multibit Delta-Sigma DAC,” in *Midwest Symposium on Circuits and Systems (MWSCAS 2000)*, Lansing, MI, Aug. 2000.
- J. J. Alter, J. O. Coleman, M. G. Parent, J. P. McConnell, and D. P. Scholnik, “An FPGA-based wideband digital beamformer using true time delay,” in *Proc. Workshop on Beamforming Technology and Applications*, Huntsville AL, July 2000.
- D. P. Scholnik and J. O. Coleman, “Vector delta-sigma modulation with integral shaping of hardware-mismatch errors,” in *IEEE 2000 Int’l Symp. on Circuits and Systems (ISCAS 2000)*, Geneva, Switzerland, May 2000.

- ———, “Formulating wideband array-pattern optimizations,” in *Proc. IEEE Int’l Symp. Phased Array Systems and Technology (ISPAST 2000)*, Dana Point, CA, May 2000.
- ———, “Optimal design of wideband array patterns,” in *Proc. IEEE Int’l Radar Conference (RADAR 2000)*, Alexandria VA, May 2000.
- J. J. Alter, M. G. Parent, J. O. Coleman, D. P. Scholnik, and F. J. Caherty, “A wideband digital beamformer using true time delay,” in *Proc. Military Sensing Symp. (MSS99)*, North Charleston SC, Nov. 1999.
- J. O. Coleman and D. P. Scholnik, “Design of nonlinear-phase FIR filters with second-order cone programming,” in *Proc. 1999 Midwest Symp. on Circuits and Systems (MWSCAS ’99)*, Las Cruces NM, Aug. 1999.
- D. P. Scholnik and J. O. Coleman, “Computationally efficient multirate passband equalization for bandpass digital/analog conversion,” in *Proc. 1999 Midwest Symp. on Circuits and Systems (MWSCAS ’99)*, New Mexico State University, Aug. 1999.
- J. O. Coleman and D. P. Scholnik, “Vector switching generalizes D/A noise shaping,” in *Proc. 1999 Midwest Symp. on Circuits and Systems (MWSCAS ’99)*, New Mexico State University, Aug. 1999.
- D. P. Scholnik and J. O. Coleman, “Nonuniformly offset polyphase synthesis of a bandpass signal from complex-envelope samples,” in *Proc. 1999 Int’l Symp. Circuits and Systems (ISCAS ’99)*, June 1999.
- ———, “Periodically nonuniform bandpass sampling as a tapped-delay-line filtering problem,” in *Proc. 1999 Int’l Conf. Acoustics, Speech, and Signal Processing (ICASSP ’99)*, Mar. 1999.
- J. O. Coleman and D. P. Scholnik, “Generalized-eigenfilter design of a hybrid FIR/analog receive filter minimizing ISI, ACI, and gaussian noise,” in *Proc. 1998 Midwest*

Symp. on Circuits and Systems (MWSCAS '98), Notre Dame University, Aug. 1998.

- D. P. Scholnik and J. O. Coleman, “Constrained quadratic design of FIR data-communication filters with linear matrix inequalities,” in *Proc. 1998 Conf. on Information Sciences and Systems (CISS '98)*, Mar. 1998.
- D. Scholnik, “Quadrature demodulation and modulation using bandpass sampling and reconstruction,” Master’s thesis, Michigan Technological University, Houghton, MI, Aug. 1997.
- D. P. Scholnik and J. O. Coleman, “Integrated I-Q demodulation, matched filtering, and symbol-rate sampling using minimum-rate IF sampling,” in *Proc. 1997 Symp. on Wireless Personal Communication*, Blacksburg, VA, June 1997.
- —, “Simple, exact models of sample-interleaving demodulators/modulators for quadrature bandpass sampling/reconstruction,” in *Proc. 1997 Conf. on Information Sciences and Systems (CISS '97)*, Baltimore, MD, Mar. 1997.

Abstract

Title of Dissertation: Shared Wideband Transmit Antenna Arrays:
Optimal Pattern Synthesis and
Spatio-Temporal Delta-Sigma Modulation

Dan P. Scholnik, Doctor of Philosophy, 2006

Dissertation directed by: Dr. Tülay Adalı, Professor
Computer Science and Electrical Engineering

Dr. Jeffrey O. Coleman
Naval Research Laboratory

The use of a single transmit array to simultaneously perform multiple independent functions requires an architecture with an elusive combination of high power, linearity, and wide bandwidth. A promising approach is delta-sigma modulation, which achieves high linearity by spectrally shaping the errors from a low-resolution quantizer away from the signal band. Delta-sigma modulation can potentially provide high power as well when combined with appropriate power driver electronics, but the bandwidth requirements can only be met with extreme clock rates. The clock rate can be reduced by jointly shaping quantization noise in temporal and spatial frequency. The spatio-temporal delta-sigma modulator introduced here reduces required clock rates by taking advantage of spatial oversampling, either by adding array elements or by taking advantage of the inherent spatial oversampling at the lower operating frequencies of wideband arrays. The loop filter in the spatio-temporal delta-sigma modulator is the key to the design, and it is shown how second-order cone programming (SOCP, an efficient form of convex optimization) can be used to optimize the

resulting signal-to-noise ratio subject to stability and computability constraints. The choice of computability constraint is shown to have a strong effect on both the resulting system performance and on the ease of parallel implementation.

Once a linear architecture is assumed, then custom optimization of transmit array patterns offers a great deal of flexibility. Although narrowband pattern synthesis is well-studied, wide-bandwidth arrays pose a more challenging design problem. In a conventional wideband array beam steering is done using time delays, resulting in a beamwidth that is proportional to frequency, and a mainlobe frequency response that shows undesired angle-dependent effects. It is shown that placing an FIR filter at each element of an array allows the direct control of such metrics as directivity, efficiency, gain, peak and mean-square sidelobe levels, polarization, and mainlobe frequency-response flatness. These metrics are formulated for wideband arrays and optimized using SOCP. The system model and the derivations are general enough to admit almost any array architecture, including arbitrary element locations, nonuniform element responses, and multiple polarizations.

ACKNOWLEDGEMENTS

I wish to thank my wife, Jill, for putting up with the odd and long hours at the computer, my parents, for dealing with all the graduation rescheduling in relatively good humor, and my daughter Lily, who always provided an excuse to put off that writing just one more day.

The Radar Division of the Naval Research Laboratory has been supporting, in various ways, my graduate education for all of my ten years as an employee. I could not possibly have finished my PhD while working without NRL's strong commitment to employee education and development. Related work undertaken at NRL was funded both internally and by the Office of Naval Research. I especially wish to acknowledge Dr. Daniel Purdy of ONR for his enthusiastic support of much of this work, both as a sponsor and as a committee member.

Much thanks to the UMBC faculty on my committee: my academic advisor, Dr. Tülay Adalı, Dr. Joel Morris and Dr. Thomas Seidman, for their time and for taking my procrastinations in stride.

Finally, Dr. Jeffrey Coleman has, over the last ten years, variously played the role of professor, academic advisor, editor, colleague, boss, research advisor, and mentor. He is very much responsible for making me the engineer I am today (which I like to think is a compliment).

TABLE OF CONTENTS

List of Tables	vii
List of Figures	viii
1. Introduction	1
1.1 Background and Motivation	2
1.1.1 A Brief History of Arrays	4
1.1.2 The Future	4
1.2 Summary of Contributions	5
2. Technical Background	10
2.1 Signal and System Representation	10
2.1.1 Notation	12
2.1.2 Signals as Complex Measures	14
2.1.3 Operations on Signal Measures	21
2.1.4 Random Signals	28
2.2 Temporal Delta-Sigma Modulation	36
2.2.1 History and Motivation	36
2.2.2 System Analysis and Design	38
2.2.3 Example	40
2.2.4 Finite-Length Analysis	43

2.2.5	Extensions	48
2.3	Spatial Delta-Sigma Modulation: Image Halftoning	49
3.	Wideband Transmit Antenna Arrays	51
3.1	System Model and Input/Output Response	53
3.1.1	System Model	53
3.1.2	Input/Output Response	55
3.2	Far-Field Propagation and the Wideband Array Pattern	60
3.2.1	The Vector Potential	61
3.2.2	The Far-Field Approximation	62
3.2.3	The Electric Field	64
3.2.4	The Wideband Array Pattern	65
3.2.5	Array-Pattern Geometry and the Helmholtz Cone	68
3.2.6	Polarization	70
3.3	Random Signal Analysis	74
3.4	Array Pattern Synthesis	77
3.4.1	Example Design Setup	77
3.4.2	Far-Field Power Density	83
3.4.3	Wideband Directive Gain and Directivity	86
3.4.4	Input Power	91
3.4.5	Efficiency	96
3.4.6	Gain	100
3.4.7	Mainbeam Frequency-Response Constraints	103
3.4.8	Sidelobe Constraints	108
3.5	Summary	112
4.	Spatio-Temporal Delta-Sigma Modulation	113
4.1	Input/Output Analysis	114

4.1.1	System Model	114
4.1.2	Random Input	115
4.1.3	The Geometry of Spatio-Temporal Oversampling	122
4.1.4	Deterministic Input	126
4.2	Loop Filter Design	127
4.2.1	Far-Field Noise Power	128
4.2.2	Stability	130
4.3	Computability and Parallelization	132
4.3.1	General Computability	134
4.3.2	Example Setup	138
4.3.3	Strict Causality	140
4.3.4	Time-Skewed Causality	144
4.3.5	Scanning Computability	146
4.4	Example Simulation	151
4.5	Summary	153
5.	Summary and Conclusions	155
	Appendix A. Glossary of Symbols	159
	Appendix B. Selected Measure Signal and Systems Derivations	163
B.1	Multidimensional Fourier Series for Signals with Lattice Support	163
B.2	Sampling	164
B.3	The Crosscorrelation of Linearly Filtered Processes	167
	Appendix C. The Wave Equation	170
	Appendix D. Elevation-Azimuth Spherical Coordinate System	172
	Appendix E. The Element Pattern of a Short, Thin Dipole	175

LIST OF TABLES

3.1	Common polarization types.	73
3.2	Comparison of results for example designs.	103

LIST OF FIGURES

2.1	An error-feedback $\Delta\Sigma$ DAC.	41
2.2	Computed and theoretical $\Delta\Sigma$ example spectra.	43
2.3	The expected noise spectra for $\Delta\Sigma$ modulated sequences of various lengths.	47
2.4	Example of Floyd-Steinberg error-diffusion halftoning.	50
3.1	Passband-equivalent model of transmit beamformer and array.	55
3.2	Elevation/azimuth spherical coordinate system.	70
3.3	Mapping the four-dimensional Helmholtz cone into three dimensions.	71
3.4	IF-synthesis hardware architecture for design example.	78
3.5	The results of maximizing wideband directivity.	90
3.6	The results of maximizing efficiency.	99
3.7	Magnitude and group-delay responses of selected element filters.	101
3.8	The results from maximizing wideband gain.	104
3.9	Maximizing wideband gain subject to mean-square passband constraints.	107
3.10	Maximizing wideband gain subject to passband and sidelobe constraints.	111
4.1	A wideband transmit array with spatio-temporal delta-sigma array D/A conversion.	115
4.2	Signal and noise geometries for a spatio-temporal $\Delta\Sigma$ array on a square lattice with element spacing d and sample spacing T	123
4.3	Time-skew transformation generates new computability constraints.	138

4.4	A comparison of the equivalent NTF's of optimized loop filters with various computability constraints.	140
4.5	A comparison of the computation order for the six-element example with various computability constraints.	142
4.6	The support regions for the strictly-causal loop filter measure.	143
4.7	The support regions for the time-skewed loop filter measure.	145
4.8	The support regions for the scanning loop filter measure.	148
4.9	A factorable spatio-temporal modulator architecture.	149
4.10	Component noise transfer functions for six-element array example.	152
4.11	Theoretical and simulated power spectra at the quantizer output for six-element example.	153
4.12	Theoretical and computed far-field power spectra at selected azimuth angles.	153
D.1	Elevation/azimuth spherical coordinate system.	174
E.1	Element pattern of a short vertical dipole.	178
E.2	Element pattern of a short vertical dipole in front of a ground plane.	179

Chapter 1.

Introduction

This dissertation attempts to answer two interrelated questions: How do we use modern optimization tools to design array patterns for digital wideband transmit antenna arrays? What kind of transmit-array architecture might allow us to implement these array patterns and transmit multiple simultaneous signals without unacceptable nonlinear distortion? The original impetus for this research, and its most ambitious potential application, is high-power shared digital transmit arrays. The terms “shared” and “digital” here imply, respectively, that multiple independent signals can be transmitted through the same elements in the array, and that the signals themselves are generated using DSP. High-power shared arrays are primarily of military interest; current commercial and research applications simply do not need the combination of high transmit power and linearity of military applications. However, the material on wideband array pattern analysis and design (Chapter 3) is equally applicable to low-power transmit arrays as well as single-waveform transmit arrays. Much of the analysis is applicable to receive arrays, as well, where linearity is much less of an issue. Chapter 4, on the other hand, can be viewed outside of the specific antenna array context as a general extension of the author’s previous work on $\Delta\Sigma$ modulation of vector signals to the case where the vector indices map to spatial locations. Possible applications include video halftoning and acoustic arrays for sonar or audio.

With this as a preface, the chapter proceeds with an overview of the past, current, and

future uses of antenna arrays and the current limitations that motivate this dissertation. This is followed by a chapter-by-chapter summary of the dissertation, highlighting the major contributions to the art.

1.1 Background and Motivation

First, some terminology: On transmit the *array pattern* describes the distribution of a given radiated signal as a function of direction and temporal frequency. This will be defined in detail in Chapter 3. On receive the array pattern describes the sensitivity of the array to radiation from each direction and frequency. Often the terms *beam* and *beam pattern* are used interchangeably with array pattern. To *steer* a beam is to orient (mechanically or electrically) the peak of the array pattern in a given direction.

Array antennas have many significant advantages over monolithic (single) antennas. The primary advantage is flexibility; arrays can be electrically steered and their patterns dynamically changed by selectively altering the frequency response applied to the signals in each array element. A dish antenna, for comparison, has a fixed beam pattern and must be physically rotated to steer the beam, a process that takes orders of magnitude longer than electrical steering. Hybrids also exist, for example arrays that are rotated to steer in azimuth but electrically steer the beam in elevation. Since an array can stay in a fixed position relative to the structure to which it is attached, it can be made larger than a rotating antenna. The disadvantages of arrays—more RF hardware and higher costs—have limited the use of larger arrays to the military, as commercial applications do not demand the same level of performance.

A potential advantage of antenna arrays that is only recently being realized is their ability to simultaneously perform multiple functions. For example, imagine a single array performing radar, communications, and electronic warfare (EW) functions simultaneously. This is the vision of the Advanced Multifunction RF Concept (AMRF-C) project [1, 2],

with the goal to improve Naval RF capability while substantially reducing the number of radiating structures on a ship. To this end, the current AMRF-C testbed has the ability to form multiple simultaneous beams on receive. On transmit, however, hardware sharing is limited to partitioning the array for different functions; only one waveform can be transmitted from an element at a time.

Array sharing on receive is straightforward because no high-power signals are involved. On transmit, however, sharing requires either that multiple signals be simultaneously amplified by the same power amplifier, or that multiple power amplifiers be used per element. The latter is generally cost-prohibitive, and so the focus is on the former. For efficiency purposes, especially in large military applications, high-power amplifiers are usually operated in moderate to heavy saturation. Constant-envelope waveforms are then used as they are immune to the resulting high nonlinearity. In general a sum of waveforms, be they constant envelope or otherwise, is itself not constant envelope, and the resulting intermodulation between simultaneously transmitted signals makes transmit sharing impractical.

Various approaches have been suggested to improve linearity in RF transmit applications. One approach is simply to reduce the total power levels (or, to keep output power constant, use larger amplifiers), which while reducing nonlinearity also reduces efficiency. This may be appropriate for commercial systems such as cellphone and wireless base stations that do not need high power and/or can tolerate low efficiencies. Another approach is to use digital predistortion to compensate for the nonlinearities in the amplifier, for example using a Volterra filter [3]. This requires precise calibration of the amplifier nonlinearity, however, and the predistortion can have a high computational cost. The linearization process is also likely to reduce the efficiency of the amplifier. An *outphasing* or LINC transmitter [4, 5] has also been considered for high-power and high-linearity applications [6]. In outphasing a non-constant envelope waveform is represented as the sum of two constant-envelope waveforms, each amplified using a saturated power amplifier and then summed at high power. This approach offers higher efficiency than a single linear amplifier, but is

still less efficient than a single saturated amplifier. Outphasing also requires very precise matching between the channels, limiting the attainable linearity. A final approach, that is considered here, is to use DSP to code waveforms in such a way as to be tolerant of nonlinearities. The preeminent example of this is $\Delta\Sigma$ modulation, also known as noise-shaped coding. It will be discussed in detail in Section 2.2, and extended in Chapter 4.

1.1.1 A Brief History of Arrays

The earliest recorded use of an antenna array appears to have been by Marconi in December, 1901 [7]. This was a fixed (nonsteerable) transmit array of two elements for trans-Atlantic telegraph communication. Arrays would not be used much in practice for many decades, in large part due to the high costs of the extra RF hardware inherent in analog arrays. Considerable theoretical and experimental work on arrays was performed in the 1920's and 1930's, however [8]. Among the first operational US Navy electronically steered arrays were the SPS-32 and SPS-33, shipboard radars in operation in 1962. Overviews of array progress since then can be found in [9, 10, 11]. Perhaps the most recognizable military arrays are those used in the SPY-1 radar, four faces of which appear prominently on AEGIS cruisers and destroyers, and the PATRIOT anti-missile radar, featured prominently in both recent Persian Gulf wars. In addition to the US and Europe, substantial array development has taken place in the Soviet Union/Russia [12], Japan [13], and China [14].

1.1.2 The Future

It is expected that next-generation radio frequency (RF) systems for radar and communications (among others) will demand orders of magnitude improvement in performance over current systems. Many will be required to receive, and possibly transmit, multiple independent signals in arbitrary directions simultaneously. Transmitted waveforms will need to

have wider bandwidths and greater spectral purity without reductions in power levels. As DSP capabilities continue to increase rapidly, these requirements inevitably lead to using digital filters to implement beam steering in antenna arrays. This follows the trend in (array and non-array) RF systems to move the boundary between analog and digital processing as close to the antenna as possible [15, 16, 17, 18, 19]. The goal is to minimize the amount of analog hardware used in favor of inherently accurate and stable DSP. Digital processing also admits more flexible designs and new techniques, especially in complex systems such as antenna arrays. The optimization techniques presented in Chapter 3 will allow for the custom design of array patterns to take full advantage of digital arrays. The extension of $\Delta\Sigma$ modulation in Chapter 4 to perform entire-array D/A conversion in a nonlinear-tolerant manner may provide a way to achieve greater linearity and spectral purity.

1.2 Summary of Contributions

What follows is a brief chapter-by-chapter overview of the dissertation, both to orient the reader and to indicate which contributions are believed original and significant. A running theme throughout this dissertation is the use of convex optimization, in particular second-order cone programming, to design linear filters and filter-like structures. Far too much of the common practice in both the fields of noise-shaping converters and antenna arrays involves heuristic design techniques that lead to suboptimal designs. These approaches were justified in the past due to nonexistent or inadequate computing power, but that is rarely the case today.

Chapter 2: Background The first section of this chapter presents an overview of the signals and systems framework used throughout the rest of the dissertation. Some of the derivation details are deferred to Appendix B in an attempt to avoid sidetracking the reader. That much detail at all is required to explain what is traditionally undergraduate electrical

engineering material owes primarily to the representation of signals and systems as complex measures, rather than the usual functions and sequences. The reasons for this choice are elaborated at the beginning of the chapter, but in short the measure representation allows substantial unification of discrete and continuous time and space representations as well as avoiding certain mathematical imprecisions inherent in Dirac-delta-based representations. Some new imprecisions are introduced in their place, however, in the interest of not attempting to write a complete signals and systems text. Although unconventional, this work is only partly original. The foundations were laid in [20], with much greater elaboration found in [21], in preparation at the time of this writing. Significant additions to [20] and [21] introduced in this dissertation include an extension to discrete-time signals with nonuniform support, a representation of uniform and nonuniform sampling, an enumeration of inverse Fourier-transform relations, the representation and frequency-domain properties of shift-varying systems, and greater elaboration on the representation of random signals (albeit using a less-general framework). While the measure representation is unconventional, with certain exceptions (the generalization of the Fourier series to lattices of arbitrary rank, for example) the underlying results parallel conventional theory. The goal here is not to reinvent signals and systems, but rather to unify and simplify notation.

The second section serves as technical background for those unfamiliar with delta-sigma ($\Delta\Sigma$) modulation and as a refresher for the rest, focusing on the digital implementation of $\Delta\Sigma$ modulation as used in digital-to-analog conversion. Although most of the basic theory of $\Delta\Sigma$ modulation is intuitively based in statistical analysis, it is rarely if ever presented as such in the literature. Because statistical analysis enters so heavily into the analysis in later chapters, here the traditional derivations are presented using explicit random-process formulations, rather than the quasi-deterministic approach prevalent in the literature. Usually overlooked (or deemed unimportant) in conventional $\Delta\Sigma$ analysis are the effects of modulating finite-length input sequences, thus an original derivation of the output spectrum for finite-length inputs is provided.

Chapter 3: Wideband Transmit Antenna Arrays The existing literature on optimal array-pattern synthesis is primarily focused on narrowband systems, and is usually receive-oriented. This is because most RF systems have been effectively narrowband, and because hardware limitations usually place severe restrictions on the transmit pattern, leaving little to optimize. There is, however, a movement towards multifunction or shared arrays on transmit which would necessarily be wideband and would support custom array patterns. This chapter begins by describing a passband-equivalent model of a transmit array that is used extensively in this chapter and the next. This model is more comprehensive than is typically found in the literature, as it does not assume identical element responses and incorporates digital beamforming, nonideal analog filter responses, and the responses of the array elements themselves. The second and third sections of the chapter trace signals through the model from input to far-field radiation, for both deterministic and random signals. Much of this parallels classic electromagnetics and antenna textbook presentations for narrowband arrays. The wideband formulations and the interpretation of the wideband problem geometry, however, are significant new contributions of this dissertation. In the fourth section of the chapter, various metrics are considered for the optimization of wideband transmit array patterns, such as directivity, efficiency, gain, and sidelobe level. A series of example designs is performed to illustrate, using second-order cone programming (SOCP) as the basic optimization framework. These optimization approaches are original and constitute the most significant contribution of this chapter. Although much of the material here applies either directly or indirectly (via reciprocity) to receive arrays, only the transmit problem is explicitly considered as it is the prerequisite for the following chapter. Receive arrays are considered in [22, 23, 24].

Chapter 4: Spatio-Temporal $\Delta\Sigma$ Modulation Implementing most of the array-pattern designs from the previous section, even in a non-shared array, requires either linear amplification in the transmitter or linear high-power digital-to-analog conversion. Tradition-

ally, however, high-power amplifiers in transmitters are run in compression for reasons of efficiency, and beam-steering using amplitude modulation is impossible (or at least impractical). In this section a new architecture is proposed to perform linear digital-to-analog conversion on the array as a whole, rather than per-element or per-subarray. Dubbed spatio-temporal delta-sigma ($\Delta\Sigma$) modulation, it is an extension of traditional $\Delta\Sigma$ modulation in which the quantization noise spectrum is shaped not just temporally, but spatially as well. By taking advantage of the extra spatial dimensions, high far-field SNR can be achieved with much lower temporal oversampling ratios (and thus clock rates) than would be required by traditional $\Delta\Sigma$ modulation. This basic idea was first published in [25, 26] for acoustic arrays, although the architecture and analysis used in those previous papers is limited to the case of uniformly spaced transducers with identical responses and a two-dimensional loop filter that consists of two nested one-dimensional loops. The present work and its preliminaries [27, 28, 29, 30, 31], which appear to be the only other publications on the subject, are far more general and require none of these restrictions. Indeed, it is shown in the section on computability that a nested (“factorable”) loop leads to quite sub-optimal performance. Thus, apart from the basic idea itself, the entire chapter represents a significant original contribution.

The first part of this chapter roughly parallels the previous chapter; the system model (based heavily on the previous wideband array model) is introduced and analyzed from input to the far-field. The desired-signal path is the same as in the previous chapter, and so the focus is on the quantization-noise path and the loop filter which determines the noise shaping. The second part of the chapter focuses on the design of the loop filter, which borrows heavily from the optimization approaches derived in the previous chapter. Because the modulator includes a feedback loop with a spatio-temporal loop filter that is in general matrix valued, ensuring computability without overconstraining the loop filter is critical. A general computability constraint and several special cases are examined and compared in the context of an example design, and it is shown that the choice of computability constraint

has a major effect on both performance and the ease of parallel implementation. Finally, signals for an example array are simulated and compared to the theoretical results.

Chapter 2.

Technical Background

2.1 Signal and System Representation

In the course of describing wideband arrays and the spatio-temporal $\Delta\Sigma$ modulator we will need mathematical representations for conventional discrete-time signals, discrete-space-and-time signals, and continuous-space-and-time signals. The support of discrete-space signals can be any set of locations. We will also need to represent both linear shift-invariant and linear shift-varying filters that operate in both the discrete and continuous domains. Conventional discrete-time sequence notation, however, is not well suited to representing signals with arbitrary spatial support. In addition, it can lead to awkward notation when analyzing mixed discrete/continuous signals, and requires separate definitions for discrete, continuous, and mixed convolution. A common way to avoid some of these difficulties is to represent discrete-time signals in continuous time as sums of weighted Dirac delta (impulse) functions. Armed only with the “sifting” property of impulses it is straightforward to demonstrate that both the continuous-time Fourier transform and convolution with a non-impulsive system response have the desired results. Convolution between two discrete-time signals is more problematic, however, leading inevitably to the mathematical fiction of multiplying impulses. Here the convention is to implicitly invoke the sequence representation and perform the convolution as a sum, casting the result back to weighted

impulses. The result is the desired one, but it requires multiple definitions of convolution depending on the arguments. Matters only get more complicated in a multidimensional space, where the nature and properties of the impulse are less clear.

I have chosen here to recognize that the impulse “function” is but engineering shorthand for a point measure at the origin, and that discrete-time signals are really complex measures in disguise. Using explicit measure notation instead provides a signal representation that cleanly separates the value of a signal from its support, makes the support explicit, and allows a unified definition of the shift-invariant and shift-varying convolution integrals. The following sections formalize this idea, and introduce the notation that will be used throughout the dissertation. This measure approach is based on [20] and [21], extended here to explicitly consider discrete-space signals with arbitrary support, linear shift-varying filters, and random signal measures. In an attempt to keep the proverbial forest in sight, this section will provide only the basic definitions and the results of important derivations, and defer the details of selected derivations to Appendix B. In addition, a section on sampling is included in Appendix B.2, both for completeness and because it provides a good example of how to obtain classic engineering results without the use of delta functions or dubious Fourier transform pairs. These results, however, are not used elsewhere in the dissertation. The reader familiar with conventional signals and systems representations will hopefully find the notation and results throughout reasonably familiar and intuitive.

Still, this section is rather long and dense for a section that purports to provide mere background material, and thus requires some motivation for the reader. The reader that is actively interested in the measure-signals and systems approach taken here will, of course, want to read this section in some detail. Much more likely, however, the reader is interested in the path of least resistance to Chapters 3 and 4 while absorbing just enough to follow the math in the later chapters. Such a reader that is familiar with both conventional engineering signals and systems theory (both analog and digital) and the basics of measure theory should be able to limit detailed reading to the first two subsections, thereafter skimming

over hopefully familiar material. The casual reader that is familiar with conventional signals and systems theory but unfamiliar with measure theory can, for the most part, skim this section to become familiar with the notation, and then rely in the later chapters on their background to intuit the meaning of unfamiliar operations. The reader unfamiliar with signals and systems theory, with or without a measure-theory background, faces a much stiffer challenge. Although this section describes the signal representations and the signal operations used in the dissertation, it is hardly a signals and systems tutorial. Luckily, this third group seems least likely to read even this far.

2.1.1 Notation

This dissertation borrows from and relates parts of several disciplines, including signal processing, electromagnetics, optimization, and measure theory. Where possible notation natural to the the relevant discipline is adopted, however the need to indicate many independent signal attributes and competition for variable names leads inevitably to conflicts. This section provides a reference to the notation used within. Much of this notation will be introduced and explained inline as appropriate.

Scalar variables and scalar-valued functions are represented using medium-weight fonts: a , A . Vectors, matrices, and vector- or matrix-valued functions are indicated using a bold font: \mathbf{a} , \mathbf{A} . Common vector/matrix operations include transpose \mathbf{A}^T , conjugate \mathbf{A}^* , and conjugate transpose \mathbf{A}^H . In addition is often convenient to indicate both a conjugate transpose and the negation of the spatial or temporal argument. This will be indicated by the dagger notation

$$\mathbf{a}^\dagger(\mathbf{x}, t) \triangleq \mathbf{a}^H(-\mathbf{x}, t) \quad (2.1)$$

$$\mathbf{a}^\ddagger(\mathbf{x}, t) \triangleq \mathbf{a}^H(\mathbf{x}, -t) \quad (2.2)$$

$$\mathbf{a}^\ddagger(\mathbf{x}, t) \triangleq \mathbf{a}^H(-\mathbf{x}, -t). \quad (2.3)$$

The single dagger will be used for functions of a single variable: $a^\dagger(t) = a^*(-t)$. The

element in the m th row and the n th column of matrix \mathbf{A} can be indicated either explicitly as $[\mathbf{A}]_{m,n}$ or implicitly as $A_{m,n}$, while the m th element of a vector \mathbf{b} is indicated similarly as $[\mathbf{b}]_m$ or b_m . The n th column of matrix \mathbf{A} is indicated by $[\mathbf{A}]_n$ or \mathbf{A}_n . Another common matrix operation is the matrix trace:

$$\text{Tr}[\mathbf{A}] \triangleq \sum_{n=1}^N A_{n,n} \quad (2.4)$$

where \mathbf{A} is an $N \times N$ matrix. The length $\|\mathbf{x}\| = \sqrt{\mathbf{x}^H \mathbf{x}}$ of a vector \mathbf{x} is the standard Euclidean norm, while the unit vector

$$\hat{\mathbf{x}} \triangleq \frac{\mathbf{x}}{\|\mathbf{x}\|} \quad (2.5)$$

is indicated with a hat. For electromagnetic field quantities such as the electric field $\vec{\mathbf{E}}$, the 3D vector nature is emphasized using an overarrow. Finally, sets \mathcal{X}, \mathcal{T} are indicated using a calligraphic font and use a bold font if the elements of the set are vectors or matrices.

Some elementary group-theory concepts and notation will be useful in the following derivations. A *group* is defined by a set \mathcal{G} and an associative binary operator “+” such that \mathcal{G} is closed under +, contains the identity element, and contains all inverses. We will assume here that the operator is also commutative, in which case the group is said to be *abelian*. For example, \mathbb{R} is an abelian group under ordinary addition. We say that \mathbb{Z} under addition is a (proper) *subgroup* of \mathbb{R} under addition, because both are groups and $\mathbb{Z} \subset \mathbb{R}$. If \mathcal{G} is an abelian group, \mathcal{H} is a subgroup of \mathcal{G} , and $g \in \mathcal{G}$, then the set $g+\mathcal{H} \triangleq \{g+h : h \in \mathcal{H}\}$ is a *coset* of \mathcal{H} . The set of all cosets is itself a group, called the *factor group* and written \mathcal{G}/\mathcal{H} . If we form a set by choosing one element from each coset, we have a set of *coset representatives*, shown as $[\mathcal{G}/\mathcal{H}]$. If $[\mathcal{G}/\mathcal{H}]$ is a set of coset representatives, then for any $g \in \mathcal{G}$ we have the unique *coset decomposition* $g = h + a$, where $h \in \mathcal{H}$ and $a \in [\mathcal{G}/\mathcal{H}]$. For example, the elements of factor group \mathbb{R}/\mathbb{Z} are the equivalence classes of real numbers modulo one (members of a class are identical to the right of the decimal point), and $[0, 1)$ is an example of a set of coset representatives. Any real number can be uniquely written as the sum of an integer and a real number in the interval $[0, 1)$.

Many of the derivations in the sequel are lengthy, and it is all too easy to lose sight of the forest for the trees. Thus important results will be outlined to visually distinguish them from intermediate expressions.

2.1.2 Signals as Complex Measures

Let signal $\underline{a} : \mathbb{B} \rightarrow \mathbb{C}^M$ be a vector-valued complex measure (a vector of complex measures with a common input) defined on the Borel subsets \mathbb{B} of \mathbb{R}^N . The measure is related to its corresponding differential form $d\underline{a}(\underline{t})$ by

$$\underline{a}(\mathcal{T}) = \int_{\mathcal{T}} d\underline{a}(\underline{t}).$$

An underbar will be used to indicate both measures and their differential forms. Vector $\underline{t} \in \mathbb{R}^N$ will variously be specialized in the sequel to four-dimensional space-time as well as to time $t \in \mathbb{R}$ and space $\underline{x} \in \mathbb{R}^3$. Conventional differential representation leads to notational ambiguity, however, in the case of a differential measure like $d\underline{a}(\underline{x}, t)$, which could correspond to a measure on both variables \underline{x} and t , or a parameterized measure on either alone. To avoid this difficulty, the notation $\underline{a}(d\underline{t}) \triangleq d\underline{a}(\underline{t})$ is used to explicitly identify the variables on which the signal is a differential measure. Thus $\underline{a}(d\underline{x}, dt)$, $\underline{b}(d\underline{x}, t)$, and $\underline{c}(\underline{x}, dt)$ are, respectively, a differential measure on the pair (\underline{x}, t) , a differential measure on \underline{x} that is parameterized on t , and a differential measure on t parameterized on \underline{x} . These are related to measures \underline{a} , \underline{b} , and \underline{c} by

$$\begin{aligned} \underline{a}(\mathcal{T}) &= \int_{\mathcal{T}}^{\int} \underline{a}(d\underline{x}, dt) \\ \underline{b}(\mathcal{X}, t) &= \int_{\mathcal{X}}^{\int} \underline{b}(d\underline{x}, t) \\ \underline{c}(\underline{x}, \mathcal{T}) &= \int_{\mathcal{T}}^{\int} \underline{c}(\underline{x}, dt), \end{aligned}$$

respectively, where \mathcal{T} is a set of points in 4D space-time, \mathcal{X} is a set of 3D locations, and \mathcal{T} is a set of 1D times. The ticks on the integrals are used to indicate the dimension of the variable of integration.

It will be convenient at times to use the common engineering convention of appending the argument list when referring to measures and other functions. Thus we might refer to the “measure $\underline{b}(\mathcal{X}, t)$,” even though formally $\underline{b}(\mathcal{X}, t)$ is not a measure but rather the value that results from evaluating the parameterized measure \underline{b} on the set \mathcal{X} with the parameter t . Here \mathcal{X} and t are “dummy” arguments that serve (through the aforementioned conventions on representing scalar and vector variables and sets) to implicitly define the domain of the function.

The differential form will be used preferentially in the derivations in Chapters 3 and 4 as it more closely resembles conventional engineering notation, with the implicit understanding that, strictly speaking, it only has meaning within an integral. For this reason, we will permit the terminological imprecision of referring to both $\underline{a}(\mathcal{T})$ and $\underline{a}(dt)$ as signal measures, rather than distinguishing the latter as a differential. At times the differential notation becomes unwieldy, however, and set arguments are used.

Reference Measure

The concept of reference measure used here arises from the Radon-Nikodym theorem: Let \underline{a} be a complex measure, and let $\underline{\mu}$ be a positive measure. We say that \underline{a} is *absolutely continuous* with respect to $\underline{\mu}$, written $\underline{a} \ll \underline{\mu}$, if $\underline{a}(\mathcal{T}) = \mathbf{0}$ for all sets \mathcal{T} such that $\underline{\mu}(\mathcal{T}) = 0$. The Radon-Nikodym theorem [32] states that if $\underline{a} \ll \underline{\mu}$ and $\underline{\mu}$ is sigma-finite, then there is a $\underline{\mu}$ -integrable function $a = d\underline{a}/d\underline{\mu}$ such that

$$\underline{a}(\mathcal{T}) = \int_{\mathcal{T}} a(\mathbf{t}) \underline{\mu}(d\mathbf{t}).$$

In differential notation we write $\underline{a}(d\mathbf{t}) = a(\mathbf{t}) \underline{\mu}(d\mathbf{t})$. The function a is called the density or the *Radon-Nikodym derivative* of the measure \underline{a} with respect to $\underline{\mu}$. Terminology for the positive measure $\underline{\mu}$ varies, but it is sometimes called the *base* or *reference* measure.

It is straightforward to extend the Radon-Nikodym theorem to vector-valued complex measures, by applying the absolute continuity and integrability conditions to each element

of vector measure \underline{a} and density \mathbf{a} , respectively. We will refer to the common (scalar) positive measure $\underline{\mu}$ as the reference measure of \underline{a} , and will require that $\underline{\mu}$ distribute mass uniformly across its support \mathcal{S} in \mathbb{R}^N . Reference measures so defined can be used to describe the support of classes of measure signals and systems. Certain properties of a reference measure will prove useful. Defining the shift operator indicated by a left subscript as

$${}_{\tau}\underline{\mu}(\mathcal{T}) \triangleq \underline{\mu}(\mathcal{T} - \tau), \quad (2.6)$$

we will say that reference measure $\underline{\mu}$ is *shift invariant* with respect to \mathcal{S} if ${}_{\tau}\underline{\mu}(\mathcal{T}) = \underline{\mu}(\mathcal{T})$ for all $\tau \in \mathcal{S}$. We will say that $\underline{\mu}$ is *flip invariant* if $\underline{\mu}(-\mathcal{T}) = \underline{\mu}(\mathcal{T})$. Both of these properties result if \mathcal{S} forms a group under vector addition. Following [20], we say that that $\underline{\mu}$ is shift-invariant with respect to a signal measure \underline{a} if

$${}_{\tau}\underline{\mu}(d\mathbf{t})\underline{a}(d\boldsymbol{\tau}) = \underline{\mu}(d\mathbf{t})\underline{a}(d\boldsymbol{\tau}) \quad (2.7)$$

for all $\tau \in \mathbb{R}^N$. Equivalently, $\underline{\mu}$ is shift invariant with respect to the support of \underline{a} .

We note that the requirement that a complex measure have bounded total variation precludes the representation of many common engineering signals, notably sinusoids and complex exponentials. The integrability requirement on the density in the Radon-Nikodym theorem representations similarly restricts the class of signals that can be represented. This is a conceptual problem but not a practical one, since physically realizable signals have compact support. An advantage of this restriction is that the Fourier transform will always exist for measure signals.

In the following sections several important reference measures are introduced to represent continuous-space/time signals and conventional discrete-time signals, as well as multidimensional discrete-space/time signals on a lattice and signals with arbitrary discrete spatial support.

Continuous-Space/Time Signal Measures

Continuous-space/time signals are measures that are absolutely continuous with respect to a reference measure that is ordinary Lebesgue measure in \mathbb{R}^N . To simplify notation Lebesgue measure is represented by a bar under the variable of integration. Thus a continuous-space/time signal \underline{a} is represented in differential notation as $d\underline{a}(t) = \underline{a}(t)dt$. The \mathbb{R}^N derivative (density) $\underline{a}(t)$ in this case is just the usual engineering representation of a continuous-time signal. The support of Lebesgue measure is all of \mathbb{R}^N , which is a group. Thus Lebesgue measure is shift-invariant with respect to \mathbb{R}^N and therefore is shift invariant with respect to all other signal measures on \mathbb{R}^N .

The Dirac Measure

The Dirac delta “function” $\delta(t)$ of conventional engineering mathematics is here replaced by the *Dirac measure* $\underline{\delta}$, which represents a point measure at the origin:

$$\underline{\delta}(\mathcal{T}) = 1_{\mathcal{T}}(0) = \begin{cases} 1, & 0 \in \mathcal{T} \\ 0, & 0 \notin \mathcal{T}, \end{cases} \quad (2.8)$$

where

$$1_{\mathcal{T}}(t) \triangleq \begin{cases} 1, & t \in \mathcal{T} \\ 0, & t \notin \mathcal{T}. \end{cases}$$

The shifted impulse $\delta(t - \tau)$ is similarly replaced by the shifted Dirac measure $\tau\underline{\delta}$. The familiar sifting property still applies:

$$\int f(t) \tau\underline{\delta}(dt) = f(\tau).$$

Discrete-Space/Time Signal Measures

Discrete-space/time signals are complex measures whose nonzero measure is concentrated on some countable set \mathcal{D} of spatial and/or temporal locations. They can be defined in

two ways. Following engineering convention, a discrete-time signal can be defined as a weighted sum of Dirac measures:

$$\mathbf{a} = \sum_{\tau \in \mathcal{D}} a(\tau) \tau \delta.$$

Equivalently, discrete-time signals can be represented as measures that are absolutely continuous with respect to counting measure $\underline{\Sigma}_{\mathcal{D}}$ on the set \mathcal{D} . This permits representing a discrete-time signal as $\underline{a}(dt) = a(\mathbf{t}) \underline{\Sigma}_{\mathcal{D}}(dt)$ in terms of its R-N derivative $a(\mathbf{t})$ and reference measure $\underline{\Sigma}_{\mathcal{D}}$.

For discrete-time signals, \mathcal{D} is the one-dimensional lattice $T\mathbb{Z}$, where T is the sample spacing. Since a lattice is a group, the discrete-time reference measure $\underline{\Sigma}_{T\mathbb{Z}}$ is shift-invariant with respect to $T\mathbb{Z}$. The reference measure is shift-invariant with respect to any signal measure whose support is contained in $T\mathbb{Z}$.

For discrete-space signals there are two categories of reference measure of interest here. If \mathcal{D} is the lattice $\Lambda\mathbb{Z}^M$, where $3 \times M$ matrix Λ has linearly independent columns, then the discrete-space reference measure $\underline{\Sigma}_{\Lambda\mathbb{Z}^M}$ is shift-invariant with respect to $\Lambda\mathbb{Z}^M$ and shift invariant with respect to any signal measure whose support is contained in $\Lambda\mathbb{Z}^M$. In the more general case, \mathcal{D} is an arbitrary countable set of spatial locations \mathcal{L} , and the corresponding reference measure $\underline{\Sigma}_{\mathcal{L}}$ is not necessarily shift invariant with respect to any nontrivial set. If \mathcal{L} is contained within a lattice $\Lambda\mathbb{Z}^M$, then we will choose the reference measure to be $\underline{\Sigma}_{\Lambda\mathbb{Z}^M}$ rather than $\underline{\Sigma}_{\mathcal{L}}$ if flip or shift-invariance is required. In this sense the choice of a reference measure for a given signal is not unique, because we can always augment the support of one reference measure to obtain another.

Space and Time Signals

Most of the signals of interest in the sequel are measures on both 3D space and 1D time. The most general differential measure representation of such signals would be of the form $\underline{a}(dt)$, with $\mathbf{t} \in \mathbb{R}^4$. We will often only explicitly define such space-time signal measures

on measurable rectangles of the form $\mathcal{X} \times \mathcal{T}$. Because these measurable rectangles form a π -system that generates the four-dimensional Borel sets, this completely defines a unique measure on \mathbb{R}^4 ([33, thm. 10.3], extended to complex measures). This leads to the equivalent representations

$$\mathbf{a}(\mathcal{X} \times \mathcal{T}) = \int_{\mathcal{X} \times \mathcal{T}} \mathbf{a}(d\mathbf{x}, dt) \quad (2.9a)$$

$$= \int_{\mathcal{T}} \mathbf{a}(\mathcal{X}, dt) \quad (2.9b)$$

$$= \int_{\mathcal{X}} \mathbf{a}(d\mathbf{x}, \mathcal{T}), \quad (2.9c)$$

where the differentials in (2.9b) and (2.9c) result from fixing \mathcal{X} and \mathcal{T} , respectively. The integrands in (2.9a)–(2.9c) are, respectively, a differential measure on the 4D variable (\mathbf{x}, t) , a differential measure on the 1D variable t parameterized on the 3D set \mathcal{X} , and a differential measure on the 3D variable \mathbf{x} parameterized on the 3D set \mathcal{T} . Fixing either \mathcal{X} and \mathcal{T} in this way will allow us to perform space- or time-only operations on a space-time measure.

We will also assume that all space-time signal measures are absolutely continuous with respect to a reference measure on \mathbb{R}^4 that is a product measure of spatial and temporal reference measures. This results in the equivalent representations

$$\mathbf{a}(\mathcal{X} \times \mathcal{T}) = \int_{\mathcal{X} \times \mathcal{T}} \mathbf{a}(\mathbf{x}, t) (\underline{\mu} \times \underline{\nu})(d\mathbf{x}, dt) \quad (2.10a)$$

$$= \int_{\mathcal{T}} \int_{\mathcal{X}} \mathbf{a}(\mathbf{x}, t) \underline{\mu}(d\mathbf{x}) \underline{\nu}(dt) \quad (2.10b)$$

$$= \int_{\mathcal{X}} \int_{\mathcal{T}} \mathbf{a}(\mathbf{x}, t) \underline{\nu}(dt) \underline{\mu}(d\mathbf{x}), \quad (2.10c)$$

where Fubini's theorem is invoked in lines two and three to separate the integral and exchange the order of integration. The representations in (2.9) and (2.10) are convenient when operating on space and time independently. As an example, a typical discrete-space and discrete-time signal in this representation would be $\mathbf{a}(\mathbf{x}, t)_{\underline{\Sigma}_{\mathcal{L}}(d\mathbf{x})_{\underline{\Sigma}_{T\mathbb{Z}}}(dt)}$, with spatial support on an arbitrary but finite set of locations \mathcal{L} and temporal support on uniformly-spaced sample times $T\mathbb{Z}$. It will often be convenient to represent the density of a space-time measure on space or time alone. Thus we have the following set of equivalent representations:

$$\underline{a}(d\mathbf{x}, dt) = \mathbf{a}(\mathbf{x}, t) \underline{\mu}(d\mathbf{x}) \underline{\nu}(dt) \quad (2.11a)$$

$$= \underline{a}(d\mathbf{x}, t) \underline{\nu}(dt) \quad (2.11b)$$

$$= \underline{a}(\mathbf{x}, dt) \underline{\mu}(d\mathbf{x}). \quad (2.11c)$$

Here \underline{a} has three distinct meanings: a space-time differential measure on the left in (2.11a), a differential measure on space parameterized on (a density on) t on the right in (2.11b), and a differential measure on time parameterized on \mathbf{x} on the right in (2.11c). Here we rely on the arguments to disambiguate.

Units

A continuous-time signal measure \underline{a} with a unitless density $a(t)$ with respect to Lebesgue measure on \mathbb{R} has units of seconds, while a continuous-space-time signal measure \underline{b} with a unitless density with respect to Lebesgue measure on $\mathbb{R}^3 \times \mathbb{R}$ has units of $\text{m}^3 \cdot \text{s}$. For discrete-time/space signals the density with respect to the appropriate counting measure is the actual point-mass value, and thus has the same units as the differential measure; if density $a(t)$ is unitless, then so is discrete-time measure \underline{a} . For mixed discrete/continuous signals, the density is also mixed; if unitless $\mathbf{a}(\mathbf{x}, t)$ is a density with respect to counting measure on space and Lebesgue measure on time, then the corresponding measure \underline{a} has units of seconds. Unless otherwise specified, the densities of measure signals will always be taken with respect to Lebesgue measure for continuous-space/time signals, and the appropriate counting measure for discrete-space/time signals.

Discrete-time signals and certain continuous-time signals will have unitless densities in the sequel. Many of the continuous-time signals, however, represent physical quantities, such as voltages, currents, and power. In most cases it is natural to let the signal densities have the “expected” units. Since this results in signal measures with somewhat unfamiliar units, signal units will usually be specified for the underlying density. For system measures

the opposite is true; the natural units attach to the measure, and not the density.

2.1.3 Operations on Signal Measures

The major operations we wish to apply to signals in the sequel include the Fourier transform, convolution (linear shift-invariant filtering), and general (shift-variant) linear filtering. We also wish to derive the filtering operations in the Fourier domain. Here the advantages of the signal measure representation become apparent, as a single definition applies to most operations without regard to the reference measure of the arguments.

Fourier and Inverse Fourier Transform

A spatio-temporal signal $\underline{\mathbf{a}}(d\mathbf{x}, dt)$ can be Fourier-transformed on time alone, space alone, or both:

$$\begin{aligned} \mathbf{A}(\mathcal{X}, f) &\triangleq \int e^{-j2\pi ft} \underline{\mathbf{a}}(\mathcal{X}, dt) \\ \underline{\mathbf{a}}(\mathbf{v}, T) &\triangleq \int e^{-j2\pi \mathbf{v} \cdot \mathbf{x}} \underline{\mathbf{a}}(d\mathbf{x}, T) \\ \mathbf{A}(\mathbf{v}, f) &\triangleq \int e^{-j2\pi(\mathbf{v} \cdot \mathbf{x} + ft)} \underline{\mathbf{a}}(d\mathbf{x}, dt) \end{aligned}$$

The first two are still measures on the untransformed variable. On the left we use upper-case fonts to indicate temporal Fourier transform and upright fonts to indicate spatial Fourier transform; on the right the variables of integration are indicated by the ticks on the integral sign as well as the differential form of the integrand.

Unfortunately this unification of the Fourier transforms of continuous and discrete time and space signals does not lead to a similar unification of the inverse Fourier transform. Here we are forced to employ special cases for continuous-time/space signals, general discrete-time/space signals, and discrete-time/space signals whose support falls on a lattice. Definitions will be given for spatial signals; the corresponding time results are just one-dimensional special cases.

Continuous-Time/Space Signals For a continuous-space signal $\underline{\mathbf{a}}$ with Fourier transform \mathbf{a} the inverse transform takes the form

$$\underline{\mathbf{a}}(d\mathbf{x}) = \left(\int e^{j2\pi\mathbf{v}\cdot\mathbf{x}} \mathbf{a}(\mathbf{v}) d\mathbf{v} \right) d\mathbf{x}, \quad (2.12)$$

where the usual continuous-space Fourier transform is the R-N derivative of the signal measure.

Discrete-Time/Space Signals with Arbitrary Support For a general discrete-space signal with support on a discrete set \mathcal{L} the integral in (2.12) would not exist. Here the Fourier transform is *almost periodic* [34], and we have the somewhat unwieldy relationship

$$\underline{\mathbf{a}}(d\mathbf{x}) = \left(\lim_{V \rightarrow \infty} \frac{1}{\int_{\mathcal{T}} \int_{\mathcal{B}_V} d\mathbf{v}} \int_{\mathcal{B}_V} \mathbf{a}(\mathbf{v}) e^{j2\pi\mathbf{v}\cdot\mathbf{x}} d\mathbf{v} \right) \Sigma_{\mathcal{L}}(d\mathbf{x}), \quad (2.13)$$

where $\mathcal{B}_V = \{\mathbf{v} : \|\mathbf{v}\| \leq V\}$ is the ball of radius V . The expression inside the parenthesis is sometimes referred to as the *Bohr transform* [35, Appendix C], and is a generalization of the Fourier series for almost-periodic functions. It reduces to a Fourier series integral when the transform is actually periodic; that is, when \mathcal{L} lies on a lattice.

Discrete-Time/Space Signals with Support on a Lattice When a discrete-time signal $\underline{\mathbf{b}}$ has support on the one-dimensional lattice $T\mathbb{Z}$, then its Fourier transform \mathbf{B} is periodic with period $1/T$, and we can write the signal in terms of a conventional Fourier-series integral over one period:

$$\underline{\mathbf{b}}(dt) = \left(T \int_{[0, T^{-1})} \mathbf{B}(f) e^{j2\pi ft} df \right) \Sigma_{T\mathbb{Z}}(dt).$$

When the support of a spatial signal lies on a lattice, then the Fourier transform also exhibits periodicity, but defining the period is not so straightforward. Fourier series results for multiple dimensions [36] usually assume that the lattice is of full rank, however, so the following generalization is presented. (The details are found in Appendix B.1, in addition the derivation of periodicity for less-than-full-rank lattices originates from [37].) Let $\mathcal{L} =$

$\Lambda\mathbb{Z}^M$ be a lattice in \mathbb{R}^N , where $N \times M$ *generating matrix* Λ has linearly independent columns. (The lattice is full rank if $M = N$.) In this case we have the inverse-transform relationship

$$\underline{\mathbf{a}}(d\mathbf{x}) = \left(\int e^{j2\pi\mathbf{v}\cdot\mathbf{x}} \mathbf{a}(\mathbf{v}) \mu_{[\Lambda\mathbb{R}^M/\Lambda+T\mathbb{Z}^M]}(d\mathbf{v}) \right) \Sigma_{\Lambda\mathbb{Z}^M}(d\mathbf{x}), \quad (2.14)$$

where $\Lambda^+ = (\Lambda^T\Lambda)^{-1}\Lambda^T$ is the Moore-Penrose pseudo-inverse of Λ , the spectral ‘‘period’’ is any set of coset representatives $[\Lambda\mathbb{R}^M/\Lambda+T\mathbb{Z}^M]$ and $\mu_{[\Lambda\mathbb{R}^M/\Lambda+T\mathbb{Z}^M]}$ is the uniform probability measure over one spectral period. When $M = N$ then $\mu_{[\mathbb{R}^N/\Lambda-T\mathbb{Z}^N]}(d\mathbf{v}) = |\Lambda|1_{[\mathbb{R}^N/\Lambda-T\mathbb{Z}^N]}d\mathbf{v}$ and the integral reduces to the somewhat more conventional

$$\underline{\mathbf{a}}(d\mathbf{x}) = \left(|\Lambda| \int_{[\mathbb{R}^N/\Lambda-T\mathbb{Z}^N]} e^{j2\pi\mathbf{v}\cdot\mathbf{x}} \mathbf{a}(\mathbf{v}) d\mathbf{v} \right) \Sigma_{\Lambda\mathbb{Z}^N}(d\mathbf{x}). \quad (2.15)$$

Linear Shift-Invariant Filtering (Convolution)

All linear, shift-invariant (LSI) systems in the sequel will be represented as measures, and the effect on the input signal will be represented as a measure convolution. This section serves as a summary of [20], with the slight generalization to vector- and matrix-valued measures.

Let vector-valued temporal input $\underline{\mathbf{a}}(\mathcal{T})$ and matrix-valued shift-invariant filter $\underline{\mathbf{h}}(\mathcal{T})$ be complex signal measures. Following [38, Ch. 8, Prob. 5(d)], define the filter output as the measure convolution $(\underline{\mathbf{h}} * \underline{\mathbf{a}})(\mathcal{T})$ such that

$$(\underline{\mathbf{h}} * \underline{\mathbf{a}})(\mathcal{T}) \triangleq \int \underline{\mathbf{h}}(\mathcal{T} - \tau) \underline{\mathbf{a}}(d\tau) \quad (2.16)$$

No assumptions are needed as to the reference measures of the input or filter; they might both be discrete time, continuous time, or one of each. To avoid ambiguity as to the dimensions involved in a convolution involving a spatio-temporal signal $\underline{\mathbf{a}}$, the notation

$$(\underline{\mathbf{h}} * \underline{\mathbf{a}})(\mathcal{X} \times \mathcal{T}) \triangleq \int \underline{\mathbf{h}}(\mathcal{T} - \tau) \underline{\mathbf{a}}(\mathcal{X}, d\tau) \quad (2.17a)$$

$$(\underline{\mathbf{h}} \circ \underline{\mathbf{a}})(\mathcal{X} \times \mathcal{T}) \triangleq \int \underline{\mathbf{h}}(\mathcal{X} - \mathbf{x}) \underline{\mathbf{a}}(d\mathbf{x}, \mathcal{T}) \quad (2.17b)$$

$$(\underline{\mathbf{h}} \circledast \underline{\mathbf{a}})(\mathcal{T}) \triangleq \int \underline{\mathbf{h}}(\mathcal{T} - (\mathbf{x}, \tau)) \underline{\mathbf{a}}(d\mathbf{x}, d\tau) \quad (2.17c)$$

will be used to describe convolution in time, space, or both. Equation (2.17c) describes the same measure if restricted to the measurable rectangles, as mentioned previously:

$$(\underline{\mathbf{h}} \circledast \underline{\mathbf{a}})(\mathcal{X} \times \mathcal{T}) \triangleq \int\!\!\!\int \underline{\mathbf{h}}((\mathcal{X} - \mathbf{x}) \times (\mathcal{T} - \tau)) \underline{\mathbf{a}}(d\mathbf{x}, d\tau).$$

Measure convolution is associative, $(\underline{\mathbf{b}} * \underline{\mathbf{h}}) * \underline{\mathbf{a}} = \underline{\mathbf{b}} * (\underline{\mathbf{h}} * \underline{\mathbf{a}})$, and commutative if one of the measures is scalar: $\underline{h} * \underline{b} = \underline{b} * \underline{h}$. In addition, we can commute the roles the two measures play within the convolution integral:

$$\int \underline{\mathbf{h}}(\mathcal{T} - \tau) \underline{\mathbf{a}}(d\tau) = \int \underline{\mathbf{h}}(dt) \underline{\mathbf{a}}(\mathcal{T} - t) \triangleq \left(\int \underline{\mathbf{a}}^T(\mathcal{T} - t) \underline{\mathbf{h}}^T(dt) \right)^T,$$

where the non-commutativity of matrix multiplication forces either the somewhat non-standard notation in the middle or the awkward double-transpose on the right. Measure convolution is also shift-invariant:

$$(\underline{\mathbf{h}} *_{\alpha} \underline{\mathbf{a}})(\mathcal{T}) =_{\alpha} (\underline{\mathbf{h}} * \underline{\mathbf{a}})(\mathcal{T}).$$

Although this holds for any $\alpha \in \mathbb{R}$, we usually are interested only in shifts such that the reference measure for $\underline{\mathbf{a}}$ is the same as for $_{\alpha}\underline{\mathbf{a}}$: for continuous time $\alpha \in \mathbb{R}$, for discrete time $\alpha \in T\mathbb{Z}$. The convolution property of the Fourier transform also holds:

$$\int e^{-j2\pi ft} (\underline{\mathbf{a}} * \underline{\mathbf{h}})(dt) = \mathbf{H}(f) \mathbf{A}(f).$$

Often we will need results in terms of the densities of measure signals and systems. Here we need to be careful to take the relationship between the reference measures of the input and filter into account. We assume first that the system measure has the differential representation $d\underline{\mathbf{h}}(t) = \underline{\mathbf{h}}(t) \underline{\mu}(dt)$, where $\underline{\mu}$ is the reference measure (i.e. either Lebesgue or counting measure). We further assume that $\underline{\mu}$ is shift-invariant with respect to input measure $\underline{\mathbf{a}}$. This condition is met, for example, if $\underline{\mathbf{h}}$ is continuous-time/space, or if both $\underline{\mathbf{h}}$ and $\underline{\mathbf{a}}$ are discrete-time/space with support on the same lattice. Under these assumptions,

$$(\underline{\mathbf{h}} * \underline{\mathbf{a}})(\mathcal{T}) = \int_{\mathcal{T}} \left(\int \underline{\mathbf{h}}(t - \tau) \underline{\mathbf{a}}(d\tau) \right) \underline{\mu}(dt), \quad (2.18)$$

where we see that the R-N derivative of the convolution is the convolution $(\mathbf{h} * \underline{\mathbf{a}})(t)$ of the density \mathbf{h} with the measure $\underline{\mathbf{a}}$. The reference measure of the convolution is $\underline{\mu}$, the same as the system measure. If we assume instead that the input measure has the differential representation $\underline{\mathbf{a}}(dt) = \mathbf{a}(t)\underline{\mu}(dt)$, and $\underline{\mu}$ is shift-invariant with respect to system measure $\underline{\mathbf{h}}$, then we find that the density of the convolution can be written as $(\underline{\mathbf{h}} * \mathbf{a})(t)$, and has the same reference measure as the input. Thus we see the common engineering result that the convolution of an impulsive signal and a continuous-time signal is continuous-time. The usual special cases of convolution (continuous-time, discrete-time, and mixed) can be quickly arrived at by substituting the appropriate reference measures.

Linear Shift-Variant Filtering

Linear filtering on spatial functions with finite support (such as arise in image or array processing) is generally not intended to change the region of support. The inevitable conclusion is that such filtering cannot be shift-invariant, as any but the most trivial linear filters would enlarge the support region. In image processing it is common to implicitly follow shift-invariant filtering with a cropping operation that restores the original support (but renders most resulting spectral representations technically inaccurate). Here a more general notion of non-shift-invariant linear filtering is needed, which will be referred to as linear shift-variant (LSV) filtering in the sequel to distinguish it from the more common LSI filtering.

The fundamental representation here of a space-varying filter will be as a parametrized matrix-valued measure $\underline{\mathbf{h}}(\mathcal{X}; -\mathbf{x}')$. (The minus sign on the parameter is simply a notational choice that will be convenient later.) The output due to input signal measure $\underline{\mathbf{a}}(\mathcal{X})$ is the integral

$$(\underline{\mathbf{h}} \square \underline{\mathbf{a}})(\mathcal{X}) \triangleq \int \underline{\mathbf{h}}(\mathcal{X}; -\mathbf{x}') \underline{\mathbf{a}}(d\mathbf{x}'). \quad (2.19)$$

The \square operator so defined is clearly not commutative, but the arguments will at times be swapped for the sake of notational convenience when it is clear by context which argument

is the input and which is the filter. When the input is a measure on two spatial variables (such as with the autocorrelation measures introduced later), then it will be convenient to adopt the convention

$$(\mathbf{h} \square \mathbf{a})(\mathcal{X} \times \mathcal{Y}) \triangleq \int \mathbf{h}(\mathcal{X}; -\mathbf{x}') \mathbf{a}(d\mathbf{x}', \mathcal{Y}) \quad (2.20)$$

$$(\mathbf{a} \square \mathbf{h})(\mathcal{X} \times \mathcal{Y}) \triangleq \int \mathbf{a}(\mathcal{X}, d\mathbf{y}') \mathbf{h}(\mathcal{Y}; -\mathbf{y}'), \quad (2.21)$$

associating the input parameter of the filter measure with the “closest” of the two spatial variables in the input measure. LSI filtering results from the special case of $\mathbf{h}(\mathcal{X}; -\mathbf{y}) = \mathbf{g}(\mathcal{X} - \mathbf{y})$. All temporal filters in the sequel will be LSI, so no notation will be introduced for a temporal LSV integral. A filter that is LSI in time and LSV in space will be represented by a parameterized measure of the form $\mathbf{h}(\mathcal{X} \times \mathcal{T}; -\mathbf{x}')$ with output

$$(\mathbf{h} \boxtimes \mathbf{a})(\mathcal{X} \times \mathcal{T}) \triangleq \int \mathbf{h}(\mathcal{X} \times (\mathcal{T} - \tau); -\mathbf{x}') \mathbf{a}(d\mathbf{y}, d\tau). \quad (2.22)$$

Example: Discrete-Space Filtering To illustrate an important special case of spatial LSV filtering, assume discrete-space input \mathbf{a} and output \mathbf{b} that are absolutely continuous with respect to counting measure $\underline{\nu}_{\mathcal{L}}$ on an arbitrary finite set of locations \mathcal{L} . Enumerating \mathcal{L} as $\{\mathbf{x}_k\}$ and expanding \mathbf{a} as a sum of Dirac measures, the output of filter \mathbf{h} is

$$\begin{aligned} \mathbf{b}(\mathcal{X}) &= \int \mathbf{h}(\mathcal{X}; -\mathbf{y}) \sum_k \mathbf{a}(\mathbf{x}_k) \delta_{\mathbf{x}_k}(d\mathbf{y}) \\ &= \sum_k \mathbf{h}(\mathcal{X}; -\mathbf{x}_k) \mathbf{a}(\mathbf{x}_k) \end{aligned}$$

For \mathbf{b} to have the desired discrete-space structure, \mathbf{h} must be of the form

$$\mathbf{h}(\mathcal{X}; -\mathbf{x}_k) = \sum_n \mathbf{h}(\mathbf{x}_n; -\mathbf{x}_k) \delta_{\mathbf{x}_n}(\mathcal{X})$$

so that the filter output can be written as

$$\mathbf{b}(\mathcal{X}) = \sum_n \delta_{\mathbf{x}_n}(\mathcal{X}) \sum_k \mathbf{h}(\mathbf{x}_n; -\mathbf{x}_k) \mathbf{a}(\mathbf{x}_k).$$

The output density has the form of a matrix-vector multiplication, except that here the “matrix” elements $\mathbf{h}(\mathbf{x}_n; -\mathbf{x}_k)$ are themselves matrices, and the vector elements $\mathbf{a}(\mathbf{x}_k)$ are themselves vectors. This highlights another advantage of using a measure-signal representation for spatial signals, rather than a vector representation: it frees up the vector dimension for other uses, without requiring often cumbersome block-matrix notation. Yet another reason is given in the next section: the measure representation leads to a meaningful spectral representation of LSV filtering.

Spectral Representation of LSV Filtering

Much of the analysis in the sequel takes place in the frequency domain, and thus we desire a spectral relationship between the input and output of a LSV filter. Fourier transforming (2.19) simply transforms the filter, but not the filter input:

$$\mathbf{b}(\mathbf{v}) = \int \mathbf{h}(\mathbf{v}; -\mathbf{x}') \mathbf{a}(d\mathbf{x}').$$

To express the output spectrum in terms of the input spectrum requires the existence of an inverse Fourier transform relationship on the parameter $-\mathbf{x}'$ between $\mathbf{h}(\mathbf{v}; -\mathbf{x}')$ and the *bifrequency map* [39] $\check{\mathbf{h}}(\mathbf{v}; \mathbf{v}')$:

$$\mathbf{h}(\mathbf{v}; -\mathbf{x}') = \int \check{\mathbf{h}}(\mathbf{v}; \mathbf{v}') e^{-j2\pi \mathbf{x}' \cdot \mathbf{v}'} d\mathbf{v}'. \quad (2.23)$$

Substituting yields

$$\mathbf{b}(\mathbf{v}) = \int \int \check{\mathbf{h}}(\mathbf{v}; \mathbf{v}') e^{-j2\pi \mathbf{x}' \cdot \mathbf{v}'} d\mathbf{v}' \mathbf{a}(d\mathbf{x}'),$$

and recognizing a Fourier transform results in

$$\boxed{\mathbf{b}(\mathbf{v}) = \int \check{\mathbf{h}}(\mathbf{v}; \mathbf{v}') \mathbf{a}(\mathbf{v}') d\mathbf{v}'.} \quad (2.24)$$

Thus the bifrequency map takes an input component with frequency \mathbf{v}' to an output component with frequency \mathbf{v} through a scaling $\check{\mathbf{h}}(\mathbf{v}; \mathbf{v}')$. Unlike LSI filters, LSV filters can and do introduce spectral content in the output where none existed in the input.

2.1.4 Random Signals

In the preceding discussion it was implicitly assumed that all signals were deterministic. Strictly speaking, the output and internal signals of a $\Delta\Sigma$ modulator with a deterministic input are completely deterministic and it is certainly possible (if ungainly) to limit the analysis accordingly. However, signals such as quantization error act sufficiently like random processes that it is common in $\Delta\Sigma$ analysis to treat them as such when it comes to determining such quantities as the output noise power. Such an assumption can greatly simplify analysis and provides a natural path to beamformer and loop filter optimization in later chapters. We thus require a representation for random signals, their auto and crosscorrelations and power spectra, and common operations to be performed on them.

Representation

A random or stochastic process is generally defined as a function whose value at each point in its domain is a random variable (or vector) drawn from a common probability space [33, Ch. 7]. A sample function then is a realization of the random variables. Random processes are defined as continuous or discrete-time/space according to the domain of the sample functions. In the spirit of the measure-signal framework introduced in the previous section, here a random signal “measure” (the quotes will be explained shortly) is defined in terms of a “density” that is an ordinary random process. We will accordingly represent continuous and discrete-time/space random signals in the differential form

$$\begin{aligned}\underline{\mathbf{a}}(dt) &= \mathbf{a}(\mathbf{t})dt \\ \underline{\mathbf{b}}(dt) &= \mathbf{b}(\mathbf{t})_{\Sigma\mathcal{D}}(dt)\end{aligned}\tag{2.25}$$

where “densities” $\mathbf{a}(\mathbf{t})$ and $\mathbf{b}(\mathbf{t})$ are ordinary continuous and discrete time vector random processes, respectively. The wavy underbar serves to distinguish random signals from deterministic signal measures. The properties of a random signal flow naturally from the properties of its “density”. This definition does not expand the class of random signals

beyond conventional random processes, but rather provides a unifying representation for random processes with various support that matches that previously introduced for deterministic signals.

Many conventional random processes, notably stationary processes, have sample functions which are not integrable with respect to Lebesgue or counting measure, and thus cannot be densities of a complex measure. The differentials defined in (2.25) are likewise not integrable, and a set function of the form

$$\underline{a}(\mathcal{T}) = \int_{\mathcal{T}} \underline{a}(dt)$$

is not well defined for sets of infinite measure, including the entire space. Therefore, \underline{a} is not a measure. We therefore refer to \underline{a} and \mathbf{a} as a random signal “measure” and “density”, respectively, to stress the parallels with the deterministic signal representation without undue abuse of terminology. The wavy underbar indicates both randomness and the fact that the quantity is not truly a measure. Such difficulty was avoided for deterministic signals by excluding such problematic “densities”, but it is unavoidable for stationary processes. Ultimately we are interested less in the random signals themselves than in their crosscorrelations, which we will restrict to be finite measures as before. Integrals with respect to random signal “measures” will always be performed with respect to the underlying reference measure, which is well defined.

Second-Order Statistics: Wide-Sense Stationary Signals

In the sequel only the second-order statistics of random signals will be needed and we will assume proper [40] random processes. (In fact, all random signals in the later chapters will be real, but the generalization to proper complex processes is trivial.) Thus, we need only define the crosscorrelation measure and cross spectral density of two random signals, with the autocorrelation and power spectral density following as a special case. It will be assumed throughout that all random signals have zero mean unless otherwise indicated.

The simpler relationships for wide-sense stationary signals are presented first, followed by more-general results for nonstationary signals.

For two temporal signals with the same reference measure we will assume wide-sense stationarity. We assume random signals $\underline{\mathbf{a}}$ and $\underline{\mathbf{b}}$ are defined in terms of vector-valued “densities” with respect to a reference measure $\underline{\mu}$ that is either Lebesgue measure on \mathbb{R} or counting measure on $T\mathbb{Z}$ and define their matrix crosscorrelation measure as

$$\mathbf{r}_{ab}(\mathcal{T}) \triangleq \int_{\mathcal{T}} \mathcal{E}\{\underline{\mathbf{a}}(t)\underline{\mathbf{b}}^H(t-\tau)\} \underline{\mu}(d\tau) \quad (2.26a)$$

$$= \int_{\mathcal{T}} \mathbf{r}_{ab}(\tau) \underline{\mu}(d\tau), \quad (2.26b)$$

where density \mathbf{r}_{ab} is the ordinary crosscorrelation for the given reference measure. As this is not a function of t for values of t in the support of $\underline{\mu}$, we say that $\underline{\mathbf{a}}$ and $\underline{\mathbf{b}}$ are wide-sense cross-correlation stationary with respect to $\underline{\mu}$. This definition generalizes the conventional continuous and discrete-time crosscorrelation functions and sequences used in analyzing stochastic systems. As defined, the crosscorrelation is a deterministic measure on the delay between the signals whose density $\mathbf{r}_{ab}(\tau)$ is just the usual definition of the matrix crosscorrelation for vector random processes $\underline{\mathbf{a}}(t)$ and $\underline{\mathbf{b}}(t)$. The autocorrelation \mathbf{r}_a of WSS random signal $\underline{\mathbf{a}}$ is the special case where $\underline{\mathbf{b}} = \underline{\mathbf{a}}$. The power of a WSS random signal (in the statistical sense) is defined as the expected value of the norm squared of the process, which can also be expressed as the trace of the density of the autocorrelation measure at the origin:

$$\begin{aligned} \mathcal{P}_a &\triangleq \mathcal{E}\{\|\underline{\mathbf{a}}(t)\|^2\} \\ &= \text{Tr}[\mathbf{r}_a(0)]. \end{aligned}$$

The power is constant with units of signal squared.

The cross spectral density (CSD) $\mathbf{R}_{ab}(f)$ of two WSS random signals and the power spectral density (PSD) $\mathbf{R}_a(f)$ of a single WSS random signal are defined as the Fourier transforms of the crosscorrelation and autocorrelation, respectively. Often we want to relate

the power in a signal to its PSD, which can be achieved if an inverse-Fourier transform relation exists between the PSD and the autocorrelation density. Here we unfortunately need to resort to special cases. For continuous-time processes, the inverse Fourier transform is given by

$$\mathbf{r}_a(t) = \int \mathbf{R}_a(f) e^{j2\pi ft} df$$

and we find the power by integrating over the entire PSD:

$$\mathcal{P}_a = \text{Tr}[\mathbf{r}_a(0)] = \int \text{Tr}[\mathbf{R}_a(f)] df. \quad (2.27)$$

The PSD in this case has units of $\text{signal}^2/\text{Hz}$. For (WSS) discrete-time processes the PSD is periodic, and so the above integral does not exist. Instead the transform integral is performed over a single period $1/T$:

$$\mathbf{r}_a(t) = T \int_{[0, T^{-1})} \mathbf{R}_a(f) e^{j2\pi ft} df$$

Thus the power is found by averaging the PSD:

$$\mathcal{P}_a = \text{Tr}[r_a(0)] = T \int_{[0, T^{-1})} \text{Tr}[\mathbf{R}_a(f)] df. \quad (2.28)$$

Here the PSD has units of $\text{signal}^2/\text{period}$, or just simply signal^2 .

Second-Order Statistics: Nonstationary Signals

Spatial signals as used in the sequel may have finite extent and arbitrary support, and thus cannot be wide-sense stationary. Thus a more general definition of crosscorrelation is needed for these signals. A similar definition to (2.26) is possible for nonstationary signals, in which case t does not drop out of the expectation. However, for signals with arbitrary support it is much less intuitive to define the crosscorrelation in terms of an offset variable like τ . Instead a more symmetric definition is used both for simplicity and because it more naturally represents autocorrelation matrices. Assume random signals $\underline{\mathbf{a}}$ and $\underline{\mathbf{b}}$ are defined in terms of “densities” with respect to reference measures $\underline{\mu}$ and $\underline{\nu}$ and define their

crosscorrelation measure as

$$\mathbf{r}_{ab}(\mathcal{X} \times \mathcal{Y}) \triangleq \int_{\mathcal{X} \times \mathcal{Y}} \mathcal{E}\{\mathbf{a}(\mathbf{x})\mathbf{b}^H(\mathbf{y})\} (\underline{\mu} \times \underline{\nu})(d\mathbf{x}, d\mathbf{y}) \quad (2.29a)$$

$$= \int_{\mathcal{X}} \int_{\mathcal{Y}} \mathbf{r}_{ab}(\mathbf{x}, \mathbf{y}) \underline{\mu}(d\mathbf{x}) \underline{\nu}(d\mathbf{y}). \quad (2.29b)$$

When densities \mathbf{a} and \mathbf{b} are $\underline{\mu}$ - and $\underline{\nu}$ -integrable, then we can apply Fubini's theorem and write this as

$$\mathbf{r}_{ab}(\mathcal{X} \times \mathcal{Y}) = \mathcal{E}\{\mathbf{a}(\mathcal{X})\mathbf{b}^H(\mathcal{Y})\}. \quad (2.30)$$

As (2.29) makes clear the crosscorrelation is a deterministic measure that is related in a straightforward way to the usual definition of the correlation of random processes. This definition provides a unified representation of the conventional continuous and discrete time crosscorrelation functions and crosscorrelation matrices used in analyzing nonstationary stochastic systems. The autocorrelation measure \mathbf{r}_a of random signal \mathbf{a} is again the special case where $\mathbf{b} = \mathbf{a}$. The power \mathcal{P}_a of a random signal \mathbf{a} is defined as before in terms of the density of the autocorrelation:

$$\begin{aligned} \mathcal{P}_a(\mathbf{x}) &\triangleq \mathcal{E}\{\|\mathbf{a}(\mathbf{x})\|^2\} \\ &= \text{Tr}[\mathbf{r}_a(\mathbf{x}, \mathbf{x})]. \end{aligned}$$

Since stationarity has not been assumed, the power varies with position. When it exists, we will call the integral of the power with respect to $\underline{\mu}$ the *total power*:

$$\begin{aligned} \mathcal{P}_{a,\text{tot}} &\triangleq \int \mathcal{P}_a(\mathbf{x}) \underline{\mu}(d\mathbf{x}) \\ &= \int \text{Tr}[\mathbf{r}_a(\mathbf{x}, \mathbf{x})] \underline{\mu}(d\mathbf{x}). \end{aligned} \quad (2.31)$$

When $\underline{\mu}$ is counting measure then total power has the same units of signal² as did power. When $\underline{\mu}$ is Lebesgue measure, then total power has units of signal² · m³, and would be more accurately described as total energy (in the spatial sense). We choose the terminology for consistency with the discrete-space case, which is ultimately of greater interest. We first

assume that \underline{a} is continuous-space and an inverse Fourier transform relationship exists for the autocorrelation on its first variable:

$$\mathbf{r}_a(\mathbf{x}, \mathbf{y}) = \iint e^{j2\pi\mathbf{v}\cdot\mathbf{x}} \iint e^{-j2\pi\mathbf{v}\cdot\mathbf{x}'} \mathbf{r}_a(\mathbf{x}', \mathbf{y}) d\mathbf{x}' d\mathbf{v}.$$

Substituting into (2.31) and rearranging results in

$$\mathcal{P}_{a_{\text{tot}}} = \iint \left(\iint e^{-j2\pi\mathbf{v}\cdot(\mathbf{x}'-\mathbf{x})} \text{Tr}[\mathbf{r}_a(\mathbf{x}', \mathbf{x})] d\mathbf{x}' d\mathbf{x} \right) d\mathbf{v},$$

and recognizing a six-dimensional Fourier transform yields

$$\boxed{\mathcal{P}_{a_{\text{tot}}} = \iint \text{Tr}[\mathbf{r}_a(\mathbf{v}, -\mathbf{v})] d\mathbf{v}}, \quad (2.32)$$

where *bispectrum* \mathbf{r}_a is the Fourier transform of the autocorrelation on both variables [39]. This is the equivalent of (2.27) for nonstationary processes, and we will refer to $\mathbf{r}_a(\mathbf{v}, -\mathbf{v})$ as the PSD for nonstationary processes. For discrete-space random signals we repeat the derivation with the appropriate inverse Fourier transform relation:

$$\boxed{\mathcal{P}_{a_{\text{tot}}} = \lim_{V \rightarrow \infty} \frac{1}{\int_{\mathcal{B}_V} d\mathbf{v}} \int_{\mathcal{B}_V} \text{Tr}[\mathbf{r}_a(\mathbf{v}, -\mathbf{v})] d\mathbf{v}} \quad (2.33)$$

for general support on the set \mathcal{L} , and

$$\boxed{\mathcal{P}_{a_{\text{tot}}} = \iint \text{Tr}[\mathbf{r}_a(\mathbf{v}, -\mathbf{v})] \mu_{[\Lambda\mathbb{R}^M/\Lambda+T\mathbb{Z}^M]}(d\mathbf{v})} \quad (2.34)$$

on the lattice $\Lambda\mathbb{Z}^M$.

For spatio-temporal signals \underline{a} and \underline{b} that are nonstationary in space but WSS in time, we combine the above definitions of crosscorrelation

$$\begin{aligned} \underline{r}_{ab}(\mathcal{X} \times \mathcal{Y} \times \mathcal{T}) &\triangleq \iint_{\mathcal{X} \times \mathcal{Y} \times \mathcal{T}} \mathcal{E}\{\mathbf{a}(\mathbf{x}, t) \mathbf{b}^H(\mathbf{y}, t - \tau)\} (\underline{\mu} \times \underline{\nu} \times \underline{\rho})(d\mathbf{x}, d\mathbf{y}, d\tau) \\ &= \iint_{\mathcal{X}} \iint_{\mathcal{Y}} \int_{\mathcal{T}} \mathbf{r}_{ab}(\mathbf{x}, \mathbf{y}, \tau) \underline{\mu}(d\mathbf{x}) \underline{\nu}(d\mathbf{y}) \underline{\rho}(d\tau), \end{aligned} \quad (2.35)$$

where $\underline{\mu}$ and $\underline{\nu}$ are the spatial reference measures of \underline{a} and \underline{b} , and $\underline{\rho}$ is the temporal reference measure for both. Similarly the power in a spatio-temporal random signal \underline{a} at location \mathbf{x} is $\mathcal{P}_a(\mathbf{x}) = \text{Tr}[\mathbf{r}_{ab}(\mathbf{x}, \mathbf{x}, 0)]$, and total power is found by integrating the power with

respect to the spatial reference measure. The power at a given location can be related to the temporal PSD using (2.27) or (2.28), and the total power can be related to the spatial PSD using (2.32), (2.33), or (2.34). For example, the total power in a continuous-time, discrete-space signal \underline{a} with lattice support in space can be written

$$\mathcal{P}_{\underline{a}_{\text{tot}}} = \int \text{Tr}[\underline{r}_{\underline{a}}(\underline{x}, \underline{x}, 0)] \underline{\nu}_{\Lambda\mathbb{Z}^M}(d\underline{x}) \quad (2.36a)$$

$$= \int \int \text{Tr}[\mathbf{R}_{\underline{a}}(\underline{v}, -\underline{v}, f)] \underline{\mu}_{[\Lambda\mathbb{R}^M/\Lambda + T\mathbb{Z}^M]}(d\underline{v}) df, \quad (2.36b)$$

where $\mathbf{R}_{\underline{a}}$ is the seven-dimensional Fourier transform of the autocorrelation which when evaluated as $\mathbf{R}_{\underline{a}}(\underline{v}, -\underline{v}, f)$ is a four-dimensional spatio-temporal PSD with units of $\text{signal}^2/\text{Hz}$.

Linear Filtering

Both LSI and LSV filtering can be defined the same for random signal measures as for deterministic ones, and we wish to derive the effects of filtering on crosscorrelations and spectral densities. Rather than derive each possible combination of (non)stationarity, shift (in)variance, and filtering on either argument, two general results are provided that reduce to most special cases of interest. Consider spatio-temporal vector random measures \underline{a} and \underline{b} , which are both spatially nonstationary but temporally wide-sense stationary with respect to temporal reference measure $\underline{\mu}$. Two new processes are produced via linear filtering as $\underline{a}' = \underline{g} \boxtimes \underline{a}$ and $\underline{b}' = \underline{h} \boxtimes \underline{b}$, where we can write the filter measures as $\underline{h}(d\underline{x}, t; -\underline{x}')\underline{\nu}(dt)$ and $\underline{g}(d\underline{x}, t; -\underline{x}')\underline{\omega}(dt)$. We wish to find the cross correlation $\underline{r}_{\underline{a}', \underline{b}'}$ in terms of $\underline{r}_{\underline{a}\underline{b}}$. We will require that \underline{a}' and \underline{b}' also have the same temporal reference measure. This results in two possibilities for the relationship between reference measures $\underline{\mu}$, $\underline{\nu}$, and $\underline{\omega}$, which we will consider in turn.

We first consider the case where $\underline{\mu}$ is shift-invariant with respect to both $\underline{\nu}$ and $\underline{\omega}$. In this case, both \underline{a}' and \underline{b}' have temporal reference measure $\underline{\mu}$, as was shown in (2.18). Examples include continuous-time \underline{a} and \underline{b} , in which case \underline{a}' and \underline{b}' will also be continuous time, and the case where \underline{a} , \underline{b} , \underline{h} , and \underline{g} all have the same reference measure. The crosscorrelation in

this case is given by

$$\underline{r}_{\mathbf{a}', \mathbf{b}'}(\mathcal{X} \times \mathcal{Y} \times \mathcal{T}) = (\underline{g} \boxtimes \underline{r}_{\mathbf{a}, \mathbf{b}} \boxtimes \underline{h}^\dagger)(\mathcal{X} \times \mathcal{Y} \times \mathcal{T}). \quad (2.37)$$

The derivation is given in Appendix B.3. Fourier transforming yields

$$\mathbf{R}_{\mathbf{a}', \mathbf{b}'}(\mathbf{v}, \mathbf{w}, f) = \iiint \mathbf{G}(\mathbf{v}, f; -\mathbf{x}') \mathbf{R}_{\mathbf{a}, \mathbf{b}}(d\mathbf{x}', d\mathbf{y}', f) \mathbf{H}^H(-\mathbf{w}, f; -\mathbf{y}') \quad (2.38)$$

or, substituting (2.23),

$$\mathbf{R}_{\mathbf{a}', \mathbf{b}'}(\mathbf{v}, \mathbf{w}, f) = \iiint \check{\mathbf{G}}(\mathbf{v}, f; \mathbf{v}') \mathbf{R}_{\mathbf{a}, \mathbf{b}}(\mathbf{v}', \mathbf{w}', f) \check{\mathbf{H}}^H(-\mathbf{w}, f; -\mathbf{w}') d\mathbf{v}' d\mathbf{w}' \quad (2.39)$$

Through appropriate choices of $\underline{\mathbf{a}}$, $\underline{\mathbf{b}}$, $\underline{\mathbf{g}}$, and $\underline{\mathbf{h}}$ this general result can be easily adapted to various special cases. If $\underline{\mathbf{g}}$ and $\underline{\mathbf{h}}$ are instead spatially shift invariant, then the derivation changes slightly but the result is very similar:

$$\underline{r}_{\mathbf{a}', \mathbf{b}'}(\mathcal{X} \times \mathcal{Y} \times \mathcal{T}) = (\underline{g} \circledast \underline{r}_{\mathbf{a}, \mathbf{b}} \circledast \underline{h}^\dagger)(\mathcal{X} \times \mathcal{Y} \times \mathcal{T}), \quad (2.40)$$

and in the frequency domain,

$$\mathbf{R}_{\mathbf{a}', \mathbf{b}'}(\mathbf{v}, \mathbf{w}, f) = \mathbf{G}(\mathbf{v}, f) \mathbf{R}_{\mathbf{a}, \mathbf{b}}(\mathbf{v}, \mathbf{w}, f) \mathbf{H}^H(\mathbf{w}, f). \quad (2.41)$$

In the second case of interest, $\underline{\nu} = \underline{\omega}$ and both are shift-invariant with respect to $\underline{\mu}$, but $\underline{\mu}$ is not shift-invariant with respect to $\underline{\nu}$. This guarantees that $\underline{\mu}$ is a discrete-time reference measure, because Lebesgue measure is shift invariant with respect to all other reference measures. If we let groups $\mathcal{M} = T\mathbb{Z}$ and \mathcal{V} be the support of $\underline{\mu} = \underline{\Sigma}_{T\mathbb{Z}}$ and $\underline{\nu}$, respectively, then this also guarantees that \mathcal{M} is a proper subgroup of \mathcal{V} . This represents the case where $\underline{\mathbf{a}}$ and $\underline{\mathbf{b}}$ are “promoted”, via filtering, from discrete-time reference measure $\underline{\mu}$ to reference measure $\underline{\nu}$, which is either continuous-time or discrete-time on a superlattice of $T\mathbb{Z}$. Here both $\underline{\mathbf{a}'}$ and $\underline{\mathbf{b}'}$ have reference measure $\underline{\nu}$. A notable example is the case where $\underline{\mathbf{a}}$ and $\underline{\mathbf{b}}$ are discrete-time, and $\underline{\mathbf{g}}$ and $\underline{\mathbf{h}}$ are continuous-time. A straightforward application of the cross-correlation definition as before will fail, because the expectation will not be a function of only the difference of the temporal arguments of the densities of $\underline{\mathbf{a}}$ and $\underline{\mathbf{b}}$. As defined, $\underline{\mathbf{a}'}$

and \underline{b}' are not stationary, but rather cyclostationary with a period in t that is defined by any set of coset representatives $[\mathcal{V}/\mathcal{M}]$. We borrow a standard approach from communication theory to remedy this, by applying a random delay u to the outputs \underline{a}' and \underline{b}' , where u is uniformly distributed over one period. This results in system outputs

$$\begin{aligned}\underline{a}'(\mathcal{X} \times (\mathcal{T} - u)) &= \int_{\mathcal{X}} \underline{h}(\mathcal{X} \times (\mathcal{T} - t' - u); -\mathbf{x}') \underline{a}(d\mathbf{x}' dt') \\ \underline{b}'(\mathcal{X} \times (\mathcal{T} - u)) &= \int_{\mathcal{X}} \underline{g}(\mathcal{X} \times (\mathcal{T} - t' - u); -\mathbf{x}') \underline{b}(d\mathbf{x}', dt')\end{aligned}$$

and the corresponding cross correlation is

$$\mathbf{r}_{\underline{a}', \underline{b}'}(\mathcal{X} \times \mathcal{Y} \times \mathcal{T}) = \frac{1}{\int_{[\mathcal{V}/\mathcal{M}]} \nu(dt)} (\mathbf{h} \boxtimes \mathbf{r}_{ab} \boxtimes \mathbf{g}^\dagger)(\mathcal{X} \times \mathcal{Y} \times \mathcal{T}), \quad (2.42)$$

which is just a scaled version of the previous result (2.37). The derivation is given in Appendix B.3. For $\mathcal{V} = \mathbb{R}$ and $\mathcal{M} = T\mathbb{Z}$, the scale factor is $1/T$.

2.2 Temporal Delta-Sigma Modulation

2.2.1 History and Motivation

Traditional or *Nyquist* converters (so called because the signal can fill the entire Nyquist band) employ a high resolution quantizer, running at the full data rate. In Nyquist DAC's the quantized output is usually generated by a binary-weighted current network, while in Nyquist ADC's the fastest (so-called flash) converters use resistive-divider networks feeding a bank of comparators. It has often been observed that performance increases in data converters considerably lags that of DSP circuits, and it seems that for high-speed (100's of MHz to ~ 1.5 GHz) DAC's and ADC's the resolution of conventional data converter architectures has hit a ceiling at around 14–16 bits. At this point, the smallest current or resistor becomes impractically small, and circuit errors start to dominate without custom trimming of the circuit.

An alternative to Nyquist conversion is *noise-shaped* conversion [41, 42], widely known as $\Delta\Sigma$ *conversion* for historical reasons. The fundamental premise of noise-shaped conversion is that it is easier to make a fast, low-resolution quantizer (A/D) or output driver (D/A) than a slower, high-resolution one. In a $\Delta\Sigma$ converter a low-resolution quantizer is used, often only a single bit (two levels). The particular attraction of a two-level quantizer is that it is, in a sense, perfect; any errors in the two levels result only in a constant offset and a gain error, effects that are harmless in many applications. This oft-repeated assumption can be misleading, however, because nonlinear intersymbol interference (ISI) can cause errors even for a two-level quantizer [43]. The fundamental tradeoff in noise-shaped conversion is resolution for speed. To achieve comparable performance to high-resolution Nyquist conversion, low-resolution noise-shaped conversion must operate at a much higher clock rate. This is called temporal *oversampling*, and the ratio of clock rate to two-sided signal bandwidth is the temporal *oversampling ratio*. As a result, to date the primary use of noise shaping has been at audio frequencies, where $\Delta\Sigma$ conversion has become the method of choice for high-resolution A/D and D/A conversion. Noise-shaping D/A conversion is found in nearly every CD player, for example.

Although noise-shaping is used for both D/A and A/D conversion, here we will focus on the former. Noise-shaped D/A conversion is normally thought of in three stages. The first is *noise-shaped coding*, widely known as $\Delta\Sigma$ *modulation* for historical reasons. Here a high-resolution digital signal is reduced to a low resolution digital signal, and the large amount of quantization noise that results from the coarse quantization is spectrally shaped to minimize interference with the signal. The resulting low-resolution digital output is then converted to an analog signal via linear pulse modulation. This analog signal contains a great deal of quantization noise outside the signal band, and so the third stage consists of analog filtering to pass only the signal band. In practice the pulse modulator and the filter might be integrated. The linear pulse modulator can be viewed as a low-resolution Nyquist DAC in its own right, which can lead to terminological confusion. We therefore adopt

the convention that the cascade of all three stages constitutes a noise-shaped or $\Delta\Sigma$ DAC, which performs noise-shaped or $\Delta\Sigma$ D/A conversion. Unqualified references to the DAC or to the DAC pulse response will refer only to the pulse modulator.

Recently there has been a great deal of interest in using $\Delta\Sigma$ DAC's at microwave rates for RF systems like radar and communications. Two primary factors motivate this. First, there is the aforementioned sluggish growth in Nyquist-converter performance, due to the complex analog circuit design. Improving the performance of a $\Delta\Sigma$ DAC, on the other hand, can be achieved by increasing the actual or effective (via parallelization [44]) clock rate. Currently DSP performance is improving far faster than Nyquist converter performance, and so we might expect that $\Delta\Sigma$ DAC's will also improve faster than Nyquist DAC's. ($\Delta\Sigma$ ADC's are primarily analog circuits, so this does not apply to them). The second factor is the need for highly linear digital-to-analog conversion at high power levels, for applications like shared transmit arrays. High power Nyquist D/A conversion has traditionally consisted of a low-power Nyquist DAC followed by a power amplifier. But RF power amplifiers are highly nonlinear devices unless operated far below their maximum power levels, at which point they become quite inefficient. With a $\Delta\Sigma$ DAC, a high-power output could be created by using a high-power output driver, without using a conventional power amplifier. In the case of a single-bit output, the pulse modulator would essentially be a high-power switch [45, 46]. This is an area of research in its infancy, however, and it does not necessarily solve the efficiency problem.

2.2.2 System Analysis and Design

Figure 2.1 shows the system model for $\Delta\Sigma$ D/A conversion, which consists of the $\Delta\Sigma$ modulator followed by linear pulse modulation and analog filtering. The modulator consists of a feedback loop wrapped around a low resolution quantizer, with an LTI filter in the feedback path. The modulator is shown in an *error feedback* architecture, where the quantization error is fed back through the loop filter. This is the most common architecture

for $\Delta\Sigma$ DAC applications due to its simplicity. Conceptually, the $\Delta\Sigma$ modulator attempts to predict the in-band portion of the quantization error, and subtracts it out before the quantizer. Thus the loop filter is a one-step-ahead signal-band predictor. The input \underline{s} and output \underline{q} of the modulator are discrete time, with a sample interval of T , while the final filtered output y is of course continuous time. We will initially assume that the input \underline{s} is a WSS random signal, because it leads to simpler analysis. We will later let the input be deterministic with finite support, and show how signal length affects the output. Finite length effects are almost universally overlooked in conventional $\Delta\Sigma$ analysis, but many potential applications (such as radar [47] and arbitrary waveform generation [48]) use pulsed or repeated waveforms.

We begin our analysis here with the quantizer input u :

$$\underline{u}(dt) = \underline{s}(dt) - (\underline{g} * \underline{e})(dt),$$

where the quantization error \underline{e} is assumed to be an additive WSS noise process. By the definition of the quantization error we have

$$\begin{aligned} \underline{q}(dt) &= \underline{u}(dt) + \underline{e}(dt) \\ &= \underline{s}(dt) - (\underline{g} * \underline{e})(dt) + \underline{e}(dt), \end{aligned}$$

or, combining the last two terms,

$$\boxed{\underline{q}(dt) = \underline{s}(dt) + (\underline{h} * \underline{e})(dt)}, \quad (2.43)$$

where *noise-shaping measure* \underline{h} is defined as

$$\underline{h}(dt) \triangleq \underline{\delta}(dt) - \underline{g}(dt). \quad (2.44)$$

The Fourier transform of \underline{h} ,

$$\boxed{H(f) = 1 - G(f)e^{-j2\pi fT}}, \quad (2.45)$$

is called the *noise transfer function* (NTF), as it is the equivalent response applied to the quantization noise at the output. Finally, the analog output results from pulse-modulating and filtering the quantizer output:

$$\boxed{y(dt) = (\underline{h}_A * \underline{s})(dt) + (\underline{h}_A * \underline{h} * \underline{e})(dt).} \quad (2.46)$$

We now make two assumptions: that the quantization noise density is white with power (variance) σ^2 , and that the input and the error signals are uncorrelated. Although it is difficult to rigorously justify either assumption [49], especially for single-bit quantization, in practice both almost always suffice. An alternative approach that models correlation introduced by the quantizer is found in [50]. The autocorrelation and power spectral density at the quantizer output are

$$r_q(dt) = r_s(dt) + (\underline{h} * r_e * \underline{h}^\dagger)(dt) \quad (2.47a)$$

$$= r_s(dt) + \sigma^2 (\underline{h} * \underline{h}^\dagger)(dt) \quad (2.47b)$$

and

$$R_q(f) = R_s(f) + |H(f)|^2 R_e(f) \quad (2.48a)$$

$$= R_s(f) + \sigma^2 |H(f)|^2 \quad (2.48b)$$

Thus the NTF completely determines the noise spectrum coming out of the quantizer. Finally, the DAC output y has the power spectrum

$$\boxed{R_y(f) = \frac{1}{T} |H_A(f)|^2 R_s(f) + \frac{\sigma^2}{T} |H_A(f)|^2 |H(f)|^2.} \quad (2.49)$$

The combination of the DAC pulse and any further analog filtering, represented by frequency response $H_A(f)$, must pass the desired signal while removing the shaped quantization noise.

2.2.3 Example

A simple example design will help illustrate. Assume a binary quantizer with output levels $\{\pm 1\}$ and a one-sided bandpass signal bandwidth of $\frac{1}{64T}$ (an oversampling ratio of 32) at a

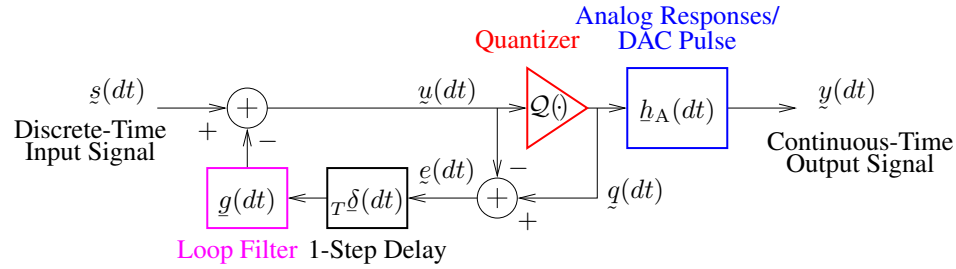


Figure 2.1: A $\Delta\Sigma$ DAC, consisting of an error-feedback $\Delta\Sigma$ modulator followed by low-resolution digital-to-analog conversion and filtering.

signal center frequency of $\frac{1}{4T}$. The loop filter is causal and FIR, with 41 coefficients:

$$\underline{g}(dt) = \sum_{n=0}^{40} g(nT) {}_{nT}\underline{\delta}(dt).$$

We wish to design the loop filter to minimize the in-band quantization noise power, which is equivalent to minimizing the mean-square value of $H(f)$ in the signal band. Why not simply make $H(f)$ small everywhere? The answer lies in (2.44); the density (coefficient) of causal filter \underline{h} at $t = 0$ is fixed at unity; thus the total noise gain $\sum_n |h(nT)|^2$ of the filter is lower bounded by unity. Pushing down H in one spectral region will result in an increased value of H elsewhere.

We can design the loop filter by solving the following optimization problem:

$$\text{minimize } \alpha \geq 0 \quad (2.50a)$$

$$\text{s.t. } \int_{\mathcal{F}} |H(f)|^2 df \leq \alpha^2 \quad (2.50b)$$

$$|G(f_k)| \leq 1.6, \quad \text{for } k = 1, \dots, K_{\text{freqs}}. \quad (2.50c)$$

This can be solved as a second-order cone program (SOCP), which is described in Appendix F. The objective (2.50a) and quadratic constraint (2.50b) together minimize the noise power in signal band \mathcal{F} , recalling the NTF definition (2.45). The auxiliary variable α is used as a “dummy” objective, since SOCP requires a linear objective. Numerically the integral was computed exactly using the approach of [51, 52], in which a test-input with power spectrum $1_{\mathcal{F}}(f)$ is (conceptually) sent through the filter, and the output power is

measured. An alternative approach is to use a Riemann sum on a dense set of frequencies covering the signal band \mathcal{F} . The set of quadratic constraints (2.50c) together serve as a *stability constraint*; they limit the maximum gain of the loop filter over a uniformly spaced set of frequencies $\{f_k\}$ across one period of the filter frequency response. Since this is the transfer function from the error to the quantizer input, if the gain becomes too large the input to the quantizer will go into overload (the input is larger than the largest output). Although the $\Delta\Sigma$ modulator can tolerate some overload, beyond a threshold it will result in oscillation, and useful operation will cease. This is referred to as instability, although it is not rigorously defined as in linear systems. In an unstable modulator, the assumption that the quantization noise is white and uncorrelated with the signal fails to hold. The maximum gain level (1.6 here) is usually determined experimentally; analytical results tend to be restricted to very simple cases [42, 50]. The maximum stable gain level increases with the number of quantizer levels, and decreases with an increasing peak input level. Alternative stability constraints include bounding mean-square (power) gain

$$\sum_n |g(nT)|^2 \leq G_{\text{mse}}$$

or peak NTF gain

$$|1 - G(f)e^{-j2\pi fT}| \leq H_{\text{peak}}.$$

Similar optimization approaches are found in [53, 54]. Many alternative or complimentary means for maintaining stability have been examined [55, 56, 57].

An input signal consisting of three sinusoids was input to the modulator; the computed power spectrum at the quantizer output is shown in the blue curve of Figure 2.2. The theoretical power spectrum of (2.48a) is overlayed in red for comparison, where we can solve for the noise power as

$$\sigma^2 = \frac{\mathcal{P}_q - \mathcal{P}_s}{T \int_{[0, T^{-1})} |H(f)|^2 df},$$

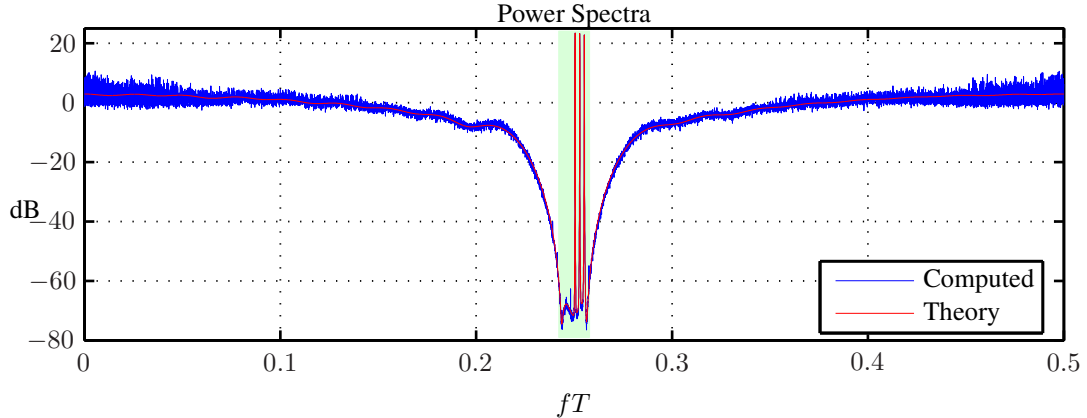


Figure 2.2: Computed and theoretical power spectra at the quantizer output for the $\Delta\Sigma$ example.

with $\mathcal{P}_q = 1$ here because of the unit-magnitude output levels. The close agreement between the two serves to validate the assumptions on the quantization noise.

2.2.4 Finite-Length Analysis

For applications such as free-running communications, the preceding random-signal analysis is sufficient as the stationarity assumption on \underline{e} is plausible. This is not the case, however, for deterministic input signals of finite duration, such as are often used in radar. Stationarity in \underline{e} would require that the modulator be free-running with zero input prior to the start of the input signal, and then left running with zero input after. In practice only the temporal portion of the quantized waveform \underline{q} containing the signal is output. We assume then that the output noise can be represented as a finite-length segment of a stationary signal. Since this finite-length waveform is not itself stationary, it does not have a true spectral density. Instead of deriving a spectral density, then, we will derive the normalized expected value of the magnitude squared of the Fourier transform of the finite-length signal $w(t)\underline{q}(dt)$, where $w(t)$ is a real, nonnegative window function with support on the interval $[0, T_s)$:

$$R_{w \times q}(f) \triangleq \frac{1}{\|w\|^2} \mathcal{E} \left\{ \left| \int e^{-j2\pi ft} w(t) \underline{q}(dt) \right|^2 \right\}, \quad (2.51)$$

where the normalization constant

$$\|w\|^2 \triangleq \int |w(t)|^2 \Sigma_{T\mathbb{Z}}(dt)$$

will be convenient later. The expression inside the expected value in (2.51), taken on a given realization of the random signal, is often referred to as the *periodogram* when a rectangular window is used, or as the *modified periodogram* in general. The periodogram is frequently used to estimate the PSD of stationary processes. As will be shown, it is an asymptotically unbiased estimator, meaning that its expected value converges to the PSD for large T_s . We use the periodogram in this section not as a spectral estimator, however, but as a tool to analyze the spectral properties of a finite-length sequence excised from a stationary process.

We wish to compute (2.51) for the sum $q = \underline{s} + \underline{x}$ of a deterministic discrete-time signal \underline{s} with support in $[0, T_s)$ and a wide-sense stationary, zero-mean discrete-time random signal \underline{x} . Expanding and rearranging yields

$$\begin{aligned} R_{w \times q}(f) &= \frac{1}{\|w\|^2} \mathcal{E} \left\{ \int e^{-j2\pi ft} w(t) [\underline{s}(dt) + \underline{x}(dt)] \left(\int e^{-j2\pi ft'} w(t') [\underline{s}(dt') + \underline{x}(dt')] \right)^* \right\} \\ &= \frac{1}{\|w\|^2} \mathcal{E} \left\{ \iint e^{-j2\pi f(t-t')} w(t) w(t') [s(t)s^*(t') + x(t)x^*(t')] \Sigma_{T\mathbb{Z}}(dt) \Sigma_{T\mathbb{Z}}(dt') \right\}. \end{aligned}$$

The integrals here are finite sums, and so we can bring the expectation inside the integrals:

$$R_{w \times q}(f) = \frac{1}{\|w\|^2} \iint e^{-j2\pi f(t-t')} w(t) w(t') [s(t)s^*(t') + r_x(t-t')] \Sigma_{T\mathbb{Z}}(dt) \Sigma_{T\mathbb{Z}}(dt').$$

Now we assume the inverse Fourier-transform relation

$$w(t) \Sigma_{T\mathbb{Z}}(dt) = \left(T \int_{[0, T^{-1})} e^{j2\pi ft} W(f) df \right) \Sigma_{T\mathbb{Z}}(dt)$$

exists, and substituting and rearranging yields

$$\begin{aligned} R_{w \times q}(f) &= \frac{T^2}{\|w\|^2} \int_{[0, T^{-1})} \int_{[0, T^{-1})} \iint e^{-j2\pi(f-f')t} e^{j2\pi(f+f'')t'} \times \\ &\quad W(f') W(f'') s(t) s^*(t') \Sigma_{T\mathbb{Z}}(dt) \Sigma_{T\mathbb{Z}}(dt') df' df'' \\ &\quad + \frac{T}{\|w\|^2} \int_{[0, T^{-1})} \iint e^{-j2\pi(f-f')t} e^{j2\pi f t'} W(f') w(t') r_x(t-t') \Sigma_{T\mathbb{Z}}(dt) \Sigma_{T\mathbb{Z}}(dt') df'. \end{aligned}$$

Recognizing multiple Fourier transforms and rearranging results in

$$R_{w \times q}(f) = \frac{T^2}{\|w\|^2} \int_{[0, T^{-1})} W(f') S(f - f') df' \int_{[0, T^{-1})} W^*(-f'') S^*(f + f'') df'' \\ + \frac{T}{\|w\|^2} \int_{[0, T^{-1})} \int e^{j2\pi f' t'} W(f') w(t') R_x(f - f') \Sigma_{T\mathbb{Z}}(dt') df',$$

and recognizing another Fourier transform in the second term and conjugate products in both terms yields

$$R_{w \times q}(f) = \frac{T^2}{\|w\|^2} \left| \int_{[0, T^{-1})} W(f') S(f - f') df' \right|^2 + \frac{T}{\|w\|^2} \int_{[0, T^{-1})} |W(f')|^2 R_x(f - f') df'.$$

Defining the circular convolution of periodic functions A and B , both with period T^{-1} , as

$$(A \star_{T^{-1}} B)(f) \triangleq T \int_{[0, T^{-1})} A(f - f') B(f') df',$$

this simplifies to

$$\boxed{R_{w \times q}(f) = \frac{1}{\|w\|^2} |(W \star_{T^{-1}} S)(f)|^2 + \frac{1}{\|w\|^2} (|W|^2 \star_{T^{-1}} R_x)(f),} \quad (2.52)$$

where we use the notation $|W|^2(f) \triangleq |W(f)|^2$ to simplify the second term. The first term is just the normalization constant times the magnitude squared of the Fourier transform of the windowed deterministic signal, verifying the classic result that the Fourier transform of the product of sequences is the circular convolution of their respective Fourier transforms. The second term of the periodogram is related to the original spectral density of \underline{x} through circular convolution with the nonnegative kernel $|W(f)|^2$. When the random signal $q(dt)$ is continuous-time, a similar derivation reveals that

$$\boxed{R_{w \times q}(f) = \frac{1}{\|w\|^2} |(W * S)(f)|^2 + \frac{1}{\|w\|^2} (|W|^2 * R_x)(f),} \quad (2.53)$$

where the window frequency response $W(f)$ is nonperiodic, the spectral convolutions are now linear, not circular, and the normalization constant is

$$\|w\|^2 \triangleq \int |w(t)|^2 dt.$$

Having obtained the general result, we can now substitute shaped $\Delta\Sigma$ output noise spectrum $R_x(f) = \sigma^2|H(f)|^2$ into (2.52):

$$R_{w \times q}(f) = \frac{1}{\|w\|^2} |(W \star_{T-1} S)(f)|^2 + \frac{\sigma^2}{\|w\|^2} (|W|^2 \star_{T-1} |H|^2)(f). \quad (2.54)$$

The effect is to replace the original NTF magnitude squared response $|H(f)|^2$ with

$$|H_w(f)|^2 = \frac{1}{\|w\|^2} (|W|^2 \star_{T-1} |H|^2)(f). \quad (2.55)$$

For $|H_w(f)|^2$ to be a good approximation of $|H(f)|^2$, $|W(f)|^2$ should have a single narrow mainlobe and low sidelobes across one spectral period. Unfortunately, for a given window length T_s these are opposing ideals. In using the periodogram for numerical analysis of $\Delta\Sigma$ outputs, preference is given to low sidelobes, because the high dynamic range between the noise floors in and out of the signal band is especially sensitive to the sidelobes of the convolution kernel spreading out-of-band noise into the previously clean signal band. If we use the periodogram instead to modeling the output of a physical $\Delta\Sigma$ -based D/A system operating on finite-length inputs, the window function cannot be chosen arbitrarily; in most cases hardware constraints enforce $w(t) = 1_{[0, T_s)}(t)$. The corresponding Fourier transform is

$$W(f) = \lceil T_s/T \rceil D_{\lceil T_s/T \rceil}(fT) e^{-j\pi fT(\lceil T_s/T \rceil - 1)},$$

where $\lceil \cdot \rceil$ denotes the ceiling (round-up) function and

$$D_N(f) \triangleq \frac{\sin(N\pi f)}{N \sin(\pi f)}$$

is a N th-order *Dirichlet kernel*, sometimes called the ‘‘sampled sinc’’ function. Since in this case $w(t)\underline{s}(dt) = \underline{s}(dt)$ and $\|w\|^2 = \lceil T_s/T \rceil$, (2.54) reduces to

$$R_{w \times q}(f) = \frac{1}{\lceil T_s/T \rceil} |S(f)|^2 + \frac{\sigma^2}{\lceil T_s/T \rceil} (|W|^2 \star_{T-1} |H|^2)(f). \quad (2.56)$$

Unfortunately, the Dirichlet kernel has relatively high (-13 dB) sidelobes, and thus the SNR achievable using conventional $\Delta\Sigma$ modulation on finite-length waveforms is limited

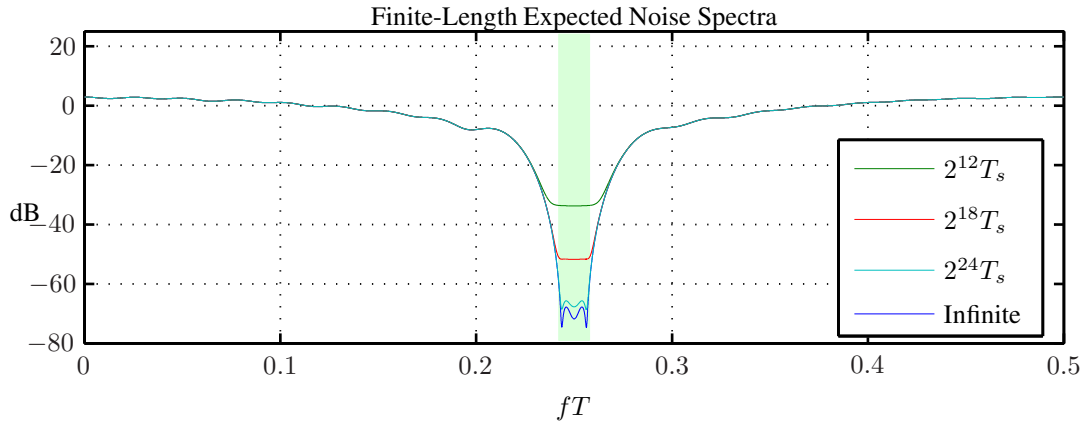


Figure 2.3: The expected noise spectra for $\Delta\Sigma$ modulated sequences of various lengths.

by the waveform length. As an example, consider the NTF designed above, with signal durations of $2^{12} \times T$, $2^{18} \times T$, and $2^{24} \times T$. Figure 2.3 plots the noise term of (2.54) for each length, and for the infinite-length (WSS) case. It takes a signal length of greater than 16 million output samples to get the expected noise periodogram close to the infinite-length case. Significant performance is lost for shorter sequences.

To be an asymptotically unbiased estimator, the expected noise periodogram must converge to the PSD of the stationary shaped noise as the window is lengthened. We write the limit as

$$\begin{aligned} \lim_{T_s \rightarrow \infty} R_{w \times q_e}(f) &= \lim_{T_s \rightarrow \infty} \frac{\sigma^2}{\lceil T_s/T \rceil} (|W|^2 \star_{T^{-1}} |H|^2)(f) \\ &= \lim_{T_s \rightarrow \infty} \sigma^2 \int_{[0, T^{-1})} \left(T \lceil T_s/T \rceil |D_{\lceil T_s/T \rceil}(f'T)|^2 \right) |H(f - f')|^2 df'. \end{aligned}$$

Here we see that the normalization constant was chosen so that the integrand factor in parenthesis has unit area per period. As the window length grows larger the window frequency response grows narrower, and the area is increasingly concentrated around the points $\{T^{-1}\mathbb{Z}\}$. Since NTF H is continuous, in the limit the integral “sifts” the value $H(f)$, and

$$\lim_{T_s \rightarrow \infty} R_{w \times q_e}(f) = \sigma^2 |H(f)|^2$$

as desired. The same result can be achieved with any standard window parameterized on

length.

A final caveat is in order. The results of this section give only the expected energy spectrum for a finite length sequence; a given realization may deviate significantly from the ensemble average. Examples can be readily constructed that greatly exceed or fall short of expected performance. $\Delta\Sigma$ modulation is a sequential computation; the modulator does not know how long it will run, and it does not optimize the spectrum for any given length. Its strength is that it gives good results in real time with a computational load that has linear dependence on sequence length. The computation required for direct optimization of integer-valued sequences, on the other hand, grows exponentially with sequence length, and is impractical for all but the shortest sequences. Another view of finite-length $\Delta\Sigma$ modulation is found in [58], in which the modulator is analyzed as a vector quantizer.

2.2.5 Extensions

Several extensions of the basic $\Delta\Sigma$ modulator have been reported. Although multilevel quantization inside the $\Delta\Sigma$ loop has many advantages, static quantizers require often impractical levels of precision when used for noise shaping. Dynamic quantizer techniques [59, 60, 61, 62, 63], commonly referred to as *dynamic element matching* (DEM), allow spectral shaping of hardware mismatch errors similar to quantization error shaping. Vector valued $\Delta\Sigma$ modulation has several applications, including power systems [64] and integrating DEM and $\Delta\Sigma$ modulation [65], among others [66, 67]. Multidimensional $\Delta\Sigma$ modulation was reported in [26], where one scalar $\Delta\Sigma$ modulator operating along a spatial dimension of a sonar beamformer was operated nested inside of a temporal modulator. This is very much in the spirit of Chapter 4 of this dissertation, which generalizes multidimensional $\Delta\Sigma$ considerably.

2.3 Spatial Delta-Sigma Modulation: Image Halftoning

Halftoning is the process of reducing a continuous-valued image to a discrete-valued image, generally for reproduction on equipment with high spatial resolution but limited color range. The most common examples are laser and inkjet printers, but many handheld computers, stadium scoreboards and bank signs have similar restrictions. Most commonly the output is binary-valued, corresponding to (for example) the decision to place or not to place a drop of ink at a given location. Halftoning takes advantage of the spatial-lowpass nature of the human visual system to filter out the inevitable quantization noise that results.

Many methods exist for halftoning [68, 69], ranging from simple pattern substitution (screening) to direct local minimization of an integer programming problem (direct binary search or DBS) [70]. The former is incredibly simple, but produces poor results. The latter generally produces the best results, but is very computationally intensive and requires an indeterminate number of iterations. Of greatest interest here, however, is *error diffusion* halftoning, introduced by Floyd and Steinberg in their now-classic 1976 paper [71]. Error diffusion, as was later recognized [72], is in fact two-dimensional (spatial) $\Delta\Sigma$ modulation. It is modeled as space-invariant by ignoring the clipping operation that maintains the image size. The error-feedback loop leads to a higher computational complexity than screening, but the number of computations per pixel is fixed and is generally much less than for DBS. Depending on the loop filter, the quality of error diffusion can be close to that of DBS. A vector version of error diffusion can be used for color images [73]. An example of Floyd-Steinberg error diffusion is shown in Figure 2.4. Viewed from far enough away, the pixelation disappears and the eye sees continuous tones.

Although structurally error-diffusion halftoning is identical to temporal $\Delta\Sigma$ modulation, the design criteria are somewhat different. In the latter case, the goal is high SNR and thus high quantization noise suppression in the band of interest. The result is a very steep transition from the signal band to the noise band, which requires correspondingly steep

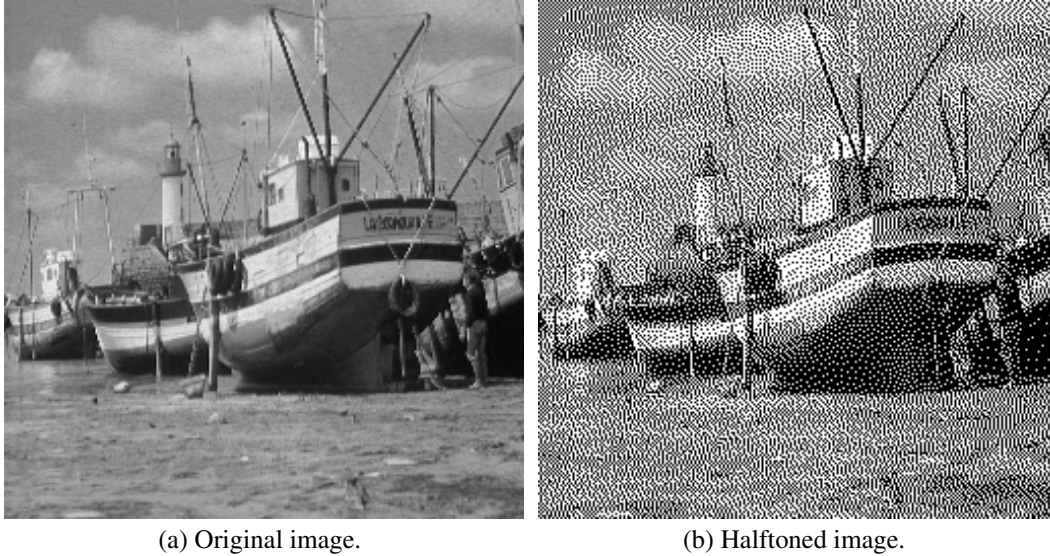


Figure 2.4: Example of Floyd-Steinberg error-diffusion halftoning.

analog filtering at the output. The transfer function of the eye, on the other hand, has a much more gradual rolloff and is a function of viewing distance. Perceptual quality is maximized with a correspondingly more gradual transition of the shaped noise spectrum from low to high frequency. One consequence of this is that filters used for halftoning tend to be fairly short (the original Floyd-Steinberg filter had just four nonzero coefficients), while those used for D/A conversion tend to be as long as is practical.

Chapter 3.

Wideband Transmit Antenna Arrays

Once computationally impractical, wideband digital antenna arrays are now a reality thanks to the continued evolution of computing power. Whereas formerly wideband arrays required switched analog delay elements and attenuators, now the (nonadaptive) array-pattern synthesis can be performed by digital filtering of data at the antenna, with the usual gains in precision and flexibility. A conventional approach to digital pattern synthesis is to simply approximate the analog hardware with digital filters. This has the same drawback as the analog system it replaces—it places artificial restrictions on the resulting array pattern. In most cases even ideal time-delay steering results in a suboptimal array response. It seems appropriate to rethink the problem of array pattern design from first principles taking an optimization viewpoint, since the tools now exist [74, 75, 76, 77] to solve large problems posed as convex programs.

Narrowband array-pattern design is a well-studied topic. The earliest works were analytical, predating widespread use of numerical optimization. Examples include Dolph's use of Chebychev polynomials to create equiripple array patterns [78] and Taylor's classic line-source distribution [79], which in its sampled form is widely used for arrays to this day. Many of the papers from that era focus on *superdirectivity* [80, 81, 82, 83, 84], an enticing but usually impractical result which represents a poorly conditioned solution to an underconstrained optimization [24]. More recently, optimization techniques have been

used to limit superdirectivity [85, 86, 87]. It has long been recognized that there is a direct relationship between the array pattern of a uniform narrowband array and the frequency response of a multidimensional FIR filter [88], an idea that was extended to wideband arrays in [22]. Thus the same tools that are used to design FIR filters can be used to design array patterns. Optimization techniques used for array-pattern design include second-order cone programming [89, 24, 23, 22], semidefinite programming [90], iterative least-squares [91, 92, 93] and eigendecomposition [94].

This chapter will focus on transmit arrays, although reciprocity could be invoked to apply most of the results to receive arrays. As mentioned in the introduction, transmit arrays have fallen behind receive arrays in terms of aperture sharing and custom array patterns due to stricter hardware requirements on transmit. Throughout it will be assumed that the array and all associated analog hardware such as amplifiers, filters, and feed structures are linear and time invariant. On transmit, most conventional systems operate their amplifiers in heavy saturation for reasons of power efficiency; this work does not directly apply to such systems. Looking ahead, the spatio-temporal $\Delta\Sigma$ modulated array of Chapter 4 offers a path to linear transmit arrays and array sharing.

This chapter contains two major points of departure from conventional narrowband array theory. The first is that multiple simultaneous transmit signals are permitted, which results in a vector array input. The second is that standard narrowband array metrics such as directivity and gain become frequency dependent when extended to the wideband case. Implicit in narrowband array theory is that the input is a sinusoid, or at least has a negligible enough bandwidth that it can be treated as such. Since all inputs (deterministic or random) are essentially the same to within a magnitude and a phase, the input can be effectively factored out of most analysis. For wideband arrays this is clearly not the case, and so we face the dilemma of how to define signal-independent wideband performance metrics for use in characterization and optimization of the array pattern. The general approach taken here for random inputs is to assume an input that is white across the array's bandwidth. The

equivalent assumption for deterministic signals is an input with a Fourier transform that is constant across the array bandwidth. In both cases the intent is to lend equal weight to the entire band in the absence of *a priori* knowledge of the input signal. Indeed, this represents a convergence of the parallel deterministic/random derivations, as identical results can be obtained for both under these assumptions.

The first part of this chapter introduces a general passband-equivalent model of a wide-band digital transmit array. Analysis of the various intermediate signals and system components is traced from input to far-field radiation. Since the input signals to the array might be either deterministic or random, parallel derivations for both cases are carried out throughout the chapter. Intuition suggests that the results should be similar, and indeed we find a convenient correspondence between the deterministic and random derivations. This material is both a self-contained treatment and a necessary prerequisite for the following chapter on spatio-temporal $\Delta\Sigma$ arrays. The second half of the chapter considers various array-pattern optimization techniques, illustrated through a running set of example optimizations.

3.1 System Model and Input/Output Response

In this section, a passband-equivalent transmit-array model is presented that will be used in this and the next chapter. Signals are then traced from the input to the array element currents, with system components described along the way. Only deterministic signals are considered here; analysis of random signals is deferred until Section 3.3.

3.1.1 System Model

We start our analysis by choosing a system model that is relatively simple yet will accommodate most common hardware architectures. There is no “standard” digital transmit array architecture, but a typical chain will involve digital filtering and (nonadaptive) beamforming followed by D/A conversion and some amount of analog processing (filtering and

possibly frequency conversion) prior to the driver (power electronics) and the antenna array itself. For most of this chapter the specifics of the underlying hardware architecture are immaterial, and so we seek a simplified system model. In Section 3.4.1 an example array architecture is introduced that is used for a running series of example designs; at that time the mapping from hardware architecture to equivalent model is considered in more detail.

In analyzing systems that incorporate frequency conversion, a standard approach is to consider a baseband-equivalent system in which the frequency conversion is factored out of the model. This is especially useful when the input and output of the system are baseband signals. Here a passband-equivalent model is chosen instead, for several reasons. First, the output of a transmit array is a passband signal, not a baseband signal; the receive array is not modeled here. Second, rather than representing just another linear response, here electromagnetic propagation is a central part of the analysis. Since the properties of propagation depend heavily on the passband frequency, it is far more convenient to represent all signals and significant responses at passband, rather than at baseband. Third, the spatio-temporal $\Delta\Sigma$ system of Chapter 4, to which a great deal of the analysis in this chapter will be applied, is necessarily a passband system for which a baseband-equivalent model would be completely unnatural.

The passband-equivalent model used throughout the rest of this dissertation is shown in Figure 3.1. Passband-equivalent signal vector \underline{s} is the input to passband-equivalent beamformer matrix response \underline{b} . All nonideal analog frequency responses prior to the driver, including that due to D/A conversion, are combined into the equivalent response \underline{h}_A , which is assumed to be identical for each underlying converted signal (and thus is scalar and space-independent). Later in this chapter it will be convenient to commute \underline{h}_A with the beamformer response, so that the beamformer input has already been filtered by the analog responses. Following the analog-filter equivalent response is the ideal driver, converting unitless inputs into either a drive-current vector \underline{i} or voltage \underline{v} (the sequel will restrict attention to current drivers). The final pair of equivalent matrix responses \underline{p} and \underline{z} represent

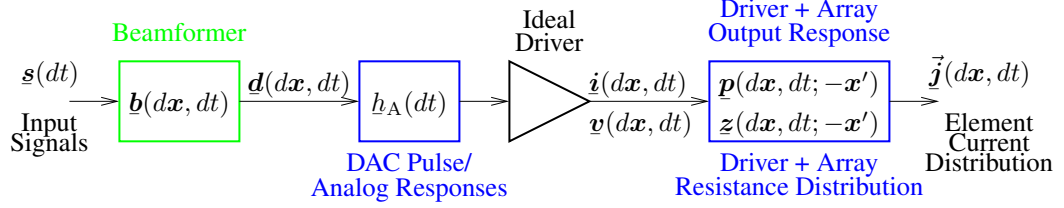


Figure 3.1: Passband-equivalent model of transmit beamformer and array.

a combination of all the underlying physical system responses after the driver, including any nonideal (linear) driver response, feed networks, and the array itself. Output response \underline{p} relates the output element-current distribution \vec{j} to the drive-current distribution \underline{i} , thus determining the radiating characteristics of the array. Resistance distribution \underline{z} relates the array input voltage \underline{v} to \underline{i} , which will be used to determine the power delivered by the drivers. These two equivalent responses are not independent, and indeed \underline{p} completely determines the component of \underline{z} that corresponds to radiation (rather than resistive losses). However, the relationship is complex and not described in the sequel; the interested reader is directed to [95].

3.1.2 Input/Output Response

Having introduced the passband-equivalent system model, we now proceed to trace signals from input to output. We will assume N independent passband-equivalent inputs to the array, represented by $N \times 1$ vector-valued signal measure $\underline{s}(dt)$. Although we assume the underlying physical input is discrete-time, the passband equivalent input can be either discrete-time or continuous-time, depending on the system architecture. Passband-equivalent beamformer response $\underline{b}(d\mathbf{x}, dt)$, an $M \times N$ matrix-valued measure, converts the temporal signals into a $M \times 1$ space-time signal $\underline{d}(d\mathbf{x}, dt)$. The beamformer is discrete-space, and has the form

$$\underline{b}(d\mathbf{x}, dt) = \sum_{\mathbf{x} \in \mathcal{L}} \underline{b}(\mathbf{x}, dt) \mathbf{x} \underline{\delta}(d\mathbf{x}), \quad (3.1)$$

where spatial support \mathcal{L} is the set of element locations in the array. (More on this shortly.) The number of rows of $\underline{\mathbf{b}}$, M , represents the number of distinct antenna elements at each location. This provides a convenient representation for configurations such as an array of dual-polarized elements. This representation is somewhat redundant in that we can equivalently represent an array of groups of M element types at K locations as an array of single elements at MK locations, by redefining the element responses to avoid duplicate locations. Likewise, we could remove the explicit spatial dependence of the beamformer altogether by assigning each array element to a vector component (indeed, this is the most common approach in the literature.) Thus the choice of how to represent a particular array is often a matter of convenience. For arrays with only one element per location, $M = 1$ and $\underline{\mathbf{d}}$ becomes a scalar. As with the input signal, the physical beamformer is discrete-time but the passband-equivalent response may be either discrete-time or continuous time depending on the underlying architecture. Beamformer output $\underline{\mathbf{d}}(d\mathbf{x}, dt)$ is also discrete-space, and can be written variously as

$$\underline{\mathbf{d}}(d\mathbf{x}, dt) = (\underline{\mathbf{b}} * \underline{\mathbf{s}})(d\mathbf{x}, dt) \quad (3.2a)$$

$$= \sum_{\mathbf{x} \in \mathcal{L}} (\underline{\mathbf{b}} * \underline{\mathbf{s}})(\mathbf{x}, dt) \mathbf{x} \delta(d\mathbf{x}) \quad (3.2b)$$

$$= \sum_{n=1}^N \sum_{\mathbf{x} \in \mathcal{L}} (\underline{\mathbf{b}}_n * \underline{\mathbf{s}}_n)(\mathbf{x}, dt) \mathbf{x} \delta(d\mathbf{x}), \quad (3.2c)$$

the last making explicit that the n th beamformer column $\underline{\mathbf{b}}_n(\mathbf{x}, dt)$ is a vector of M LTI filter responses mapping the n th input signal $\underline{\mathbf{s}}_n$ to the M elements located at position \mathbf{x} . As mentioned previously, the analog responses of the DAC and any other analog filtering that precedes the final power driver are combined into the scalar response $\underline{h}_A(dt)$, implicitly assuming that each DAC/filter chain is identical. Normally precompensation for unwanted analog responses would take place in the generation of the input signal. Since \underline{h}_A is scalar we can commute the operation to the beginning in the math to associate it with $\underline{\mathbf{s}}$, and define

the equivalent converted signal measure

$$\underline{\mathbf{s}}_A \triangleq (\underline{\mathbf{s}} * \underline{h}_A)(dt). \quad (3.3)$$

This provides notational convenience for the derivations to come and also stresses the primacy of the converted signal over the original digital signal. At the output of this equivalent filter the signal is unitless, and lacks physical meaning. The driver in the model serves simply to convert this unitless signal into the physical array drive signal, either drive-current distribution $\underline{\mathbf{i}}(d\mathbf{x}, dt)$ or drive-voltage measure $\underline{\mathbf{v}}(d\mathbf{x}, dt)$. Both are discrete-space and continuous-time. We will assume current drivers in the sequel, and so we have

$$\underline{\mathbf{i}}(d\mathbf{x}, dt) = (\underline{\mathbf{d}} * \underline{h}_A)(d\mathbf{x}, dt) \quad (3.4a)$$

$$= (\underline{\mathbf{b}} * \underline{\mathbf{s}} * \underline{h}_A)(d\mathbf{x}, dt) \quad (3.4b)$$

$$= (\underline{\mathbf{b}} * \underline{\mathbf{s}}_A)(d\mathbf{x}, dt) \quad (3.4c)$$

The density of the drive-current distribution with respect to counting measure on space and Lebesgue measure on time has units of Amps, and the corresponding density of the voltage measure has units of Volts. This ideal driver represents the source in the Norton or Thevenin equivalent circuit for a real driver; the equivalent impedance here is merged with the array for simplicity. The *resistance distribution* $\underline{\mathbf{z}}(d\mathbf{x}, dt; -\mathbf{x}')$, is real-valued and has units of Ohms. It provides an linear time-invariant but space-varying model of the cascade of the nonideal part of the driver, the feed network, and the array proper as seen by the ideal driver. It relates the drive current and voltage as

$$\underline{\mathbf{v}}(d\mathbf{x}, dt) = (\underline{\mathbf{z}} \boxtimes \underline{\mathbf{i}})(d\mathbf{x}, dt). \quad (3.5)$$

As the driver output voltage does not directly affect radiation in this model, further discussion of the resistance distribution will be deferred until Section 3.4.4.

We are ultimately concerned with the fields radiated by the array, which by Maxwell's equations are dependent on the currents in the radiating elements of the array. These cur-

rents are represented here by the element-current distribution $\vec{\mathbf{j}}(d\mathbf{x}, dt)$, which has units $\text{A}\cdot\text{m}\cdot\text{s}$. If $\vec{\mathbf{j}}$ is absolutely continuous with respect to Lebesgue measure on $\mathbb{R}^3 \times \mathbb{R}$, then the corresponding element-current density $\vec{\mathbf{j}}$ has units A/m^2 . If the element currents are concentrated on the surfaces or lines defined by spatial base measures $\underline{\mu}$ or $\underline{\nu}$, respectively, then $\vec{\mathbf{j}}$ is absolutely continuous with respect to the product measure of $\underline{\mu}$ or $\underline{\nu}$ with Lebesgue measure on \mathbb{R} . The corresponding R-N derivative is either the current density on the element surfaces, with units A/m , or the current along the lines, with units of Amps. If the topology of an element results in a mixture of volume, surface, and line currents, then the element-current distribution can be defined as the sum of components with different reference measures.

The linear time-invariant but space-varying output response $\underline{\mathbf{p}}(d\mathbf{x}, dt; -\mathbf{x}')$ relates the element-current distribution to the drive current $\underline{\mathbf{i}}$. The element-current distribution $\vec{\mathbf{j}}$ is a 3×1 field vector (indicated by the overarrow), and thus $\underline{\mathbf{p}}$ has dimension $3 \times M$. For units consistency, $\underline{\mathbf{p}}$ has units of meters. The spatial reference measure (or measures) of $\underline{\mathbf{p}}$ is necessarily the same as for $\vec{\mathbf{j}}$. The element-current distribution is related to the drive current by

$$\vec{\mathbf{j}}(d\mathbf{x}, dt) = (\underline{\mathbf{p}} \boxtimes \underline{\mathbf{i}})(d\mathbf{x}, dt) \quad (3.6a)$$

$$\vec{\mathbf{j}}(\mathcal{X} \times \mathcal{T}) = \sum_{\mathbf{x}' \in \mathcal{L}} \int \underline{\mathbf{p}}(\mathcal{X} \times (\mathcal{T} - \tau); -\mathbf{x}') \underline{\mathbf{i}}(\mathbf{x}', d\tau) \quad (3.6b)$$

with the second line making the discrete-space nature of the drive current distribution explicit. Here we see that the measure $\underline{\mathbf{p}}(d\mathbf{x}, dt; -\mathbf{x}')$ is the spatio-temporal response of the element group at location \mathbf{x}' to the corresponding drive currents (representing the feeds for the multiple elements) in vector $\underline{\mathbf{i}}(\mathbf{x}', dt)$. We can see from (3.6b) that the spatial support \mathcal{L} of the driver current distribution $\underline{\mathbf{i}}$ is mathematically somewhat arbitrary, in the sense that $\underline{\mathbf{p}}$ can simply be redefined such that an identical element-current distribution $\vec{\mathbf{j}}$ will result if the spatial support of the drive-current is changed to some other set \mathcal{L}' of K locations. In practice we usually choose \mathcal{L} to match the physical locations of the element phase centers

at some reference frequency, and we will therefore refer to \mathcal{L} as the element locations in the sequel. (The phase center of an antenna is the point from which the far-field spherical wavefronts appear to emanate [95, Ch. 12.7].) In general the element response at each location can be different, but in the common special case where identical element responses are assumed at each location we have

$$\underline{p}(\mathcal{X} \times \mathcal{T}; -\mathbf{x}') = \underline{p}_0((\mathcal{X} - \mathbf{x}') \times \mathcal{T}) \quad (3.7)$$

and

$$\vec{\underline{j}}(d\mathbf{x}, dt) = (\underline{p}_0 \otimes \underline{i})(d\mathbf{x}, dt), \quad (3.8)$$

where $\underline{p}_0(d\mathbf{x}, dt)$ is the spatially and temporally shift-invariant element response. Now the choice of \mathcal{L} is not arbitrary, as the offsets between the various locations must match the physical offsets of the elements. An overall spatial shift of \mathcal{L} can still be accommodated through redefinition of \underline{p}_0 , however. As we will see, the identical element-response assumption (when it applies) greatly simplifies analysis. Let us substitute (3.4c) into (3.6a) and (3.8), respectively:

$$\vec{\underline{j}}(d\mathbf{x}, dt) = (\underline{p} \boxtimes \underline{b} * \underline{s}_A)(d\mathbf{x}, dt) \quad (\text{LSV}) \quad (3.9a)$$

$$\vec{\underline{j}}(d\mathbf{x}, dt) = (\underline{p}_0 \otimes \underline{b} * \underline{s}_A)(d\mathbf{x}, dt). \quad (\text{LSI}) \quad (3.9b)$$

Fourier transforming on \mathbf{x} and t to spatial frequency \mathbf{v} and temporal frequency f yields

$$\vec{\underline{J}}(\mathbf{v}, f) = \int \underline{P}(\mathbf{v}, f; -\mathbf{x}') \underline{B}(d\mathbf{x}', f) \underline{S}_A(f) \quad (\text{LSV}) \quad (3.10a)$$

$$\vec{\underline{J}}(\mathbf{v}, f) = \underline{P}_0(\mathbf{v}, f) \underline{B}(\mathbf{v}, f) \underline{S}_A(f). \quad (\text{LSI}) \quad (3.10b)$$

In the identical element-response (LSI) case the element response and the beamformer response factor. In the next section we will see that $\vec{\underline{J}}$ figures prominently in determining the far-field electric field.

3.2 Far-Field Propagation and the Wideband Array Pattern

The spatial and temporal output of the array is given in (3.9) as the element-current distribution \vec{j} . We are primarily interested in the corresponding far-field array response, which can be found by solving Maxwell's equations. Rather than solve directly for the electric field from the element-current distribution, a common approach [95] is to first solve for the *vector potential* $\vec{\alpha}$, an intermediate value that has a convenient physical interpretation. Although somewhat complicated in general, the relationship between the vector potential and the electric field is greatly simplified in the far field. In the following sections the vector potential is described, restricted to the far field, and related to the electric field. This then allows us to define the wideband array pattern, which serves as a transfer function from the array input to the far-field.

Much of this section follows standard textbook treatments such as found in [95], adapted here to the measure signal representation and extended to explicitly model the time and frequency dependence of wideband signals rather than using the usual narrowband assumptions. Signal processing conventions are generally given preference over traditional electromagnetics, for example in using temporal and spatial frequency rather than wavelength and direction and in defining the array pattern, element pattern, and array factor as four-dimensional Fourier transforms. Section 3.2.5 provides a novel approach to describing the geometry of wideband array patterns, and introduces the idea of the Helmholtz cone to illustrate the relationship between direction and spatial frequency. Section 3.2.6 provides a wideband extension of the classic narrowband approach to describing polarization.

3.2.1 The Vector Potential

The density of the vector potential $\vec{\alpha}(d\mathbf{x}, dt)$ is often defined to be a solution to the inhomogeneous vector wave equation

$$\nabla^2 \vec{\alpha}(\mathbf{x}, t) + \frac{\partial^2}{\partial t^2} \vec{\alpha}(\mathbf{x}, t) = -\mu_0 \vec{j}(\mathbf{x}, t),$$

with the element-current density \vec{j} as the forcing function. This differential-equation form is inconvenient for a measure signal representation, however, especially if the element-current distribution is spatially impulsive (for example, when confined to a wire). Instead we use the integral form of the solution, in which the vector potential consists of the superposition of spherical waves propagating away from each point on the antenna weighted by the element-current density at that point. Mathematically this is represented by the convolution

$$\vec{\alpha}(d\mathbf{x}, dt) = \frac{\mu_0}{4\pi} (\underline{\rho} \circledast \vec{j})(d\mathbf{x}, dt) \quad (3.11)$$

of the element-current distribution with the propagation measure

$$\underline{\rho}(d\mathbf{x}, dt) \triangleq \frac{(\|\mathbf{x}\|/c)\delta(dt)}{\|\mathbf{x}\|} d\mathbf{x}. \quad (3.12)$$

The constants $\mu_0 = 4\pi \times 10^{-7} \text{ V}\cdot\text{s}/\text{A}\cdot\text{m}$ and $c = 2.998 \times 10^8 \text{ m/s}$ are the permeability of free space and the propagation speed of light in free space, respectively. The propagation measure, often referred to as the *retarded*¹ *Green's function* for free space, has units of m^2 . The shift on the temporal impulse in the numerator of (3.12) determines the propagation speed, while the denominator sets the scaling with distance required to satisfy the conservation of energy.

The vector potential is both continuous-space and continuous-time, and thus the vector potential density with respect to Lebesgue measure on \mathbb{R}^4 has units $\text{V}\cdot\text{s}/\text{m}$. Writing (3.11) as a density in \mathbf{x} and integrated in time over a set \mathcal{T} yields

$$\vec{\alpha}(\mathbf{x}, \mathcal{T}) = \frac{\mu_0}{4\pi} \int \frac{(t' + \|\mathbf{x} - \mathbf{x}'\|/c)\delta(\mathcal{T})}{\|\mathbf{x} - \mathbf{x}'\|} \vec{j}(d\mathbf{x}', dt'), \quad (3.13)$$

¹as opposed to the advanced Green's function, which describes propagation backwards in time

a weighted integral of spherical waves originating at space-time locations (\mathbf{x}', t') of nonzero element-current density and propagating away at a speed c . Fourier transforming on time yields

$$\vec{\mathcal{A}}(\mathbf{x}, f) = \frac{\mu_0}{4\pi} \rlap{-}\int \frac{e^{-j2\pi\|\mathbf{x}-\mathbf{x}'\|f/c}}{\|\mathbf{x}-\mathbf{x}'\|} e^{-j2\pi ft'} \vec{\mathcal{J}}(d\mathbf{x}', dt'),$$

and writing the element-current differential as the product differential

$$\vec{\mathcal{J}}(d\mathbf{x}', dt') = \vec{\mathcal{J}}(\mathbf{x}', dt') \underline{\nu}(d\mathbf{x}')$$

and splitting the integral yields

$$\vec{\mathcal{A}}(\mathbf{x}, f) = \frac{\mu_0}{4\pi} \rlap{-}\int \frac{e^{-j2\pi\|\mathbf{x}-\mathbf{x}'\|f/c}}{\|\mathbf{x}-\mathbf{x}'\|} \int e^{-j2\pi ft'} \vec{\mathcal{J}}(\mathbf{x}', dt') \underline{\mu}(d\mathbf{x}'),$$

where $\underline{\nu}$ is the spatial reference measure for the current density. Recognizing another Fourier transform on time yields

$$\boxed{\vec{\mathcal{A}}(\mathbf{x}, f) = \frac{\mu_0}{4\pi} \rlap{-}\int \frac{e^{-j2\pi\|\mathbf{x}-\mathbf{x}'\|f/c}}{\|\mathbf{x}-\mathbf{x}'\|} \vec{\mathcal{J}}(d\mathbf{x}', f),} \quad (3.14)$$

where $\vec{\mathcal{J}}(d\mathbf{x}', f) = \vec{\mathcal{J}}(\mathbf{x}', f) \underline{\mu}(d\mathbf{x}')$. This expression is nearly identical to a standard textbook result [95, Eq. (3-27)], with the exceptions that the element-current distribution and vector potential transforms here are conjugate-symmetric, rather than one-sided, functions of temporal frequency, and that the textbook form suppresses explicit frequency dependence in favor of *wavenumber* $k = 2\pi f/c = 2\pi/\lambda$.

3.2.2 The Far-Field Approximation

In optics and electromagnetics it is common to split analysis of fields into multiple regions according to the relative distance from the source of the fields to the observer. The most general (and complicated) analysis must be applied in the *near-field*, where propagating spherical waves are modeled exactly and non-propagating and static fields must also be considered. Further away, in the *Fresnel region*, only propagating radiation is considered significant, and spherical waves are modeled locally as parabolas. Yet farther away is the

far field or *Fraunhofer region*, where spherical waves are modeled locally as plane waves. Texts on antennas offer various rules of thumb for the boundaries between these regions as functions of wavelength and array dimension, but the vast majority of antenna arrays operate well into the far field by any rule of thumb. For the sake of simplification the far field is here defined here simply as $\|\mathbf{x}\| \gg D$, where D is the radius of the smallest ball containing the array. The origin is assumed to be contained inside the same ball.

The essence of the far-field approximation is to expand the norm $\|\mathbf{x} - \mathbf{x}'\|$ in a two-term Taylor series about \mathbf{x} :

$$\|\mathbf{x} - \mathbf{x}'\| \approx \|\mathbf{x}\| - \mathbf{x}' \cdot \frac{\mathbf{x}}{\|\mathbf{x}\|} = \|\mathbf{x}\| - \mathbf{x}' \cdot \hat{\mathbf{x}},$$

recalling that the unit-vector operator $\hat{\cdot}$ is defined as $\hat{\mathbf{x}} \triangleq \mathbf{x}/\|\mathbf{x}\|$. Since both (3.13) and (3.14) are less sensitive functions of the norm in the denominator, only the first term will be used there. Substituting yields

$$\vec{\mathcal{A}}(\mathbf{x}, \mathcal{T}) \approx \frac{\mu_0}{4\pi\|\mathbf{x}\|} \rlap{-}\int\limits_{(t'+(\|\mathbf{x}\|-\mathbf{x}'\cdot\hat{\mathbf{x}})/c)}^f \delta(\mathcal{T}) \vec{\mathcal{J}}(d\mathbf{x}', dt'). \quad (3.15)$$

and

$$\vec{\mathcal{A}}(\mathbf{x}, f) \approx \frac{\mu_0}{4\pi} \frac{e^{-j2\pi\|\mathbf{x}\|f/c}}{\|\mathbf{x}\|} \rlap{-}\int\limits_{\mathcal{V}} e^{j2\pi\mathbf{x}'\cdot\hat{\mathbf{x}}f/c} \vec{\mathcal{J}}(d\mathbf{x}', f). \quad (3.16)$$

In (3.16) we recognize a spatial Fourier transform, and write

$$\vec{\mathcal{A}}(\mathbf{x}, f) \approx \frac{\mu_0}{4\pi} \frac{e^{-j2\pi\|\mathbf{x}\|f/c}}{\|\mathbf{x}\|} \vec{\mathcal{J}}(-\hat{\mathbf{x}}f/c, f). \quad (3.17)$$

This remarkably elegant result is the key upon which much of the sequel is based. The far-field vector potential resulting from element-current distribution $\vec{\mathcal{J}}$ is just a spherical wave weighted in the direction $\hat{\mathbf{x}}$ by the spatio-temporal Fourier transform $\mathbf{J}(\mathbf{v}, f)$ of the element-current distribution evaluated at spatial frequency $\mathbf{v} = -\hat{\mathbf{x}}f/c$. As a consequence of the far-field assumption the dependencies on distance $\|\mathbf{x}\|$ and direction $\hat{\mathbf{x}}$ have been completely decoupled. In most cases the dependence on distance is of little interest, and so often the far-field pattern is described as a function of $\hat{\mathbf{x}}$ alone.

If we further restrict our attention to locations \mathbf{x} in a neighborhood around some far-field location \mathbf{x}_0 , we can make the further approximations $\|\mathbf{x}\| \approx \|\mathbf{x}_0\|$ in the denominator of (3.17) and $\|\mathbf{x}\| \approx \mathbf{x} \cdot \hat{\mathbf{x}}_0$ in the numerator, as well as $\hat{\mathbf{x}} \approx \hat{\mathbf{x}}_0$. This results in

$$\vec{\mathcal{A}}(\mathbf{x}, f) \Big|_{\|\mathbf{x}-\mathbf{x}_0\| \ll \|\mathbf{x}_0\|} \approx \frac{\mu_0}{4\pi} \frac{1}{\|\mathbf{x}_0\|} e^{-j2\pi\mathbf{x} \cdot \hat{\mathbf{x}}_0 f/c} \vec{\mathbf{J}}(-\hat{\mathbf{x}}_0 f/c, f), \quad (3.18)$$

which describes a polychromatic plane wave traveling in the $\hat{\mathbf{x}}_0$ direction (see Appendix C). Thus from the perspective of a fixed far-field observer the array radiates a plane wave, which is known as the *Fraunhofer approximation*.

3.2.3 The Electric Field

The electric field is both continuous-space and continuous-time. In the following analysis it will prove more convenient to operate on the spatio-temporal density of the electric field measure than on the measure itself, and so following convention (and to simplify terminology) the density will be simply referred to as the electric field. Ignoring any DC terms, the electric field at an arbitrary location \mathbf{x} is found from the density of the vector potential via [95]

$$\vec{\mathcal{E}}(\mathbf{x}, t) = -\frac{\partial}{\partial t} \vec{\mathcal{A}}(\mathbf{x}, t) + c^2 \int_{-\infty}^t \nabla(\nabla \cdot \vec{\mathcal{A}}(\mathbf{x}, \tau)) d\tau.$$

In the far field ($\|\mathbf{x}\| \gg D$) this simplifies considerably to

$$\vec{\mathcal{E}}(\mathbf{x}, t) \Big|_{\|\mathbf{x}\| \gg D} \approx -\frac{\partial}{\partial t} \Gamma_{\hat{\mathbf{x}}} \vec{\mathcal{A}}(\mathbf{x}, t), \quad (3.19)$$

or, Fourier transforming on t ,

$$\vec{\mathcal{E}}(\mathbf{x}, f) \Big|_{\|\mathbf{x}\| \gg D} \approx -j2\pi f \Gamma_{\hat{\mathbf{x}}} \vec{\mathcal{A}}(\mathbf{x}, f). \quad (3.20)$$

Matrix $\Gamma_{\hat{\mathbf{x}}} \triangleq \mathbf{I} - \hat{\mathbf{x}}\hat{\mathbf{x}}^T$ projects onto the plane perpendicular to direction vector $\hat{\mathbf{x}} = \mathbf{x}/\|\mathbf{x}\|$, and so the far-field electric field is always oriented perpendicular to the direction of propagation. The electric field has units of V/m, and its temporal Fourier transform has

units of $\text{V}\cdot\text{s}/\text{m}$. Substituting for the vector potential from (3.17) yields

$$\boxed{\vec{\mathcal{E}}(\mathbf{x}, f) \Big|_{\|\mathbf{x}\| \gg D} \approx -\frac{e^{-j2\pi\|\mathbf{x}\|f/c}}{\|\mathbf{x}\|} \frac{\mu_0}{4\pi} j2\pi f \Gamma_{\hat{\mathbf{x}}} \vec{\mathbf{J}}(-\hat{\mathbf{x}}f/c, f),} \quad (3.21)$$

the electric field directly as a function of the spatio-temporal Fourier transform of the antenna element-current distribution. Thus the far-field electric field due to element-current distribution $\vec{\mathbf{j}}$ is, like the vector potential, a direction-weighted spherical wave, with an additional weighting of $-j2\pi f$ (due to the time derivative) and with only the radial vector components retained. As with the vector potential, the electric field can also be locally approximated as a plane wave in a neighborhood around far-field location \mathbf{x}_0 :

$$\vec{\mathcal{E}}(\mathbf{x}, f) \Big|_{\substack{\|\mathbf{x}\| \gg D \\ \|\mathbf{x} - \mathbf{x}_0\| \ll \|\mathbf{x}_0\|}} \approx -e^{-j2\pi\mathbf{x} \cdot \hat{\mathbf{x}}_0 f/c} \frac{1}{\|\mathbf{x}_0\|} \frac{\mu_0}{4\pi} j2\pi f \Gamma_{\hat{\mathbf{x}}_0} \vec{\mathbf{J}}(-\hat{\mathbf{x}}_0 f/c, f). \quad (3.22)$$

3.2.4 The Wideband Array Pattern

In the preceding sections the input-output relationship of the array was found in terms of the element-current distribution, from which the far-field electric field was found in (3.21). In this section we return to the system of Fig. 3.1 and consider the effective transfer function applied to the input signals, known as the *wideband array pattern*. The array pattern is the usual method of characterizing the far-field performance of an array as a function of direction.

We find the far-field electric field by substituting (3.10) into (3.21):

$$\vec{\mathcal{E}}(\mathbf{x}, f) \Big|_{\|\mathbf{x}\| \gg D} \approx -\frac{e^{-j2\pi\|\mathbf{x}\|f/c}}{\|\mathbf{x}\|} \frac{\mu_0}{4\pi} j2\pi f \Gamma_{\hat{\mathbf{x}}} \int \mathbf{P}(-\hat{\mathbf{x}}f/c, f; -\mathbf{x}') \mathbf{B}(d\mathbf{x}', f) \mathbf{S}_A(f) \quad (\text{LSV}) \quad (3.23a)$$

$$\vec{\mathcal{E}}(\mathbf{x}, f) \Big|_{\|\mathbf{x}\| \gg D} \approx -\frac{e^{-j2\pi\|\mathbf{x}\|f/c}}{\|\mathbf{x}\|} \frac{\mu_0}{4\pi} j2\pi f \Gamma_{\hat{\mathbf{x}}} \mathbf{P}_0(-\hat{\mathbf{x}}f/c, f) \mathbf{B}(\mathbf{v}, f) \mathbf{S}_A(f). \quad (\text{LSI}) \quad (3.23b)$$

The dependence on distance $\|\mathbf{x}\|$ is limited to the spherical-wave factor $e^{-j2\pi\|\mathbf{x}\|f/c}/\|\mathbf{x}\|$, with the numerator representing propagation delay and the denominator representing the

attenuation of the electric field with distance. Since arrays are seldom designed for specific distances and all arrays have the same distance dependence, it is customary to drop the spherical wave factor. Here the *array pattern* is defined as the direction-dependent, distance-independent response

$$\vec{\mathbf{A}}(\mathbf{v}, f) \triangleq -\frac{\mu_0}{4\pi} j2\pi f \Gamma_{\hat{\mathbf{v}}} \iint \mathbf{P}(\mathbf{v}, f; -\mathbf{x}') \mathbf{B}(d\mathbf{x}', f) \quad (\text{LSV}) \quad (3.24a)$$

$$\vec{\mathbf{A}}(\mathbf{v}, f) \triangleq -\frac{\mu_0}{4\pi} j2\pi f \Gamma_{\hat{\mathbf{v}}} \mathbf{P}_0(\mathbf{v}, f) \mathbf{B}(\mathbf{v}, f), \quad (\text{LSI}) \quad (3.24b)$$

which has dimension $3 \times N$ and units of $\text{V} \cdot \text{s}$. Under both the LSV and LSI definitions of the array pattern, the electric field reduces to

$$\vec{\mathcal{E}}(\mathbf{x}, f) \Big|_{\|\mathbf{x}\| \gg D} \approx \frac{e^{-j2\pi\|\mathbf{x}\|f/c}}{\|\mathbf{x}\|} \vec{\mathbf{A}}(-\hat{\mathbf{x}}f/c, f) \mathbf{S}_A(f), \quad (3.25)$$

the product of a spherical wave, the array pattern, and the post-conversion signal spectrum.

At this point it is appropriate to further consider the consequences of the identical element-response (LSI) assumption. In the LSI case the effects of the beamformer and the physical array separate cleanly. The factor

$$\vec{\mathbf{A}}_{\text{el}}(\mathbf{v}, f) \triangleq -\frac{\mu_0}{4\pi} j2\pi f \Gamma_{\hat{\mathbf{v}}} \mathbf{P}_0(\mathbf{v}, f) \quad (3.26)$$

is called the *wideband element pattern*, as it represents the response of a single element (or element group, for $M > 1$) of the array located at the origin. The response $\mathbf{B}(\mathbf{v}, f)$ is called the *array factor*, as it characterizes the part of the overall response that is due solely to the element locations and the weighting applied by the beamformer. The n th column of (3.24b) corresponds to the n th input signal, and can be written as

$$\vec{\mathbf{A}}_n(\mathbf{v}, f) = \sum_{m=1}^M [\vec{\mathbf{A}}_{\text{el}}]_m(\mathbf{v}, f) \mathbf{B}_{m,n}(\mathbf{v}, f) \quad (3.27)$$

to make explicit that the m th row and n th column of the array factor corresponds to the n th input signal and the m th element type. Each such scalar component of the array factor can also be viewed as the amplitude (to within a scale factor) of the array pattern of a theoretical

array of perfect isotropic radiators, which have a uniform element pattern in both angle and frequency. The conceptual advantage to the identical element-response assumption is that the array factor largely determines the overall array pattern, with the (fixed) element pattern merely serving as a spectral weighting. Thus if the array factor has low sidelobes in a region (for example) then so will the array pattern. Indeed, in practice the array factor is often designed with minimal knowledge of the element pattern.

In the LSV case we have not a single common element pattern, but one pattern per element location, which can be seen by Fourier transforming (3.1) and substituting it into (3.24a):

$$\vec{\mathbf{A}}(\mathbf{v}, f) \triangleq -\frac{\mu_0}{4\pi} j2\pi f \Gamma_{\hat{\mathbf{v}}} \sum_{\mathbf{x}' \in \mathcal{L}} \mathbf{P}(\mathbf{v}, f; -\mathbf{x}') \mathbf{B}(\mathbf{x}', f). \quad (3.28)$$

Thus the element (or element group) at location \mathbf{x} has the pattern

$$\boxed{\vec{\mathbf{A}}_{\text{el}}(\mathbf{v}, f; -\mathbf{x}') \triangleq -\frac{\mu_0}{4\pi} j2\pi f \Gamma_{\hat{\mathbf{v}}} \mathbf{P}(\mathbf{v}, f; -\mathbf{x}')} \quad (3.29)$$

and is driven by the output of the temporal filter with frequency response $\mathbf{B}(\mathbf{x}', f)$. The extra parameter distinguishes this from the common (LSI) element pattern previously defined in (3.26). Here it is quite unclear just from inspection how the element patterns and the beamformer contribute to the overall array pattern. Some insight is gained by rewriting (3.24a) using the bifrequency representation of (2.24):

$$\boxed{\vec{\mathbf{A}}(\mathbf{v}, f) \triangleq -\frac{\mu_0}{4\pi} j2\pi f \Gamma_{\hat{\mathbf{v}}} \int \check{\mathbf{P}}(\mathbf{v}, f; \mathbf{v}') \mathbf{B}(\mathbf{v}', f) d\mathbf{v}'} \quad (3.30)$$

Here we have the array factor \mathbf{B} as in the LSI case, but now the role of the element pattern is played by the bifrequency map $\check{\mathbf{P}}$, which maps input spatial frequencies \mathbf{v}' to output spatial frequencies \mathbf{v} . Because of this mapping, structure in the array factor (such as low sidelobes) may not carry over into the overall array pattern. In the LSV case it is critical to know the element patterns in order to design the array factor.

There is a considerable gray area between the LSV and LSI assumptions, as nominally identical elements are never exactly matched due to differences in their electromagnetic

surroundings. In this regime it comes down to a design decision; if assuming identical element responses results in poor designs, then the element patterns must be measured and the LSI assumption abandoned.

3.2.5 Array-Pattern Geometry and the Helmholtz Cone

The preceding derivation of the far-field electric field took place initially in the four-dimensional (\mathbf{x}, f) space consisting of three spatial dimensions and one temporal frequency dimension. By considering only the far-field we factored out the dependence on distance $\|\mathbf{x}\|$, effectively restricting our attention to the set of direction vectors $\hat{\mathbf{x}}$ which form the spatial unit sphere $\|\mathbf{x}\| = 1$ for all temporal frequency (a four-dimensional cylindrical shell). This is a natural and traditional way to specify array patterns: as functions of direction and temporal frequency. On the other hand, in (3.21) the electric field is described in terms of the four-dimensional Fourier transform of the element-current distribution, which is a function on the four-dimensional space of transform variables (\mathbf{v}, f) . This is a natural space in which to visualize the array factor, for example, as it is simply the Fourier transform of the beamformer impulse response. The relationship between these two representations was found in (3.17) to be $\mathbf{v} = -\hat{\mathbf{x}}f/c$, which maps the four-dimensional cylinder defined by $\|\mathbf{x}\| = 1$ in (\mathbf{x}, f) space to the four-dimensional cone defined by $\|\mathbf{v}\| = |f|/c$ in (\mathbf{v}, f) space. From (3.22) we see that the radiation traveling in the direction $\hat{\mathbf{x}}_0$ looks locally like a plane wave and results from the component of the element-current distribution that has spatial frequency $\mathbf{v} = -\hat{\mathbf{x}}_0 f/c$. This is the Helmholtz equation applied to plane waves (Appendix C), which describes the conditions for plane-wave propagation. Accordingly, we will refer to the surface $\|\mathbf{v}\| = |f|/c$ as the *Helmholtz cone*, and will refer to points on the cone as propagating or “visible” spatio-temporal frequencies. Spatio-temporal frequencies not on the Helmholtz cone, referred to as nonpropagating or “invisible”, are effectively filtered out by far-field propagation, and in this way the array acts as a particular kind of spatio-temporal bandpass filter. This filtering will prove key in the next chapter for spatio-

temporal $\Delta\Sigma$ modulation.

Describing and plotting array patterns and array factors in these two geometries presents a challenge. Although the surface $\|\mathbf{x}\| = 1$ lies in the 4D space (\mathbf{x}, f) , it is really only 3D. We can describe the unit sphere at a given temporal frequency in the spherical coordinate system shown in Figure 3.2 and described in more detail in Appendix D. Now unit-vector $\hat{\mathbf{x}}$ can be described by the elevation-azimuth pair (ϕ, θ) , and the array pattern can be viewed as a function on the 3D volume $[-90^\circ, 90^\circ] \times [-180^\circ, 180^\circ] \times \mathbb{R}$ in the space (ϕ, θ, f) . For plotting purposes, we will typically either fix one or two coordinates. When we only wish to visualize one hemisphere of the array pattern (such as with most planar arrays), we can instead project the hemisphere into the bisecting plane. For example, the unit hemisphere in the positive- y halfspace can be projected into the x - z plane by the invertible mapping

$$\begin{aligned}\Upsilon(x, y, z) &= (x, z) \\ \Upsilon^{-1}(x, z) &= \left(x, \sqrt{1 - x^2 - z^2}, z\right).\end{aligned}$$

The projected hemisphere occupies the unit disk $x^2 + z^2 \leq 1$ in (x, z) space, and the array pattern occupies a solid 3D cylinder in (x, z, f) space.

Similar projection approaches can be used to reduce the dimensionality of the array pattern or array factor when described in terms of spatial frequency. Consider a function $\Phi : \mathbb{R}^3 \times \mathbb{R}^+ \rightarrow \mathbb{R}^3$ defined as $\Phi(\mathbf{v}, f) = \mathbf{v}$ that projects the half-cone corresponding to positive temporal frequencies f onto \mathbb{R}^3 . This mapping has an inverse $\Phi^{-1}(\mathbf{v}) = (\mathbf{v}, c\|\mathbf{v}\|)$ for spatial frequencies on the cone. The result of this mapping is to fill all of spatial frequency with concentric shells whose radius is proportional to temporal frequency, as shown in Fig. 3.3(a). Likewise, one spatial frequency dimension can be projected out. Consider a function $\Upsilon : (\mathbb{R}^2 \times \mathbb{R}^+) \times \mathbb{R} \rightarrow (\mathbb{R}^2 \times \mathbb{R})$ and its inverse that map the half-cone corresponding to non-positive v_y to $\mathbb{R}^2 \times \mathbb{R}$ and back:

$$\begin{aligned}\Upsilon(v_x, v_y, v_z, f) &= (v_x, v_z, f) \\ \Upsilon^{-1}(v_x, v_z, f) &= \left(v_x, -\sqrt{(f/c)^2 - v_x^2 - v_z^2}, v_z, f\right).\end{aligned}$$

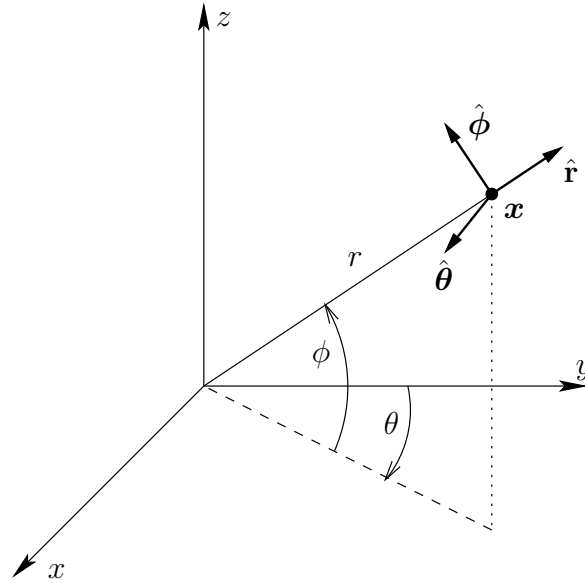


Figure 3.2: A spherical coordinate system is used to describe antenna array patterns. Elevation angle ϕ is measured up from the horizon (the x - y plane), and azimuth angle θ is measured clockwise from due north (the y -axis). Range r is included for completeness but not used.

At each frequency f the hemispherical shell corresponding to $v_y \leq 0$ is “flattened” to form a disk of radius f/c , and the disks are stacked in frequency to form the classic 3D “ice-cream” cone of Fig. 3.3(b). This solid cone is just a frequency scaled version of the solid cylinder previously derived. This approach is most natural for planar arrays, because the beamformer impulse response is a function of a 2D spatial variable and its corresponding frequency response (the array factor) is thus only a function of 2D spatial frequency. Thus no information is lost in projecting out the third spatial-frequency dimension. For a wideband array whose elements are not confined to a plane, four dimensions are required to fully specify the array factor.

3.2.6 Polarization

At a far-field location \boldsymbol{x} , the electric field vector of a propagating wave lies in the plane perpendicular to \boldsymbol{x} . The most common orthogonal basis used to describe this 2D subspace is

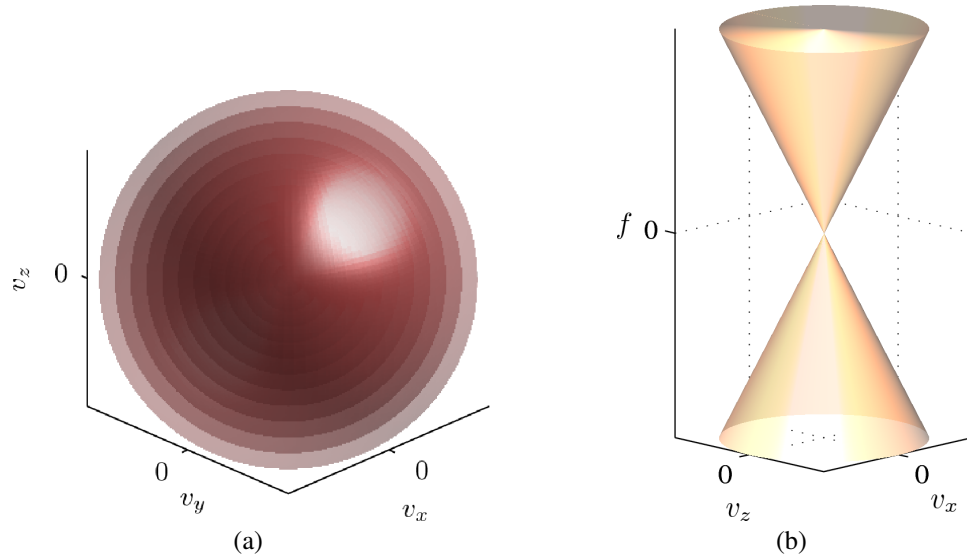


Figure 3.3: (a) Projecting the positive temporal-frequency half of the four-dimensional Helmholtz cone into three-dimensional spatial frequency fills \mathbb{Z}^3 with concentric spherical shells. (b) Projecting the negative v_y half of the four-dimensional cone into (v_x, v_z, f) space results in the classic two-sided “ice-cream” cone.

the pair of standard spherical coordinate unit vectors $\hat{\phi}(\mathbf{x})$ and $\hat{\theta}(\mathbf{x})$, shown in Figure D.1, which are the (position-dependent) directions of increasing elevation and azimuth, respectively. Since $\hat{\theta}$ always lies in the plane parallel to the earth’s surface, it is often referred to as the “horizontal” unit vector. Likewise, since $\hat{\phi}$ is perpendicular $\hat{\theta}$ it is referred to as the “vertical” unit vector. We can write the electric field as the sum of the horizontal and vertical components:

$$\vec{\mathcal{E}}(\mathbf{x}, f) = \vec{\mathcal{E}}_V(\mathbf{x}, f) + \vec{\mathcal{E}}_H(\mathbf{x}, f) \quad (3.31a)$$

$$= \mathcal{E}_V(\mathbf{x}, f)\hat{\phi}(\mathbf{x}) + \mathcal{E}_H(\mathbf{x}, f)\hat{\theta}(\mathbf{x}), \quad (3.31b)$$

where \mathcal{E}_V and \mathcal{E}_H are the vertical and horizontal scalar electric fields. These component scalar fields can be found as

$$\mathcal{E}_V(\mathbf{x}, f) = \hat{\phi}^T(\mathbf{x})\vec{\mathcal{E}}(\mathbf{x}, f)$$

$$\mathcal{E}_H(\mathbf{x}, f) = \hat{\theta}^T(\mathbf{x})\vec{\mathcal{E}}(\mathbf{x}, f).$$

More generally, an arbitrary scalar polarization component can be defined as

$$\mathcal{E}(\mathbf{x}, f) = \hat{\boldsymbol{\psi}}^H(f) \begin{pmatrix} \hat{\boldsymbol{\phi}}^T(\mathbf{x}) \\ \hat{\boldsymbol{\theta}}^T(\mathbf{x}) \end{pmatrix} \vec{\mathcal{E}}(\mathbf{x}, f), \quad (3.33)$$

where 2×1 complex unit vector $\hat{\boldsymbol{\psi}}$ is a wideband extension of the *Jones vector* [96], which compactly describes the polarization as a linear combination of the horizontal and vertical components. The corresponding vector component is

$$\mathcal{E}(\mathbf{x}, f) \begin{pmatrix} \hat{\boldsymbol{\phi}}(\mathbf{x}) & \hat{\boldsymbol{\theta}}(\mathbf{x}) \end{pmatrix} \hat{\boldsymbol{\psi}}(f) = \begin{pmatrix} \hat{\boldsymbol{\phi}}(\mathbf{x}) & \hat{\boldsymbol{\theta}}(\mathbf{x}) \end{pmatrix} \boldsymbol{\Psi}(f) \begin{pmatrix} \hat{\boldsymbol{\phi}}^T(\mathbf{x}) \\ \hat{\boldsymbol{\theta}}^T(\mathbf{x}) \end{pmatrix} \vec{\mathcal{E}}(\mathbf{x}, f) \quad (3.34)$$

where 2×2 matrix $\boldsymbol{\Psi}(f) = \hat{\boldsymbol{\psi}}(f)\hat{\boldsymbol{\psi}}^H(f)$ is the wideband extension of the *Jones matrix*. Wideband Jones vector and matrix values for common polarization types are given in Table 3.1, where $\mathcal{H}(f) \triangleq -j \operatorname{sgn}(f)$ is the frequency response of the Hilbert transformer. The Hilbert is required to preserve conjugate symmetry, as $\vec{\mathcal{E}}$ is the Fourier transform of a real signal. Polarization types come in pairs, with the associated Jones vectors forming an orthogonal basis for the complex 2D space of possible polarizations. So, for example, defining 3×3 projection matrices

$$\boldsymbol{\Gamma}_V(\mathbf{x}) = \begin{pmatrix} \hat{\boldsymbol{\phi}}(\mathbf{x}) & \hat{\boldsymbol{\theta}}(\mathbf{x}) \end{pmatrix} \begin{pmatrix} 1 & 0 \\ 0 & 0 \end{pmatrix} \begin{pmatrix} \hat{\boldsymbol{\phi}}^T(\mathbf{x}) \\ \hat{\boldsymbol{\theta}}^T(\mathbf{x}) \end{pmatrix} \quad (3.35a)$$

$$\boldsymbol{\Gamma}_H(\mathbf{x}) = \begin{pmatrix} \hat{\boldsymbol{\phi}}(\mathbf{x}) & \hat{\boldsymbol{\theta}}(\mathbf{x}) \end{pmatrix} \begin{pmatrix} 0 & 0 \\ 0 & 1 \end{pmatrix} \begin{pmatrix} \hat{\boldsymbol{\phi}}^T(\mathbf{x}) \\ \hat{\boldsymbol{\theta}}^T(\mathbf{x}) \end{pmatrix}, \quad (3.35b)$$

we can also write the decomposition in (3.31a) as

$$\vec{\mathcal{E}}(\mathbf{x}, f) = \boldsymbol{\Gamma}_V(\mathbf{x})\vec{\mathcal{E}}(\mathbf{x}, f) + \boldsymbol{\Gamma}_H(\mathbf{x})\vec{\mathcal{E}}(\mathbf{x}, f). \quad (3.36)$$

Similar to the electric field, the n th column of the array pattern (corresponding to the

type:	linear (V)	linear (H)	circular (RH)	circular (LH)
Jones vector $\hat{\boldsymbol{\psi}}(f)$	$\begin{pmatrix} 1 \\ 0 \end{pmatrix}$	$\begin{pmatrix} 0 \\ 1 \end{pmatrix}$	$\frac{1}{\sqrt{2}} \begin{pmatrix} 1 \\ \mathcal{H}(f) \end{pmatrix}$	$\frac{1}{\sqrt{2}} \begin{pmatrix} 1 \\ -\mathcal{H}(f) \end{pmatrix}$
Jones matrix $\boldsymbol{\Psi}(f) = \hat{\boldsymbol{\psi}}(f)\hat{\boldsymbol{\psi}}^H(f)$	$\begin{pmatrix} 1 & 0 \\ 0 & 0 \end{pmatrix}$	$\begin{pmatrix} 0 & 0 \\ 0 & 1 \end{pmatrix}$	$\frac{1}{2} \begin{pmatrix} 1 & -\mathcal{H}(f) \\ \mathcal{H}(f) & 1 \end{pmatrix}$	$\frac{1}{2} \begin{pmatrix} 1 & \mathcal{H}(f) \\ -\mathcal{H}(f) & 1 \end{pmatrix}$

Table 3.1: Common polarization types, and their associated wideband Jones vectors and matrices.

n th input signal) can be decomposed into horizontal and vertical polarization components:

$$\begin{aligned}
\vec{\mathbf{A}}_n(\mathbf{v}, f) &= \vec{\mathbf{A}}_{nV}(\mathbf{v}, f) + \vec{\mathbf{A}}_{nH}(\mathbf{v}, f) \\
&= \boldsymbol{\Gamma}_V(-\mathbf{v})\vec{\mathbf{A}}_n(\mathbf{v}, f) + \boldsymbol{\Gamma}_H(-\mathbf{v})\vec{\mathbf{A}}_n(\mathbf{v}, f) \\
&= A_{nV}(\mathbf{v}, f)\hat{\boldsymbol{\phi}}(-\mathbf{v}) + A_{nH}(\mathbf{v}, f)\hat{\boldsymbol{\theta}}(-\mathbf{v}),
\end{aligned}$$

although the decomposition is only meaningful for propagating spatial frequencies $\mathbf{v} = -\mathbf{x}f/c$.

The polarization of an array pattern is a linear combination of the polarizations of its elements, and thus an array with identical element responses permits no control over the polarization. The array polarization in this case will be that of the common element pattern:

$$\begin{aligned}
\vec{\mathbf{A}}_n(\mathbf{v}, f) &= \vec{\mathbf{A}}_{\text{el}}(\mathbf{v}, f)\mathbf{B}_n(\mathbf{v}, f) \\
&= \left[A_{\text{elV}}(\mathbf{v}, f)\hat{\boldsymbol{\phi}}(-\mathbf{v}) + A_{\text{elH}}(\mathbf{v}, f)\hat{\boldsymbol{\theta}}(-\mathbf{v}) \right] \mathbf{B}_n(\mathbf{v}, f)
\end{aligned}$$

When polarization control is desired, two or more sets of elements with differing polarizations are typically used, either co-located in pairs (or triples, etc.) or arranged in offset lattices. Conceptually, one beam is formed for each type of element so that the combination in the far field produces the desired polarization:

$$\vec{\mathbf{A}}_n(\mathbf{v}, f) = \sum_{m=1}^M [\vec{\mathbf{A}}_{\text{el}}]_m(\mathbf{v}, f)\mathbf{B}_{m,n}(\mathbf{v}, f)$$

where $[\vec{\mathbf{A}}_{\text{el}}]_m$ is the m th column of $\vec{\mathbf{A}}_{\text{el}}$.

3.3 Random Signal Analysis

For reasons of familiarity and notational simplicity, the preceding derivations assumed that the input signal \underline{s} and thus all subsequent signals are deterministic and that the associated Fourier transforms exist. In many applications the input signals are random processes, and so we wish to also characterize the response of the array to such inputs. Intuition suggests that similar results will be obtained, which is verified in this section.

Let input $\underline{s}(dt)$ be a wide-sense stationary vector random signal with autocorrelation matrix $\underline{r}_s(dt)$. As before, define the equivalent post-conversion signal

$$\underline{s}_A(dt) \triangleq (\underline{s} * \underline{h}_A)(dt). \quad (3.39)$$

The expression for the autocorrelation \underline{r}_{s_A} depends on the nature of the passband-equivalent input \underline{s} . If the underlying hardware architecture involves analog frequency conversion, then \underline{s} will be continuous-time. This is shown in greater detail in Section 3.4.1. In this case,

$$\underline{r}_{s_A} = (\underline{h}_A * \underline{r}_s * \underline{h}_A^\dagger)(dt).$$

If \underline{s} is discrete-time with support on $T\mathbb{Z}$, then

$$\underline{r}_{s_A} = \frac{1}{T} (\underline{h}_A * \underline{r}_s * \underline{h}_A^\dagger)(dt).$$

Since the elements of \underline{s} usually represent independent signals, \underline{r}_s and \underline{r}_{s_A} will usually be diagonal. From (3.9a) we see that the resulting element-current distribution is the continuous-time continuous-space random measure

$$\vec{j}(d\mathbf{x}, dt) = (\underline{\mathbf{p}} \boxtimes \underline{\mathbf{b}} * \underline{s}_A)(d\mathbf{x}, dt). \quad (3.40)$$

The corresponding spatio-temporal autocorrelation density is

$$\begin{aligned} \underline{r}_j(\mathbf{x}, \mathbf{y}, \tau) &= \mathcal{E} \left\{ \vec{j}(\mathbf{x}, t) \vec{j}^H(\mathbf{y}, t - \tau) \right\} \\ &= \mathcal{E} \left\{ ((\underline{\mathbf{p}} \boxtimes \underline{\mathbf{b}}) * \underline{s}_A)(\mathbf{x}, t) \times (\underline{s}_A^H * (\underline{\mathbf{p}} \boxtimes \underline{\mathbf{b}})^H)(\mathbf{y}, t - \tau) \right\}, \end{aligned}$$

and by (2.37) the autocorrelation measure is the matrix measure

$$\boxed{\mathbf{r}_{\vec{j}}(d\mathbf{x}, d\mathbf{y}, d\tau) = \left((\underline{\mathbf{p}} \boxtimes \underline{\mathbf{b}}) * \mathbf{r}_{s_A} * (\underline{\mathbf{p}} \boxtimes \underline{\mathbf{b}})^\dagger \right) (d\mathbf{x}, d\mathbf{y}, d\tau),} \quad (3.41)$$

which is compact if slightly abusive notation for the temporal convolution of the differential measures $(\underline{\mathbf{p}} \boxtimes \underline{\mathbf{b}})(d\mathbf{x}, d\tau)$, $\mathbf{r}_{s_A}(d\tau)$, and $(\underline{\mathbf{p}} \boxtimes \underline{\mathbf{b}})^\dagger(d\mathbf{y}, d\tau)$. The spatial dimension of the element-current distribution comes from the deterministic beamformer and array response, and thus the autocorrelation results from spatio-temporal filtering of the purely temporal input signal autocorrelation. The corresponding temporal PSD is found by Fourier transforming on time:

$$\mathbf{R}_{\vec{j}}(d\mathbf{x}, d\mathbf{y}, f) = (\underline{\mathbf{P}} \square \underline{\mathbf{B}})(d\mathbf{x}, f) \mathbf{R}_{s_A}(f) (\underline{\mathbf{P}} \square \underline{\mathbf{B}})^H(d\mathbf{y}, f), \quad (3.42)$$

and the spatio-temporal PSD is found by further transforming on space:

$$\boxed{\mathbf{R}_{\vec{j}}(\mathbf{v}, \mathbf{w}, f) = \left(\int \! \! \! \int \mathbf{P}(\mathbf{v}, f; -\mathbf{x}') \underline{\mathbf{B}}(d\mathbf{x}', f) \right) \mathbf{R}_{s_A}(f) \left(\int \! \! \! \int \mathbf{P}(\mathbf{w}, f; -\mathbf{y}') \underline{\mathbf{B}}(d\mathbf{y}', f) \right)^\dagger} \quad (3.43)$$

With identical element responses this simplifies to

$$\boxed{\mathbf{R}_{\vec{j}}(\mathbf{v}, \mathbf{w}, f) = \mathbf{P}_0(\mathbf{v}, f) \mathbf{B}(\mathbf{v}, f) \mathbf{R}_{s_A}(f) \mathbf{B}^H(-\mathbf{w}, f) \mathbf{P}_0^H(-\mathbf{w}, f)} \quad (3.44)$$

Having characterized the random element-current distribution in terms of the input signals, we now turn to the far-field vector potential. Rearranging (3.15) as a convolution and substituting a random element-current distribution yields

$$\begin{aligned} \vec{\mathcal{A}}(\mathbf{x}, dt) &\approx \frac{\mu_0}{4\pi\|\mathbf{x}\|} \left(\int \! \! \! \int \left((\|\mathbf{x}\| - \mathbf{x}' \cdot \hat{\mathbf{x}}) / c \delta * \vec{\mathbf{j}} \right) (d\mathbf{x}', t) \right) dt \\ &= \frac{\mu_0}{4\pi\|\mathbf{x}\|} \left(\int \! \! \! \int \vec{\mathbf{j}}(\mathbf{x}', t - (\|\mathbf{x}\| - \mathbf{x}' \cdot \hat{\mathbf{x}}) / c) \underline{\nu}(d\mathbf{x}') \right) dt, \end{aligned} \quad (3.45)$$

where $\underline{\nu}$ is a reference measure for $\vec{\mathbf{j}}$. The corresponding autocorrelation matrix has spatial

density

$$\begin{aligned}
\mathbf{r}_{\alpha^-}(\mathbf{x}, \mathbf{y}, \mathcal{T}) &= \frac{\mu_0^2}{(4\pi)^2 \|\mathbf{x}\| \|\mathbf{y}\|} \int_{\mathcal{T}} \mathcal{E} \left\{ \iiint \vec{\mathbf{j}}(\mathbf{x}', t - (\|\mathbf{x}\| - \mathbf{x}' \cdot \hat{\mathbf{x}})/c) \times \right. \\
&\quad \left. \vec{\mathbf{j}}^H(\mathbf{y}', t - \tau - (\|\mathbf{y}\| - \mathbf{y}' \cdot \hat{\mathbf{y}})/c) \nu(d\mathbf{x}') \nu(d\mathbf{y}') \right\} d\mathcal{T} \\
&= \frac{\mu_0^2}{(4\pi)^2 \|\mathbf{x}\| \|\mathbf{y}\|} \times \\
&\quad \int_{\mathcal{T}} \iiint \mathbf{r}_j^-(\mathbf{x}', \mathbf{y}', \tau - (\|\mathbf{x}\| - \mathbf{x}' \cdot \hat{\mathbf{x}})/c + (\|\mathbf{y}\| - \mathbf{y}' \cdot \hat{\mathbf{y}})/c) \nu(d\mathbf{x}') \nu(d\mathbf{y}') d\mathcal{T}.
\end{aligned} \tag{3.46}$$

Fourier transforming on τ yields the temporal PSD

$$\begin{aligned}
\mathbf{R}_{\alpha^-}(\mathbf{x}, \mathbf{y}, f) &= \frac{\mu_0^2}{(4\pi)^2 \|\mathbf{x}\| \|\mathbf{y}\|} \times \\
&\quad \iiint \mathbf{R}_j^-(\mathbf{x}', \mathbf{y}', f) e^{-j2\pi(\|\mathbf{x}\| - \mathbf{x}' \cdot \hat{\mathbf{x}})f/c} e^{j2\pi(\|\mathbf{y}\| - \mathbf{y}' \cdot \hat{\mathbf{y}})f/c} \nu(d\mathbf{x}') \nu(d\mathbf{y}') \\
&= \left(\frac{\mu_0}{4\pi} \right)^2 \frac{e^{-j2\pi(\|\mathbf{x}\| - \|\mathbf{y}\|)f/c}}{\|\mathbf{x}\| \|\mathbf{y}\|} \times \\
&\quad \iiint \mathbf{R}_j^-(\mathbf{x}', \mathbf{y}', f) e^{j2\pi\mathbf{x}' \cdot \hat{\mathbf{x}}f/c} e^{-j2\pi\mathbf{y}' \cdot \hat{\mathbf{y}}f/c} \nu(d\mathbf{x}') \nu(d\mathbf{y}').
\end{aligned} \tag{3.47}$$

Recognizing Fourier transforms on \mathbf{x}' and \mathbf{y}' , we can write this as

$$\boxed{\mathbf{R}_{\alpha^-}(\mathbf{x}, \mathbf{y}, f) = \left(\frac{\mu_0}{4\pi} \right)^2 \frac{e^{-j2\pi(\|\mathbf{x}\| - \|\mathbf{y}\|)f/c}}{\|\mathbf{x}\| \|\mathbf{y}\|} \mathbf{R}_j^-(\hat{\mathbf{x}}f/c, \hat{\mathbf{y}}f/c, f)}. \tag{3.48}$$

This result is the random-signal equivalent to (3.17), here relating the temporal PSD of the far-field vector-potential to the spatio-temporal PSD of the element-current distribution.

The random-signal equivalent of (3.20) gives the temporal PSD of the far-field electric field:

$$\mathbf{R}_{\mathbf{E}}(\mathbf{x}, \mathbf{y}, f) = |j2\pi f|^2 \Gamma_{\hat{\mathbf{x}}} \mathbf{R}_{\alpha^-}(\mathbf{x}, \mathbf{y}, f) \Gamma_{\hat{\mathbf{y}}}^T \tag{3.49a}$$

$$= \frac{e^{-j2\pi(\|\mathbf{x}\| - \|\mathbf{y}\|)f/c}}{\|\mathbf{x}\| \|\mathbf{y}\|} \left(\frac{\mu_0}{4\pi} \right)^2 |j2\pi f|^2 \Gamma_{\hat{\mathbf{x}}} \mathbf{R}_j^-(\hat{\mathbf{x}}f/c, \hat{\mathbf{y}}f/c, f) \Gamma_{\hat{\mathbf{y}}}^T \tag{3.49b}$$

$$\begin{aligned}
&= \frac{e^{-j2\pi(\|\mathbf{x}\| - \|\mathbf{y}\|)f/c}}{\|\mathbf{x}\| \|\mathbf{y}\|} \left(\frac{\mu_0}{4\pi} \right)^2 |j2\pi f|^2 \Gamma_{\hat{\mathbf{x}}} \left(\int \mathbf{P}(-\hat{\mathbf{x}}f/c, f; -\mathbf{x}') \mathbf{B}(d\mathbf{x}', f) \right) \times \\
&\quad \mathbf{R}_{s_A}(f) \left(\int \mathbf{P}(-\hat{\mathbf{y}}f/c, f; -\mathbf{y}') \mathbf{B}(d\mathbf{y}', f) \right)^H \Gamma_{\hat{\mathbf{y}}}^T
\end{aligned} \tag{3.49c}$$

The last line is the random-signal version of (3.23a). Recognizing the array pattern (3.24a), we can write this as

$$\mathbf{R}_{\varepsilon}(\mathbf{x}, \mathbf{y}, f) = \frac{e^{-j2\pi(\|\mathbf{x}\| - \|\mathbf{y}\|)f/c}}{\|\mathbf{x}\|\|\mathbf{y}\|} \vec{\mathbf{A}}(-\hat{\mathbf{x}}f/c, f) \mathbf{R}_{s_A}(f) \vec{\mathbf{A}}^H(-\hat{\mathbf{y}}f/c, f), \quad (3.50)$$

the random-signal versions of (3.25). We see again that all relevant information about the spatial distribution of the far-field electric field is contained in the array pattern.

3.4 Array Pattern Synthesis

The preceding sections focused on the analysis of a wideband transmit array, tracing deterministic and random signals from input to far-field electric field. The ultimate goal, however, is synthesis: to control the electric field through design of the array pattern. In this section, we will derive performance metrics for the array pattern, and show that efficient numerical optimization can be used for design. These metrics largely concern the transfer of power, resulting in expressions that are quadratic in the coefficients of the beamformer. Thus the optimization framework used throughout will be second-order cone programming [97] (SOCP), which can handle linear and convex quadratic constraints. An overview of SOCP is given in Appendix F. Several example designs will be interspersed with the derivations, and so we begin with a description of the example transmit array architecture.

3.4.1 Example Design Setup

A common setup will be used for a series of incremental example designs to allow for direct comparisons between various designs. An intermediate-frequency (IF) synthesis architecture will be used for the examples. IF-synthesis is widely used when the final RF is higher than the desired DAC can support directly. Although analog frequency conversion is required, the errors associated with analog quadrature modulation are avoided by directly synthesizing the IF signal. Here IF-synthesis was also chosen to show in somewhat

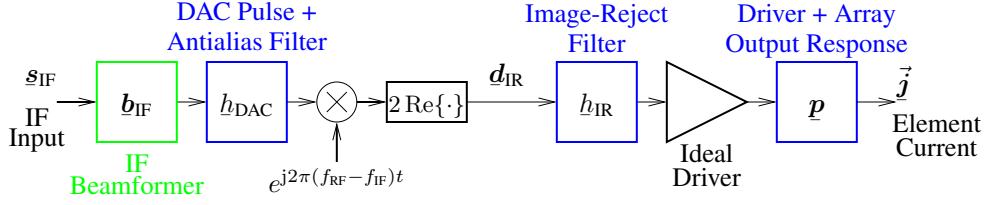


Figure 3.4: IF-synthesis hardware architecture for design example.

more detail how the passband-equivalent model of Figure 3.1 can be related to a particular architecture.

The underlying IF-synthesis architecture for the examples is shown in Figure 3.4. IF input $\underline{s}_{\text{IF}}$ is a real, bandpass discrete-time signal with support on $T\mathbb{Z}$ and a signal band centered at IF f_{IF} . IF beamformer $\underline{b}_{\text{IF}}$ is real, discrete-space on the set of locations \mathcal{L} , and discrete-time on $T\mathbb{Z}$. The beamformer output is converted via the DAC pulse and associated reconstruction filtering, represented by $\underline{h}_{\text{DAC}}$, to a discrete-space, continuous-time IF signal. Analog frequency conversion is used to translate this signal from IF f_{IF} up to the final RF f_{RF} , and bandpass image-reject filter $\underline{h}_{\text{IR}}$ removes unwanted mixing products. The filter output feeds the driver, which in turn drives the array elements.

To simplify this architecture and reduce it to the form of Figure 3.1, we need to determine the RF passband-equivalent input \underline{s} , beamformer \underline{b} , and analog response \underline{h}_A . We will assume that $\underline{h}_{\text{DAC}}$, the combination of the DAC pulse and antialiasing filter, bandlimits its output so that there is no image interference in the frequency conversion:

$$H_{\text{DAC}}(f) = H_{\text{BW}}(f)H_{\text{DAC}}(f),$$

where

$$H_{\text{BW}}(f) = 1_{(-f_{\text{RF}}-f_{\text{IF}}, f_{\text{RF}}-f_{\text{IF}})}(f)$$

is the frequency response of “brick wall” lowpass filter $\underline{h}_{\text{BW}}$. We can now write the input

to the image-rejection filter as

$$\begin{aligned} \underline{d}_{\text{IR}}(d\mathbf{x}, dt) &= 2 \operatorname{Re} \left\{ e^{j2\pi(f_{\text{RF}} - f_{\text{IF}})t} \left(\underline{h}_{\text{DAC}} * \underline{\mathbf{b}}_{\text{IF}} * \underline{\mathbf{s}}_{\text{IF}} \right) (d\mathbf{x}, dt) \right\} \\ &= 2 \operatorname{Re} \left\{ e^{j2\pi(f_{\text{RF}} - f_{\text{IF}})t} \left(\underline{h}_{\text{BW}} * \underline{h}_{\text{DAC}} * \underline{\mathbf{b}}_{\text{IF}} * \underline{\mathbf{s}}_{\text{IF}} \right) (d\mathbf{x}, dt) \right\} \\ &= 2 \operatorname{Re} \left\{ e^{j2\pi(f_{\text{RF}} - f_{\text{IF}})t} \left(\underline{h}_{\text{BW}} * \underline{h}_{\text{DAC}} * \underline{h}_{\text{BW}} * \underline{\mathbf{b}}_{\text{IF}} * \underline{h}_{\text{BW}} * \underline{\mathbf{s}}_{\text{IF}} \right) (d\mathbf{x}, dt) \right\}, \end{aligned}$$

the last because $\underline{h}_{\text{BW}} * \underline{h}_{\text{BW}} = \underline{h}_{\text{BW}}$. Having now bandlimited each signal and filter in the chain, we can distribute the frequency conversion:

$$\underline{d}_{\text{IR}} = \left(\underline{h}'_{\text{DAC}} * \underline{\mathbf{b}} * \underline{\mathbf{s}} \right) (d\mathbf{x}, dt),$$

where the passband-equivalent input, beamformer, and DAC/antialias filter are given by

$$\underline{\mathbf{s}}(dt) = 2 \operatorname{Re} \left\{ e^{j2\pi(f_{\text{RF}} - f_{\text{IF}})t} \left(\underline{h}_{\text{BW}} * \underline{\mathbf{s}}_{\text{IF}} \right) (dt) \right\} \quad (3.51a)$$

$$\underline{\mathbf{b}}(d\mathbf{x}, dt) = 2 \operatorname{Re} \left\{ e^{j2\pi(f_{\text{RF}} - f_{\text{IF}})t} \left(\underline{h}_{\text{BW}} * \underline{\mathbf{b}}_{\text{IF}} \right) (d\mathbf{x}, dt) \right\} \quad (3.51b)$$

$$\underline{h}'_{\text{DAC}}(dt) = 2 \operatorname{Re} \left\{ e^{j2\pi(f_{\text{RF}} - f_{\text{IF}})t} \left(\underline{h}_{\text{BW}} * \underline{h}_{\text{DAC}} \right) (dt) \right\}.$$

We now combine the last with the image-reject filter to get the passband-equivalent analog response

$$\underline{h}_{\text{A}}(dt) = \left(\underline{h}_{\text{IR}} * \underline{h}'_{\text{DAC}} \right) (dt). \quad (3.52)$$

Although the physical input and beamformer are discrete-time, their passband-equivalents are continuous time. If the input is random, then the the corresponding autocorrelation is found as the appropriate special case of (2.42):

$$\underline{\mathbf{r}}_{\mathbf{s}}(dt) = \frac{2}{T} \operatorname{Re} \left\{ e^{j2\pi(f_{\text{RF}} - f_{\text{IF}})t} \left(\underline{h}_{\text{BW}} * \underline{\mathbf{r}}_{\mathbf{s}_{\text{IF}}} * \underline{h}_{\text{BW}}^{\dagger} \right) (dt) \right\}. \quad (3.53)$$

In our examples we will design the array pattern for a single signal and a single type of element ($N = M = 1$), and so we have a scalar IF beamformer of the form

$$\underline{b}_{\text{IF}}(d\mathbf{x}, dt) = \sum_{\mathbf{x} \in \mathcal{L}} \underline{b}_{\text{IF}}(\mathbf{x}, dt) \underline{\mathbf{x}} \delta(d\mathbf{x})$$

where the subfilter at each element location \mathbf{x} is an FIR filter with 16 real coefficients located symmetrically about the origin with spacing T :

$$b_{\text{IF}}(\mathbf{x}, dt) = \sum_{k=0}^{15} b_{\text{IF}}(\mathbf{x}, (k - 7.5)T) \delta_{(k-7.5)T}(dt)$$

This symmetric arrangement simplifies analysis by allowing us to later impose coefficient symmetry about the origin. The magnitude response of each filter $|B_{\text{IF}}(\mathbf{x}, f)|$ has period $f_s = 1/T$, but since the coefficients lie on the offset lattice $T\mathbb{Z} + \frac{1}{2}$ the phase response has twice the period. We will refer to f_s as “the” period nonetheless, as defining the filter frequency response over an interval of width f_s fully defines it everywhere. Further, since the coefficients $\{b_{\text{IF}}(\mathbf{x}, (k - 7.5)T)\}$ are real, the frequency response is also conjugate symmetric, and so defining it on the interval $[0, 0.5f_s]$ defines it everywhere. We can see from (3.51b) that since b_{IF} is linear in its coefficients, so is \mathbf{b} , a fact that will prove convenient for the solving optimization problems that follow.

We will define the system parameters relative to the filter sample rate: the one-sided signal bandwidth is $0.4f_s$, the intermediate frequency is $f_{\text{IF}} = 0.25f_s$, and the nominal transmit center frequency is $f_{\text{RF}} = 0.75f_s$. The IF is at the center of the first Nyquist zone, which the interval $[0, 0.5f_s]$. This is a common choice for the IF as it results in equispaced spectral replicas in the pre-conversion digital signal, and thus symmetric transition bands between replicas for the reconstruction filtering. The choice of RF here happens to lie at the center of the second Nyquist band, and indeed we could consider generating the signal at this RF frequency directly out of the DAC by use of the appropriate reconstruction filter. However, the RF signal band $\mathcal{F} = [0.55f_s, 0.95f_s]$ lies perilously close to the sampling rate, and the zero-order hold pulse response that is typical of most DACs has a null at the sampling rate. As a result, a great deal of digital compensation would be required to flatten the hold response if direct RF synthesis was used. The RF here was chosen primarily to achieve a moderately high ratio of bandwidth to RF, but it has the side effect of demonstrating the potential tradeoffs between various system architectures. In

using the IF architecture, by (3.51b) the RF signal band \mathcal{F} of the passband-equivalent frequency response $B(\mathbf{x}, f)$ maps to the IF signal band $[0.05f_s, 0.45f_s]$ of the underlying IF frequency response $B_{\text{IF}}(\mathbf{x}, f)$. Due to conjugate symmetry, defining the former over the range $[0.5f_s, f_s]$ completely defines both.

The example array consists of a square grid of elements in the x - z plane, 16 elements wide along the x -axis and 7 elements high along the z -axis, symmetrically located about the origin. Array normal is thus the y -axis. The elements lie on the offset lattice

$$\begin{pmatrix} d & 0 \\ 0 & 0 \\ 0 & d \end{pmatrix} \mathbb{Z}^2 + \begin{pmatrix} d/2 \\ 0 \\ 0 \end{pmatrix}$$

where inter-element spacing d is one-half wavelength at the highest frequency of operation: $d = c/(2 \times 0.95f_s)$. As with the temporal coefficient locations, the offset allows symmetric placement of an even number of elements about the origin. From the generalized Fourier-series derivation of Section 2.1.3, we see that the resulting spatial-frequency periodicity of the array factor magnitude is defined by

$$|\mathbf{B}(\mathbf{v} - \mathbf{v}', f)| = |\mathbf{B}(\mathbf{v}, f)| \text{ for } \mathbf{v}' \in \begin{pmatrix} \frac{1}{d} & 0 \\ 0 & 0 \\ 0 & \frac{1}{d} \end{pmatrix} \mathbb{Z}^2 + \begin{pmatrix} 0 \\ 1 \\ 0 \end{pmatrix} \mathbb{R}.$$

In words, the array factor magnitude is independently periodic in spatial frequency components v_x and v_z with period $1/d$, and is constant in v_y . (Because of the offset, the array factor phase has twice the period in v_x .) The array factor is completely defined by its value on the set of spatial frequencies $[-1/2d, 1/2d] \times \{0\} \times [-1/2d, 1/2d]$, which we will hereafter refer to simply as a spatial frequency period of the array factor. By the given choice of d , at $f = 0.95f_s$ the projection of the Helmholtz cone onto the (v_x, v_z) plane exactly inscribes this array factor period, allowing full control over the entire visible pattern.

The array elements are identical short vertical ($\hat{\mathbf{z}}$ -oriented) dipoles of length $\lambda_{\text{RF}}/20$ located a distance h in front of a perfect ground in the x - z plane, where $h = c/4f_0$ is a quarter-wavelength at the geometric band center $f_0 = \sqrt{0.55f_s \times 0.95f_s} \approx 0.72f_s$. The corresponding element pattern is derived and plotted in Appendix E. In particular, due to

symmetry the element pattern is purely real. Short dipoles were chosen here because their element pattern is easy to derive and they are relatively wideband and omnidirectional over a hemisphere. They do not, in most cases, represent a particularly good choice for practical designs because their small size leads to low radiation resistance. Indeed, we will see later that even a small series loss resistance in the element or its feed can have a significant effect on the performance of an array of small dipoles. Another advantage of using electrically small elements is that we do not need *guard elements*, which are dummy (terminated) elements placed on the same lattice surrounding the active elements to provide a uniform electromagnetic environment to each active element and thus ensure nearly identical element patterns. Because we assume ideal current drivers, and because the terminal current of each element is the radiating current by the electrically small assumption, the element patterns are necessarily identical. (The response of the terminal voltages, on the other hand, may vary wildly due to the differences in electromagnetic environment across the array.)

Since all elements have identical responses, the array pattern factors as

$$\vec{\mathbf{A}}(\mathbf{v}, f) = \vec{\mathbf{A}}_{\text{el}}(\mathbf{v}, f)B(\mathbf{v}, f),$$

and thus imposing the further symmetry condition $\mathbf{b} = \mathbf{b}^\dagger$ on the (real) beamformer coefficients ensures that the array factor and the overall array pattern are purely real also. This restriction has the added benefits of reducing by half the number of independent optimization variables and simplifying certain constraints. We can also simplify notation in the examples by using the factorization in (E.3) to write the visible array pattern as

$$\vec{\mathbf{A}}(-\hat{\mathbf{x}}f/c, f) = A_{\text{elV}}(-\hat{\mathbf{x}}f/c, f)\hat{\phi}(\hat{\mathbf{x}})B(-\hat{\mathbf{x}}f/c, f),$$

as the unit vector will fall out of most expressions.

In a conventional narrowband or wideband array design, a prototype array pattern is designed to point to boresight, and then that prototype is used to generate patterns pointing in all other directions by applying direction-dependent phase shifts (narrowband) or time delays (wideband) to the signal entering each element. The result is a family of array

patterns that at each temporal frequency are simply shifted copies of the prototype. While this is a computationally efficient approach, it precludes performing truly optimal designs for each beam-center direction. The approach advocated here is to optimize a custom array pattern for each beam-center direction, and thus a non-boresight beam-center direction of $\hat{\mathbf{x}}_0 = \frac{1}{\sqrt{2}} \begin{pmatrix} 1 \\ 1 \\ 0 \end{pmatrix}$ is used for all example designs as a typical example of one of many related designs. In polar coordinates this is elevation $\phi = 0^\circ$ and azimuth $\theta = 45^\circ$.

3.4.2 Far-Field Power Density and Intensity

Having characterized the electric field for deterministic and random signals, it is natural to consider how this is related to the transfer of power. Traditional electromagnetics texts often assume sinusoidal inputs, and derive the average power accordingly. The instantaneous, average (deterministic), and expected (random) radiation power densities and intensities given below are defined the same for narrow and wideband inputs, and as presented here are largely derived from standard results in [95]. To more fully characterize wideband inputs, both deterministic and wide-sense stationary random signals, the radiation power spectral intensity is then introduced, which extends the narrowband notion of power intensity to describe its distribution across frequency.

Deterministic Inputs

The *instantaneous radiation power density* of the propagating wave in the far field is a measure of the power flow through a unit area, and is found from the electric field as the norm of the Poynting vector:

$$\frac{1}{\eta} \|\vec{\mathbf{e}}(\mathbf{x}, t)\|^2, \quad (3.54)$$

where $\eta = 376.73 \Omega$ is the impedance of free space. The instantaneous radiation power density is a function of time and has units of W/m^2 . The radiation power density has an inverse-square dependence on the distance $\|\mathbf{x}\|$, while we are primarily interested in the

distribution of power across direction. This is measured by the *instantaneous radiation power intensity*

$$\frac{\|\mathbf{x}\|^2}{\eta} \|\vec{\mathcal{E}}(\mathbf{x}, t)\|^2, \quad (3.55)$$

which has units of W/sr , where steradian sr is a unit of solid angle. Due to the time variation the instantaneous intensity is seldom directly useful. For deterministic waveforms of finite duration, we are primarily interested in the *average radiation power intensity* at far-field position \mathbf{x} :

$$\mathcal{U}_{\text{avg}}(\mathbf{x}) = \frac{\|\mathbf{x}\|^2}{\eta T_s} \int \|\vec{\mathcal{E}}(\mathbf{x}, t)\|^2 dt, \quad (3.56)$$

where T_s is the duration of the input signal. By Parseval's theorem this is equivalent to

$$\begin{aligned} \mathcal{U}_{\text{avg}}(\mathbf{x}) &= \frac{\|\mathbf{x}\|^2}{\eta T_s} \int \|\vec{\mathcal{E}}(\mathbf{x}, f)\|^2 df \\ &= \int \mathcal{U}(\mathbf{x}, f) df, \end{aligned} \quad (3.57)$$

implicitly defining the *radiation power spectral intensity* $\mathcal{U}(\mathbf{x}, f)$, with units $\text{W}/\text{Hz}\cdot\text{sr}$. Writing \mathcal{U} in terms of (3.25) yields

$$\mathcal{U}(\mathbf{x}, f) \triangleq \frac{\|\mathbf{x}\|^2}{\eta T_s} \|\vec{\mathcal{E}}(\mathbf{x}, f)\|^2 \quad (3.58a)$$

$$= \frac{1}{\eta T_s} \|\vec{\mathbf{A}}(-\hat{\mathbf{x}}f/c, f) \mathbf{S}_A(f)\|^2 \quad (3.58b)$$

making explicit that the intensity is a function of direction only, and not distance. If only a single signal is to be transmitted, this further reduces to

$$\mathcal{U}(\mathbf{x}, f) = \frac{1}{\eta} \|\vec{\mathbf{A}}(-\hat{\mathbf{x}}f/c, f)\|^2 \frac{1}{T_s} |S_A(f)|^2. \quad (3.59)$$

To find the total time-average radiated power in all directions and frequencies, we integrate \mathcal{U} over the unit sphere and temporal frequency:

$$\mathcal{P}_{\text{rad}} = \int \int \mathcal{U}(\mathbf{x}, f) \underline{\Omega}(d\mathbf{x}) df, \quad (3.60)$$

where $\underline{\Omega}$ is the surface-area measure on the unit sphere with total measure 4π steradians. Total radiated energy is found simply as $T_s \mathcal{P}_{\text{rad}}$. Power in a particular set of directions of frequencies is found via appropriate integral limits in (3.60).

Random Signals

For WSS random processes, the analog of the average radiation power intensity is the *expected radiation power intensity* (again with units of W/sr):

$$\begin{aligned}\mathcal{U}_{\text{exp}}(\mathbf{x}) &\triangleq \frac{\|\mathbf{x}\|^2}{\eta} \mathcal{E} \{ \|\vec{\epsilon}(\mathbf{x}, t)\|^2 \} \\ &= \frac{\|\mathbf{x}\|^2}{\eta} \text{Tr} [\mathbf{r}_{\vec{\epsilon}}(\mathbf{x}, \mathbf{x}, 0)].\end{aligned}\quad (3.61)$$

In terms of the temporal PSD this is

$$\begin{aligned}\mathcal{U}_{\text{exp}}(\mathbf{x}) &= \frac{\|\mathbf{x}\|^2}{\eta} \int \text{Tr} [\mathbf{R}_{\vec{\epsilon}}(\mathbf{x}, \mathbf{x}, f)] df \\ &= \int \mathcal{U}(\mathbf{x}, f) df,\end{aligned}\quad (3.62)$$

now defining the radiation power spectral intensity as

$$\mathcal{U}(\mathbf{x}, f) \triangleq \frac{\|\mathbf{x}\|^2}{\eta} \text{Tr} [\mathbf{R}_{\vec{\epsilon}}(\mathbf{x}, \mathbf{x}, f)] \quad (3.63a)$$

$$= \frac{1}{\eta} \text{Tr} [\vec{\mathbf{A}}(-\hat{\mathbf{x}}f/c, f) \mathbf{R}_{s_A}(f) \vec{\mathbf{A}}^H(-\hat{\mathbf{x}}f/c, f)]. \quad (3.63b)$$

The second line results from substituting (3.50) and yields the power intensity in terms of the antenna pattern and the input signal power spectrum. In the common case where the input signals are all uncorrelated, the PSD is diagonal: $\mathbf{R}_{s_A} = \text{diag}\{(R_{s_{A1}}, \dots, R_{s_{AN}})\}$. Now (3.63) reduces to

$$\mathcal{U}(\mathbf{x}, f) = \frac{1}{\eta} \sum_{n=1}^N \|\vec{\mathbf{A}}_n(-\hat{\mathbf{x}}f/c, f)\|^2 R_{s_{A_n}}(f) \quad (3.64)$$

where $\vec{\mathbf{A}}_n$ is the n th column of the array pattern. Since the total power density is just the sum of the power densities due to the individual signals, each signal and array pattern can be considered separately. Total radiated power is found using (3.60) as in the deterministic signal case.

Comparing (3.59) to (3.64) with $N = 1$, we see that the two expressions are essentially identical, with the quantity $|\mathbf{S}_A(f)|^2/T_s$ acting as the deterministic-signal equivalent of the power spectral density of the input signal. More generally, we can compare the

deterministic-signal intensity (3.58b) and the random-signal intensity (3.63b) by rewriting the former as the equivalent

$$\mathcal{U}(\mathbf{x}, f) = \frac{1}{\eta} \text{Tr} \left[\vec{\mathbf{A}}(-\hat{\mathbf{x}}f/c, f) \frac{1}{T_s} \mathbf{S}_A(f) \mathbf{S}_A^H(f) \vec{\mathbf{A}}^H(-\hat{\mathbf{x}}f/c, f) \right]. \quad (3.65)$$

This is essentially identical to (3.63b) but with the quantity $\mathbf{S}_A(f) \mathbf{S}_A^H(f)/T_s$ serving as the deterministic equivalent of the power spectral density matrix. Rather than statistical independence, the condition for this deterministic PSD to be diagonal is disjoint spectral support regions among the component signals of \mathbf{S}_A .

Power intensity and radiated power are both convex and quadratic in the beamformer coefficients $\{\mathbf{b}(\mathbf{x}, nT)\}$, and thus SOCP can be used to place upper bounds on both. The next section will demonstrate with the first of several example designs.

3.4.3 Wideband Directive Gain and Directivity

One of the most fundamental antenna parameters is *directivity*, which is a measure of how well an antenna can focus far-field radiation compared to a theoretical isotropic antenna. This is traditionally a narrowband parameter, but is readily extended here to wideband antennas. Along the way we will define a wideband extension of *directive gain*, which provides a meaningful way to normalize the array pattern.

In narrowband array analysis, the *directive gain* at a given location and frequency is the ratio of the radiation power intensity of the antenna to that of an isotropic antenna radiating the same total power:

$$\mathcal{D}_{\text{nb}}(\mathbf{x}, f) \triangleq \frac{\mathcal{U}(\mathbf{x}, f)}{\frac{1}{4\pi} \int \mathcal{U}(\mathbf{x}, f) \Omega(d\mathbf{x})} \quad (3.66)$$

Substituting (3.59) or (3.64) with a single input signal yields

$$\mathcal{D}_{\text{nb}}(\mathbf{x}, f) = \frac{\|\vec{\mathbf{A}}(-\hat{\mathbf{x}}f/c, f)\|^2}{\frac{1}{4\pi} \int \|\vec{\mathbf{A}}(-\hat{\mathbf{x}}f/c, f)\|^2 \Omega(d\mathbf{x})}. \quad (3.67)$$

The signal spectrum drops out, revealing that the directive gain is a function of the array pattern only. Like the radiation intensity, the directive gain is also a function of direction

only and not distance. The directive gain represents a frequency dependent normalization of the array pattern, however, which is undesirable in a wideband setting. Narrowband *directivity* is defined as the maximum value of the directive gain at the single frequency of interest:

$$\mathcal{D}_{\text{nb0}}(f) = \max_{\hat{\mathbf{x}}} \mathcal{D}_{\text{nb}}(\mathbf{x}, f). \quad (3.68)$$

Directivity defined in this way is a function of frequency, and the direction of greatest directive gain may also be a function of frequency.

For wideband systems we seek a frequency-independent normalization to define directive gain. Let \mathcal{F} be the spectral support of the converted input signal. Then the *wideband directive gain* over the frequency band \mathcal{F} is defined as the ratio of the power intensity to the intensity that would result if the same amount of power were instead radiated uniformly over \mathcal{F} from an isotropic antenna:

$$\mathcal{D}(\mathbf{x}, f) \triangleq \frac{\mathcal{U}(\mathbf{x}, f)}{\frac{1}{4\pi \int_{\mathcal{F}} df} \mathcal{P}_{\text{rad}}} \quad (3.69)$$

This normalization, while frequency-independent, is signal dependent. In most cases we wish to define wideband directivity as a signal-independent function of the array. For this we assume a single random input with unit power and a white spectral density over \mathcal{F} :

$$R_{\mathbf{s}_A}(f) = \frac{1_{\mathcal{F}}(f)}{\int_{\mathcal{F}} df}. \quad (3.70)$$

Now (3.69) reduces to

$$\mathcal{D}(\mathbf{x}, f) = \frac{\|\vec{\mathbf{A}}(-\hat{\mathbf{x}}f/c, f)\|^2}{\frac{1}{4\pi \int_{\mathcal{F}} df} \int_{\mathcal{F}} \int_{\mathcal{F}} \|\vec{\mathbf{A}}(-\hat{\mathbf{x}}f/c, f)\|^2 \Omega(d\mathbf{x}) df}, \quad (3.71)$$

a function of the array pattern only. This definition of wideband directive gain was introduced in [24]. This definition provides a convenient way to normalize various antenna patterns for comparison purposes, and will be used throughout the examples to come.

Wideband directivity is found by averaging the wideband directive gain across frequency and taking the maximum value over direction:

$$\mathcal{D}_0 \triangleq \max_{\hat{\mathbf{x}}} \left\{ \frac{1}{\int_{\mathcal{F}} df} \int_{\mathcal{F}} \mathcal{D}(\hat{\mathbf{x}}, f) df \right\} \quad (3.72a)$$

$$= \frac{1}{\int_{\mathcal{F}} df} \int_{\mathcal{F}} \mathcal{D}(\hat{\mathbf{x}}_0, f) df \quad (3.72b)$$

$$= \frac{\int_{\mathcal{F}} \mathcal{U}(\hat{\mathbf{x}}_0, f) df}{\frac{1}{4\pi} \mathcal{P}_{\text{rad}}}, \quad (3.72c)$$

where $\hat{\mathbf{x}}_0$ is the direction of maximum average directive gain. Substituting (3.71) into (3.72b) yields

$$\mathcal{D}_0 = \frac{\int_{\mathcal{F}} \|\vec{\mathbf{A}}(-\hat{\mathbf{x}}_0 f/c, f)\|^2 df}{\frac{1}{4\pi} \int_{\mathcal{F}} \int_{\mathcal{F}} \|\vec{\mathbf{A}}(-\hat{\mathbf{x}} f/c, f)\|^2 \Omega(d\mathbf{x}) df}, \quad (3.73)$$

the signal-independent definition of wideband directivity. Wideband directivity provides a metric which we might wish to maximize in a design. The numerator and denominator are each convex quadratic functions of the beamformer coefficients, but with SOCP we cannot directly optimize the ratio. Instead, we can effectively fix the numerator and minimize the denominator, as demonstrated in the following example.

Example: Maximizing Wideband Directivity

For a first example design, we will maximize the wideband directivity by solving the following SOCP problem:

$$\text{minimize } \alpha > 0 \quad (3.74a)$$

$$\text{s.t. } \int_{\mathcal{F}} \int_{\mathcal{F}} |A_{\text{elV}}(-\hat{\mathbf{x}} f/c, f) B(-\hat{\mathbf{x}} f/c, f)|^2 \Omega(d\mathbf{x}) df \leq \alpha^2 \quad (3.74b)$$

$$\frac{1}{\int_{\mathcal{F}} df} \int_{\mathcal{F}} |A_{\text{elV}}(-\hat{\mathbf{x}}_0 f/c, f) B(-\hat{\mathbf{x}}_0 f/c, f) - 1|^2 df \leq 10^{-\frac{40}{10}}. \quad (3.74c)$$

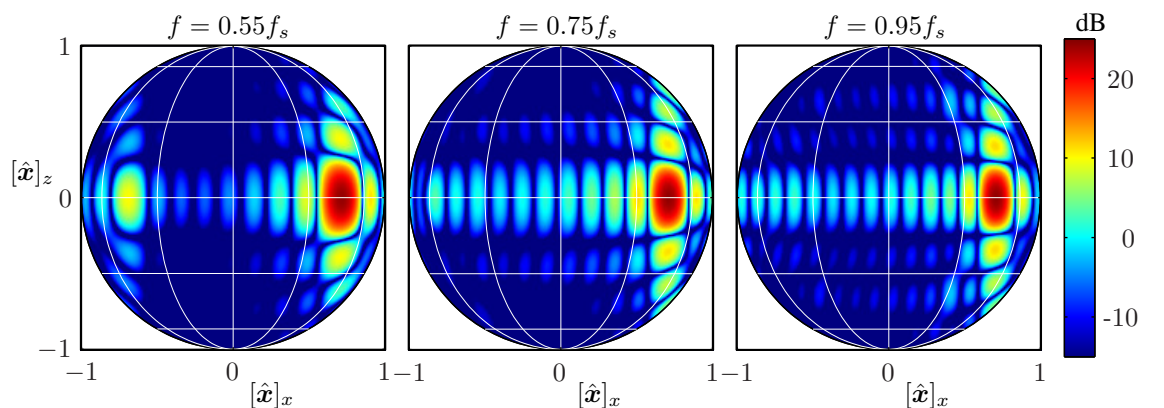
Lines (3.74a) and (3.74b) together serve to minimize the denominator of (3.73); auxiliary variable α is used because SOCP requires a linear objective. Mainbeam passband con-

straint (3.74c) limits the mean-square difference across the passband \mathcal{F} between the array pattern in the steering direction \mathbf{x}_0 and the desired response (in this case, unity) to -40 dB. This effectively fixes the numerator of (3.73), and thus the result of the optimization is to maximize wideband directivity.

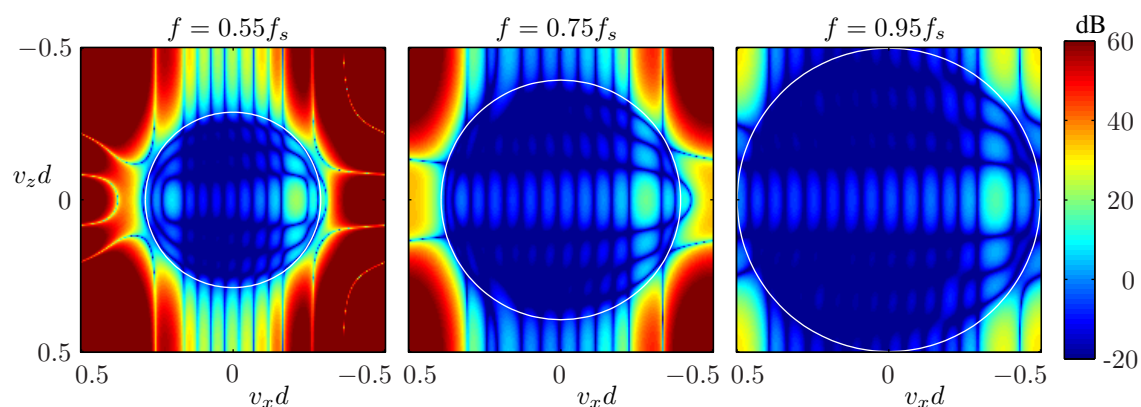
The problem was setup using a custom Matlab toolbox [74], which then passed a canonical SOCP to one of several available solvers [76, 77, 75, 98]. The integral in (3.74b) was approximated using a weighted Riemann sum over a dense grid of spatio-temporal frequencies. The result was a single, full-rank SOC constraint. Likewise the integral in (3.74c) was approximated using a Riemann sum over a dense grid of temporal frequencies, resulting in a second SOC constraint. Since it was formed from responses on a single line through the array pattern, this SOC constraint was of much less than full rank. Total problem setup time on a 1.6 GHz Pentium-M laptop took 465 s, and solving took another 445 s. The optimal wideband directivity was found to be 24.3 dB, and the resulting optimal array pattern and array factor are shown in Figure 3.5.

Figure 3.5(a) shows the wideband directive gain of the optimal array pattern over the entire visible hemisphere of look directions $\hat{\mathbf{x}}$, projected onto the x - z plane, for temporal frequencies at the band edges and the band center. The horizontal lines indicate constant elevation angle, while the vertical curved lines indicate constant azimuth angle, both in increments of 30° . Figure 3.5(c) also shows the array pattern, this time a slice across temporal frequency and azimuth angle at zero elevation, while Figures 3.5(e) and 3.5(f) show selected one-dimensional details. A notable feature seen in these plots is that the angular resolution of the array pattern is very nearly constant across temporal frequency.

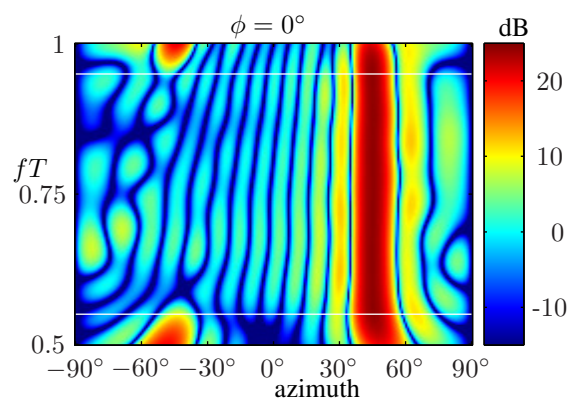
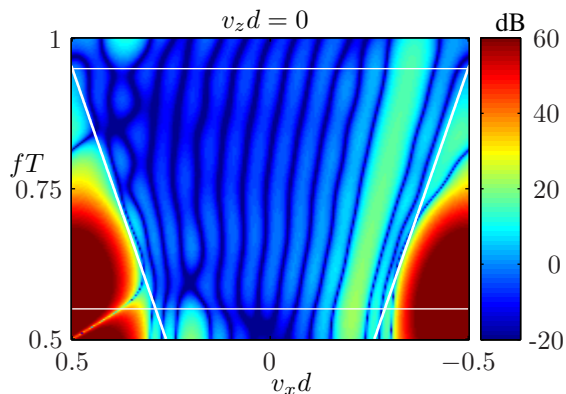
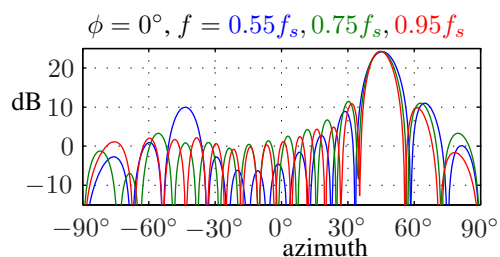
Figure 3.5(b) shows one spatial-frequency period of the array factor at the same temporal frequencies as Figure 3.5(a), with the white circles indicating the Helmholtz cone boundary. Similarly, Figure 3.5(d) shows a slice across temporal frequency and spatial-frequency component v_x at $v_z = 0$, with the diagonal white lines indicating the Helmholtz boundary. The array factor has been normalized so that the wideband directive gain of



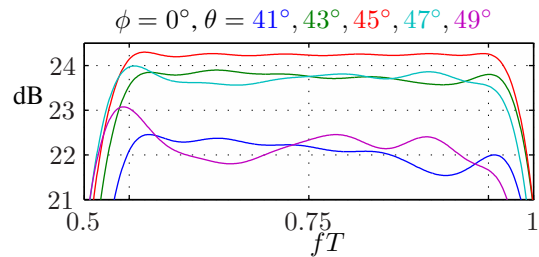
(a) Array pattern wideband directive gain as a function of direction.



(b) Array factor as a function of spatial frequency.

(c) Slice of array pattern directive gain at $\phi = 0^\circ$.(d) Slice of array factor at $v_z d = 0$.

(e) Passband angular response detail.



(f) Mainbeam frequency response detail.

Figure 3.5: The results of maximizing wideband directivity.

the array pattern is the product of the wideband directive gain of the element pattern and the array factor. Inside the Helmholtz cone the array factor is well behaved, and we can see that because of the temporal-frequency-dependent relationship between direction and spatial frequency, the spatial-frequency resolution of the array factor must be greater at lower temporal frequencies than at higher ones to maintain constant angular resolution in the array pattern. Outside the Helmholtz cone, however, the array factor grows extremely large, exceeding 100 dB (the plots are clipped to retain detail within the cone). These huge “invisible” sidelobes are most prominent at lower temporal frequencies, where there is a larger transition zone between the cone in the displayed spatial-frequency period and the adjacent ones. This type of result is often seen in filter optimization problems where a large spectral region is left unconstrained, and here we have no constraints that directly affect the invisible sidelobes. If we were to measure the narrowband directivity of the array pattern at the lower band edge, we would find that it slightly exceeded (by 1 – 2 dB) the classical textbook directivity limit for an array of this size at that frequency. In the language of array design, this array pattern exhibits *superdirectivity*, a topic which is very well covered in the literature [24, 99, 87, 86, 85, 100, 101, 83, 84, 102, 103, 104, 105]. Most of the work on superdirectivity has concluded (properly) that it leads to impractical designs, and this is no exception. To understand why, we need to derive and define *input power*, *efficiency* and *gain*, the topics of the next sections.

3.4.4 Input Power

In the preceding sections, the array was primarily viewed as a linear spatio-temporal system transforming input signals to far-field radiation. The metrics derived so far describe the transfer and distribution of power to the far field via radiation. This approach, while convenient for the analysis to this point, is insufficient to account for power flow within the driving circuit prior to the radiating elements. To model internal power flow, we return to the passband-equivalent system model of Figure 3.1, now focusing on the voltage/current

relationship at the ideal-driver output. This allows us to derive metrics that depend in part on power transfer from the active circuit (drivers) to the array. As will be seen, such constraints are essential to the design of practical wideband arrays.

Earlier we derived expressions for current and voltage with deterministic inputs in (3.4c) and (3.5), repeated here:

$$\underline{\mathbf{i}}(d\mathbf{x}, dt) = (\underline{\mathbf{b}} * \underline{\mathbf{s}}_A)(d\mathbf{x}, dt) \quad (3.75a)$$

$$\underline{\mathbf{v}}(d\mathbf{x}, dt) = (\underline{\mathbf{z}} \boxtimes \underline{\mathbf{i}})(d\mathbf{x}, dt) \quad (3.75b)$$

The resistance distribution $\underline{\mathbf{z}}(d\mathbf{x}, dt; -\mathbf{x}')$ models the nonideal, linear characteristics of the driver, the matching and feed networks, and the array. As noted previously, the resistance distribution is real and has units of Ohms. Since both voltage and current are $M \times 1$ vectors with spatial support on the discrete set \mathcal{L} , $\underline{\mathbf{z}}$ necessarily has dimension $M \times M$ and the form

$$\underline{\mathbf{z}}(d\mathbf{x}, dt; -\mathbf{x}') = \sum_{\mathbf{x} \in \mathcal{L}} \underline{\mathbf{z}}(\mathbf{x}, dt; -\mathbf{x}') \underline{\mathbf{x}} \delta(d\mathbf{x}). \quad (3.76)$$

The temporal Fourier transform $\underline{\mathbf{Z}}(d\mathbf{x}, f; -\mathbf{x}')$ of the resistance distribution is the *impedance measure*, which also has units of Ohms but is complex valued in general. The impedance measure is the measure-system equivalent to a frequency-dependent impedance matrix, as can be seen by manipulating its defining relation

$$\begin{aligned} \underline{\mathbf{V}}(\mathcal{X}, f) &= (\underline{\mathbf{Z}} \square \underline{\mathbf{I}})(\mathcal{X}, f) \\ &= \int \underline{\mathbf{Z}}(\mathcal{X}, f; -\mathbf{x}') \underline{\mathbf{I}}(d\mathbf{x}', f) \\ &= \int \int \int_{\mathcal{X}} \underline{\mathbf{Z}}(\mathbf{x}, f; -\mathbf{x}') \underline{\mathbf{x}} \delta(d\mathbf{x}) \underline{\mathbf{I}}(\mathbf{x}', f) \underline{\mathbf{x}} \delta(d\mathbf{x}') \\ &= \sum_{\mathbf{x} \in \mathcal{L}} \sum_{\mathbf{x}' \in \mathcal{L}} \underline{\mathbf{Z}}(\mathbf{x}, f; -\mathbf{x}') \underline{\mathbf{I}}(\mathbf{x}', f) \underline{\mathbf{x}} \delta(\mathcal{X}). \end{aligned}$$

The density of the voltage measure at location \mathbf{x} is just a weighted sum of the currents at all locations $\mathbf{x}' \in \mathcal{L}$, which is analogous to a matrix multiply. In general the current is vector-valued (to allow multiple elements to occupy the same nominal location), and so the

weight $\mathbf{Z}(\mathbf{x}, f; -\mathbf{x}')$ is matrix valued. If \mathcal{L} has K distinct locations, then the impedance measure is exactly equivalent to the $MK \times MK$ impedance matrix that would be used in a non-measure-signal context; here $[\mathbf{Z}(\mathbf{x}, -\mathbf{x}', f)]_{m,n}$ is the frequency response relating the voltage contribution at the m th element at location \mathbf{x} due to the current at the n th element at location \mathbf{x}' . We will assume that the circuit is reciprocal, in which case the impedance density obeys the symmetry relationship

$$\mathbf{Z}(\mathbf{x}, f; -\mathbf{x}') = \mathbf{Z}^T(\mathbf{x}', f; -\mathbf{x}). \quad (3.77)$$

The component of the impedance measure that corresponds to radiation is fully determined by the array response \vec{p} , and can be calculated by solving Maxwell's equations in the near field for a series of test inputs [95].

The input power delivered to the array by the ideal driver is found by integrating the time-average (for deterministic signals) or expected (for random signals) product of the current and voltage:

$$\mathcal{P}_{\text{in}} = \frac{1}{T_s} \int \mathbf{i}^T(\mathbf{x}, t) \mathbf{v}(d\mathbf{x}, dt) \quad (3.78)$$

and

$$\mathcal{P}_{\text{in}} = \int \mathcal{E} \{ \mathbf{i}^T(\mathbf{x}, t) \mathbf{v}(d\mathbf{x}, t) \}, \quad (3.79)$$

respectively. We proceed now to analyze the random-signal case in some detail, and to relate the input power back to the input signal autocorrelation; the deterministic result then quickly follows by substituting the time-average autocorrelation. We can rewrite (3.79) in steps as

$$\mathcal{P}_{\text{in}} = \int \mathcal{E} \{ \mathbf{i}(\mathbf{x}, t)^T \mathbf{v}(\mathbf{x}, t) \} \Sigma_{\mathcal{L}}(d\mathbf{x}) \quad (3.80a)$$

$$= \int \text{Tr}[\mathbf{r}_{v,i}](\mathbf{x}, \mathbf{x}, 0) \Sigma_{\mathcal{L}}(d\mathbf{x}) \quad (3.80b)$$

$$= \int \text{Tr}[\mathbf{z} \boxtimes \mathbf{r}_i](\mathbf{x}, \mathbf{x}, 0) \Sigma_{\mathcal{L}}(d\mathbf{x}), \quad (3.80c)$$

invoking (2.39) in the last line. A frequency-domain representation provides more insight.

Since \mathcal{P}_{in} is real, we can write

$$\mathcal{P}_{\text{in}} = \text{Re} \left\{ \int \int \text{Tr} [\underline{\mathbf{z}} \boxtimes \underline{\mathbf{r}}_i](\mathbf{x}, \mathbf{x}, 0) \underline{\Sigma}_{\mathcal{L}}(d\mathbf{x}) \right\} \quad (3.81\text{a})$$

$$= \int \int \int \text{Tr} [\text{Re}\{\mathbf{Z} \square \underline{\mathbf{R}}_i\}](\mathbf{x}, \mathbf{x}, f) \underline{\Sigma}_{\mathcal{L}}(d\mathbf{x}) df \quad (3.81\text{b})$$

$$= \int \int \int \text{Tr} [\text{Re}\{\mathbf{Z}\} \square \underline{\mathbf{R}}_i](\mathbf{x}, \mathbf{x}, f) \underline{\Sigma}_{\mathcal{L}}(d\mathbf{x}) df. \quad (3.81\text{c})$$

The last step is a consequence of (3.77) and the Hermitian symmetry of $\underline{\mathbf{R}}_i$, and it reveals that the input power depends only on the real part of the impedance. This is just a multi-dimensional restatement of a first-year circuits result: reactive elements consume no real power. In (3.81c) we can see that the trace expression represents a power density across space and temporal frequency.

To relate \mathcal{P}_{in} to the input signal we first expand the space-variant filtering in (3.81c) and invoke (3.77) (anticipating the latter by swapping the roles of \mathbf{x} and \mathbf{y} in the second line):

$$\begin{aligned} \mathcal{P}_{\text{in}} &= \text{Tr} \left[\int \int \int \text{Re}\{\mathbf{Z}\}(\mathbf{x}, f; -\mathbf{y}) \underline{\mathbf{R}}_i(d\mathbf{y}, \mathbf{x}, f) \underline{\Sigma}_{\mathcal{L}}(d\mathbf{x}) df \right] \\ &= \text{Tr} \left[\int \int \int \text{Re}\{\mathbf{Z}\}(\mathbf{y}, f; -\mathbf{x}) \underline{\mathbf{R}}_i(d\mathbf{x}, \mathbf{y}, f) \underline{\Sigma}_{\mathcal{L}}(d\mathbf{y}) df \right] \\ &= \text{Tr} \left[\int \int \int \text{Re}\{\mathbf{Z}^T\}(\mathbf{x}, f; -\mathbf{y}) \underline{\mathbf{R}}_i(d\mathbf{x}, d\mathbf{y}, f) df \right]. \end{aligned}$$

In the last line we absorb the reference measure into the spectral density measure. Substituting for the current autocorrelation yields

$$\boxed{\mathcal{P}_{\text{in}} = \int \int \int \text{Tr} [\text{Re}\{\mathbf{Z}^T\}(\mathbf{x}, f; -\mathbf{y}) \underline{\mathbf{B}}(d\mathbf{x}, f) \underline{\mathbf{R}}_{\mathbf{s}_A}(f) \underline{\mathbf{B}}^H(d\mathbf{y}, f)] df,} \quad (3.82)$$

which relates \mathcal{P}_{in} back to the input autocorrelation. The corresponding deterministic-signal result is

$$\boxed{\mathcal{P}_{\text{in}} = \int \int \int \text{Tr} [\text{Re}\{\mathbf{Z}^T\}(\mathbf{x}, f; -\mathbf{y}) \underline{\mathbf{B}}(d\mathbf{x}, f) \frac{1}{T_s} \underline{\mathbf{S}}_A(f) \underline{\mathbf{S}}_A^H(f) \underline{\mathbf{B}}^H(d\mathbf{y}, f)] df,} \quad (3.83)$$

Both expressions are quadratic in the coefficients of the beamformer $\underline{\mathbf{b}}$. Since \mathbf{Z} here represents a passive system, \mathcal{P}_{in} is necessarily nonnegative and the quadratic is also convex. Thus we can constrain input power directly using second-order cone programming.

The power input to the array is either radiated or is lost as heat in the driver circuits, feed network, or elements. Thus we can trivially write $\mathcal{P}_{\text{in}} = \mathcal{P}_{\text{rad}} + \mathcal{P}_{\text{loss}}$. In some cases we can derive $\mathcal{P}_{\text{loss}}$ directly without knowledge of the impedance measure. Consider an array of identical electrically small elements driven by our ideal current source. If the sources and array are ideal, then the equivalent impedance Z (a scalar, because all elements are identical) seen by the current drivers is just Z_{rad} , the radiation impedance of the array. In this case the input power (3.81c) simplifies to

$$\mathcal{P}_{\text{in}} = \iint_{\mathcal{L}} (\text{Re}\{Z_{\text{rad}}\} \square R_i)(\mathbf{x}, \mathbf{x}, f) \underline{\Sigma}_{\mathcal{L}}(d\mathbf{x}) df,$$

and since no power is lost in the source or array, we have $\mathcal{P}_{\text{in}} = \mathcal{P}_{\text{rad}}$. Of course, in a real array, losses are inevitable. Unless superconducting elements are used [106], elements will have series resistive losses that are a function of material, cross-section, and length. If Z_0 is the (resistive) impedance of one dipole, then the equivalent circuit impedance is now $Z = Z_{\text{rad}} + Z_{\text{loss}}$, where

$$Z_{\text{loss}}(x, f; -y) = \begin{cases} Z_0, & x = y \\ 0, & \text{otherwise} \end{cases}.$$

Now the input power is

$$\begin{aligned} \mathcal{P}_{\text{in}} &= \iint_{\mathcal{L}} (Z_{\text{rad}} \square R_i)(\mathbf{x}, \mathbf{x}, f) \underline{\Sigma}_{\mathcal{L}}(d\mathbf{x}) df + \iint_{\mathcal{L}} Z_0 R_i(\mathbf{x}, \mathbf{x}, f) \underline{\Sigma}_{\mathcal{L}}(d\mathbf{x}) df \\ &= \mathcal{P}_{\text{rad}} + \mathcal{P}_{\text{loss}}. \end{aligned}$$

Expanding $\mathcal{P}_{\text{loss}}$ for a single input yields

$$\mathcal{P}_{\text{loss}} = Z_0 \int R_{s_A}(f) \iint_{\mathcal{L}} |B(\mathbf{x}, f)|^2 \underline{\Sigma}_{\mathcal{L}}(d\mathbf{x}) df \quad (3.85a)$$

$$= Z_0 \int R_{s_A}(f) \sum_{\mathbf{x} \in \mathcal{L}} |B(\mathbf{x}, f)|^2 df \quad (3.85b)$$

a spectrally weighted integral of the sum of the magnitude-squared frequency responses of all the component filters in the beamformer. Applying a version of Parseval's relation

based on (2.13) to (3.85a) yields

$$\mathcal{P}_{\text{loss}} = \lim_{V \rightarrow \infty} \frac{Z_0}{\int_{\mathcal{B}_V} d\mathbf{v}} \int R_{s_A}(f) \int_{\mathcal{B}_V} |\mathbf{B}(\mathbf{v}, f)|^2 d\mathbf{v} df \quad (3.86)$$

in general, and similarly applying (2.14) yields

$$\mathcal{P}_{\text{loss}} = Z_0 \int R_{s_A}(f) \int |\mathbf{B}(\mathbf{v}, f)|^2 \mu_{[\Lambda \mathbb{R}^M / \Lambda + T \mathbb{Z}^M]}(d\mathbf{v}) df \quad (3.87)$$

when the elements lie on the lattice $\Lambda \mathbb{Z}^M$. Nearly identical results follow for deterministic inputs. We can see that the power lost to resistive heating is equally dependent on the array factor for all spatial frequencies, which in the lattice case is equivalent to equal dependence for all frequencies in one spatial-frequency period. In contrast, from (3.27) and (3.59) we see that for arrays with identical element responses the radiated power depends on the array pattern (and thus the array factor) only for spatio-temporal frequencies on the Helmholtz cone. Thus we expect large values of the array factor off the cone to lead to large power losses, without offsetting increases in transmitted power. The result is poor efficiency, the subject of the next section.

3.4.5 Efficiency

Traditionally, antenna efficiency is defined as the ratio of the total power “accepted by the antenna from a connected transmitter” [95] to the total power radiated, thus not including the efficiency of the transmitter itself. Since our simple model does not cleanly separate the transmitter and the antenna, we will define the efficiency of an array as the ratio of radiated power to driver input power:

$$\xi = \frac{\mathcal{P}_{\text{rad}}}{\mathcal{P}_{\text{in}}} \quad (3.88a)$$

$$= \frac{\mathcal{P}_{\text{rad}}}{\mathcal{P}_{\text{rad}} + \mathcal{P}_{\text{loss}}}. \quad (3.88b)$$

This definition might include driver losses not included in the classical definition. If we return to the example design of Section 3.4.3, we see that the array factor has extremely

large values outside of the Helmholtz cone, and thus we suspect that efficiency will be poor with non-zero element series resistance. If we assume that the series resistance of a single small dipole is $Z_0 = 0.1 \Omega$ (for the sake of comparison, the radiation resistance of a single isolated small dipole with the given dimensions at the nominal signal frequency is approximately 1Ω), and that the input signal has the flat bandlimited spectrum (3.70) as before, then we find that the efficiency of the example design is a vanishingly small $\xi = 9.3 \cdot 10^{-8}$. Essentially all input power is lost as heat. Physically we would find that the currents going into each element are extremely large, but with alternating polarity in adjacent elements. This results in cancellation in the far field, and little radiated power.

Example: Maximizing Efficiency

Clearly optimizing wideband directivity alone leads to impractical designs. Given the low efficiency that resulted from maximizing wideband directivity, we might wish to maximize efficiency instead. Like wideband directivity, efficiency is a ratio of quadratics, but in this case we can't directly fix the numerator. Instead we minimize $\mathcal{P}_{\text{loss}}$ by solving the following SOC program:

$$\text{minimize } \alpha > 0 \tag{3.89a}$$

$$\text{s.t. } \int_{\mathcal{F}} \sum_{\mathbf{x} \in \mathcal{L}} |B(\mathbf{x}, f)|^2 df \leq \alpha^2 \tag{3.89b}$$

$$\frac{1}{\int_{\mathcal{F}} df} \int_{\mathcal{F}} |A_{\text{elV}}(-\hat{\mathbf{x}}_0 f/c, f)B(-\hat{\mathbf{x}}_0 f/c, f) - 1|^2 df \leq 10^{-\frac{40}{10}}. \tag{3.89c}$$

Objective (3.89a) and SOC constraint (3.89b) together minimize the power lost to heating. The mainbeam passband constraint (3.89c) is exactly as in the previous design: it limits the mean-square difference across the passband \mathcal{F} between the array pattern in the steering direction \mathbf{x}_0 and the desired response (in this case, unity) to -40 dB. Here it serves to effectively lower bound the radiated power \mathcal{P}_{rad} , so that by (3.88b) minimizing $\mathcal{P}_{\text{loss}}$ maximizes efficiency. Interestingly, although the value of Z_0 is critical to the actual value of the lost power, it is irrelevant as far as the optimization is concerned; the same solution minimizes

power loss regardless of the value of the series resistance. All integrals are again computed as Riemann sums over sets of discrete frequencies. Total setup time for this example was 30 s, while the solver took less than 1 s by taking advantage of the sparse internal representation of the SOC constraint (3.89b). Assuming as before that $Z_0 = 0.1 \Omega$, the optimal efficiency was found to be 94%, and the corresponding wideband directivity is 22.2 dB. Thus the price of the increased efficiency is a decrease of 2.1 dB in wideband directivity. The resulting array pattern and array factor are shown in Figure 3.6.

Examining the array factor, we can see that the huge invisible sidelobes are gone, and that the sidelobes are continuous across the Helmholtz boundary. This provides visual confirmation that (3.89b) has indeed constrained the array factor uniformly across the spatial-frequency period. The array-factor mainbeam width in spatial frequency is now nearly constant across temporal frequency. As a consequence, and in contrast to the previous example, the array-pattern mainbeam angular width here narrows with increasing frequency. The loss of directivity is evident at lower frequencies, where the mainbeam is much wider than in the previous example. A side-effect of the narrowing beam is that the frequency response at angles in the mainbeam offset from the steering direction exhibit noticeable rolloff at higher frequencies, as seen in 3.6(f).

If we momentarily relax the requirement that the beamformer filters be FIR and set passband error on the left in (3.89c) identically to zero, then we find that this problem has an exact analytic solution for any band \mathcal{F} :

$$B_{\text{opt}}(\mathbf{x}, f) = \frac{1}{K} A_{\text{elV}}^{-1}(-\hat{\mathbf{x}}_0 f/c, f) e^{-j2\pi \mathbf{x} \cdot \hat{\mathbf{x}}_0 f/c}. \quad (3.90)$$

Except for the element-pattern inverse (which might be factored out and moved to the signal generation), this is just the classic time-delay approach to wideband pattern synthesis. The drive current for each element is identical save a time delay by $\mathbf{x} \cdot \hat{\mathbf{x}}_0/c$ that depends on element position and steering direction. We thus expect that in the FIR solution the beamformer filters will approximate (3.90). This is verified in Figure 3.7, which shows

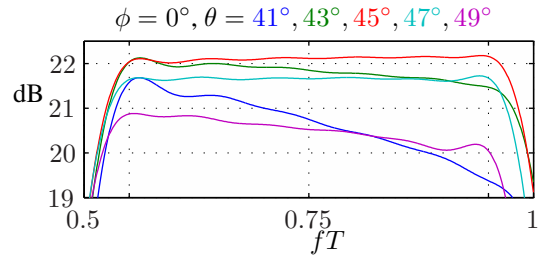
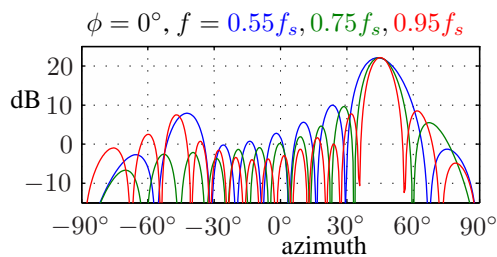
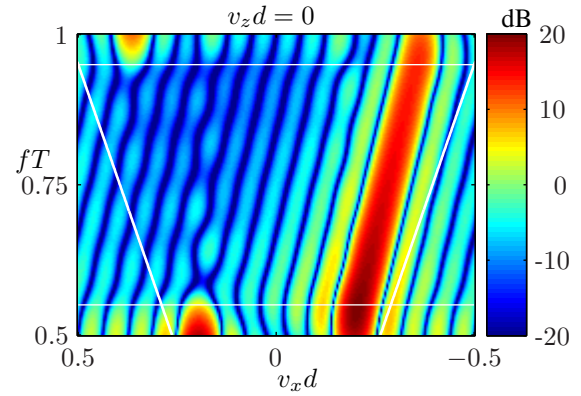
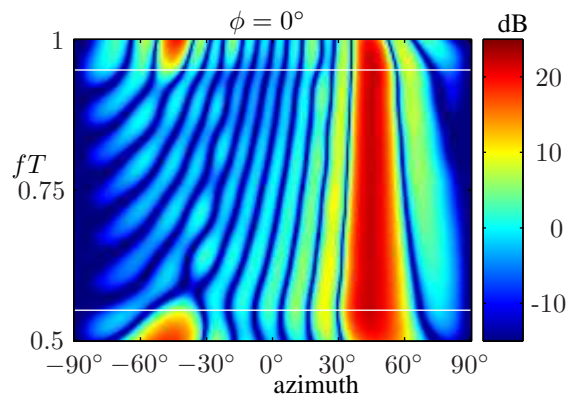
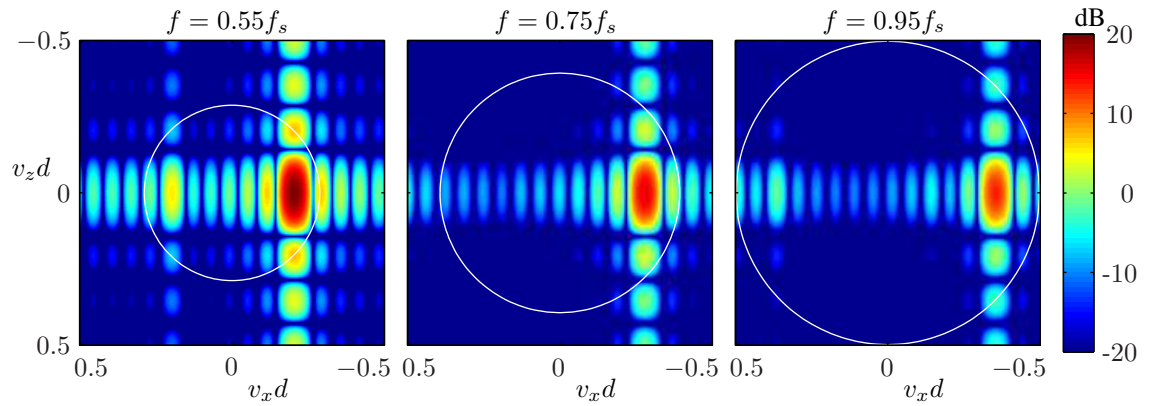
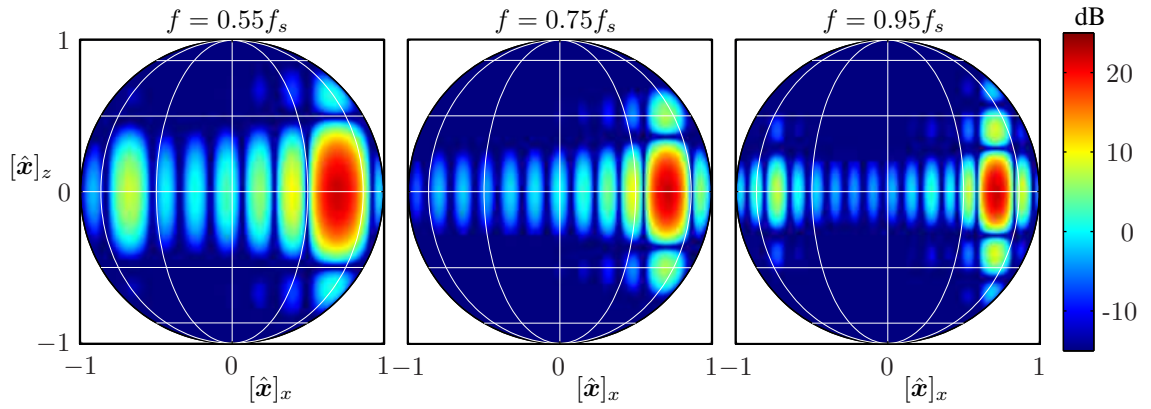


Figure 3.6: The results of maximizing efficiency.

the magnitude and group-delay responses for the eight beamformer filters corresponding to elements located on the x -axis at positions $x = d/2, 3d/2, \dots, 15d/2$. All filters have nearly the same magnitude response, as predicted. On the group-delay plot, each colored horizontal line indicates the theoretical delay of the filter response with the corresponding color. Although the group-delay curves have large error ripples, we can see that the mean group delay of each filter matches the theory. Given these relatively large group-delay and magnitude response ripples, it might seem surprising that the overall array-pattern passband could be made so flat. Indeed, had the filters been independently designed to approximate (3.90), then the passband specification might not have been met. This is because the complex-error ripples in the individually designed filters might add constructively in the array factor, producing greater array-factor errors. In a joint design the focus is not on the approximation error in a single filter, but rather on the entire response.

3.4.6 Wideband Gain and Power Gain

Although maximizing efficiency produced a reasonable design which matches the classical time-delay solution, it is clear from the definition that efficiency does not provide a measure of where the radiated power goes. Directivity provides a measure of how focused a beam is, but as we have seen optimizing wideband directivity alone leads to impractical designs. A metric which combines efficiency and wideband directivity is *wideband gain*, which is defined over a frequency band \mathcal{F} as the ratio of the average far-field power intensity over \mathcal{F} in the direction $\hat{\mathbf{x}}_0$ to the average density that would result from a lossless isotropic radiator with the same input power:

$$\mathcal{G}_0 \triangleq \frac{\int_{\mathcal{F}} \mathcal{U}(\hat{\mathbf{x}}_0, f) df}{\frac{1}{4\pi} \mathcal{P}_{\text{in}}}. \quad (3.91)$$

Comparing this to (3.72) and (3.88a), we see that wideband gain is simply the product of efficiency and wideband directivity:

$$\boxed{\mathcal{G}_0 = \xi \mathcal{D}_0.}$$

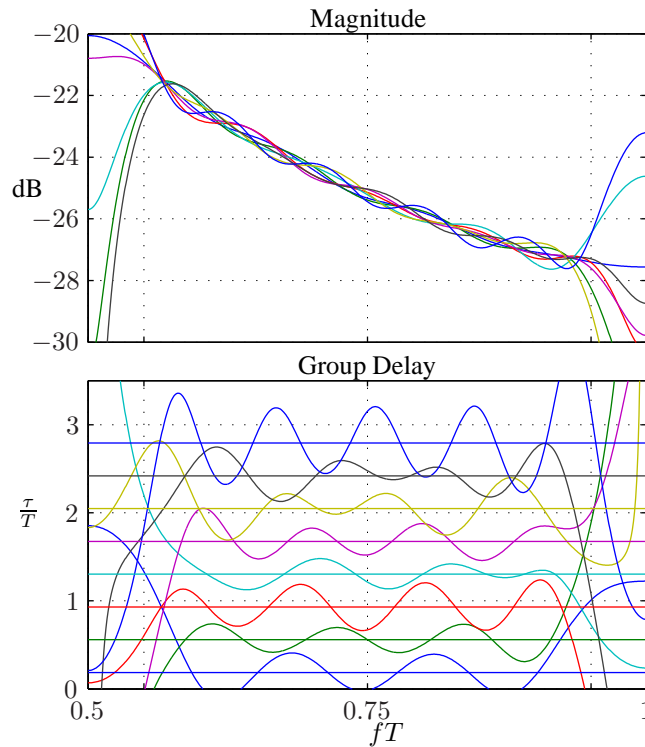


Figure 3.7: Magnitude and group-delay responses of selected element filters for maximum-efficiency example design. Horizontal group-delay lines indicate theoretical ideal delay of the filter response of the corresponding color.

Analogous to the relationship between wideband gain and wideband directivity, *wideband power gain* is defined as the product of efficiency and wideband directive gain

$$\mathcal{G}(\mathbf{x}, f) \triangleq \xi \mathcal{D}(\mathbf{x}, f).$$

Narrowband power gain (the product of efficiency and narrowband directive gain) and is often used instead of directive gain to plot array patterns, and wideband power gain can be used similarly.

Wideband gain measures how well the array converts input power into far-field radiation in a given direction. As such, it is often a more appropriate metric than either wideband directivity or efficiency alone. If we assume the white input characterized by (3.70), then we can substitute (3.64) and (3.82) into (3.91) to derive a signal-independent definition of

wideband gain as

$$\mathcal{G}_0 = \frac{\frac{1}{\eta} \int_{\mathcal{F}} \|\vec{\mathbf{A}}(-\hat{\mathbf{x}}_0 f/c, f)\|^2 df}{\frac{1}{4\pi} \int_{\mathcal{F}} \int_{\mathcal{L}} \text{Tr}[\text{Re}\{\mathbf{Z}^T\}(\mathbf{x}, f; -\mathbf{y}) \mathbf{B}(d\mathbf{x}, f) \mathbf{B}^H(d\mathbf{y}, f)] df}. \quad (3.92)$$

If we additionally assume that $\mathcal{P}_{\text{loss}}$ is dominated by series element resistance, then we can use $\mathcal{P}_{\text{in}} = \mathcal{P}_{\text{rad}} + \mathcal{P}_{\text{loss}}$ and substitute (3.64), (3.60), (3.85a), and (3.82) into (3.91):

$$\mathcal{G}_0 = \frac{\frac{1}{\eta} \int_{\mathcal{F}} \|\vec{\mathbf{A}}(-\hat{\mathbf{x}}_0 f/c, f)\|^2 df}{\frac{1}{4\pi\eta} \int_{\mathcal{F}} \int_{\mathcal{L}} \|\vec{\mathbf{A}}(-\hat{\mathbf{x}} f/c, f)\|^2 \Omega(d\mathbf{x}) df + \frac{1}{4\pi} Z_0 \int_{\mathcal{F}} \int_{\mathcal{L}} |B(\mathbf{x}, f)|^2 \Sigma_{\mathcal{L}}(d\mathbf{x}) df}. \quad (3.93)$$

Numerator and denominator are both convex and quadratic in the beamformer coefficients. We can optimize wideband gain by fixing the numerator with a passband constraint as before, and minimize the denominator.

Example: Maximizing Wideband Gain

We can optimize the wideband gain of the example array by solving the SOC program

$$\text{minimize } \alpha > 0 \quad (3.94a)$$

$$\text{s.t. } \frac{1}{\eta} \int_{\mathcal{F}} \int_{\mathcal{L}} |A_{\text{elV}}(-\hat{\mathbf{x}} f/c, f) B(-\hat{\mathbf{x}} f/c, f)|^2 \Omega(d\mathbf{x}) df \quad (3.94b)$$

$$+ Z_0 \int_{\mathcal{F}} \sum_{\mathbf{x} \in \mathcal{L}} |B(\mathbf{x}, f)|^2 df \leq \alpha^2$$

$$\frac{1}{\int_{\mathcal{F}} df} \int_{\mathcal{F}} |A_{\text{elV}}(-\hat{\mathbf{x}}_0 f/c, f) B(-\hat{\mathbf{x}}_0 f/c, f) - 1|^2 df \leq 10^{-\frac{40}{10}}. \quad (3.94c)$$

The mainbeam passband constraint (3.94c) is the same as in the previous designs: it limits the mean-square difference across the passband \mathcal{F} between the array pattern in the steering direction \mathbf{x}_0 and the desired response (in this case, unity) to -40 dB. Here it also serves to fix the numerator of (3.93), while the SOC constraint (3.94b) minimizes the denominator (input power), thus maximizing wideband gain. This program was setup in 1150 s and solved in 307 s. Maximum wideband gain was found to be 22.4 dB, with an efficiency

Example	\mathcal{D}_0	ξ	\mathcal{G}_0
Max. Directivity	24.3 dB	$9.3 \cdot 10^{-8}$	-46.0 dB
Max. Efficiency	22.2 dB	94%	21.9 dB
Max. Gain	22.9 dB	90%	22.4 dB

Table 3.2: Comparison of results for example designs.

of 90% and a wideband directivity of 22.9 dB. Figure 3.8 shows the optimal array pattern and array factor. Compared to the previous example, the array-pattern mainbeam is somewhat narrower at lower frequencies, and has less variation in width over frequency. The array-pattern frequency response for off-center mainbeam directions still exhibits significant rolloff. The array factor now has larger invisible sidelobes, and there is a clear delineation between the visible sidelobes and the larger invisible sidelobes.

For purposes of comparison, the wideband directivity, efficiency, and wideband gain for the three examples presented so far are given in Table 3.2. Clearly the maximum-directivity example is the outlier, with efficiency near zero and extremely small wideband gain. Of the other two designs, the maximum-gain design is clearly superior, as it has 0.7 dB more wideband directivity and 0.5 dB more wideband gain.

3.4.7 Mainbeam Frequency-Response Constraints

In the preceding examples, the frequency response of the array pattern was constrained only at the nominal beam steering direction $\hat{\mathbf{x}}_0$. However, in practice the exact direction to a target is rarely known, and lies anywhere within some region around the center. As was shown in the previous examples, significant rolloff in the array-pattern frequency response occurs even for relatively small angular offsets from the beam center. It is tempting to consider adding many more constraints of the form (3.93) over a dense grid of angles around $\hat{\mathbf{x}}_0$, but the result would be a flat-topped array pattern that would in turn result in reduced

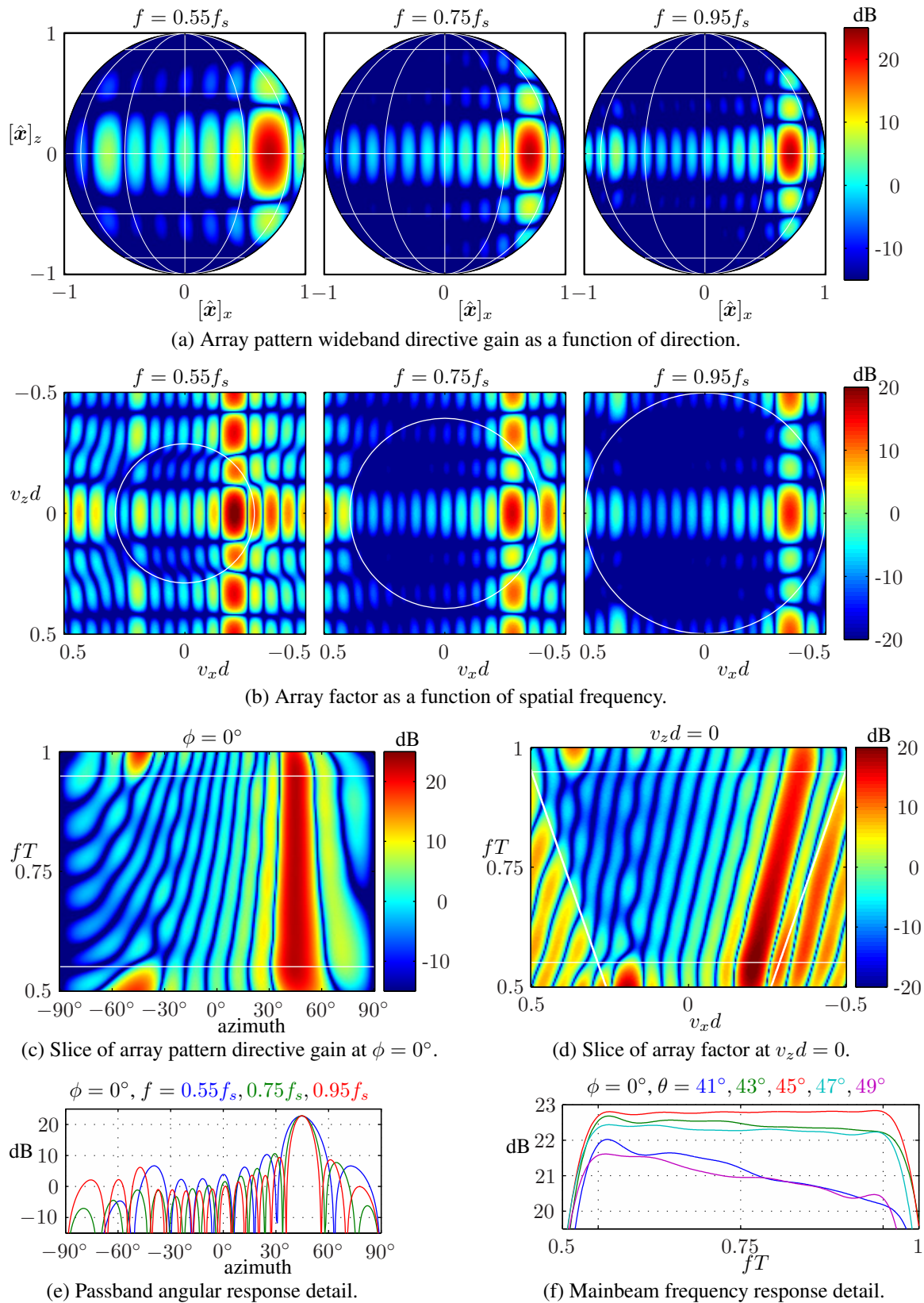


Figure 3.8: The results from maximizing wideband gain.

wideband gain. Instead, we would like to constrain the shape of the frequency response at a given angle without setting the overall level. Consider the following modification of the previous example specification:

$$\text{minimize } \alpha > 0 \quad (3.95a)$$

$$\text{s.t. } \frac{1}{\eta} \int_{\mathcal{F}} \int_{\mathcal{L}} |A_{\text{elV}}(-\hat{\mathbf{x}}f/c, f)B(-\hat{\mathbf{x}}f/c, f)|^2 \Omega(d\mathbf{x}) df \quad (3.95b)$$

$$+ Z_0 \int_{\mathcal{F}} \sum_{\mathbf{x} \in \mathcal{L}} |B(\mathbf{x}, f)|^2 df \leq \alpha^2$$

$$\frac{1}{\int_{\mathcal{F}} df} \int_{\mathcal{F}} |A_{\text{elV}}(-\hat{\mathbf{x}}_0 f/c, f)B(-\hat{\mathbf{x}}_0 f/c, f) - 1|^2 df \leq 10^{-\frac{40}{10}} \quad (3.95c)$$

$$\frac{1}{\int_{\mathcal{F}} df} \int_{\mathcal{F}} |A_{\text{elV}}(-\hat{\mathbf{x}}_k f/c, f)B(-\hat{\mathbf{x}}_k f/c, f) - \beta_k|^2 df \leq 10^{-\frac{40}{10}} \beta_k^2, \quad (3.95d)$$

$$k = 1, \dots, K_{\text{mb}}$$

In (3.95d) we have added $K_{\text{mb}} = 24$ new main-beam frequency-response constraints in directions $\{\hat{\mathbf{x}}_k\}$, which range $\pm 4^\circ$ from $\hat{\mathbf{x}}_0$ in 2° steps in both azimuth and elevation. Each SOC constraint upper-bounds the mean-square error between the array pattern and real auxiliary variable β_k . Since β_k is otherwise unconstrained, this allows the overall level of the frequency response at each direction $\hat{\mathbf{x}}_k$ to float. By making the bound on the right proportional to β_k^2 we constrain relative, rather than absolute, mean-square error. The optimization problem of (3.95) was setup and solved, taking 522 s and 730 s respectively. The resulting array pattern and array factor are shown in Figure 3.9. The direct effects of the added constraints can be seen in Figure 3.9(f), showing that the frequency responses have indeed been flattened. In Figures 3.9(c) and 3.9(e) we see that a side effect of the frequency-response constraints is to enforce an array pattern whose mainbeam has uniform width across frequency. Since it was not possible to efficiently narrow the mainbeam at lower frequencies, the result of the optimization was primarily to widen the mainbeam at higher frequencies. Mainbeam width in such designs is largely dictated by the lowest operating frequency. Accompanying the beam widening is a drop in the sidelobe levels at higher frequencies. Since the optimization cannot increase wideband gain by narrowing

the mainbeam (as in the previous designs), it partially compensates by reducing sidelobes. The wideband directivity, efficiency, and wideband gain for this example are 22.6 dB, 89%, and 22.1 dB, respectively. Adding the mainbeam constraints has cost 0.3 dB in wideband gain and wideband directivity, with little loss of efficiency.

As an alternative to mean-square error constraints, we can also bound the peak passband error, with constraints of the form

$$\boxed{\left| A_{\text{elV}}(-\hat{\mathbf{x}}_k f_n/c, f_n) B(-\hat{\mathbf{x}}_k f_n/c, f_n) - \beta_k D_0(f_n) \right| \leq 10^{-\frac{40}{20}} \beta_k, \quad \begin{array}{l} k = 1, \dots, K_{\text{mb}} \\ n = 1, \dots, N_{\text{pb}}, \end{array}} \quad (3.96)$$

where $D_0(f)$ is the desired passband response, $\{\hat{\mathbf{x}}_k\}$ is a dense grid of angles around the nominal beam center, $\{f_n\}$ is a dense set of frequencies across the passband \mathcal{F} , and $10^{-40/20}$ is the upper bound placed on the peak passband error. Here the passband error is defined relative to the nominal passband level β_k , but dropping the β_k on the right will instead bound the absolute peak passband error. If the array pattern is complex and the beamformer does not have linear-phase symmetry, then this results in $K_{\text{mb}} \times N_{\text{pb}}$ SOC constraints, each of rank two. If the array pattern is real (or linear phase) then this results in $K_{\text{mb}} \times N_{\text{pb}}$ pairs of linear constraints, which are more efficient to solve.

The example array used throughout this section is composed of identical vertically oriented (polarized) dipoles, and thus the resulting array pattern is necessarily vertically polarized. For arrays without identical element responses, especially those composed of elements with multiple orientations, the polarization is determined by the beamformer coefficients. The general formulations for wideband directivity, efficiency, and wideband gain previously derived make no assumptions about polarization, but the passband constraints used in the example designs and extended in this section implicitly assume that the polarization is fixed, and that we effectively have a scalar array pattern. When this is not the case, then constraints of the form (3.95c) and (3.95d) are not sufficient, as they only control one vector component of the array pattern. Instead, we require a pair of constraints for each

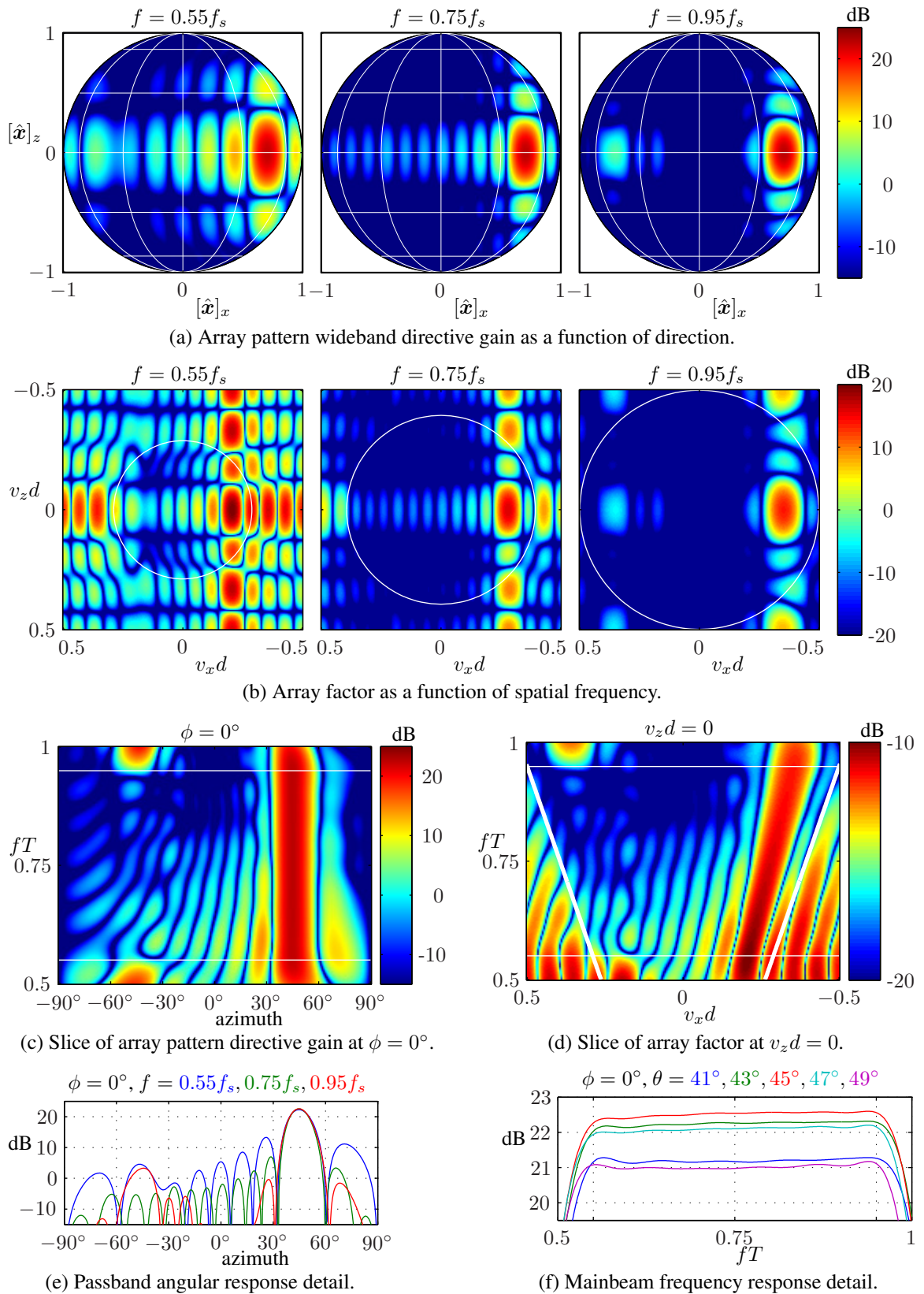


Figure 3.9: Maximizing wideband gain subject to mean-square passband constraints.

direction; one of the form of (3.95c) or (3.95d) to control the response of the desired scalar polarization component A_{\parallel} , and a second to bound (generally in the peak or mean-square sense) the perpendicular scalar polarization component A_{\perp} . Applying (3.33) to the array pattern for each component, we have

$$A_{\parallel}(\mathbf{v}, f) \triangleq \hat{\boldsymbol{\psi}}_{\parallel}^H(f) \begin{pmatrix} \hat{\boldsymbol{\phi}}^T(-\mathbf{v}) \\ \hat{\boldsymbol{\theta}}^T(-\mathbf{v}) \end{pmatrix} \vec{\mathbf{A}}(\mathbf{v}, f)$$

$$A_{\perp}(\mathbf{v}, f) \triangleq \hat{\boldsymbol{\psi}}_{\perp}^H(f) \begin{pmatrix} \hat{\boldsymbol{\phi}}^T(-\mathbf{v}) \\ \hat{\boldsymbol{\theta}}^T(-\mathbf{v}) \end{pmatrix} \vec{\mathbf{A}}(\mathbf{v}, f),$$

where $\hat{\boldsymbol{\psi}}_{\parallel}^H(f)$ and $\hat{\boldsymbol{\psi}}_{\perp}^H(f)$ are orthogonal Jones vectors describing the desired and perpendicular polarizations. Now we might have sets of passband constraint pairs of the form

$$\frac{1}{\int_{\mathcal{F}} df} \int_{\mathcal{F}} |A_{\parallel}(-\hat{\mathbf{x}}_k f/c, f) - \beta_k|^2 df \leq \epsilon_{\parallel} \beta_k^2$$

$$\frac{1}{\int_{\mathcal{F}} df} \int_{\mathcal{F}} |A_{\perp}(-\hat{\mathbf{x}}_k f/c, f)|^2 df \leq \epsilon_{\perp}, \quad k = 1, \dots, K_{\text{mb}}$$

where the set of locations $\{\hat{\mathbf{x}}_k\}$ discretizes the mainbeam-control region, β_k can be an auxiliary variable or a constant, and ϵ_{\parallel} and ϵ_{\perp} are the mean-square desired-polarization and perpendicular-polarization errors, respectively. This approach is used and illustrated in [107] for an array of orthogonal dipole pairs. We can also bound the peak error of either or both polarization components using constraints of the form of (3.96).

3.4.8 Sidelobe Constraints

Often in array-pattern design we are concerned not just with the mainlobe response, but also with the sidelobes. Stray power radiated in sidelobes may interfere with other systems, or may illuminate clutter and return to the array. Minimizing total input or radiated power tends to have a stronger effect on the mainlobe than on the sidelobes because, to paraphrase bank robber Willie Sutton, that's where the power is. The mainlobe frequency-response constraints used in the previous section somewhat counterintuitively improved the

sidelobes at higher frequencies by preventing the optimization from narrowing the main-beam at those frequencies. This can be seen by comparing Figure 3.8 to Figure 3.9. However, at lower frequencies the sidelobes, especially those close to the mainlobe, worsened. Thus we wish to consider explicit constraints on the sidelobes.

The suppression of sidelobes in array pattern design is analogous to stopband suppression in a frequency selective filter, and so many of the same approaches can be used. By far the most common measure specified is the peak array-pattern sidelobe level. Peak sidelobes can be constrained by defining the sidelobe region, choosing a dense set of points covering the region, and placing a constraint at each point. The sidelobe region might include all directions and frequencies except the mainlobe, but in some cases a smaller region might be appropriate. Examples include angles below the horizon to suppress ground clutter, or directions of known large scatterers. In a shared array we might place extra constraints on the sidelobes of one pattern in the mainlobe direction of another pattern. Unlike the discretization used for computing radiated power, in which a single SOC constraint is the result, here bounding the array pattern at each point $(\hat{\mathbf{x}}_k, f_k)$ by peak error ϵ_{peak} leads to a SOC constraint of the form

$$\|\vec{\mathbf{A}}(-\hat{\mathbf{x}}_k f_k/c, f_k)\| \leq \epsilon_{\text{peak}}$$

in general, and the pair of linear constraints

$$-\epsilon_{\text{peak}} \leq \|\vec{\mathbf{A}}_{\text{el}}(-\hat{\mathbf{x}}_k f_k/c, f_k)\| \leq \epsilon_{\text{peak}}$$

when the element responses are all identical and the array factor is real.

Adding -25 dB peak sidelobe constraints to the previous example design yields the

following SOC program:

$$\text{minimize } \alpha > 0 \quad (3.97a)$$

$$\text{s.t. } \frac{1}{\eta} \int_{\mathcal{F}} \int_{\mathcal{L}} |A_{\text{elV}}(-\hat{\mathbf{x}}f/c, f)B(-\hat{\mathbf{x}}f/c, f)|^2 \Omega(d\mathbf{x}) df \quad (3.97b)$$

$$+ Z_0 \int_{\mathcal{F}} \sum_{\mathbf{x} \in \mathcal{L}} |B(\mathbf{x}, f)|^2 df \leq \alpha^2$$

$$\frac{1}{\int_{\mathcal{F}} df} \int_{\mathcal{F}} |A_{\text{elV}}(-\hat{\mathbf{x}}_0 f/c, f)B(-\hat{\mathbf{x}}_0 f/c, f) - 1|^2 df \leq 10^{-\frac{40}{10}} \quad (3.97c)$$

$$\frac{1}{\int_{\mathcal{F}} df} \int_{\mathcal{F}} |A_{\text{elV}}(-\hat{\mathbf{x}}_k f/c, f)B(-\hat{\mathbf{x}}_k f/c, f) - \beta_k|^2 df \leq 10^{-\frac{40}{10}} \beta_k, \quad (3.97d)$$

$$k = 1, \dots, K_{\text{mb}}$$

$$-10^{-\frac{25}{20}} \leq A_{\text{elV}}(-\hat{\mathbf{x}}_k f_k/c, f_k)B(-\hat{\mathbf{x}}_k f_k/c, f_k) \leq 10^{-\frac{25}{20}} \beta_k, \quad (3.97e)$$

$$k = 1, \dots, K_{\text{sl}}$$

There are $K_{\text{sl}} = 13591$ pairs of linear constraints spread across the sidelobe region, here defined to be all visible directions and temporal frequencies in \mathcal{F} outside of the mainlobe region. The mainlobe region, in turn, was defined as elevation angles $-25^\circ \leq \phi \leq 25^\circ$ and azimuth angles $30^\circ \leq \theta \leq 66^\circ$. Although this is asymmetric about the beam center in angle, it is symmetric in spatial frequency and thus is a more natural specification for the array factor. This is analogous to choosing symmetric transition bands in a frequency selective filter. Problem setup took 517 s while solving took 6510 s, the large number of peak constraints causing a large increase in solution time. The resulting responses are plotted in Figure 3.10. The beam has grown yet wider to accommodate the peak constraints, an expected if always unwelcome tradeoff. Wideband directivity, efficiency, and wideband gain are 22.0 dB, 89%, and 21.4 dB, respectively, the latter a loss of 0.7 dB from the previous example. As wideband gain has lowered over the three previous examples, it has been largely a result of reduced wideband directivity, with efficiency essentially fixed.

An alternative approach to constraining peak sidelobes is to constrain mean-square sidelobes, sometimes referred to as the *integrated sidelobe level*. This can be constrained with the SOC

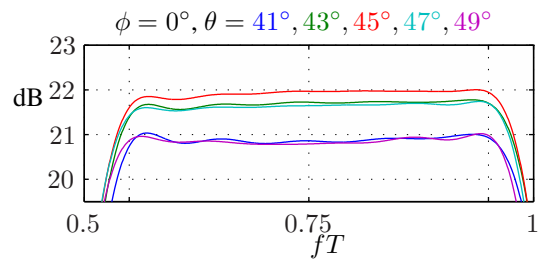
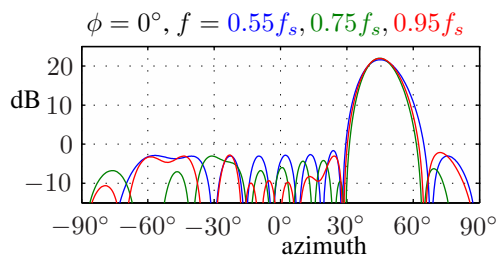
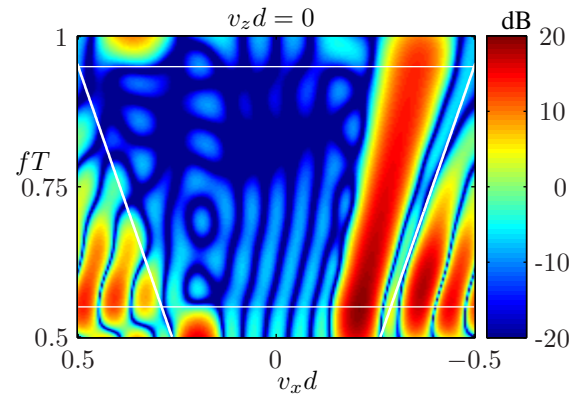
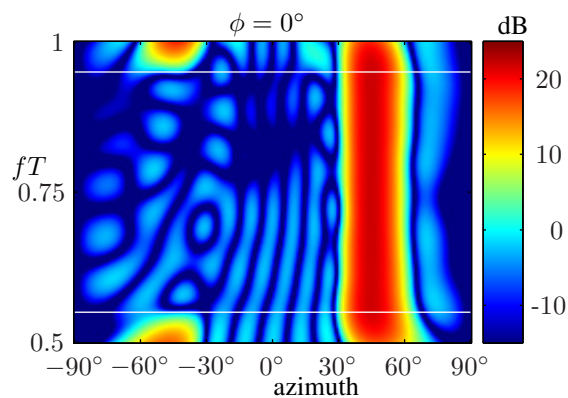
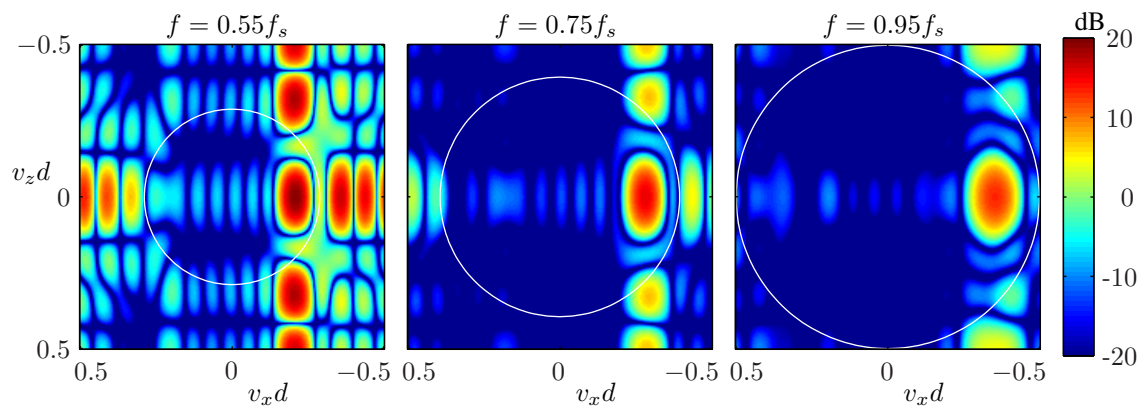
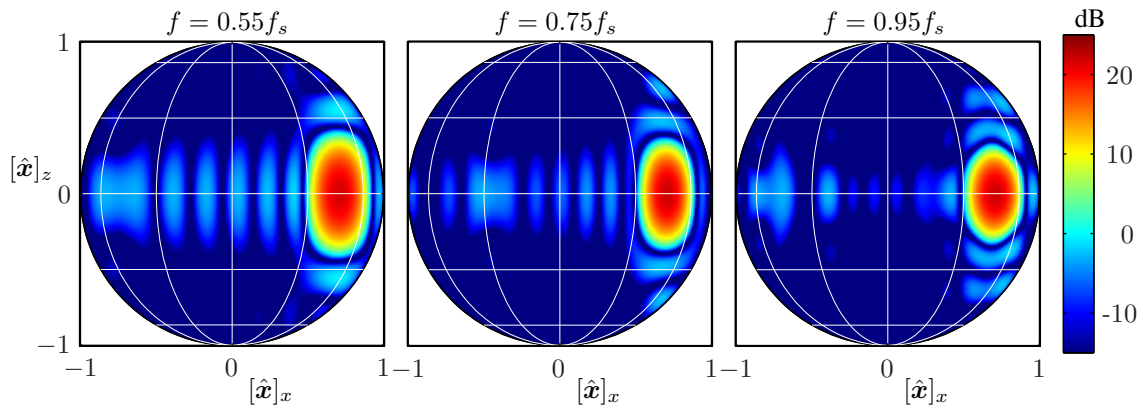


Figure 3.10: Maximizing wideband gain subject to passband and sidelobe constraints.

$$\frac{1}{\int_{\mathcal{F}} \int d\Omega_{\text{sl}}(\mathbf{x}) df} \int_{\mathcal{F}} \int \|\vec{\mathbf{A}}(-\hat{\mathbf{x}}f/c, f)\|^2 d\Omega_{\text{sl}}(\mathbf{x}) df \leq 10^{\frac{40}{10}},$$

where Ω_{sl} is a surface-area measure defining the sidelobe region.

3.5 Summary

This chapter considered both the analysis of wideband arrays and the synthesis of wideband array patterns. A general passband-equivalent system model was introduced, and signals were traced from the input to radiation in the far-field. It was shown that far-field radiation partitions the four-dimensional space of spatial and temporal frequency, separating propagating from nonpropagating frequencies according to the Helmholtz equation. Along the way, the wideband array pattern was defined, as were important metrics such as radiated power and input power. To take full advantage of the flexibility provided by digital beamforming, optimization using second-order cone programming was used to design the array pattern. A running example design was used to compare various figures of merit, including wideband directivity, efficiency, wideband gain, passband flatness, and sidelobe level. In most cases maximizing wideband gain is the appropriate objective, subject to application-specific constraints on the frequency response in the mainbeam and on the sidelobes. In particular, it was shown that the classical time-delay method of wideband array pattern synthesis results from maximizing efficiency, and that such a design exhibits a loss of wideband gain compared to a maximum-gain design.

Chapter 4.

Spatio-Temporal Delta-Sigma Modulation

The underlying assumption of the previous chapter was that the DAC and the entire analog circuit chain that followed, including the power amplifiers, were linear. In most current array transmit systems this is not the case; the amplifiers are too nonlinear for all but a highly restricted class of optimal array patterns to be realized. In Section 2.2 temporal $\Delta\Sigma$ modulation was introduced as a promising technique for linear D/A conversion, potentially at high power. One considerable drawback of conventional temporal $\Delta\Sigma$ modulation is that the oversampling requirements lead to extremely high clock rates.

In a conventional (non-noise-shaped) D/A or A/D converter the usual assumption is that quantization noise samples are uncorrelated with each other, while a noise-shaping converter intentionally produces correlation in order to reduce the noise power in the signal band. Likewise, in an array driven by amplifiers or $\Delta\Sigma$ power DAC's the in-band noise (be it quantization errors or true thermal noise) in the far field is generally assumed to be the combination of uncorrelated contributions from each element. This suggests that the individual channel quantization errors could be intentionally correlated temporally and spatially in order to improve performance over temporal-only noise shaping. The output of such a spatio-temporal noise-shaper would be a coarsely quantized signal corresponding to each element, just as if a temporal-only high-power $\Delta\Sigma$ DAC was to be used, and so the analog electronics required would largely be the same in both cases.

In this chapter the wideband array model of the previous chapter is extended to incorporate *spatio-temporal* $\Delta\Sigma$ modulation, in which the quantization noise is shaped jointly in spatial and temporal frequency. This approach has the potential to reduce clock-rate requirements relative to temporal-only $\Delta\Sigma$ modulation by taking advantage of spatial oversampling, which arises naturally in wideband arrays or might be intentionally built in. In the sections that follow the extended spatio-temporal $\Delta\Sigma$ array model is introduced and analyzed to determine the spatio-temporal noise spectrum. This spectrum is controlled by a spatio-temporal loop filter, which we can then optimize. The conditions for the multidimensional loop to be computable are determined, and the effect of special cases on performance and ease of implementation is shown. Finally, the output of a small example array is computed to compare its noise spectrum to the theory.

4.1 Input/Output Analysis

4.1.1 System Model

The system model used in this chapter is shown in Figure 4.1. Comparing to Figures 2.1 and 3.1, we see that this is essentially our previous wideband beamforming system with an error-feedback $\Delta\Sigma$ modulator inserted between the beamformer and the equivalent analog responses. The system model in this case is also representative of the hardware architecture; there are no practical means to perform analog upconversion in this system. Thus the beamformer \underline{b} and all signals through the modulator output \underline{q} are discrete-time, with sample interval T . The discrete-space beamformer converts the temporal input to a discrete-space spatio-temporal signal with support on the set \mathcal{L} of element locations. All signals from the beamformer output through the array input current have the same spatial support. As mentioned in the previous chapter, mathematically \mathcal{L} is somewhat arbitrary.

In contrast to Figure 2.1, here the modulator signals are $M \times 1$ vector-valued measures on both space and time, and thus the loop filter is an $M \times M$ matrix. The quantizer is a

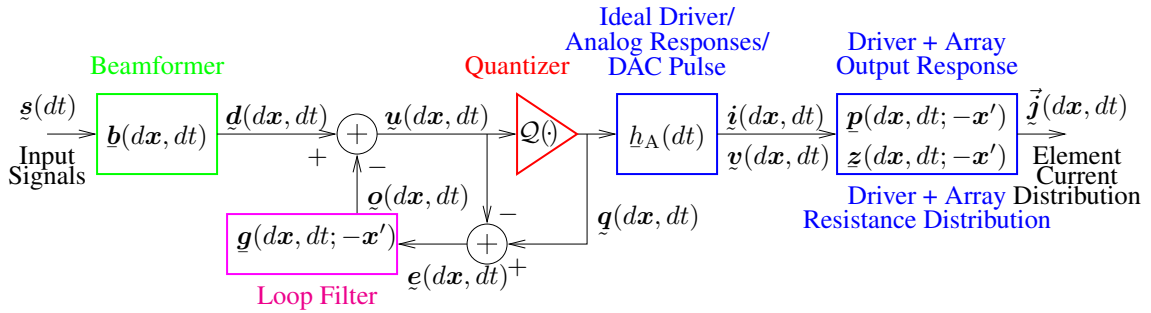


Figure 4.1: A wideband transmit array with spatio-temporal delta-sigma array D/A conversion.

vector quantizer, and in general can exhibit both temporal and spatial memory; here we will restrict our attention to the memoryless case. The quantizer output \underline{q} drives the equivalent DAC pulse (now incorporating the ideal driver), which in a physical array would be a high-power linear pulse modulator rather than a continuously variable current source. The driver output is the current \underline{i} as before, and the array model is unchanged.

We will linearize the $\Delta\Sigma$ loop as in Section 2.2 by treating quantization error \underline{e} as an independent additive noise process that is WSS in time. We wish to derive two quantities: the spectral density of quantizer output \underline{q} and the far-field power intensity, as a function now of the input \underline{s} and quantization error \underline{e} . The input might be deterministic or random, and the results for both cases will parallel the results of Section 2.2.

4.1.2 Random Input

Since we analyzed the effect of the beamformer extensively in the previous chapter, we start our analysis here with the quantizer input, the $M \times 1$ vector \underline{u} :

$$\underline{u}(d\mathbf{x}, dt) = \underline{d}(d\mathbf{x}, dt) - (\underline{g} \boxtimes \underline{e})(d\mathbf{x}, dt). \quad (4.1)$$

By the definition of the $M \times 1$ vector quantization error \underline{e} we have

$$\begin{aligned}\underline{q}(d\mathbf{x}, dt) &= \underline{u}(d\mathbf{x}, dt) + \underline{e}(d\mathbf{x}, dt) \\ &= \underline{d}(d\mathbf{x}, dt) - \underline{o}(d\mathbf{x}, dt) + \underline{e}(d\mathbf{x}, dt) \\ &= \underline{d}(d\mathbf{x}, dt) - (\underline{g} \boxtimes \underline{e})(d\mathbf{x}, dt) + \underline{e}(d\mathbf{x}, dt).\end{aligned}$$

Combining the last two terms on the right results in

$$\underline{q}(d\mathbf{x}, dt) = (\underline{\mathbf{b}} * \underline{\mathbf{s}})(d\mathbf{x}, dt) + (\underline{\mathbf{h}} \boxtimes \underline{e})(d\mathbf{x}, dt) \quad (4.2a)$$

$$\triangleq \underline{\mathbf{q}}_s(d\mathbf{x}, dt) + \underline{\mathbf{q}}_e(d\mathbf{x}, dt), \quad (4.2b)$$

where $M \times M$ matrix *noise-shaping measure* $\underline{\mathbf{h}}$ is defined as

$$\underline{\mathbf{h}}(d\mathbf{x}, dt; -\mathbf{x}') \triangleq \underline{\mathbf{x}}' \delta(d\mathbf{x}) \delta(dt) \mathbf{I} - \underline{\mathbf{g}}(d\mathbf{x}, dt; -\mathbf{x}'). \quad (4.3)$$

We will now assume that input $\underline{\mathbf{s}}$ and the quantization error \underline{e} are uncorrelated, so we can write

$$\underline{\mathbf{r}}_q(d\mathbf{x}, d\mathbf{y}, d\tau) = \underline{\mathbf{r}}_{q_s}(d\mathbf{x}, d\mathbf{y}, d\tau) + \underline{\mathbf{r}}_{q_e}(d\mathbf{x}, d\mathbf{y}, d\tau) \quad (4.4a)$$

$$= (\underline{\mathbf{b}} * \underline{\mathbf{r}}_s * \underline{\mathbf{b}}^\dagger)(d\mathbf{x}, d\mathbf{y}, d\tau) + (\underline{\mathbf{h}} \boxtimes \underline{\mathbf{r}}_e \boxtimes \underline{\mathbf{h}}^\dagger)(d\mathbf{x}, d\mathbf{y}, d\tau) \quad (4.4b)$$

The signal component $\underline{\mathbf{q}}_s$ of the quantizer output is just the beamformer output from the previous chapter, thus here we will focus on the error component $\underline{\mathbf{q}}_e$. We are primarily interested in the trace of the spatio-temporal PSD of the error component at the quantizer output so that we can later compare it to the far-field noise intensity. We find the trace of this PSD by applying (2.38) to the second term of (4.4b):

$$\text{Tr}[\underline{\mathbf{R}}_{q_e}(\mathbf{v}, -\mathbf{v}, f)] = \iiint \text{Tr}[\underline{\mathbf{H}}(\mathbf{v}, f; -\mathbf{x}') \underline{\mathbf{R}}_e(d\mathbf{x}', d\mathbf{y}', f) \underline{\mathbf{H}}^H(\mathbf{v}, f; -\mathbf{y}')]. \quad (4.5)$$

In Section 2.2 we assumed that the scalar temporal noise was white. The equivalent assumption here is that

$$\underline{\mathbf{r}}_e(d\mathbf{x}, d\mathbf{y}, d\tau) = \sigma^2 \mathbf{I} \underline{\mathbf{x}} \delta(d\mathbf{y}) \underline{\Sigma}_{\mathcal{L}}(d\mathbf{x}) \delta(d\tau) \quad (4.6)$$

and

$$\boxed{\mathbf{R}_e(d\mathbf{x}, d\mathbf{y}, f) = \sigma^2 \mathbf{I}_{\mathbf{x}} \delta(d\mathbf{y}) \underline{\Sigma}_{\mathcal{L}}(d\mathbf{x})}. \quad (4.7)$$

At any fixed time t , the quantization error density $e(\mathbf{x}, t)$ is an $M \times 1$ vector function of space representing $M \times K$ distinct scalar values: one for each combination of one of the K element locations in \mathcal{L} and one of the M elements types at each location. The assumption embodied in (4.6) is that each of these scalar components of the noise density e has variance σ^2 and is uncorrelated with every other component of e . Substituting (4.7) into (4.5) yields

$$\text{Tr}[\mathbf{R}_{q_e}(\mathbf{v}, -\mathbf{v}, f)] = \sigma^2 \int \text{Tr}[\mathbf{H}(\mathbf{v}, f; -\mathbf{x}') \mathbf{H}^H(\mathbf{v}, f; -\mathbf{x}')] \underline{\Sigma}_{\mathcal{L}}(d\mathbf{x}'),$$

or writing the integral and trace as sums,

$$\boxed{\text{Tr}[\mathbf{R}_{q_e}(\mathbf{v}, -\mathbf{v}, f)] = \sigma^2 \sum_{\mathbf{x}' \in \mathcal{L}} \sum_{m=1}^M \|\mathbf{H}_m(\mathbf{v}, f; -\mathbf{x}')\|^2} \quad (4.8a)$$

$$= \sigma^2 \sum_{\mathbf{x}' \in \mathcal{L}} \sum_{m=1}^M \sum_{k=1}^M |H_{k,m}(\mathbf{v}, f; -\mathbf{x}')|^2 \quad (4.8b)$$

where \mathbf{H}_m is the m th column of the spatio-temporal Fourier transform of the noise-shaping measure. We see that the PSD is just the sum of the magnitude squared frequency responses of the noise-shaping measure components, scaled by the noise variance. This sum is the equivalent of the noise transfer function in the scalar case; it determines the noise power spectrum when the noise is white.

To find the far-field electric field spectral density, we follow (3.9) and write the element-current distribution as

$$\vec{\mathbf{j}}(d\mathbf{x}, dt) = \vec{\mathbf{j}}_s(d\mathbf{x}, dt) + \vec{\mathbf{j}}_e(d\mathbf{x}, dt) \quad (4.9a)$$

$$= (\underline{\mathbf{p}} \boxtimes \underline{\mathbf{b}} * \underline{\mathbf{s}}_A)(d\mathbf{x}, dt) + (\underline{\mathbf{p}} \boxtimes \underline{\mathbf{h}} \boxtimes \underline{\mathbf{e}}_A)(d\mathbf{x}, dt), \quad (4.9b)$$

again defining

$$\underline{\mathbf{s}}_A(dt) \triangleq (\underline{\mathbf{s}} * \underline{\mathbf{h}}_A)(dt)$$

as in the previous chapter and likewise defining

$$\boxed{\mathbf{e}_A(d\mathbf{x}, dt) \triangleq (\mathbf{e} * h_A)(d\mathbf{x}, dt)}$$

as the equivalent post-conversion quantization noise. By (2.42), the corresponding auto-correlation and power spectrum are

$$\mathbf{r}_{e_A}(d\mathbf{x}, d\mathbf{y}, d\tau) = \frac{1}{T} (h_A * \mathbf{r}_e * h_A^\dagger)(d\mathbf{x}, d\mathbf{y}, d\tau)$$

and

$$\mathbf{R}_{e_A}(d\mathbf{x}, d\mathbf{y}, f) = \frac{1}{T} |H_A(f)|^2 \mathbf{R}_e(d\mathbf{x}, d\mathbf{y}, f). \quad (4.10)$$

The signal component \vec{j}_s of the element-current distribution is identical to that derived in the last chapter, and so we now focus on the error component, \vec{j}_e . We previously assumed that the signal and error are uncorrelated, so that $\mathbf{r}_{\vec{j}}^- = \mathbf{r}_{\vec{j}_s}^- + \mathbf{r}_{\vec{j}_e}^-$. We find the error-component autocorrelation via (2.37) as

$$\mathbf{r}_{\vec{j}_e}^-(d\mathbf{x}, d\mathbf{y}, d\tau) = \left((\underline{\mathbf{p}} \boxtimes \mathbf{h}) \boxtimes \mathbf{r}_{e_A} \boxtimes (\underline{\mathbf{p}} \boxtimes \mathbf{h})^\dagger \right) (d\mathbf{x}, d\mathbf{y}, d\tau), \quad (4.11)$$

and Fourier transforming on space and time and substituting (4.7) and (4.10) yields

$$\begin{aligned} \mathbf{R}_{\vec{j}_e}^-(\mathbf{v}, \mathbf{w}, f) &= \frac{\sigma^2}{T} |H_A(f)|^2 \int \int \left(\int \mathbf{P}(\mathbf{v}, f; -\mathbf{x}'') \underline{\mathbf{H}}(d\mathbf{x}'', f; -\mathbf{x}') \right) \times \\ &\quad \left(\int \mathbf{P}(\mathbf{w}, f; -\mathbf{y}'') \underline{\mathbf{H}}(d\mathbf{y}'', f; -\mathbf{x}') \right)^\dagger_{\Sigma_{\mathcal{L}}(d\mathbf{x}')}. \end{aligned} \quad (4.12)$$

We now find the spectral density of the error component of the electric field by substituting into (3.49b):

$$\begin{aligned} \mathbf{R}_{\vec{\varepsilon}_e}(\mathbf{x}, \mathbf{y}, f) &= \frac{e^{-j2\pi(\|\mathbf{x}\| - \|\mathbf{y}\|)f/c} \sigma^2}{\|\mathbf{x}\| \|\mathbf{y}\|} \frac{\sigma^2}{T} |H_A(f)|^2 \int \int \left(\frac{\mu_0}{4\pi} \right)^2 |j2\pi f|^2 \times \\ &\quad \Gamma_{\hat{\mathbf{x}}} \left(\int \mathbf{P}(-\hat{\mathbf{x}}f/c, f; -\mathbf{x}'') \underline{\mathbf{H}}(d\mathbf{x}'', f; -\mathbf{x}') \right) \times \\ &\quad \left(\int \mathbf{P}(-\hat{\mathbf{y}}f/c, f; -\mathbf{x}'') \underline{\mathbf{H}}(d\mathbf{x}'', f; -\mathbf{x}') \right)^H \Gamma_{\hat{\mathbf{y}}}^T_{\Sigma_{\mathcal{L}}(d\mathbf{x}')}. \end{aligned}$$

Defining the LSV noise array pattern

$$\vec{\mathbf{A}}_e(\mathbf{v}, f; -\mathbf{x}') \triangleq -\frac{\mu_0}{4\pi} j2\pi f \Gamma_{\hat{\mathbf{v}}} \oint \mathbf{P}(\mathbf{v}, f; -\mathbf{x}'') \underline{\mathbf{H}}(d\mathbf{x}'', f; -\mathbf{x}') \quad (4.13a)$$

$$= \oint \vec{\mathbf{A}}_{el}(\mathbf{v}, f; -\mathbf{x}'') \underline{\mathbf{H}}(d\mathbf{x}'', f; -\mathbf{x}'), \quad (4.13b)$$

where we recall the definition of the $3 \times M$ shift-varying element pattern from (3.29) in the second line, reduces this to

$$\mathbf{R}_{\vec{e}_e}(\mathbf{x}, \mathbf{y}, f) = \frac{e^{-j2\pi(\|\mathbf{x}\| - \|\mathbf{y}\|)f/c} \sigma^2}{\|\mathbf{x}\| \|\mathbf{y}\| T} |H_A(f)|^2 \times \oint \vec{\mathbf{A}}_e(-\hat{\mathbf{x}}f/c, f; -\mathbf{x}') \vec{\mathbf{A}}_e^H(-\hat{\mathbf{y}}f/c, f; -\mathbf{x}') \underline{\Sigma}_{\mathcal{L}}(d\mathbf{x}'). \quad (4.14)$$

To interpret this, we can rearrange (4.14) and write the integral as a sum to directly compare it to (3.50), the spectral density of the signal component of the electric field (repeated here in the first line with additional subscripts to distinguish it from the noise component):

$$\mathbf{R}_{\vec{e}_s}(\mathbf{x}, \mathbf{y}, f) = \frac{e^{-j2\pi(\|\mathbf{x}\| - \|\mathbf{y}\|)f/c}}{\|\mathbf{x}\| \|\mathbf{y}\|} \vec{\mathbf{A}}_s(-\hat{\mathbf{x}}f/c, f) \mathbf{R}_{s_A}(f) \vec{\mathbf{A}}_s^H(-\hat{\mathbf{y}}f/c, f) \quad (4.15a)$$

$$\mathbf{R}_{\vec{e}_e}(\mathbf{x}, \mathbf{y}, f) = \frac{e^{-j2\pi(\|\mathbf{x}\| - \|\mathbf{y}\|)f/c}}{\|\mathbf{x}\| \|\mathbf{y}\|} \times \sum_{\mathbf{x}' \in \mathcal{L}} \vec{\mathbf{A}}_e(-\hat{\mathbf{x}}f/c, f; -\mathbf{x}') \left(\frac{\sigma^2}{T} |H_A(f)|^2 \mathbf{I} \right) \vec{\mathbf{A}}_e^H(-\hat{\mathbf{y}}f/c, f; -\mathbf{x}') \quad (4.15b)$$

In the previous chapter it was shown that the signal array pattern $\vec{\mathbf{A}}_s$ in (4.15a) has dimension $3 \times N$, where there are N input signals, and that the n th column of $\vec{\mathbf{A}}_s(\mathbf{v}, f)$ was effectively a 3×1 spatio-temporal transfer function from the n th temporal input signal $[\mathbf{s}_A]_n$ to the far-field electric field. In (4.15b), the noise array pattern has dimension $3 \times M$ and is space-varying, in contrast to the signal array pattern. The “input” signal in the noise term is the post-conversion quantization error e_A , which like the quantization error e is an $M \times 1$ vector-valued discrete-space spatio-temporal signal that represents $M \times K$ scalar temporal signals. Whereas the signal array pattern $\vec{\mathbf{A}}_s$ comprises the N spatio-temporal transfer functions $\{[\vec{\mathbf{A}}_s]_n(\mathbf{v}, f)\}$ for $n = 1, \dots, N$, the noise array pattern $\vec{\mathbf{A}}_e$ comprises the $M \times K$ spatio-temporal transfer functions $\{[\vec{\mathbf{A}}_e]_m(\mathbf{v}, f; -\mathbf{x}')\}$ for $m = 1, \dots, M$ and

$\mathbf{x}' \in \mathcal{L}$. In other words, each underlying scalar input signal and each scalar, temporal noise component has its own spatio-temporal transfer function. In (4.15a) the signal spectral density matrix $\mathbf{R}_{s_A}(f)$ describes the statistical correlation between the scalar input signals; similarly in (4.15b) the expression $\frac{\sigma^2}{T}|H_A(f)|^2 \mathbf{I}$ results from our assumption that the scalar error terms are uncorrelated. If the element response $\underline{\mathbf{p}}$ is shift-invariant, then (4.13) simplifies to

$$\begin{aligned}\vec{\mathbf{A}}_e(\mathbf{v}, f; -\mathbf{x}') &\triangleq -\frac{\mu_0}{4\pi} j 2\pi f \Gamma_{\hat{\nu}} \mathbf{P}(\mathbf{v}, f) \mathbf{H}(\mathbf{v}, f; -\mathbf{x}') \\ &= \vec{\mathbf{A}}_{el}(\mathbf{v}, f) \mathbf{H}(\mathbf{v}, f; -\mathbf{x}'),\end{aligned}\quad (4.16)$$

where $\vec{\mathbf{A}}_{el}(\mathbf{v}, f)$ is the $3 \times M$ shift invariant element pattern of (3.26), and $\mathbf{H}(\mathbf{v}, f; -\mathbf{x}')$ is the $M \times M$ matrix of space-varying noise array factors.

Having derived the electric field power spectrum, we can now find the quantization-noise component of the far-field radiation intensity from (3.63a) as

$$\begin{aligned}\mathcal{U}_e(\mathbf{x}, f) &= \frac{1}{\eta} \frac{\sigma^2}{T} |H_A(f)|^2 \int_{\Sigma_{\mathcal{L}}} \text{Tr} \left[\vec{\mathbf{A}}_e(-\hat{\mathbf{x}}f/c, f; -\mathbf{x}') \vec{\mathbf{A}}_e^H(-\hat{\mathbf{x}}f/c, f; -\mathbf{x}') \right] \Sigma_{\mathcal{L}}(d\mathbf{x}') \\ &= \frac{1}{\eta} \frac{\sigma^2}{T} |H_A(f)|^2 \sum_{\mathbf{x}' \in \mathcal{L}} \sum_{m=1}^M \left\| [\vec{\mathbf{A}}_e]_m(-\hat{\mathbf{x}}f/c, f; -\mathbf{x}') \right\|^2.\end{aligned}\quad (4.17)$$

The radiation intensity is just the sum of the contributions from each of the $M \times K$ scalar quantization-noise components, a result of the uncorrelated noise assumption. Writing this explicitly as a function of the noise-shaping measure for both the general case of a shift-varying element pattern and the special case of a shift-invariant element pattern yields

$$\mathcal{U}_e(\mathbf{x}, f) = \frac{1}{\eta} \frac{\sigma^2}{T} |H_A(f)|^2 \sum_{\mathbf{x}' \in \mathcal{L}} \sum_{m=1}^M \left\| \int_{\Sigma_{\mathcal{L}}} \vec{\mathbf{A}}_{el}(-\hat{\mathbf{x}}f/c, f; -\mathbf{x}'') \underline{\mathbf{H}}_m(d\mathbf{x}'', f; -\mathbf{x}') \right\|^2 \quad (\text{LSV}) \quad (4.18a)$$

$$\mathcal{U}_e(\mathbf{x}, f) = \frac{1}{\eta} \frac{\sigma^2}{T} |H_A(f)|^2 \sum_{\mathbf{x}' \in \mathcal{L}} \sum_{m=1}^M \left\| \vec{\mathbf{A}}_{el}(-\hat{\mathbf{x}}f/c, f) \mathbf{H}_m(-\hat{\mathbf{x}}f/c, f; -\mathbf{x}') \right\|^2 \quad (\text{LSI}) \quad (4.18b)$$

where $\underline{\mathbf{H}}_m$ and \mathbf{H}_m are the m th columns of the temporal and spatio-temporal Fourier transforms of the noise-shaping measure, respectively. Comparing (4.18b) to (4.8a) we see that

the noise shaping is controlled in both cases by a sum of the weighted squared norms of the $M \times K$ noise transfer function columns $\mathbf{H}_m(-\hat{\mathbf{x}}f/c, f; -\mathbf{x}')$ for $m = 1, \dots, M$ and $\mathbf{x}' \in \mathcal{L}$. In (4.8a) the weights are unity, while in (4.18b) the weights are the product of the equivalent analog filter frequency response and the common element pattern, the result of the quantization error propagating through the system and out to the far field. In the common case where we have only one “type” of element per location ($M = 1$) and all the element responses are identical, the noise shaping measure \underline{h} is a scalar and the power intensity (4.18b) reduces to

$$\mathcal{U}_e(\mathbf{x}, f) = \frac{1}{\eta T} \sigma^2 |H_A(f)|^2 \|\vec{\mathbf{A}}_{\text{el}}(-\hat{\mathbf{x}}f/c, f)\|^2 \sum_{\mathbf{x}' \in \mathcal{L}} |\mathbf{H}(-\hat{\mathbf{x}}f/c, f; -\mathbf{x}')|^2 \quad (4.19a)$$

$$= \frac{1}{\eta T} |H_A(f)|^2 \|\vec{\mathbf{A}}_{\text{el}}(-\hat{\mathbf{x}}f/c, f)\|^2 \text{Tr}[\mathbf{R}_{q_e}(-\hat{\mathbf{x}}f/c, \hat{\mathbf{x}}f/c, f)]. \quad (4.19b)$$

In (4.19b) we have recognized and substituted the shaped quantization error PSD (4.8b) for $M = 1$. In this case the power intensity factors cleanly and is proportional to the product of the squared magnitude of the analog filter frequency response, the norm of the element pattern, and the PSD of the shaped quantization error. Because in most cases the element pattern is relatively omnidirectional and the analog filtering is relatively flat across the signal band, one could perform a reasonable design of \underline{h} alone without knowledge of h_A and $\vec{\mathbf{A}}_{\text{el}}$.

It is instructive to compare (4.19a) to the noise (second) term of (2.49):

$$R_{y_e}(f) = \frac{\sigma^2}{T} |H_A(f)|^2 |H(f)|^2, \quad (4.20)$$

the shaped-noise component of the output PSD of a temporal-only $\Delta\Sigma$ converter. In (4.20) the squared NTF $|H(f)|^2$ is the digital filter response that controls the output quantization noise spectrum. In (4.19a), the same role is played by the sum of the squared responses $\sum_{\mathbf{x}' \in \mathcal{L}} |\mathbf{H}(\mathbf{v}, f; -\mathbf{x}')|^2$. Here we have control over the spatio-temporal quantization-noise spectrum, rather than just the temporal spectrum. In (4.20) the equivalent analog filter frequency response $H_A(f)$ serves to pass only the temporal-frequency signal band while

removing the bulk of the shaped quantization noise outside the signal band. In (4.19a), such temporal filtering is shared between $H_A(f)$ and the common element pattern $\vec{A}_{\text{el}}(\mathbf{v}, f)$, which incorporates any post-driver analog filtering. The element pattern also provides spatial-frequency filtering of the shaped quantization noise, although in most cases the element pattern is fairly omnidirectional and the spatial-frequency “signal band” consists of all propagating spatial frequencies. Instead, the bulk of the quantization-noise filtering in spatial-frequency is a result of far-field propagation, specifically the restriction of the spatio-temporal frequency of propagating radiation to the Helmholtz cone. This is indicated in (4.19a) as the restriction of spatial frequency to $\mathbf{v} = -\hat{\mathbf{x}}f/c$. Thus in the far field we see only the spatio-temporal frequencies on the cone, even though all the spatio-temporal signals in the system from the beamformer output \underline{d} to the element current distribution \vec{j} have spatio-temporal frequency content that lies outside the cone. Likewise, the noise transfer functions $\{H(\mathbf{v}, f; -\mathbf{x}')\}$, for $\mathbf{x}' \in \mathcal{L}$, give us control over the quantization noise spectrum outside the cone. As will be shown in Section 4.2, we can design the noise transfer functions so as to minimize the quantization noise at propagating spatio-temporal frequencies at the expense of increased quantization noise at nonpropagating frequencies.

In the more general cases of multiple element types or a space-varying element pattern, as in (4.18), the element patterns don’t factor out as in (4.19), but every term in the sum is still weighted by an element pattern that provides spatio-temporal noise filtering and is evaluated only for propagating spatial frequencies. The far-field noise intensity and noise power are still quadratic in the coefficients of the underlying loop filter if that filter is FIR, and thus the optimization techniques in Section 4.2 still apply.

4.1.3 The Geometry of Spatio-Temporal Oversampling

To understand the geometry involved in spatio-temporal noise shaping, we use an example to help clarify. Assume we have array of elements on a square lattice in the x - z plane with spacing d and a loop filter (and thus quantizer output) with sample rate $1/T$. The analysis

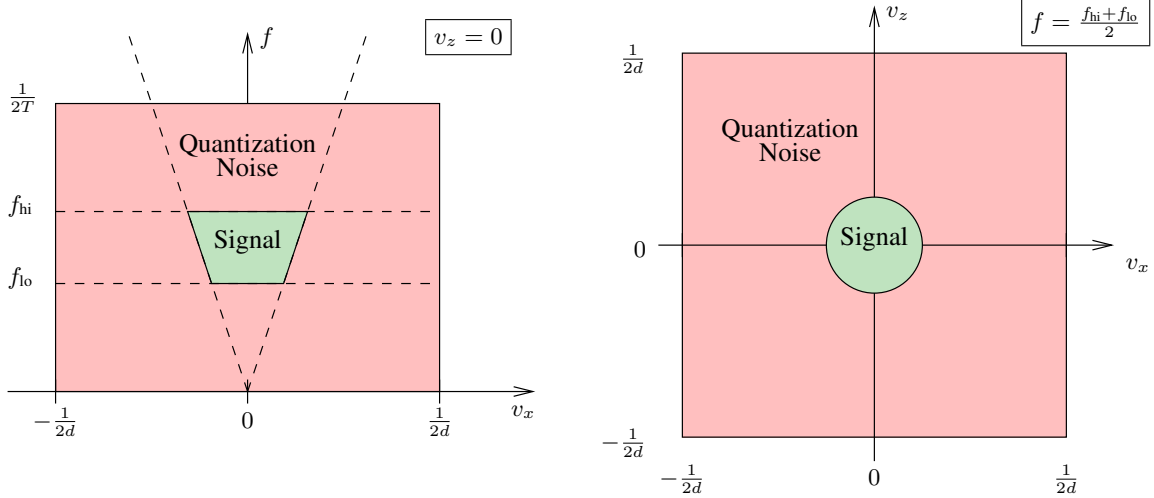


Figure 4.2: Signal and noise geometries for a spatio-temporal $\Delta\Sigma$ array on a square lattice with element spacing d and sample spacing T .

of Section B.1 shows that the corresponding noise transfer functions and quantizer output spectrum are constant in spatial frequency component v_y and periodic in (v_x, v_z, f) space with one period defined by the hyperrectangle $(-\frac{1}{2d}, \frac{1}{2d}] \times (-\frac{1}{2d}, \frac{1}{2d}] \times (-\frac{1}{2T}, \frac{1}{2T}]$. This represents the spatio-temporal spectral region over which we have direct control through design of the noise shaping measure \underline{h} . Figure 4.2 shows two 2D slices of the positive temporal-frequency half of this 3D period (the other half is determined by conjugate symmetry through the origin). In the slice on the left we fix $v_z = 0$ and indicate the boundary of the Helmholtz cone with diagonal dashed lines and the upper and lower edges of the positive-frequency portion of the signal band $\mathcal{F} = [-f_{hi}, -f_{lo}] \cup [f_{lo}, f_{hi}]$ with horizontal dashed lines. The central shaded “signal” region represents the intersection of the Helmholtz cone with \mathcal{F} for positive temporal frequencies, and represents the portion of the spatio-temporal spectrum that corresponds to far-field radiation. We will usually wish to suppress quantization noise in this region to the extent possible. The outer “quantization noise” region, on the other hand, does not correspond to propagating radiation, and so we allow high quantization noise here; analog filtering and propagation will remove the noise prior to the far-field.

In Section 2.2 the oversampling ratio for a temporal $\Delta\Sigma$ modulator was defined as the ratio of the sample rate to the two-sided signal bandwidth. The greater the oversampling ratio, the greater the possible noise suppression in the signal band, and thus improving the SNR for a fixed bandwidth requires increasing the clock rate. This represents the primary drawback to using temporal-only $\Delta\Sigma$ conversion at microwave frequencies. Here we will refer to the ratio of the sample rate to the two-sided signal bandwidth as the *temporal oversampling ratio*, which in this example has the value $\frac{1}{2(f_{hi}-f_{lo})T}$. We can see in the example figures that the spectral period is larger than the signal region both spatially and temporally. Thus, it makes sense to also define the *spatial oversampling ratio* for a planar array on a lattice at a temporal frequency f as the ratio of the area of a spatial period of the quantizer output spectrum to the area of the spatial-frequency region over which the noise should be suppressed at f (i.e. the signal region). Since the latter will usually vary with temporal frequency, the spatial oversampling ratio is a function of frequency. In the example it takes the value $\frac{c^2}{\pi f^2 d^2} = \frac{\lambda^2}{\pi d^2}$. The overall *spatio-temporal oversampling ratio* is the ratio of the volume of one spatio-temporal period of the quantizer output spectrum to the volume of the spatio-temporal signal region. In the example, this value is $\frac{3c^2}{2\pi(f_{hi}^3-f_{lo}^3)d^2T}$. The spatio-temporal oversampling ratio is the fundamental measure of noise-shaping ability in a space-time $\Delta\Sigma$ modulator. It is directly proportional to sample rate and inversely proportional to the element spacing squared, and thus we can increase the overall ratio by increasing the sample rate, or by increasing the element density. This is the fundamental tradeoff introduced by spatio-temporal $\Delta\Sigma$ modulation.

Since the costs of significantly increasing the element density (and thus the number of elements and associated driver electronics and feed networks) may be considerable, we might consider applications in which spatio-temporal $\Delta\Sigma$ modulation might be used without modifying the element layout. In a conventionally spaced square-lattice array, the element spacing is chosen to be $d = \frac{c}{2f_0} = \frac{\lambda_0}{2}$, where f_0 is the highest operating frequency of the array (as distinct from f_{hi} , the upper band edge for a particular signal or set of

signals). With this spacing, the top of the trapezoid on the left in Figure 4.2 would have the same width as the outer box, and a slice through the (v_x, v_z) plane at $f = f_0$ would show the circular signal region exactly inscribing the square spatial-frequency period. This choice of spacing ensures that we have full control over the visible array pattern (to avoid grating lobes) at f_0 with the minimal element density for this lattice. (A triangular lattice allows for full control while reducing the density by about 15% relative to a square lattice [108].) This minimal spacing results in a spatial oversampling ratio of $\frac{4}{\pi} \left(\frac{f_0}{f}\right)^2$, which is $\frac{4}{\pi} \approx 1.27$ at $f = f_0$. Thus a wideband array designed to operate over a decade of bandwidth offers spatial oversampling ratios as high as 127 for signals at the low end of its operating range.

A planar array with lattice support is a most-common special case, but there are several other possible array configurations. For uniform line arrays, the quantizer output spectrum is a periodic function of temporal frequency and a single scalar spatial frequency. If the array lies on the x -axis with element spacing d , then the left plot in Figure 4.2 shows the reduced geometry. Here the spatial oversampling ratio reduces to $\frac{c}{2fd} = \frac{\lambda}{2d}$, and the spatio-temporal oversampling ratio is the ratio of the area of the outer box to the area of the inner trapezoid, or $\frac{c}{2(f_{hi}^2 - f_{lo}^2)dT}$. For arrays with nonlattice element locations, the oversampling ratio does not have a clear definition since the resulting quantizer output spectrum is not periodic. Here the average linear element density might take the place of d . For 3D wideband arrays on a lattice (possible in theory, although unlikely in practice) we have the added complication that the spectral period is now a 4D region with a nonzero volume, but the Helmholtz cone is a surface in 4D. Here our previous definition would lead to an infinite oversampling ratio, indicating that the limitation on noise suppression performance in this case is not oversampling ratio, but rather the finite array dimension and signal duration.

4.1.4 Deterministic Input

In the case where the input \underline{s} is deterministic and has finite time extent, the quantizer output is

$$\begin{aligned}\underline{q}(d\mathbf{x}, dt) &= w(t)(\underline{\mathbf{b}} * \underline{\mathbf{s}})(d\mathbf{x}, dt) + w(t)(\underline{\mathbf{h}} \boxtimes \underline{\mathbf{e}})(d\mathbf{x}, dt) \\ &= w(t)\underline{\mathbf{q}}_s(d\mathbf{x}, dt) + w(t)\underline{\mathbf{q}}_e(d\mathbf{x}, dt),\end{aligned}$$

which is random but nonstationary. As before $w(t)$ is a nonnegative windowing function.

Now we wish to compute the expected spatio-temporal periodogram

$$\mathbf{R}_{w \times \underline{q}}(\mathbf{v}, f) \triangleq \frac{1}{\|w\|^2} \mathcal{E} \left\{ \left(\int e^{-j2\pi(ft + \mathbf{v} \cdot \mathbf{x})} w(t) \underline{q}(\mathbf{x}, dt) \right) \left(\int e^{-j2\pi(ft + \mathbf{v} \cdot \mathbf{x})} w(t) \underline{q}(\mathbf{x}, dt) \right)^H \right\},$$

the outer product of the spatio-temporal Fourier transform of the quantizer output with itself. Following the derivation of (2.52), we find the result

$$\begin{aligned}\mathbf{R}_{w \times \underline{q}}(\mathbf{v}, f) &= \frac{1}{\|w\|^2} (W \star_{T-1} \mathbf{B}\mathbf{S})(\mathbf{v}, f) \times (W \star_{T-1} \mathbf{B}\mathbf{S})^H(\mathbf{v}, f) + \\ &\quad \frac{1}{\|w\|^2} (|W|^2 \star_{T-1} \mathbf{R}_{\underline{q}_e})(\mathbf{v}, -\mathbf{v}, f) \\ &= \mathbf{R}_{w \times \underline{q}_s}(\mathbf{v}, f) + \mathbf{R}_{w \times \underline{q}_e}(\mathbf{v}, f).\end{aligned}$$

The first term is the deterministic equivalent of the power spectrum of the beamformed signal convolved with the Fourier transform of the window function. Beamforming for deterministic signals was covered in the previous chapter, and so as in the previous section for random inputs we will focus on the noise term. Substituting (4.8a) yields

$$\text{Tr}[\mathbf{R}_{w \times \underline{q}_e}(\mathbf{v}, f)] = \frac{\sigma^2}{\|w\|^2} \sum_{m=1}^M \sum_{\mathbf{x}' \in \mathcal{L}} (|W|^2 * \|\mathbf{H}_m\|^2)(\mathbf{v}, f; -\mathbf{x}'),$$

where $|W|^2(f) \triangleq |W(f)|^2$ and $\|\mathbf{H}_m\|^2(\mathbf{v}, f; -\mathbf{x}') \triangleq \|\mathbf{H}_m(\mathbf{v}, f; -\mathbf{x}')\|^2$. We see that the effective noise-shaping response is now convolved with the magnitude-squared response of the window function.

The equivalent to the error-component power intensity for finite-length signals can be found via the weighted periodogram of the error component of the electric field:

$$\begin{aligned} \mathcal{U}_{w \times \vec{\epsilon}_e}(\mathbf{x}, f) &= \frac{1}{\eta} \frac{\|\mathbf{x}\|^2}{\|w\|^2} \mathcal{E} \left\{ \left\| \int e^{-j2\pi ft} w(t) \vec{\epsilon}_e(\mathbf{x}, t) dt \right\|^2 \right\} \\ &= \frac{1}{\eta} \frac{\|\mathbf{x}\|^2}{\|w\|^2} (|W|^2 * \text{Tr}[\mathbf{R}_{\vec{\epsilon}_e}]) (\mathbf{x}, \mathbf{x}, f) \\ &= \frac{1}{\|w\|^2} (|W|^2 * \mathcal{U}_e) (\mathbf{x}, f), \end{aligned}$$

substituting the second term on the right from (2.53) in the second line and substituting (3.63a) in the third line. Here for notational simplicity the electric field itself is windowed, which is not quite the same as windowing the quantizer output since in the latter case any analog filters will continue to ring beyond the end of the window. In most cases the difference is negligible. Substituting (4.17) results in

$$\mathcal{U}_{w \times \vec{\epsilon}_e}(\mathbf{x}, f) = \frac{1}{\eta} \frac{\sigma^2}{T \|w\|^2} \sum_{\mathbf{x}' \in \mathcal{L}} \sum_{m=1}^M \left(|W|^2 * \left(|H_A|^2 \times \|\vec{\mathbf{A}}_e\|_m^2 \right) \right) (-\hat{\mathbf{x}} f/c, f; -\mathbf{x}'),$$

and this result can be further specialized by substituting (4.18) or (4.19). We can see that the component noise-shaping frequency responses are each subject to convolution with the window frequency response. This can lead to the same increase in the in-band quantization noise as was detailed in Section 2.2.4.

4.2 Loop Filter Design

In this section we will consider the design of the loop filter response \mathbf{g} , or equivalently of the noise-shaping response \mathbf{h} . Our primary goal is to design \mathbf{h} so as to minimize in some sense the noise contribution to the far-field radiation intensity over the spatio-temporal signal band of interest, which will be some subset of the Helmholtz cone. In most cases we want to suppress noise power over all directions, and so the signal band will be a temporally bandlimited portion of the cone as in Figure 4.2. As was the case for the NTF of a temporal $\Delta\Sigma$ modulator, \mathbf{h} cannot be made uniformly small; the tradeoff for a low NTF value in the

signal band is a high value elsewhere. “Elsewhere” now includes nonpropagating spatio-temporal frequencies as well as temporal frequencies out of the input signal band.

We can see from (4.3) that if the loop filter measure \underline{g} is FIR (has finite support) then noise-shaping measure \underline{h} is also FIR, and if so we can see from (4.18) that the power intensity is a convex quadratic function of the coefficients of \underline{h} . Thus we can use SOCP to optimize the loop filter. There are three considerations for loop filter design: controlling the amount and distribution of the radiated noise, maintaining modulator stability, and enforcing computability. The first two lead to explicit optimization constraints which we consider in this section. Computability, on the other hand, is enforced implicitly through the support of the loop filter measure; we defer discussion of that until the next section.

4.2.1 Far-Field Noise Power

There are two primary considerations in constraining the far-field noise power: the signal-to-noise ratio in a given transmit direction and the noise power radiated in all other directions. The latter is the simpler of the two; the expected noise power intensity over the frequency band \mathcal{F} transmitted in the direction $\hat{\mathbf{x}}$ is found as in (3.62) by integrating the power intensity

$$\int_{\mathcal{F}} \mathcal{U}_e(\hat{\mathbf{x}}, f) df.$$

Substituting (4.17) we can constrain the peak expected noise intensity with a set of SOC constraints of the form

$$\boxed{\frac{1}{\eta} \frac{\sigma^2}{T} \int_{\mathcal{F}} |H_A(f)|^2 \sum_{\mathbf{x}' \in \mathcal{L}} \sum_{m=1}^M \left\| [\vec{\mathbf{A}}_e]_m(-\hat{\mathbf{x}}_k f/c, f; -\mathbf{x}') \right\|^2 df \leq \alpha^2, \quad k = 1, \dots, K_{\text{dir}},}$$

(4.22)

where $\{\hat{\mathbf{x}}_k\}$ is a set of K_{dir} directions distributed on the unit sphere and α is a constant bound or an auxiliary optimization variable. The total radiated noise power is found by integrating the power intensity over both frequency and the unit sphere, and can be controlled

with a single SOC constraint of the form

$$\boxed{\frac{1}{\eta} \frac{\sigma^2}{T} \int \int_{\mathcal{F}} |H_A(f)|^2 \sum_{\mathbf{x}' \in \mathcal{L}} \sum_{m=1}^M \left\| [\vec{\mathbf{A}}_e]_m(-\hat{\mathbf{x}}f/c, f; -\mathbf{x}') \right\|^2 df \Omega(d\mathbf{x}) \leq \alpha^2,} \quad (4.23)$$

where again α is a constant bound or an auxiliary optimization variable.

To constrain far-field SNR, we assume that \mathcal{X}_{tx} is the subset of the unit sphere that corresponds to potential transmit steering directions. The signal-to-noise ratio (SNR) over the signal band \mathcal{F} in the far field direction $\hat{\mathbf{x}} \in \mathcal{X}_{\text{tx}}$ is found by integrating the signal and noise components of the radiation intensity and taking the ratio:

$$\text{SNR}(\hat{\mathbf{x}}) = \frac{\int_{\mathcal{F}} \mathcal{U}_s(\hat{\mathbf{x}}, f) df}{\int_{\mathcal{F}} \mathcal{U}_e(\hat{\mathbf{x}}, f) df}.$$

The signal and noise intensities are found in general according to (3.64) and (4.17). The noise intensity is independent of any signal array patterns, but the signal intensity is both signal and array-pattern dependent. Thus we will assume that the signal intensity in the direction $\hat{\mathbf{x}}$ results from an array with a predesigned array pattern $\vec{\mathbf{A}}_{\hat{\mathbf{x}}}$ whose peak is in the direction $\hat{\mathbf{x}}$, transmitting a signal with the power spectrum

$$R_{s_A}(f) = \frac{\sigma^2}{T} 1_{\mathcal{F}}(f).$$

This provides both a signal-independent metric and a convenient normalization. Now the SNR is

$$\boxed{\text{SNR}(\hat{\mathbf{x}}) = \frac{\int_{\mathcal{F}} \left\| \vec{\mathbf{A}}_{\hat{\mathbf{x}}}(-\hat{\mathbf{x}}f/c, f) \right\|^2 df}{\int_{\mathcal{F}} |H_A(f)|^2 \sum_{\mathbf{x}' \in \mathcal{L}} \sum_{m=1}^M \left\| [\vec{\mathbf{A}}_e]_m(-\hat{\mathbf{x}}f/c, f; -\mathbf{x}') \right\|^2 df}}$$

where the denominator is a convex quadratic in the coefficients of the loop filter by either (4.18) or (4.19). Since the numerator does not depend on the loop filter, we can lower-bound SNR by upper-bounding its inverse. We can do this pointwise, with SOC constraints

of the form

$$\frac{\int_{\mathcal{F}} |H_A(f)|^2 \sum_{\mathbf{x}' \in \mathcal{L}} \sum_{m=1}^M \left\| [\vec{\mathbf{A}}_e]_m(-\hat{\mathbf{x}}_k f/c, f; -\mathbf{x}') \right\|^2 df}{\int_{\mathcal{F}} \left\| \vec{\mathbf{A}}_{\hat{\mathbf{x}}_k}(-\hat{\mathbf{x}}_k f/c, f) \right\|^2 df} \leq \alpha^2 \quad (4.24)$$

over a set of discrete directions $\{\hat{\mathbf{x}}_k\} \subset \mathcal{X}_{\text{tx}}$. Here α can be a constant bound or an auxiliary optimization variable. This will constrain the worst-case SNR. Alternatively, we can constrain average SNR with a single SOC constraint of the form

$$\frac{1}{\int_{\mathcal{X}_{\text{tx}}} \Omega(d\mathbf{x})} \int_{\mathcal{X}_{\text{tx}}} \frac{\int_{\mathcal{F}} |H_A(f)|^2 \sum_{\mathbf{x}' \in \mathcal{L}} \sum_{m=1}^M \left\| [\vec{\mathbf{A}}_e]_m(-\hat{\mathbf{x}} f/c, f; -\mathbf{x}') \right\|^2 df}{\int_{\mathcal{F}} \left\| \vec{\mathbf{A}}_{\hat{\mathbf{x}}}(-\hat{\mathbf{x}} f/c, f) \right\|^2 df} \Omega(d\mathbf{x}) \leq \alpha^2, \quad (4.25)$$

where Ω is the surface-area measure on the unit sphere. If \mathcal{X}_{tx} is the entire unit sphere (or at least that part over which any of the elements radiates any power) and the array patterns $\vec{\mathbf{A}}_{\hat{\mathbf{x}}}$ have been designed for constant signal power over directions \mathcal{X}_{tx} , then to within a constant scale factor, Equations (4.24) and (4.25) reduce to (4.22) and (4.23).

4.2.2 Stability

Just like a scalar $\Delta\Sigma$ modulator, a spatio-temporal $\Delta\Sigma$ modulator can become unstable if the input to the quantizer grows too large. This can happen if the modulator input grows too large or if the loop filter amplifies the noise too much (generally most of the noise gain occurs outside of the signal band). The error component of the quantizer input is

$$\mathbf{u}_e(d\mathbf{x}, dt) = (\underline{\mathbf{g}} \boxtimes \underline{\mathbf{e}})(d\mathbf{x}, dt),$$

the loop-filtered quantization error, with autocorrelation

$$\mathbf{r}_{\mathbf{u}_e}(d\mathbf{x}, d\mathbf{y}, dt) = (\underline{\mathbf{g}} \boxtimes \mathbf{r}_e \boxtimes \underline{\mathbf{g}}^\dagger)(d\mathbf{x}, d\mathbf{y}, dt) \quad (4.26)$$

found from (2.37). As discussed in Section 4.1.2, at a given time t the density of this error component is represented by the $M \times K$ values $\{[\mathbf{u}_e]_m(\mathbf{x}, t)\}$ for $m = 1, \dots, M$ and

$\mathbf{x} \in \mathcal{L}$. The assumption of (4.6) generally implies a simple quantizer model in which each of these values is independently quantized. Thus we are primarily concerned with limiting the power of each of these input components. The power of the m th noise component of the quantizer input at location \mathbf{x} can be found in terms of the autocorrelation as

$$\begin{aligned}
\mathcal{P}_{[\mathbf{u}_e]_m}(\mathbf{x}) &= \mathbf{r}_{[\mathbf{u}_e]_m}(\mathbf{x}, \mathbf{x}, 0) \\
&= [\mathbf{r}_{\mathbf{u}_e}]_{m,m}(\mathbf{x}, \mathbf{x}, 0) \\
&= \sum_{\mathbf{x}', \mathbf{y}' \in \mathcal{L}} \sum_{t, t' \in T\mathbb{Z}} \mathbf{g}(\mathbf{x}, t; -\mathbf{x}') \mathbf{r}_e(\mathbf{x}', \mathbf{y}', t' - t) \mathbf{g}^H(\mathbf{x}, t'; -\mathbf{y}') \\
&= \sum_{\mathbf{x}', \mathbf{y}' \in \mathcal{L}} \sum_{t, t' \in T\mathbb{Z}} \sum_{n, k=1}^M g_{m,n}(\mathbf{x}, t; -\mathbf{x}') [\mathbf{r}_e]_{n,k}(\mathbf{x}', \mathbf{y}', t' - t) g_{m,k}^*(\mathbf{x}, t'; -\mathbf{y}'),
\end{aligned}$$

expanding the density of (4.26) in the third line, and further expanding the matrix multiplies in the last line to make explicit the parallel between shift-varying filtering and matrix multiplication. Under the whiteness assumption (4.6) this reduces to

$$\begin{aligned}
\mathcal{P}_{[\mathbf{u}_e]_m}(\mathbf{x}) &= \sigma^2 \sum_{n=1}^M \sum_{\mathbf{x}' \in \mathcal{L}} \sum_{t \in T\mathbb{Z}} |g_{m,n}(\mathbf{x}, t; -\mathbf{x}')|^2 \\
&= \sigma^2 T \sum_{n=1}^M \sum_{\mathbf{x}' \in \mathcal{L}} \int_{-\frac{1}{2T}}^{\frac{1}{2T}} |G_{m,n}(\mathbf{x}, f; -\mathbf{x}')|^2 df,
\end{aligned}$$

invoking Parseval's relation in the second line. In the spirit of the stability bounds previously considered for scalar $\Delta\Sigma$, we can either bound the noise power at each combination of quantizer vector component m and input location \mathbf{x} with a set of SOC constraints of the form

$$\boxed{\sum_{n=1}^M \sum_{\mathbf{x}' \in \mathcal{L}} \sum_{t \in T\mathbb{Z}} |g_{m,n}(\mathbf{x}, t; -\mathbf{x}')|^2 \leq \alpha^2, \quad \mathbf{x} \in \mathcal{L}, \quad m = 1, \dots, M,} \quad (4.27)$$

or bound the peak noise gain at each quantizer vector component and input location with a much larger set of SOC constraints of the form

$$\boxed{\sum_{n=1}^M \sum_{\mathbf{x}' \in \mathcal{L}} |G_{m,n}(\mathbf{x}, f_k; -\mathbf{x}')|^2 \leq \alpha^2, \quad k = 1, \dots, K_f, \quad \mathbf{x} \in \mathcal{L}, \quad m = 1, \dots, M} \quad (4.28)$$

where $\{f_k\}$ is a dense set of frequencies over one-half period $[0, T^{-1}/2]$. The former is generally preferable as it leads to fewer constraints. In both cases the bound constant α is determined experimentally.

4.3 Computability and Parallelization

So far, the support of the loop filter measure has remained unspecified. Two issues drive the choice of the filter support: computability and parallelization. For our purposes *computability* means that for any input signal to the modulator the internal signals and the output are well-defined in terms of a sequential computation that is consistent with the defining equations of the various components in the modulator. Computability in general ensures that there exists some order in which the elements of the output can be computed, and in a spatio-temporal $\Delta\Sigma$ modulator that order is determined by the support of the loop filter measure. A *computability constraint*, then, is a restriction on the support of the loop filter measure that ensures computability. The choice of computability constraint will be shown to have a strong effect on the noise-shaping performance. It will also affect the extent to which the modulator can be easily parallelized. For real-time implementations, parallel architectures are often imperative to minimize the required clock rate. This has serious implications for the loop filtering in the modulator, as the feedback loop represents the critical delay in the system. Of the possible computability constraints, some lead to systems that parallelize well and some do not. Unfortunately, the constraints that result in the best performance are the hardest to implement in parallel.

For a simple example of (un)computability, we consider the temporal-only $\Delta\Sigma$ modulator of Section 2.2. Here computation proceeds along the time axis and computability equals *strict causality* in the loop filter—that is, the loop filter output o can only depend on past inputs, not current or future inputs. This is usually shown, as in Figure 2.1, as an explicit one-step delay in the feedback loop followed by a filter that is causal, but not strictly

so (that is, it can depend on past and current input values). At time t , computation starts at the output of the delay, proceeds throughout the loop filter and the quantizer, and ends at the input of the delay. If that delay were not present, then at time t the filter output would depend in part on the filter input, which in turn would depend on the quantizer input, which in turn would depend on the filter output: a circular dependency. It is not clear where to start or stop the computation, and the internal and output signals are not well-defined.

In a spatio-temporal $\Delta\Sigma$ modulator, computation need not proceed strictly along the time dimension, as we assume in most cases that the quantizer operates on each vector component, location, and time independently. Consider the analogy to image halftoning, for example, in which there is no time dimension. Thus computability for a spatio-temporal modulator is more complicated, and we will see that there are several different ways to attain computability. As an example of a spatio-temporal modulator system that is not computable, let $M = 1$ and let $g(\mathbf{x}, 0; -\mathbf{x}) \neq 0$ for some $\mathbf{x} \in \mathcal{L}$. In this case the output density $o(\mathbf{x}, t)$ of the loop filter at position \mathbf{x} and time t depends on, among other things, the input $e(\mathbf{x}, t)$ at position \mathbf{x} and time t , but from Figure 4.1 we see that if the quantizer is memoryless then there is no net delay around the loop; we have a circular dependency as in the scalar modulator, and the loop-filter and modulator outputs are not well defined.

The rest of the section proceeds as follows: First, the most general case of computability to be considered will be defined, both in terms of a computation path and the corresponding restriction on the support of the loop-filter measure. Then a simple example design will be introduced, followed by several special cases of the general computability constraint. For each special case the loop filter is optimized subject to that computability constraint, and the constraints are compared according to the corresponding noise-shaping performance and ease of parallelizability.

4.3.1 General Computability

A general definition of computability is simplified here by our previous restriction to time-invariant filtering. This ensures that computability can be completely defined in terms of the computation performed at a given time step. At a given time t , each of the spatio-temporal signals in the modulator is defined by $M \times K$ values, representing the M vector components of the signal density evaluated at the K locations in \mathcal{L} . Each of these values will be computed at each computational time step. Traditionally all vector components and locations would be computed for the current (computational) time, but it will be convenient to allow time-skew between the signal components at the various locations. In this section we will define the computation path, and derive from that restrictions on the support of the loop filter measure. In the sections that follow, notable special cases of the general result will be derived.

We define the computation path through two functions. The invertible index function $\kappa : \mathbb{N}_{MK} \rightarrow \mathbb{N}_M \times \mathcal{L}$, where $\mathbb{N}_M = \{1, 2, \dots, M\}$ and \mathcal{L} is the set of K element locations, determines the order in which the MK distinct values represented by the M vector components and K locations of the loop filter output are computed at each time step. Evaluated for an index k , the index function returns the pair $(m, \mathbf{x}) = \kappa(k)$, indicating that the m th signal component at location \mathbf{x} is to be computed in the k th computation of each time step. We will let $\kappa(n) = (\kappa_i(n), \kappa_x(n))$, to refer to the vector component and position separately. Evaluating the inverse index function returns the index $k = \kappa^{-1}(m, \mathbf{x})$ of the computation of component m at position \mathbf{x} . The time-skew function $\gamma : \mathbb{N}_M \times \mathcal{L} \rightarrow T\mathbb{Z}^+$, where \mathbb{Z}^+ is the nonnegative integers, maps each vector component and spatial location to an integer-sample delay. Thus, at time t we first compute $o_{\kappa_i(1)}(\kappa_x(1), t - \gamma(\kappa(1)))$, the $\kappa_i(1)$ -th component of the loop filter output at location $\kappa_x(1)$ and time $t - \gamma(\kappa(1))$, then $o_{\kappa_i(2)}(\kappa_x(2), t - \gamma(\kappa(2)))$, and so on through $o_{\kappa_i(MK)}(\kappa_x(MK), t - \gamma(\kappa(MK)))$.

If the quantizer is memoryless and acts independently on all vector components, then there is a zero-delay path from each vector component and location of the loop-filter output

ϱ to the corresponding component and location of the loop-filter input \underline{e} . Thus, to avoid circular dependencies each scalar output component can only depend on input vector components and locations at which the corresponding output has already been computed in this or a previous time step. This is equivalent to a restriction on the support of the loop-filter measure \underline{g} , which we can see by writing the definition of the loop-filter output density as

$$o_m(\mathbf{x}, t) = \sum_{\tau \in T\mathbb{Z}} \sum_{\mathbf{x}' \in \mathcal{L}} g_{m,n}(\mathbf{x}, t - \tau; -\mathbf{x}') e_n(\mathbf{x}', \tau).$$

The loop-filter coefficient $g_{m,n}(\mathbf{x}, t - \tau; -\mathbf{x}')$ is the weight applied to $e_n(\mathbf{x}', \tau)$, the n th component of the loop-filter input density at position \mathbf{x}' and time τ , in the defining sum of $o_m(\mathbf{x}, t)$, the m th component of the loop-filter output density at position \mathbf{x} and time t . Applying this output definition at time step t and computational step k , we compute the output value

$$o_{\kappa_i(k)}(\kappa_x(k), t - \gamma(\kappa(k))) = \sum_{\tau \in T\mathbb{Z}} \sum_{\mathbf{x}' \in \mathcal{L}} g_{\kappa_i(k),n}(\kappa_x(k), t - \gamma(\kappa(k)) - \tau; -\mathbf{x}') e_n(\mathbf{x}', \tau),$$

which can depend on all error values computed in previous time steps as well as values previously computed in the current time step. The former are described by

$$\{e_n(\mathbf{x}', t' - \gamma(n, \mathbf{x}')) : t' < t, n \in \mathbb{N}_M, \mathbf{x}' \in \mathcal{L}, t' \in T\mathbb{Z}\},$$

and the latter by

$$\{e_n(\mathbf{x}', t - \gamma(n, \mathbf{x}')) : \kappa^{-1}(n, \mathbf{x}') < k, n \in \mathbb{N}_M, \mathbf{x}' \in \mathcal{L}\}.$$

The loop-filter coefficients that map these values to the current output are

$$\{g_{\kappa_i(k),n}(\kappa_x(k), t' + \gamma(n, \mathbf{x}') - \gamma(\kappa(k)); -\mathbf{x}') : n \in \mathbb{N}_M, \mathbf{x}' \in \mathcal{L}, 0 < t' \in T\mathbb{Z}\}$$

and

$$\{g_{\kappa_i(k),n}(\kappa_x(k), \gamma(n, \mathbf{x}') - \gamma(\kappa(k)); -\mathbf{x}') : \kappa^{-1}(n, \mathbf{x}') < k, n \in \mathbb{N}_M, \mathbf{x}' \in \mathcal{L}\};$$

all others must be zero. The support of the m th row and n th column of the loop filter measure is therefore contained in the disjoint union

$$\begin{aligned} & \{(\mathbf{x}, t; -\mathbf{x}') : \gamma(n, \mathbf{x}') - \gamma(m, \mathbf{x}) < t \in T\mathbb{Z}, \mathbf{x} \in \mathcal{L}, \mathbf{x}' \in \mathcal{L}\} \cup \\ & \{(\mathbf{x}, \gamma(n, \mathbf{x}') - \gamma(m, \mathbf{x}); -\mathbf{x}') : \kappa^{-1}(n, \mathbf{x}') < \kappa^{-1}(m, \mathbf{x}), \mathbf{x} \in \mathcal{L}, \mathbf{x}' \in \mathcal{L}\}. \end{aligned}$$

This can also be compactly expressed in terms of which coefficients of the loop filter must be identically zero, which we will call the general *computability constraint*:

$$\boxed{g_{m,n}(\mathbf{x}, t; -\mathbf{x}') = 0, \quad t < \gamma(n, \mathbf{x}') - \gamma(m, \mathbf{x})} \quad (4.29a)$$

$$\boxed{g_{m,n}(\mathbf{x}, \gamma(n, \mathbf{x}') - \gamma(m, \mathbf{x}); -\mathbf{x}') = 0, \quad \kappa^{-1}(m, \mathbf{x}) \leq \kappa^{-1}(n, \mathbf{x}')} \quad (4.29b)$$

The first part, (4.29a), enforces causality, modified to allow for time-skewed computation. It ensures that the output values computed at the current time step do not depend on output values that will be computed in a future time step. The second part, (4.29b), enforces computability within a time step, ensuring that computation can occur along the chosen path.

A more implementation-oriented way to represent the time skew results from slightly modifying the system model. A simple transformation can be used to convert a time-skewed loop filter into an equivalent unskewed filter, by instead skewing the signals. We define the *skew measure*

$$\boxed{\Delta(d\mathbf{x}, dt; -\mathbf{x}') = \sum_{\mathbf{x} \in \mathcal{L}} \delta(d\mathbf{x}) 1_{\{\mathbf{x}\}}(\mathbf{x}') \text{diag} \left\{ \gamma_{(1,\mathbf{x})} \delta(dt), \gamma_{(2,\mathbf{x})} \delta(dt), \dots, \gamma_{(M,\mathbf{x})} \delta(dt) \right\}} \quad (4.30)$$

which has an “inverse”

$$\Delta^{-1}(d\mathbf{x}, dt; -\mathbf{x}') = \sum_{\mathbf{x} \in \mathcal{L}} \delta(d\mathbf{x}) 1_{\{\mathbf{x}\}}(\mathbf{x}') \text{diag} \left\{ -\gamma_{(1,\mathbf{x})} \delta(dt), -\gamma_{(2,\mathbf{x})} \delta(dt), \dots, -\gamma_{(M,\mathbf{x})} \delta(dt) \right\} \quad (4.31)$$

in the sense that

$$(\Delta \boxtimes \Delta^{-1})(d\mathbf{x}, dt; -\mathbf{x}') = (\Delta^{-1} \boxtimes \Delta)(d\mathbf{x}, dt; -\mathbf{x}') = \mathbf{I} \sum_{\mathbf{x} \in \mathcal{L}} \delta(d\mathbf{x}) 1_{\{\mathbf{x}\}}(\mathbf{x}') \delta(dt)$$

which acts as an identity operator on the class of discrete-space signals of interest:

$$\Delta \boxtimes \Delta^{-1} \boxtimes \mathbf{d} = \mathbf{d}.$$

If the quantizer is both spatially and temporally memoryless and acts independently on all vector components, then the spatio-temporal modulator of Figure 4.3(b) is completely equivalent to that of Figure 4.3(a), which is just the original modulator from Figure 4.1 with an extra output delay. The input signal in Figure 4.3(b) is delayed in time selectively based on spatial location and vector position, as defined by γ . The output signal is then advanced by the corresponding amount. Although this operation is not causal by itself, the cascade with the delay of γ_{\max} is, where γ_{\max} is the greatest advance in Δ^{-1} . Defining the “unskewed” loop filter $\mathbf{g}_{\Delta} \triangleq \Delta \boxtimes \mathbf{g} \boxtimes \Delta^{-1}$, we now compare it to the original “time-skewed” loop filter:

$$\begin{aligned} [\mathbf{g}_{\Delta}]_{m,n}(d\mathbf{x}, dt; -\mathbf{x}') &\triangleq [\Delta \boxtimes \mathbf{g} \boxtimes \Delta^{-1}]_{m,n}(d\mathbf{x}, dt; -\mathbf{x}') \\ &=_{(\gamma(n, \mathbf{x}') - \gamma(m, \mathbf{x}))} g_{m,n}(d\mathbf{x}, dt; -\mathbf{x}') \\ &= g_{m,n}(\mathbf{x}, t - \gamma(n, \mathbf{x}') + \gamma(m, \mathbf{x}); -\mathbf{x}')_{\Sigma_{\mathcal{L}}(d\mathbf{x})\Sigma_{T\mathbb{Z}}(dt)}, \end{aligned}$$

from which we see that the densities are related by

$$[\mathbf{g}_{\Delta}]_{m,n}(\mathbf{x}, t; -\mathbf{x}') = g_{m,n}(\mathbf{x}, t - \gamma(n, \mathbf{x}') + \gamma(m, \mathbf{x}); -\mathbf{x}'). \quad (4.32)$$

Substituting (4.32) into the computability constraint (4.29) yields an equivalent computability constraint in terms of the unskewed density:

$$\mathbf{g}_{\Delta}(\mathbf{x}, t; -\mathbf{x}') = \mathbf{0}, \quad t < 0 \quad (4.33a)$$

$$[\mathbf{g}_{\Delta}]_{m,n}(\mathbf{x}, 0; -\mathbf{x}') = 0, \quad \kappa^{-1}(m, \mathbf{x}) \leq \kappa^{-1}(n, \mathbf{x}'). \quad (4.33b)$$

Here the time skew is absorbed into the definition of \mathbf{g}_{Δ} , simplifying the computability constraint.

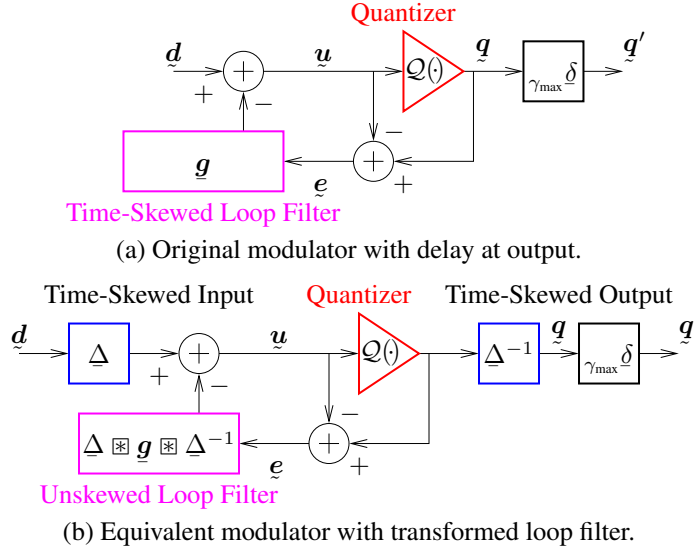


Figure 4.3: Time-skew transformation generates new computability constraints.

4.3.2 Example Setup

In the following sections several important special cases of the general computability constraint (4.29) are presented. These constraints vary in ease of implementation, suitability for parallel implementation, and noise-shaping performance. To allow direct comparison of the latter, the loop filter corresponding to each computability constraint for an example array was optimized. The example array consists of $K = 6$ vertical dipoles spaced uniformly about the origin along the x -axis in front of an ideal ground in the x - z plane. The pattern for this element is found in Appendix E. The interelement spacing is $d = \frac{c}{8f_c}$, which results in four-times spatial oversampling at center frequency f_c . The $\Delta\Sigma$ modulator operates at a rate $f_s = 1/T = 4f_c$ with a signal bandwidth of $\frac{f_s}{8}$, which represents four-times temporal oversampling. Although the spatial and temporal oversampling ratios are equal here, they can be independently chosen. Each loop filter has a temporal extent of 15 coefficients, although the number of independent optimization variables that this represents varies by computability constraint. We will assume that the equivalent analog frequency response $H_A(f)$ is approximately unity on the signal band \mathcal{F} . Each loop filter was optimized by

solving the following SOCP:

$$\text{minimize } \alpha \quad (4.34a)$$

$$\text{s.t. } \frac{\int_{\mathcal{F}} \left\| \vec{\mathbf{A}}_{\text{el}}(-\hat{\mathbf{x}}_n f/c, f) \right\|^2 \sum_{\mathbf{x}' \in \mathcal{L}} |H(-\hat{\mathbf{x}}_n f/c, f; -\mathbf{x}')|^2 df}{6 \int_{\mathcal{F}} \left\| \vec{\mathbf{A}}_{\text{el}}(-\hat{\mathbf{x}}_0 f/c, f) \right\|^2 df} \leq \alpha^2, \quad n = 1, \dots, N_{\text{dir}} \quad (4.34b)$$

$$\sum_n \sum_{\mathbf{x}' \in \mathcal{L}} |g(\mathbf{x}, nT; -\mathbf{x}')|^2 \leq 1.5, \quad \mathbf{x} \in \mathcal{L} \quad (4.34c)$$

Objective (4.34a) and constraint (4.34b) together minimize the worst-case transmitted noise gain over the set of directions $\{\hat{\mathbf{x}}_n\}$, which was chosen to discretize the set of potential steering directions (here, the entire visible hemisphere). The noise gain in a direction $\hat{\mathbf{x}}$ is here defined as the ratio of the far-field noise intensity in the direction $\hat{\mathbf{x}}$ to the intensity that would result in reference direction $\hat{\mathbf{x}}_0$ (boresight here) from a theoretical reference system with no noise shaping and the same quantization noise level. By this we mean that the reference system has an identically zero loop filter and thus a noise-shaping measure from (4.3) of $\underline{\mathbf{h}}(d\mathbf{x}, dt; -\mathbf{x}') = {}_{\mathbf{x}'}\underline{\delta}(d\mathbf{x})\underline{\delta}(dt)\mathbf{I}$. This response is in fact spatially shift-invariant, and so we can write this as the LSI and LTI response $\underline{\mathbf{h}}_0(d\mathbf{x}, dt) \triangleq \underline{\mathbf{h}}(d\mathbf{x}, dt; 0) = \underline{\delta}(d\mathbf{x})\underline{\delta}(dt)\mathbf{I}$ with a spatio-temporal Fourier transform $\mathbf{H}_0(\mathbf{v}, f) = \mathbf{I}$. Since this clearly provides no noise shaping, it provides a convenient reference by which to compare the noise-shaping performance of the various designs. The numerator and denominator, respectively, of the n th constraint in (4.34b) thus result from integrating (4.19a) over the signal band \mathcal{F} with the actual and reference NTF's in the steering and reference directions $\hat{\mathbf{x}}_n$ and $\hat{\mathbf{x}}_0$, canceling common factors. The constant 6 in the denominator results from the sum over six elements in (4.19a). Since the denominator is just a constant, we can also view the constraints (4.34b) as a normalized special case of (4.22) with $M = 1$, $H_A(f) \approx 1$, and the common element-response simplification of (4.16). Stability constraint (4.34c) follows from (4.27) with $M = 1$, bounding the noise power at each quantizer input location $\mathbf{x} \in \mathcal{L}$. The constant bound of 1.5 was determined experimentally.

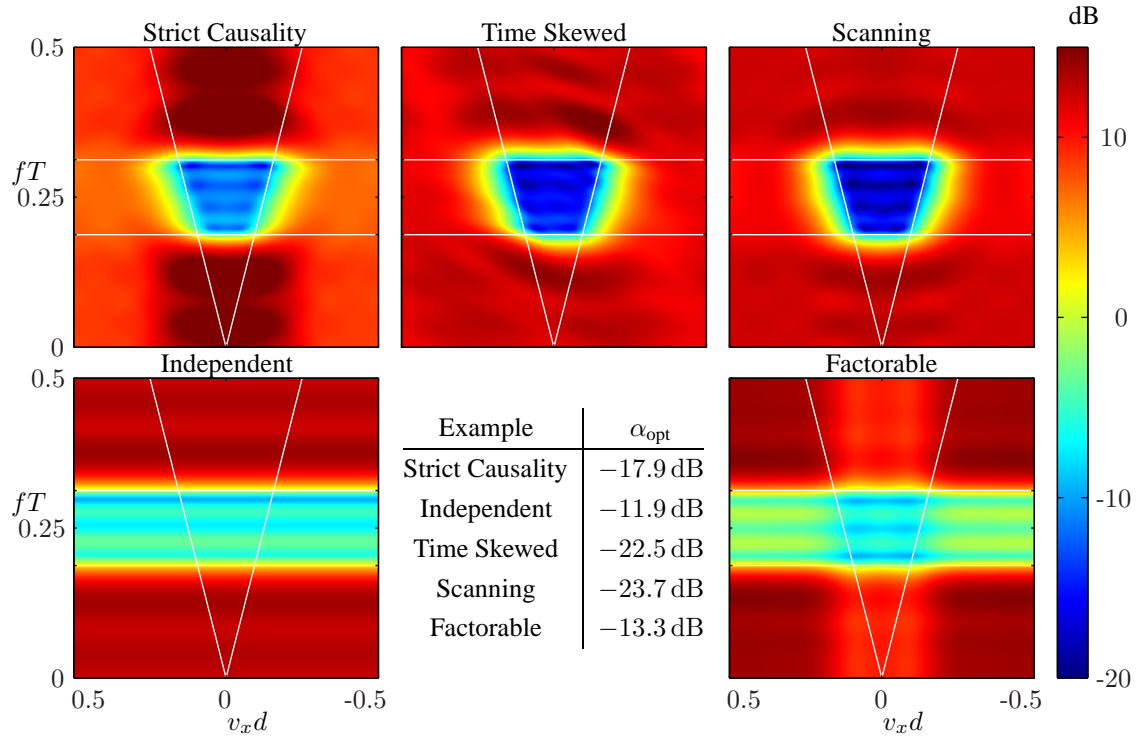


Figure 4.4: A comparison of the equivalent NTF's of optimized loop filters with various computability constraints.

The results of the various optimizations are shown in Figure 4.4, and will be referred to in the following sections as the special cases of computability are introduced. None of these examples exhibits performance that would be seen as acceptable, much less good, in most practical systems; greater oversampling in time and/or space would be required. The modest oversampling here was chosen so that signal-band details could be seen on the same scale as an entire period of the NTF.

4.3.3 Strict Causality

The most straightforward extension of the causality requirement in scalar $\Delta\Sigma$ modulators to our case is the *strict causality* constraint

$$\mathbf{g}(\mathbf{x}, t; -\mathbf{x}') = \mathbf{0}, \quad t \leq 0, \quad (4.35)$$

so that at each time instant the filter output depends only on previous values of the filter input for all vector indices and locations. Here there is no time skew, as $\gamma(m, \mathbf{x}) = 0$, and the stronger constraint (4.35) implies (4.29). The computation path defined by the function κ is arbitrary, as there are no computational dependencies within any given time step. (Computation of any given vector component and location is still required to proceed in strict time order, however.) Since the computation path within a time step does not matter, this represents a good structure for parallel implementation; the computation of all vector components of the output at all locations can be done simultaneously and independently.

For the six-element example, Figure 4.5(a) shows the order of computation of the loop filter output density $o(\mathbf{x}, t)$. Each row corresponds to an element location \mathbf{x} , and each column corresponds to a time t , starting from $t = 0$. The values in the table indicate the time step (in units of T) in which the corresponding value is computed. For strict causality this is quite straightforward; the values of $o(\mathbf{x}, t)$ at time t are computed at time step t . No computational ordering within a time step is implied in the ordering of the rows, and thus the six output values corresponding to each time step can be computed independently.

Equation (4.35) and Figure 4.5(a) both determine the support of the loop filter density $g(\mathbf{x}, t; -\mathbf{x}')$ and the associated NTF density $h(\mathbf{x}, t; -\mathbf{x}')$, as shown in Figure 4.6. Each of the six subtables represents one of the six possible values of output location \mathbf{x} , while each row represents an input location \mathbf{x}' . The columns represent time t . In the table, a value of “0” indicates a value that is identically zero, a value of “X” indicates a value that might be nonzero, and the “•” entry in each subtable at $\mathbf{x} = \mathbf{x}'$ and $t = 0$ indicates a value of 0 in g and a value of 1 in h . We can quickly see that each output value depends only on input values from a previous time, since all the nonzero coefficients correspond to positive time and thus to past input values (due to the temporal flip in the convolution operation). The result of optimizing this example loop filter (that is, optimizing the “X” values) subject to strict causality is shown in the upper-left plot of Figure 4.4.

	$t = 0$	T	$2T$	$3T$	$4T$	$5T$	$6T$	\dots
$\mathbf{x} = -2.5d$	0	1	2	3	4	5	6	\dots
$-1.5d$	0	1	2	3	4	5	6	\dots
$-0.5d$	0	1	2	3	4	5	6	\dots
$0.5d$	0	1	2	3	4	5	6	\dots
$1.5d$	0	1	2	3	4	5	6	\dots
$2.5d$	0	1	2	3	4	5	6	\dots

(a) Strictly causal.

	$t = 0$	T	$2T$	$3T$	$4T$	$5T$	$6T$	\dots
$\mathbf{x} = -2.5d$	0	1	2	3	4	5	6	\dots
$-1.5d$	1	2	3	4	5	6	7	\dots
$-0.5d$	2	3	4	5	6	7	8	\dots
$0.5d$	3	4	5	6	7	8	9	\dots
$1.5d$	4	5	6	7	8	9	10	\dots
$2.5d$	5	6	7	8	9	10	11	\dots

(b) Time-skewed.

	$t = 0$	T	$2T$	$3T$	$4T$	$5T$	$6T$	\dots
$\mathbf{x} = -2.5d$	$0a$	$1a$	$2a$	$3a$	$4a$	$5a$	$6a$	\dots
$-1.5d$	$0c$	$1c$	$2c$	$3c$	$4c$	$5c$	$6c$	\dots
$-0.5d$	$0f$	$1f$	$2f$	$3f$	$4f$	$5f$	$6f$	\dots
$0.5d$	$0e$	$1e$	$2e$	$3e$	$4e$	$5e$	$6e$	\dots
$1.5d$	$0d$	$1d$	$2d$	$3d$	$4d$	$5d$	$6d$	\dots
$2.5d$	$0b$	$1b$	$2b$	$3b$	$4b$	$5b$	$6b$	\dots

(c) Scanning.

Figure 4.5: A comparison of the computation order for the six-element example with various computability constraints. Each number in the tables indicates the time step (in units of T) in which the corresponding filter output value $o(\mathbf{x}, t)$ is computed. Lowercase letters in the scanning computability example indicate the computational steps within each time step.

Special Case: Independent Scalar (Temporal) Modulators

An important special case of strict causality results from the additional constraint

$$\boxed{g_{m,n}(\mathbf{x}, t; -\mathbf{x}') = 0, \quad \mathbf{x} \neq \mathbf{x}' \text{ or } m \neq n.} \quad (4.36)$$

Here the m th component of the quantizer input at location \mathbf{x} depends only on the past values of the m th component of the quantizer output at location \mathbf{x} . If the quantizer operates independently on each vector component and spatial location, then this results in $M \times K$

	$\mathbf{x} = -2.5d$				$\mathbf{x} = -1.5d$				$\mathbf{x} = -0.5d$			
	$t = 0$	T	$2T$...	$t = 0$	T	$2T$...	$t = 0$	T	$2T$...
$\mathbf{x}' = -2.5d$	•	X	X	...	0	X	X	...	0	X	X	...
$-1.5d$	0	X	X	...	•	X	X	...	0	X	X	...
$-0.5d$	0	X	X	...	0	X	X	...	•	X	X	...
$0.5d$	0	X	X	...	0	X	X	...	0	X	X	...
$1.5d$	0	X	X	...	0	X	X	...	0	X	X	...
$2.5d$	0	X	X	...	0	X	X	...	0	X	X	...

	$\mathbf{x} = 0.5d$				$\mathbf{x} = 1.5d$				$\mathbf{x} = 2.5d$			
	$t = 0$	T	$2T$...	$t = 0$	T	$2T$...	$t = 0$	T	$2T$...
$\mathbf{x}' = -2.5d$	0	X	X	...	0	X	X	...	0	X	X	...
$-1.5d$	0	X	X	...	0	X	X	...	0	X	X	...
$-0.5d$	0	X	X	...	0	X	X	...	0	X	X	...
$0.5d$	•	X	X	...	0	X	X	...	0	X	X	...
$1.5d$	0	X	X	...	•	X	X	...	0	X	X	...
$2.5d$	0	X	X	...	0	X	X	...	•	X	X	...

Figure 4.6: A representation of the support regions for the strictly-causal loop and noise-shaping filter measure components $\underline{g}(d\mathbf{x}, dt; -\mathbf{x}')$ and $\underline{h}(d\mathbf{x}, dt; -\mathbf{x}')$. An entry of “X” indicates an independent optimization variable, while an entry of “•” indicates an entry that is 0 in g and 1 in h .

independent temporal $\Delta\Sigma$ modulators, each driving one antenna element. In this case no spatial noise shaping is done, and the improvement over a single scalar $\Delta\Sigma$ is limited to the factor of K SNR gain that results from adding K identical signals with uncorrelated noise of identical variance. This represents the best case for parallel implementation, and reduces the computational burden significantly. However, as might be expected the performance is the worst of all the examples given here. The result of optimizing the example loop filter subject to (4.36) is shown in Figure 4.4. Because all the elements were identical in the example and the other constraints were location-neutral, all six temporal loop filters had the same optimal value. The cost of eliminating the spatial noise shaping in this example is 6 dB of noise suppression vs. the strictly causal example, a figure that would grow for larger arrays or for higher spatial oversampling ratios.

4.3.4 Time-Skewed Causality

More general than strict causality, but less general than (4.29), is *time-skewed* causality, defined by

$$\boxed{g_{m,n}(\mathbf{x}, t; -\mathbf{x}') = 0, \quad t \leq \gamma(n, \mathbf{x}') - \gamma(m, \mathbf{x})} \quad (4.37)$$

or

$$\boxed{(\underline{\Delta} \boxtimes \underline{g} \boxtimes \underline{\Delta}^{-1})(\mathbf{x}, t; -\mathbf{x}') = \mathbf{0}, \quad t \leq 0,} \quad (4.38)$$

which are stronger than and thus imply (4.29) and (4.33), respectively. Here again the index function κ is arbitrary and all vector components of the output at all locations can be computed simultaneously in a given time step, as in the strictly causal case, but here the output values computed in the time step need not correspond to the current time.

Even if we restrict the maximum time skew for the small six-element example, there are far too many possible skew functions γ to brute-force optimize them all. Experimentation, however, suggests that the choice $\gamma(m, \mathbf{x}) = (\mathbf{x}/d + 2.5)T$ provides the best performance in this case. This choice results in zero delay at one end, increasing linearly to a delay of $5T$ at the other. Thus we have uniform time-skew across the array face. The constraint (4.37) now reduces to

$$g(\mathbf{x}, t; -\mathbf{x}') = 0, \quad t \leq (\mathbf{x}' - \mathbf{x})T/d. \quad (4.39)$$

This particular support constraint was termed *diagonal computability* in [29] because the computation path proceeds along a diagonal in the (x, t) plane, as shown in Figure 4.5(b). At time step 0 we compute the value of the loop filter output $o(-2.5d, 0)$, at time step 1 we compute both $o(-2.5d, T)$ and $o(-1.5d, 0)$, and so on computing one more value in each time step until step 5, at which point we reach steady state and compute six values in each time step.

The corresponding support of the loop filter is shown in Figure 4.7, where we see a diagonal arrangement of nonzero coefficients. Rather than all coefficients lying to the right of $t = 0$, here they lie above and to the right of the diagonal passing through $t =$

$t =$	$\mathbf{x} = -2.5d$							$\mathbf{x} = -1.5d$						
	0	T	$2T$	$3T$	$4T$	$5T$	$6T\dots$	$-T$	0	T	$2T$	$3T$	$4T$	$5T\dots$
$\mathbf{x}' = -2.5d$	•	X	X	X	X	X	X...	0	X	X	X	X	X	X...
$-1.5d$	0	0	X	X	X	X	X...	0	•	X	X	X	X	X...
$-0.5d$	0	0	0	X	X	X	X...	0	0	0	X	X	X	X...
$0.5d$	0	0	0	0	X	X	X...	0	0	0	0	X	X	X...
$1.5d$	0	0	0	0	0	X	X...	0	0	0	0	0	X	X...
$2.5d$	0	0	0	0	0	0	X...	0	0	0	0	0	0	X...

$t =$	$\mathbf{x} = -0.5d$							$\mathbf{x} = 0.5d$						
	$-2T$	$-T$	0	T	$2T$	$3T$	$4T\dots$	$-3T$	$-2T$	$-T$	0	T	$2T$	$3T\dots$
$\mathbf{x}' = -2.5d$	0	X	X	X	X	X	X...	0	X	X	X	X	X	X...
$-1.5d$	0	0	X	X	X	X	X...	0	0	X	X	X	X	X...
$-0.5d$	0	0	•	X	X	X	X...	0	0	0	X	X	X	X...
$0.5d$	0	0	0	0	X	X	X...	0	0	0	•	X	X	X...
$1.5d$	0	0	0	0	0	X	X...	0	0	0	0	0	X	X...
$2.5d$	0	0	0	0	0	0	X...	0	0	0	0	0	0	X...

$t =$	$\mathbf{x} = 1.5d$							$\mathbf{x} = 2.5d$						
	$-4T$	$-3T$	$-2T$	$-T$	0	T	$2T\dots$	$-5T$	$-4T$	$-3T$	$-2T$	$-T$	0	$T\dots$
$\mathbf{x}' = -2.5d$	0	X	X	X	X	X	X...	0	X	X	X	X	X	X...
$-1.5d$	0	0	X	X	X	X	X...	0	0	X	X	X	X	X...
$-0.5d$	0	0	0	X	X	X	X...	0	0	0	X	X	X	X...
$0.5d$	0	0	0	0	X	X	X...	0	0	0	0	X	X	X...
$1.5d$	0	0	0	0	•	X	X...	0	0	0	0	0	X	X...
$2.5d$	0	0	0	0	0	0	X...	0	0	0	0	0	•	X...

Figure 4.7: A representation of the support regions for the time-skewed loop and noise-shaping filter measure components $\underline{g}(d\mathbf{x}, dt; -\mathbf{x}')$ and $\underline{h}(d\mathbf{x}, dt; -\mathbf{x}')$. An entry of “X” indicates an independent optimization variable, while an entry of “•” indicates an entry that is 0 in g and 1 in h .

0. Applying the transformation of (4.38) would make Figure 4.7 identical to Figure 4.6. The result of optimizing the example subject to this time-skewed constraint is shown in Figure 4.4. Adding the time skew has improved performance considerably, at very little additional implementation cost versus strict causality.

4.3.5 Scanning Computability

Time-skewed causality represents one example of a non-strictly causal computability constraint, albeit one that can be transformed into a strictly causal constraint. What strict causality and time-skewed causality have in common is that the index function κ of the general computability constraint (4.29) is irrelevant. When this is not the case, then the loop-filter outputs at a given time can depend on the inputs at the same time as defined by κ . We define *scanning computability* as the restriction

$$\boxed{\begin{aligned} \mathbf{g}(\mathbf{x}, t; -\mathbf{x}') &= \mathbf{0}, & t < 0 \\ g_{m,n}(\mathbf{x}, 0; -\mathbf{x}') &= 0, & \kappa^{-1}(m, \mathbf{x}) \leq \kappa^{-1}(n, \mathbf{x}'), \end{aligned}} \quad (4.40a)$$

which results from setting $\gamma(m, \mathbf{x}) = 0$ in (4.29). The resulting response is causal (but not strictly so) and at time 0 the support is restricted so as to enforce the computation order. Scanning computability is in some sense the most natural extension of causality to multiple dimensions. However, the explicitly sequential nature of the computation represents a real obstacle to parallel implementation. This will be illustrated shortly for the six-element example.

In our six-element example we have $6! = 720$ possible unique scan paths. Because the optimization constraints of (4.34) are symmetric in \mathbf{x} , we can reduce this to 360 scan paths by eliminating one of each flip-symmetric pair. An exhaustive search was performed to find the optimal scan path (in the sense that it resulted in the smallest value of α in (4.34)), which was found to be

$$\begin{aligned} \{\kappa_x(1), \dots, \kappa_x(6)\} &= \{(-2.5d, 0, 0), (2.5d, 0, 0), (-1.5d, 0, 0), \\ &\quad (1.5d, 0, 0), (0.5d, 0, 0), (-0.5d, 0, 0)\} \\ &\triangleq \{\mathbf{x}_1, \dots, \mathbf{x}_6\}. \end{aligned}$$

Figure 4.5(c) shows the corresponding computational order of the output values $o(\mathbf{x}, t)$ for $\mathbf{x} \in \mathcal{L}$ and $t \in T\mathbb{Z}$. Here numerical entries indicate the time step (in units of T)

in which the corresponding output value is computed, while lowercase letters indicate the order of computation within each time step. The corresponding loop-filter support is shown in Figure 4.8. The key difference from Figure 4.6 is found in the first column of each subtable, where some values of $g(\mathbf{x}, t; -\mathbf{x}')$ can be nonzero for $t = 0$ as determined by the index function κ in the second line of (4.40a). The nonzero entries represent dependencies on loop-filter input values at the current time step, which will depend in general on loop filter outputs. So at a given time step t' we first compute $o(\mathbf{x}_1, t')$, as it depends only on past values of the filter input e . There is no delay between $o(\mathbf{x}_1, t')$ and $e(\mathbf{x}_1, t')$, and so only after computing the former can we compute $o(\mathbf{x}_2, t')$, which depends on the latter. Then we can compute $o(\mathbf{x}_3, t')$, which depends on $o(\mathbf{x}_1, t')$ and $o(\mathbf{x}_2, t')$ through $e(\mathbf{x}_1, t')$ and $e(\mathbf{x}_2, t')$, and so on. This sequential dependency chain is the reason it is difficult to parallelize a modulator using scanning computability.

The result of optimizing the example loop filter with the support of Figure 4.8 is shown in Figure 4.4. The scanning loop filter results in better performance than the time-skewed filter, if only slightly. In three dimensions and for larger arrays the disparity would likely be larger. It was found empirically that adding time skew to the scanning system did not improve performance for the example design, although it might prove useful for other geometries.

Special Case: Factorable

In general there exists no simple transformation to convert a scanning-computable system into a strictly causal one for the sake of parallelism. (Although for some special cases some parallelism may be achieved this way). However, we can decompose a scanning-computable impulse response into its strictly causal and time-zero components,

$$\boxed{\underline{\mathbf{g}}(d\mathbf{x}, t; -\mathbf{x}') = \underline{\mathbf{g}}_c(d\mathbf{x}, t; -\mathbf{x}') + \underline{\mathbf{g}}_z(d\mathbf{x}; -\mathbf{x}')\delta(dt)}, \quad (4.41)$$

	$x = -2.5d$				$x = -1.5d$				$x = -0.5d$			
	$t = 0$	T	$2T$...	$t = 0$	T	$2T$...	$t = 0$	T	$2T$...
$x' = -2.5d$	•	X	X	...	X	X	X	...	X	X	X	...
$-1.5d$	0	X	X	...	•	X	X	...	X	X	X	...
$-0.5d$	0	X	X	...	0	X	X	...	•	X	X	...
$0.5d$	0	X	X	...	0	X	X	...	X	X	X	...
$1.5d$	0	X	X	...	0	X	X	...	X	X	X	...
$2.5d$	0	X	X	...	X	X	X	...	X	X	X	...

	$x = 0.5d$				$x = 1.5d$				$x = 2.5d$			
	$t = 0$	T	$2T$...	$t = 0$	T	$2T$...	$t = 0$	T	$2T$...
$x' = -2.5d$	X	X	X	...	X	X	X	...	X	X	X	...
$-1.5d$	X	X	X	...	X	X	X	...	0	X	X	...
$-0.5d$	0	X	X	...	0	X	X	...	0	X	X	...
$0.5d$	•	X	X	...	0	X	X	...	0	X	X	...
$1.5d$	X	X	X	...	•	X	X	...	0	X	X	...
$2.5d$	X	X	X	...	X	X	X	...	•	X	X	...

Figure 4.8: A representation of the support regions for the scanning loop and noise-shaping filter measure components $\underline{g}(d\mathbf{x}, dt; -\mathbf{x}')$ and $\underline{h}(d\mathbf{x}, dt; -\mathbf{x}')$. An entry of “X” indicates an independent optimization variable, while an entry of “•” indicates an entry that is 0 in g and 1 in h .

where $\underline{g}_z(d\mathbf{x}; -\mathbf{x}') \triangleq \underline{g}(d\mathbf{x}, 0; -\mathbf{x}')$. Now the time-zero response can be moved into the definition of the quantizer, as was done in [44]. No longer a simple memoryless quantizer, now it becomes a spatial $\Delta\Sigma$ modulator (as for image halftoning) with loop filter \underline{g}_z . While in this case the quantizer is sequential and the parallelization approach in [44] appears limited to small designs, the remaining loop filter (which in most cases contains the bulk of the total computation) is strictly causal.

A convenient special case of scanning computability results from applying the strictly-causal special case of independent temporal modulators to the decomposition of (4.41). Consider the spatio-temporal $\Delta\Sigma$ system shown in Figure 4.9, where a spatial-only modulator with loop filter $\underline{g}_z(d\mathbf{x}; -\mathbf{x}')$ (the time-zero response) is nested within a temporal-only modulator with strictly causal loop filter ${}_T\underline{g}_t(dt)$. This is the approach that was taken in [26], with the spatial portion of the modulator implemented as if a finite-length temporal modulator (thus further restricting the loop filter in ways that are of no particular interest

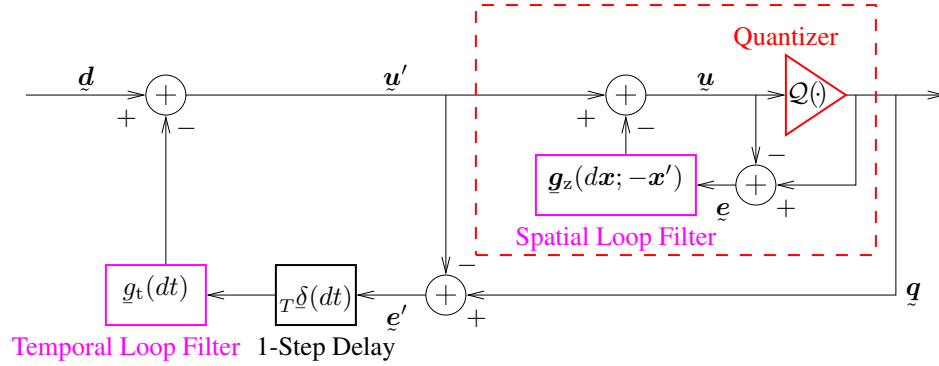


Figure 4.9: A factorable spatio-temporal modulator architecture where the nested inner spatial modulator serves as the quantizer for the outer temporal modulator.

here) . The inner spatial modulator acts as the quantizer for the outer temporal modulator.

Paralleling the analysis of Section 4.1, we first analyze the outer loop to find that

$$\underline{q}(d\mathbf{x}, dt) = \underline{u}'(d\mathbf{x}, dt) + \underline{e}'(d\mathbf{x}, dt) \quad (4.42a)$$

$$= \underline{d}(d\mathbf{x}, dt) - (\underline{g}_t * \underline{e}')(d\mathbf{x}, dt) + \underline{e}'(d\mathbf{x}, dt) \quad (4.42b)$$

$$= \underline{d}(d\mathbf{x}, dt) + (\underline{h}_t * \underline{e}')(d\mathbf{x}, dt), \quad (4.42c)$$

where the temporal noise-shaping measure is

$$\underline{h}_t(dt) \triangleq \underline{\delta}(dt) - \underline{g}_t(dt). \quad (4.43)$$

Next we analyze the inner loop, and find that

$$\underline{q}(d\mathbf{x}, dt) = \underline{u}(d\mathbf{x}, dt) + \underline{e}(d\mathbf{x}, dt) \quad (4.44a)$$

$$= \underline{u}'(d\mathbf{x}, dt) - (\underline{g}_z \square \underline{e})(d\mathbf{x}, dt) + \underline{e}(d\mathbf{x}, dt) \quad (4.44b)$$

$$= \underline{u}'(d\mathbf{x}, dt) + (\underline{h}_z \square \underline{e})(d\mathbf{x}, dt), \quad (4.44c)$$

where the spatial noise-shaping measure is

$$\underline{h}_z(\mathbf{x}; -\mathbf{x}') \triangleq \underline{\delta}_{\mathbf{x}'}(d\mathbf{x})\mathbf{I} - \underline{g}_z(d\mathbf{x}; -\mathbf{x}'). \quad (4.45)$$

Comparing (4.42a) and (4.44c), we see that

$$\underline{e}'(d\mathbf{x}, dt) = (\underline{h}_z \square \underline{e})(d\mathbf{x}, dt),$$

and substituting into (4.42c) yields

$$\underline{\mathbf{g}}(d\mathbf{x}, dt) = \underline{\mathbf{d}}(d\mathbf{x}, dt) + (\underline{\mathbf{h}} \boxtimes \underline{\mathbf{e}})(d\mathbf{x}, dt)$$

where the overall noise-shaping measure is

$$\boxed{\underline{\mathbf{h}}(d\mathbf{x}, dt; -\mathbf{x}') = \underline{\mathbf{h}}_z(d\mathbf{x}; -\mathbf{x}')\underline{\mathbf{h}}_t(dt)}, \quad (4.46)$$

the product of the spatial and temporal noise-shaping measures. This is indeed a special case of (4.41), as shown by solving for the single equivalent loop filter measure $\underline{\mathbf{g}}$ using (4.3):

$$\begin{aligned} \underline{\mathbf{g}}(d\mathbf{x}, dt; -\mathbf{x}') &= {}_{\mathbf{x}'}\underline{\delta}(d\mathbf{x})\underline{\delta}(dt)\mathbf{I} - \underline{\mathbf{h}}(d\mathbf{x}, dt; -\mathbf{x}') \\ &= {}_{\mathbf{x}'}\underline{\delta}(d\mathbf{x})\underline{\delta}(dt)\mathbf{I} - \underline{\mathbf{h}}_z(d\mathbf{x}; -\mathbf{x}')(\underline{\delta}(dt) - {}_T\underline{g}_t(dt)). \end{aligned}$$

Combining terms yields

$$\boxed{\underline{\mathbf{g}}(d\mathbf{x}, dt; -\mathbf{x}') = \underline{\mathbf{h}}_z(d\mathbf{x}; -\mathbf{x}'){}_T\underline{g}_t(dt) + \underline{\mathbf{g}}_z(d\mathbf{x}; -\mathbf{x}')\underline{\delta}(dt)}.$$

Comparing to (4.41) we see that this is indeed a special case, where the causal part of the equivalent loop filter is the product of the spatial noise-shaping measure and the temporal loop filter and the time-zero component is just the inner spatial loop filter. Because the noise-shaping measure factors, we call this *factorable computability*. Although the nested structure reduces the computational load relative to the general scanning case, it doesn't simplify parallelization significantly as the spatial quantizer is still inherently sequential.

In the example design problem, $\underline{\mathbf{g}}_z$ and \underline{g}_t cannot be optimized simultaneously using SOCP, because the constraints on the combined loop filter are no longer convex. Instead, first the temporal loop-filter was designed, and then the spatial loop filter was optimized taking the (now fixed) temporal response into account. The result is shown in Figure 4.4. The added spatial modulation has improved performance slightly over the case of temporal-only modulation. Like the temporal-only case, here noise is necessarily suppressed outside of the signal band and the Helmholtz cone due to the factorization of the filter.

4.4 Example Simulation

In the preceding section five potential loop-filter designs were compared. In this section we take a closer look at the scanning-computable design, and compare the theoretical results of Section 4.1 to a numerical simulation. A similar transmit-array system that was built and tested is described in [30].

The composite NTF for the example design with scanning computability was shown in Figure 4.4, but it is interesting to look at the component responses. The six optimized NTF component responses $\{H(\mathbf{v}, f; -\mathbf{x}')\}$, for $\mathbf{x}' \in \mathcal{L}$, are plotted in Figure 4.10 as functions of spatial frequency component v_x and temporal frequency f . We can see that in this design, with its short array, the component frequency responses are each distinct, with the responses corresponding to the errors at the end positions showing the greatest deviation from the average. The middle four responses are reasonably similar, and in a system with a longer array we could reasonably expect that filters corresponding to errors away from the array ends would look quite similar. These differences are due to the different support of each component, which was shown in Figure 4.8.

To demonstrate the operation of the modulator and compare the simulated response to the theory, three input signals were generated, and the modulator output was computed. Since wideband signals would obscure the noise spectrum, the inputs were sinusoids with frequencies $\{0.21f_s, 0.25f_s, 0.29f_s\}$. Since these inputs are narrowband, wideband beamforming is unnecessary. Because the array is so short, the mainbeam covers nearly all directions, and so elaborate sidelobe constraints are largely pointless. Thus the sinusoids were steered to azimuth directions $\{-45^\circ, 0^\circ, 45^\circ\}$, respectively, using simple time-delay steering:

$$B_k(\mathbf{x}, f) = e^{-j2\pi\mathbf{x}\cdot\hat{\mathbf{x}}_k f/c}, \quad k = 1, \dots, 3.$$

Figure 4.11 shows both the spatio-temporal power spectrum predicted by (4.8b) and the simulated spectrum computed at the quantizer output. As we can see, the approximation is

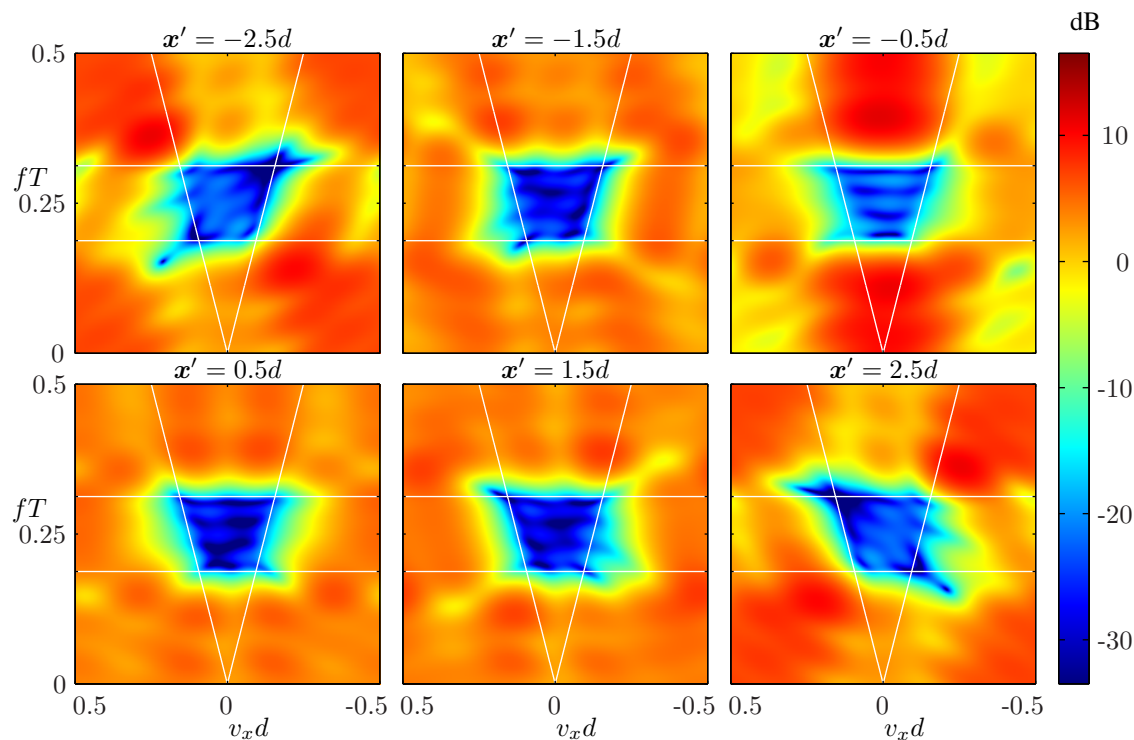


Figure 4.10: Component noise transfer functions for six-element array example.

quite good, validating the assumption on the noise statistics. The color scale is set to allow a direct comparison between the component responses of Figure 4.10 and the noise spectra of Figure 4.11, which is proportional to the average of the component responses. The three beamformed signals show up as the three horizontal streaks across the passband.

We can also look at the power spectrum seen in the far field, after propagation has removed the noise power outside of the Helmholtz cone. To better show the noise shaping, temporal filtering is not simulated here. Figure 4.12 shows the theoretical spectrum of (4.19a) overlaid on the simulated spectrum for azimuth angles corresponding to the steering directions of the three input sinusoids. (Because the array is so short, significant power is transmitted from all inputs in each of the directions, but we can verify that the appropriate signal dominates in each direction.)

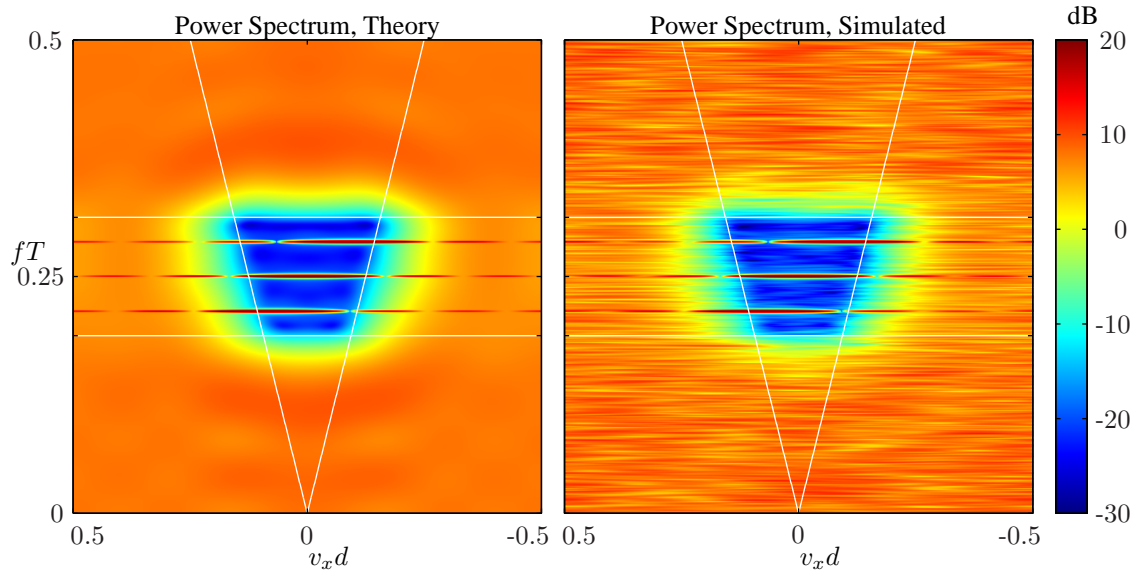


Figure 4.11: Theoretical and simulated power spectra at the quantizer output for six-element example.

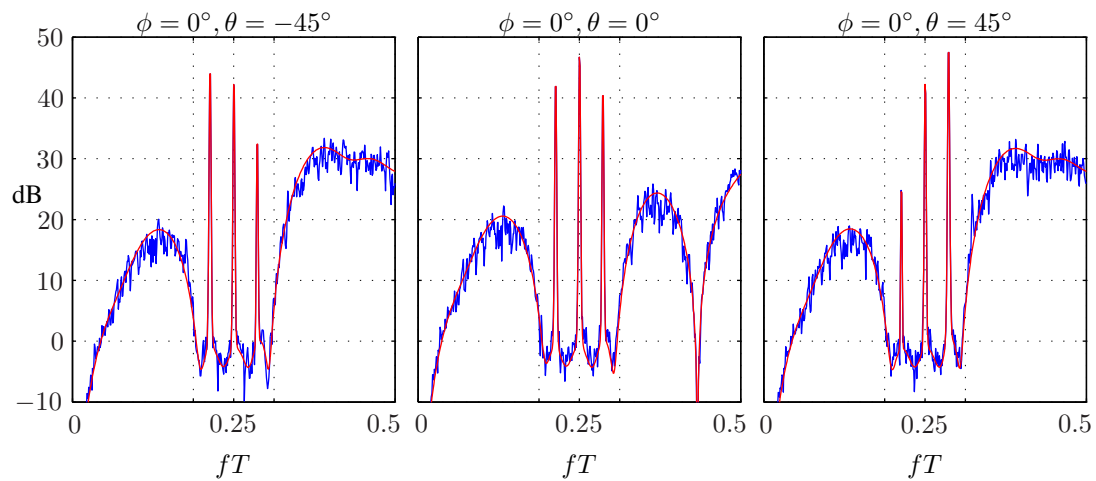


Figure 4.12: **Theoretical** and **simulated** far-field power spectra at selected azimuth angles.

4.5 Summary

In this chapter $\Delta\Sigma$ modulation was extended to perform joint quantization noise shaping in spatial and temporal frequency, specifically for use in converting transmit antenna array signals. By incorporating the spatial dimension, greater performance or lower clock rates can be achieved relative to temporal-only noise shaping. As in the temporal case,

the modulator outputs are coarsely quantized, and thus the output electronics required (a linear pulse modulator) can in principle be simpler than a linear amplifier. The relationship between the shaped quantization noise and the loop filter is somewhat more complicated than in a temporal-only $\Delta\Sigma$ modulator, and so a large part of the chapter was dedicated to establishing the relationship and using SOCP to optimize the loop filter.

Critical issues remain to be worked out to make spatio-temporal $\Delta\Sigma$ arrays practical. Spatial oversampling of antenna elements necessarily results in elements that are small (relative to a wavelength) and closely spaced. In general this results in elements with small radiation resistance but high reactance. The elements used in [30], for example, had impedances at the nominal signal frequency of approximately $(0.5 + j200) \Omega$. In addition, the elements will typically exhibit a great deal of mutual coupling. This is a very stressing environment for the driver electronics and is quite different than that seen in a conventional array. The driver needs to be able to handle highly reactive loads efficiently and without distortion. In addition, the computational requirements for real-time implementation are quite high for nontrivial arrays. That the bulk of the computation occurs in a nonlinear feedback loop increases the challenge considerably.

Chapter 5.

Summary and Conclusions

Antenna arrays are increasingly used to achieve greater performance and flexibility than a monolithic antenna can deliver. Applications ranging from radar to cellular phone base stations to consumer-grade WiFi routers now use arrays. Existing transmit antenna arrays are mostly limited to transmitting a single constant-envelope signal per element (or per amplifier), because efficiency currently dictates the use of nonlinear amplification. For such arrays to realize their full potential, allowing multiple simultaneous signals to be transmitted, requires high-power linear D/A conversion of RF signals. This enables not just aperture sharing, but also far more control over the wideband array pattern. To take advantage of this flexibility, wideband array patterns can be designed using optimization to maximize gain subject to constraints on passband flatness and sidelobes.

A candidate approach for high-power linear D/A conversion is quantization noise shaping, also known as $\Delta\Sigma$ modulation, combined with a high-power output pulse modulator. The $\Delta\Sigma$ modulator consists of a feedback loop around a low-resolution quantizer, where the loop filter is designed to spectrally shape the quantization noise away from the signal band to improve the SNR. Noise shaping achieves high linearity by converting the high-resolution input signal into a low-resolution output, potentially simplifying the output circuit. Rather than requiring linear amplification, the output must perform linear pulse modulation. In its simplest form, the output circuit is a high-power switch. A major draw-

back of conventional $\Delta\Sigma$ modulation is that the signal band is much less than the clock rate, and so very high clock rates are required for wide bandwidths. One approach to reduce the clock-rate requirements in an array is to use spatio-temporal $\Delta\Sigma$ modulation to jointly shape the quantization noise in temporal and spatial frequency. The increased dimensionality provides more “room” in which to push the quantization noise by taking advantage of spatial oversampling in the array.

In this dissertation both the theory and optimization of wideband array patterns and the theory and design of spatio-temporal noise-shaped arrays were considered. A brief recap of the major results from each chapter follows.

In Chapter 2, the measure-signal representation used throughout the dissertation was introduced, including representations of deterministic and random signals and linear shift-invariant and shift-varying filtering. This somewhat nonstandard signals and systems framework was chosen to unify the usual engineering representations for discrete and continuous-time and discrete and continuous-space signals, which generally require multiple special-case definitions for each operation depending on the combination of input types. Also in this chapter, $\Delta\Sigma$ modulation was introduced and analyzed in some detail. It was shown that $\Delta\Sigma$ modulation spectrally shapes the errors due to a coarse quantizer, allowing for high performance within a defined signal band. This analysis was performed for both random and deterministic inputs, and it was shown that for finite-length signals the noise shaping performance depends not just on the loop filter and the signal bandwidth, but on the signal duration as well. Although $\Delta\Sigma$ modulation is already widely used for low-speed D/A conversion, its suitability for RF applications is limited by the high clock speeds required. This in turn suggests reducing temporal oversampling in exchange for spatial oversampling in a spatio-temporal $\Delta\Sigma$ modulator, the subject of Chapter 4.

Chapter 3 first introduced several potential wideband transmit array architectures, and showed how a single passband-equivalent model could represent each. This equivalent model was then analyzed to relate the output current density back to the input signals. The

far-field electric field was determined from the current density, and was also related back to the input signals. Based on this analysis the wideband array pattern was defined, and it was shown that in the case of identical elements that the array pattern factored into an element pattern and an array factor. This analysis was done for both deterministic and random inputs. It was shown that the array pattern is partitioned by the laws of wave propagation into propagating (visible) and nonpropagating (invisible) regions. The former is defined by the Helmholtz equation, and represents a cone in four-dimensional space-time. Expressions for wideband directivity, efficiency, and gain were derived, and example optimizations were performed to maximize each. It was shown the maximizing directivity led to a completely impractical design, and that maximizing efficiency led to the classic time-delay solution. Gain was determined to be the appropriate measure to maximize, as this allows better performance than the classic solution. Additional constraints on passband flatness and sidelobe levels were derived and used in examples.

In Chapter 4 the array model of Chapter 3 was extended to include a spatio-temporal $\Delta\Sigma$ modulator. It was shown that this adds a shaped-noise term at the quantizer output and in the far field. By making basic assumptions on the quantization-noise statistics, expressions for the shaped noise were derived as a function of the loop filter. It was shown that the loop filter could be optimized to minimize noise power in the signal band, subject to constraints on stability and computability. A general constraint to ensure computability was derived, and several special cases were considered based on ease of implementation and the potential for parallel computation. An example design was optimized for each computability constraint of interest to compare the performance of each. It was shown that several special cases resulted in improved performance over using independent temporal $\Delta\Sigma$ modulators. Finally, the output was computed for an example array to verify the noise spectrum matched the theoretical result.

Although the focus here was on antenna arrays, some intriguing potential non-array uses for spatio-temporal noise shaping exist. Propagating sound waves, although longitu-

dinal rather than transverse, also obey a Helmholtz-like restriction on spatial frequency as a function of propagation speed and temporal frequency. Thus speaker arrays for audio or sonar might also employ spatio-temporal noise shaping (as suggested in [26]). The use of spatial $\Delta\Sigma$ modulation for halftoning suggests that spatio-temporal $\Delta\Sigma$ could be used for video halftoning, for applications with binary pixels such as scoreboards, bank signs, or simple computing displays.

Appendix A.

Glossary of Symbols

Sets

- \mathbb{B} The Borel sets
- \mathbb{C} The set of complex numbers
- \mathbb{N} The set of positive integers
- \mathbb{R} The set of real numbers
- \mathbb{Z} The set of integers

Constants

- c The speed of light in free space: 2.998×10^8 m/s
- η The impedance of free space, 376.73Ω , see equation (3.54), page 83
- j $\sqrt{-1}$
- μ_0 The permeability of free space: $4\pi \times 10^{-7}$ Wb/A.m
- $\hat{\phi}$ Direction of increasing elevation, see equation (D.1), page 173
- $\hat{\theta}$ Direction of increasing azimuth, see equation (D.1), page 173

Functions and Measures

- $1_{\mathcal{T}}$ The indicator function for set \mathcal{T} , see equation (2.8), page 17
- $\vec{\alpha}$ The vector potential, see equation (3.11), page 61
- $\vec{\mathcal{A}}$ The temporal Fourier transform of the vector potential, see equation (3.14), page 62
- $\vec{\mathbf{A}}$ The wideband array pattern, see equation (3.24), page 66
- $\vec{\mathbf{A}}_{\text{el}}$ The wideband element pattern, see equation (3.26), page 66
- \mathbf{b} passband-equivalent beamformer response, see equation (3.1), page 56
- δ The Dirac delta measure, see equation (2.8), page 17
- \mathbf{d} Beamformer output, see equation (3.2), page 56
- \mathcal{D}_{nb} Narrowband directive gain, see equation (3.66), page 86
- \mathcal{D} Wideband directive gain, see equation (3.69), page 87
- $\mathcal{D}_{\text{nb}0}$ Narrowband directivity, see equation (3.68), page 87
- \mathcal{D}_0 Wideband directivity, see equation (3.72), page 88
- $\vec{\mathbf{e}}$ The electric field, see equation (3.19), page 64
- ϵ Quantization error, see equation (4.2), page 116
- ξ Efficiency, see equation (3.88), page 96
- $\vec{\mathcal{E}}$ The temporal Fourier transform of the electric field, see equation (3.20), page 64
- $\vec{\mathcal{E}}_{\text{H}}$ Horizontal component of electric field, see equation (3.31), page 71
- $\vec{\mathcal{E}}_{\text{V}}$ Vertical component of electric field, see equation (3.31), page 71
- \mathcal{G}_0 Wideband gain, see equation (3.91), page 100

- $\Gamma_{\hat{x}}$ Projection matrix normal to unit-vector \hat{x} , see equation (3.20), page 64
- \underline{h}_A Passband-equivalent response of DAC and analog filters, page 56
- \underline{i} Drive-current distribution, see equation (3.4), page 57
- $\underline{\vec{j}}$ Element-current distribution, see equation (3.9), page 59
- \vec{J} Spatio-temporal Fourier transform of the current density, see equation (3.10), page 59
- ϱ Loop-filter output, page 116
- ρ Free-space propagation measure, see equation (3.12), page 61
- \mathcal{P}_{in} Input power, see equation (3.78), page 93
- $\mathcal{P}_{\text{loss}}$ Lost power, see equation (3.85), page 95
- \mathcal{P}_{rad} Total radiated power, see equation (3.60), page 84
- \underline{q} Quantizer output, see equation (4.2), page 116
- \underline{s} $N \times 1$ passband-equivalent beamformer input vector, page 55
- \underline{s}_A Equivalent D/A-converted input signal, see equation (3.3), page 57
- \underline{u} Quantizer input, see equation (4.1), page 116
- \mathcal{U}_{avg} Average radiation power intensity, see equation (3.56), page 84
- \mathcal{U}_{exp} Expected radiation power intensity, see equation (3.61), page 85
- \mathcal{U} Radiation power spectral intensity, see equation (3.58), page 84
- \underline{v} Driver output voltage, see equation (3.5), page 57
- \underline{z} Resistance distribution, see equation (3.76), page 92
- \underline{Z} Impedance measure, page 92

Operators

- Spatial convolution, see equation (2.17), page 24
- * Temporal convolution, see equation (2.17), page 24
- ⊗ Spatio-temporal convolution, see equation (2.17), page 24
- Linear shift-varying spatial filtering operation, see equation (2.19), page 25
- ⊠ Linear space-varying, time-invariant filtering operation, see equation (2.22), page 26
- $(\cdot)^\dagger$ Spatial adjoint operator, see equation (2.1), page 12
- $(\cdot)^\ddagger$ Temporal adjoint operator, see equation (2.2), page 12
- $(\cdot)^\ddagger$ Spatio-temporal adjoint operator, see equation (2.3), page 12
- \triangleq Defined as
- $\text{Tr}[\cdot]$ Matrix trace, see equation (2.4), page 13
- $\hat{\cdot}$ Unit vector operator, see equation (2.5), page 13

Appendix B.

Selected Measure Signal and Systems

Derivations

B.1 Multidimensional Fourier Series for Signals with Lattice Support

Let $\mathcal{L} = \Lambda\mathbb{Z}^M$ be a lattice in \mathbb{R}^N , where $N \times M$ generating matrix Λ has linearly independent columns. The Fourier transform of a signal $\mathbf{a}(d\mathbf{x})$ with support on \mathcal{L} has the form

$$\begin{aligned}\mathbf{a}(\mathbf{v}) &= \int e^{-j2\pi\mathbf{v}\cdot\mathbf{x}} \mathbf{a}(\mathbf{x}) \Sigma_{\mathcal{L}}(d\mathbf{x}) \\ &= \sum_{\mathbf{x} \in \Lambda\mathbb{Z}^M} e^{-j2\pi\mathbf{v}\cdot\mathbf{x}} \mathbf{a}(\mathbf{x}).\end{aligned}$$

This is invariant to translation by \mathbf{v}' if $\mathbf{v}' \cdot \mathbf{x} \in \mathbb{Z}$ for all $\mathbf{x} \in \Lambda\mathbb{Z}^M$, or equivalently if $\Lambda^T \mathbf{v}' \in \mathbb{Z}^M$. Let $\Lambda^+ = (\Lambda^T \Lambda)^{-1} \Lambda^T$ be the Moore-Penrose pseudo-inverse of Λ . Further let the columns of Λ^\perp be an orthonormal basis for the nullspace of Λ^T , so that the columns of the matrix (Λ, Λ^\perp) form a basis for \mathbb{R}^N . Then $\mathbf{a}(\mathbf{v}) = \mathbf{a}(\mathbf{v} - \mathbf{v}')$ if $\mathbf{v}' \in \Lambda^{+T} \mathbb{Z}^M + \Lambda^\perp \mathbb{R}^{N-M}$. In words, the Fourier transform is constant on translations by elements of the *dual lattice* $\Lambda^{+T} \mathbb{Z}^M$ of the $N - M$ dimensional subspace spanned by the columns of Λ^\perp . Thus the Fourier transform is periodic, with the spectral “period”

defined by any set of coset representatives $[\Lambda\mathbb{R}^M/\Lambda^+T\mathbb{Z}^M]$. Once the Fourier transform is defined on one period, it is defined everywhere. We compute the Fourier series coefficients by integrating over one period of the function. Since the period has zero volume in \mathbb{R}^N for $M < N$, we need to take care in defining the integral. The simplest way is to define $\underline{\mu}_{[\Lambda\mathbb{R}^M/\Lambda^+T\mathbb{Z}^M]}$ as the uniform probability measure over one spectral period. The general Fourier series result is thus

$$\underline{\mathbf{a}}(d\mathbf{x}) = \left(\int e^{j2\pi\mathbf{v}\cdot\mathbf{x}} \mathbf{a}(\mathbf{v}) \underline{\mu}_{[\Lambda\mathbb{R}^M/\Lambda^+T\mathbb{Z}^M]}(d\mathbf{v}) \right)_{\Sigma_{\Lambda\mathbb{Z}^M}}(d\mathbf{x}), \quad (\text{B.1})$$

where we integrate with respect to a probability measure because it has unit total measure and support on one period, and not because any randomness is involved. When $M = N$ then Λ is full rank, $\Lambda^+ = \Lambda^{-1}$, and Λ^\perp is empty. In this case the spectral period can be written $[\mathbb{R}^N/\Lambda^{-T}\mathbb{Z}^N]$, which has volume $|\Lambda|^{-1}$ in \mathbb{R}^N . Thus the probability measure reduces to $\underline{\mu}_{[\mathbb{R}^N/\Lambda^{-T}\mathbb{Z}^N]}(d\mathbf{v}) = |\Lambda|^{-1} 1_{[\mathbb{R}^N/\Lambda^{-T}\mathbb{Z}^N]} d\mathbf{v}$, and the integral reduces to a volume integral over one period:

$$\underline{\mathbf{a}}(d\mathbf{x}) = \left(|\Lambda| \int_{[\mathbb{R}^N/\Lambda^{-T}\mathbb{Z}^N]} e^{j2\pi\mathbf{v}\cdot\mathbf{x}} \mathbf{a}(\mathbf{v}) d\mathbf{v} \right)_{\Sigma_{\Lambda\mathbb{Z}^N}}(d\mathbf{x}). \quad (\text{B.2})$$

B.2 Sampling

Sampling is the process of converting a continuous-space and/or time signal into a discrete-space/time one. Given a continuous-time signal measure with differential form $\underline{a}(dt) = a(t)dt$ and a set of sample times \mathcal{D} , the sampled signal is formed by multiplying the Radon-Nikodym derivative times the *sampling differential* $\Sigma_{\mathcal{D}}(dt)$:

$$\underline{a}_{\mathcal{D}}(dt) = a(t) \Sigma_{\mathcal{D}}(dt). \quad (\text{B.3})$$

We wish to determine the Fourier transform property of sampling for two cases: where \mathcal{D} is finite but arbitrary, and where \mathcal{D} is a lattice. If \mathcal{D} is finite, then we start with (B.3) and

assume that density $a(t)$ can be represented as an inverse transform:

$$\begin{aligned} A_{\mathcal{D}}(f) &= \int e^{-j2\pi ft} a(t) \underline{\Sigma}_{\mathcal{D}}(dt) \\ &= \int e^{-j2\pi ft} \int A(f') e^{j2\pi f' t} df' \underline{\Sigma}_{\mathcal{D}}(dt) \\ &= \int A(f') \int e^{-j2\pi(f-f')t} \underline{\Sigma}_{\mathcal{D}}(dt) df'. \end{aligned}$$

If \mathcal{D} was infinite then the inner integral in the last line would not exist. Denoting the Fourier transform of the sampling measure as $\chi_{\mathcal{D}}$ and performing a change of variable, this becomes

$$\begin{aligned} A_{\mathcal{D}}(f) &= \int A(f-f') \chi_{\mathcal{D}}(f') df' \\ A_{\mathcal{D}}(f) &= \int A(f-f') \underline{\chi}_{\mathcal{D}}(df'). \end{aligned} \tag{B.4}$$

a convolution of the original signal transform with the sampling measure transform.

In the common case of uniform temporal sampling where $\mathcal{D} = T\mathbb{Z}$, it is convenient to use the normalized sampling differential $T\underline{\Sigma}_{T\mathbb{Z}}(dt)$. Here the Fourier integral with respect to the sampling differential is not defined, so we take a slightly different approach. Assume $a(t)$ and $A(f)$ form a transform pair, and sample $a(t)$ as before to get

$$\begin{aligned} \underline{a}_{\mathcal{D}}(T) &= T a(t) \underline{\Sigma}_{T\mathbb{Z}}(dt) \\ &= T \sum_n a(nT) \underline{nT} \underline{\delta}(dt). \end{aligned}$$

This is a discrete-time signal with periodic Fourier transform

$$\begin{aligned} A_{\mathcal{D}}(f) &= \int e^{-j2\pi ft} \underline{a}_{\mathcal{D}}(dt) \\ &= T \sum_n a(nT) e^{-j2\pi fnT}, \end{aligned}$$

or equivalently $\{Ta(nT)\}$ are Fourier series coefficients of the periodic function $A_{\mathcal{D}}(f)$. (The sign in the exponential of the Fourier series representation has been negated here and below to match the usual engineering convention for forward and inverse transforms.) We wish to relate this periodic spectrum to the Fourier transform $A(f)$ of the original signal.

Start with the inverse Fourier relation, and split the integral over \mathbb{R} into integrals over contiguous intervals:

$$\begin{aligned}
Ta(nT) &= T \int A(f) e^{j2\pi f n T} df \\
&= T \sum_k \int_{\left[\frac{k}{T}, \frac{k+1}{T}\right)} A(f) e^{j2\pi f n T} df \\
&= T \sum_k \int_{\left[0, \frac{1}{T}\right)} A(f - k/T) e^{j2\pi(f - k/T)nT} df \\
&= T \int_{\left[0, \frac{1}{T}\right)} \sum_k A(f - k/T) e^{j2\pi f n T} df.
\end{aligned}$$

In the last line we see that in fact $\{Ta(nT)\}$ are also the Fourier series coefficients of the periodic function $\sum_k A(f - k/T)$. Thus

$$A_{\mathcal{D}}(f) = \sum_{k \in \mathbb{Z}} A(f - k/T), \quad (\text{B.5})$$

confirming the familiar spectral-replication property of sampling. Note that we can write (B.5) as

$$A_{\mathcal{D}}(f) = \int A(f - f') \Sigma_{T^{-1}\mathbb{Z}}(df'), \quad (\text{B.6})$$

the convolution of the original spectrum $A(f)$ and counting measure $\Sigma_{T^{-1}\mathbb{Z}}$. Comparing this to (B.4) suggests that, in a limited sense, the measures $T\Sigma_{T\mathbb{Z}}$ and $\Sigma_{T^{-1}\mathbb{Z}}$ form a Fourier transform pair. This is just a somewhat more careful restatement of the conventional engineering assertion that

$$T \sum_k \delta(t - kT) \xleftrightarrow{\text{F.T.}} \sum_k \delta(f - k/T),$$

a claim which is made almost exclusively in the discussion of sampling.

For N -dimensional spatial sampling this generalizes to sampling on a lattice $\Lambda\mathbb{Z}^N$. Now the normalized sampling differential is $|\Lambda|_{\Sigma_{\Lambda\mathbb{Z}^N}}(d\mathbf{x})$ and the corresponding spectral property is

$$a_{\Lambda}(\mathbf{v}) = \sum_{\mathbf{k} \in \mathbb{Z}^N} a(\mathbf{v} - \Lambda^{-T}\mathbf{k}). \quad (\text{B.7})$$

We can again assert a limited Fourier transform relationship between the measures $|\Lambda|_{\Sigma_{\Lambda\mathbb{Z}^N}}$ and $\Sigma_{\Lambda^{-T}\mathbb{Z}^N}$.

B.3 The Crosscorrelation of Linearly Filtered Processes

Let spatio-temporal vector random signals $\underline{\mathbf{a}}$ and $\underline{\mathbf{b}}$ be spatially nonstationary with reference measures $\underline{\mu}_{\mathbf{a}}$ and $\underline{\mu}_{\mathbf{b}}$, and temporally wide-sense stationary with respect to reference measure $\underline{\mu}$. Create the processes $\underline{\mathbf{a}}' = \underline{\mathbf{g}} \boxtimes \underline{\mathbf{a}}$ and $\underline{\mathbf{b}}' = \underline{\mathbf{h}} \boxtimes \underline{\mathbf{b}}$ through linear filtering, where $\underline{\mathbf{a}}'$ and $\underline{\mathbf{b}}'$ have spatial reference measures $\underline{\mu}_{\mathbf{a}'}$ and $\underline{\mu}_{\mathbf{b}'}$ and we can write the filter measures as $\underline{\mathbf{h}}(d\mathbf{x}, t; -\mathbf{x}')\underline{\nu}(dt)$ and $\underline{\mathbf{g}}(d\mathbf{x}, t; -\mathbf{x}')\underline{\omega}(dt)$. We wish to find the cross-correlation $\underline{\mathbf{r}}_{\mathbf{a}', \mathbf{b}'}$ in terms of $\underline{\mathbf{r}}_{\mathbf{a}, \mathbf{b}}$. We will require that $\underline{\mathbf{a}}'$ and $\underline{\mathbf{b}}'$ also have the same reference measure, which results in two possibilities for the relationship between reference measures $\underline{\mu}$, $\underline{\nu}$, and $\underline{\omega}$, which we will consider in turn.

Case 1: $\underline{\mu}$ is shift-invariant with respect to both $\underline{\nu}$ and $\underline{\omega}$. In this case, both $\underline{\mathbf{a}}'$ and $\underline{\mathbf{b}}'$ have reference measure $\underline{\mu}$, as shown in (2.18). Starting from the definition, we have

$$\begin{aligned}
 \underline{\mathbf{r}}_{\mathbf{a}', \mathbf{b}'}(\mathcal{X} \times \mathcal{Y} \times \mathcal{T}) &= \int_{\mathcal{T}} \int_{\mathcal{Y}} \int_{\mathcal{X}} \mathcal{E} \left\{ \underline{\mathbf{a}}'(\mathbf{x}, t) \underline{\mathbf{b}}'^H(\mathbf{y}, t - \tau) \right\} \underline{\mu}_{\mathbf{a}'}(d\mathbf{x}) \underline{\mu}_{\mathbf{b}'}(d\mathbf{y}) \underline{\mu}(d\tau) \\
 &= \int_{\mathcal{T}} \int_{\mathcal{Y}} \int_{\mathcal{X}} \mathcal{E} \left\{ (\underline{\mathbf{g}} \boxtimes \underline{\mathbf{a}})(\mathbf{x}, t) \times \right. \\
 &\quad \left. (\underline{\mathbf{h}} \boxtimes \underline{\mathbf{b}})^H(\mathbf{y}, t - \tau) \right\} \underline{\mu}_{\mathbf{a}'}(d\mathbf{x}) \underline{\mu}_{\mathbf{b}'}(d\mathbf{y}) \underline{\mu}(d\tau) \\
 &= \int_{\mathcal{T}} \int_{\mathcal{Y}} \int_{\mathcal{X}} \mathcal{E} \left\{ \int_{\mathcal{T}} \int_{\mathcal{Y}} \int_{\mathcal{X}} \underline{\mathbf{g}}(\mathbf{x}, t'; -\mathbf{x}') \underline{\mathbf{a}}(\mathbf{x}', t - t') \underline{\mu}_{\mathbf{a}}(d\mathbf{x}') \underline{\mu}(dt') \times \right. \\
 &\quad \left. \int_{\mathcal{T}} \int_{\mathcal{Y}} \underline{\mathbf{b}}^H(\mathbf{y}', t - \tau - t'') \underline{\mathbf{h}}^H(\mathbf{y}, t''; -\mathbf{y}') \underline{\mu}_{\mathbf{b}}(d\mathbf{y}') \underline{\mu}(dt'') \right\} \times \\
 &\quad \underline{\mu}_{\mathbf{a}'}(d\mathbf{x}) \underline{\mu}_{\mathbf{b}'}(d\mathbf{y}) \underline{\mu}(d\tau) \\
 &= \int_{\mathcal{T}} \int_{\mathcal{Y}} \int_{\mathcal{X}} \underline{\mathbf{g}}(\mathcal{X}, t'; -\mathbf{x}') \underline{\mathbf{r}}_{\mathbf{a}, \mathbf{b}}(d\mathbf{x}', d\mathbf{y}', \tau - t' + t'') \times \\
 &\quad \underline{\mathbf{h}}^H(\mathcal{Y}, t''; -\mathbf{y}') \underline{\mu}(dt') \underline{\mu}(dt'') \underline{\mu}(d\tau)
 \end{aligned}$$

In the last line the conditions for Fubini's theorem are assumed to be satisfied, so that the expectation can be brought inside the integrals. Recalling (2.20) and (2.21), this simplifies to

$$\boxed{\underline{\mathbf{r}}_{\mathbf{a}', \mathbf{b}'}(\mathcal{X} \times \mathcal{Y} \times \mathcal{T}) = (\underline{\mathbf{g}} \boxtimes \underline{\mathbf{r}}_{\mathbf{a}, \mathbf{b}} \boxtimes \underline{\mathbf{h}}^\dagger)(\mathcal{X} \times \mathcal{Y} \times \mathcal{T})}. \quad (\text{B.8})$$

Case 2: $\underline{\nu} = \underline{\omega}$ and both are shift-invariant with respect to $\underline{\mu}$, but $\underline{\mu}$ is not shift-invariant with respect to $\underline{\nu}$. This guarantees that $\underline{\mu}$ is a discrete-time reference measure, because

Lebesgue measure is shift invariant with respect to all other reference measures. Let groups $\mathcal{M} = T\mathbb{Z}$ and \mathcal{V} be the support of $\underline{\mu} = \underline{\Sigma}_{T\mathbb{Z}}$ and $\underline{\nu}$, respectively. Here both $\underline{\mathbf{a}}'$ and $\underline{\mathbf{b}}'$ have temporal reference measure $\underline{\nu}$. A straightforward application of the cross-correlation definition as before will fail, because the expectation will not be a function of only the difference of the temporal arguments of the densities of $\underline{\mathbf{a}}$ and $\underline{\mathbf{b}}$. As defined, $\underline{\mathbf{a}}'$ and $\underline{\mathbf{b}}'$ are not stationary, but rather cyclostationary with period $[\mathcal{V}/\mathcal{M}]$. We borrow a standard approach from communication theory to remedy this, by assuming a random delay u to the outputs $\underline{\mathbf{a}}'$ and $\underline{\mathbf{b}}'$, where u is uniformly distributed over a period. This results in system outputs

$$\begin{aligned} \underline{\mathbf{a}}'(d\mathbf{x}, dt) &= \left(\int \int \underline{\mathbf{h}}(\mathbf{x}, t - t' - u; -\mathbf{x}') \underline{\mathbf{a}}(d\mathbf{x}', dt') \right) \underline{\mu}_{\mathbf{a}'}(d\mathbf{x}) \underline{\nu}(dt) \\ \underline{\mathbf{b}}'(d\mathbf{x}, dt) &= \left(\int \int \underline{\mathbf{g}}(\mathbf{x}, t - t' - u; -\mathbf{x}') \underline{\mathbf{b}}(d\mathbf{x}', dt') \right) \underline{\mu}_{\mathbf{b}'}(d\mathbf{x}) \underline{\nu}(dt) \end{aligned}$$

We find the corresponding cross-correlation in several stages. We start by invoking the definition, and expanding:

$$\begin{aligned} \underline{\mathbf{r}}_{\mathbf{a}', \mathbf{b}'}(\mathcal{X} \times \mathcal{Y} \times \mathcal{T}) &= \int_{\mathcal{T}} \int_{\mathcal{Y}} \int_{\mathcal{X}} \mathcal{E} \{ \underline{\mathbf{a}}'(\mathbf{x}, t - u) \underline{\mathbf{b}}'^H(\mathbf{y}, t - \tau - u) \} \underline{\mu}_{\mathbf{a}'}(d\mathbf{x}) \underline{\mu}_{\mathbf{b}'}(d\mathbf{y}) \underline{\nu}(d\tau) \\ &= \int_{\mathcal{T}} \int_{\mathcal{Y}} \int_{\mathcal{X}} \mathcal{E} \left\{ \int \int \underline{\mathbf{h}}(\mathbf{x}, t - t' - u; -\mathbf{x}') \underline{\mathbf{a}}(d\mathbf{x}', dt') \times \right. \\ &\quad \left. \int \int \underline{\mathbf{b}}^H(d\mathbf{y}', dt'') \underline{\mathbf{g}}^H(\mathbf{y}, t - \tau - t'' - u; -\mathbf{y}') \right\} \underline{\mu}_{\mathbf{a}'}(d\mathbf{x}) \underline{\mu}_{\mathbf{b}'}(d\mathbf{y}) \underline{\nu}(d\tau) \\ &= \int_{\mathcal{T}} \int_{\mathcal{Y}} \int_{\mathcal{X}} \mathcal{E} \left\{ \int \int \int \int \underline{\mathbf{h}}(\mathbf{x}, t - t' - u; -\mathbf{x}') \underline{\mathbf{a}}(\mathbf{x}', t') \underline{\mu}_{\mathbf{a}}(d\mathbf{x}') \underline{\mu}(dt') \times \right. \\ &\quad \left. \int \int \int \int \underline{\mathbf{b}}^H(\mathbf{y}', t'') \underline{\mathbf{g}}^H(\mathbf{y}, t - \tau - t'' - u; -\mathbf{y}') \underline{\mu}_{\mathbf{b}}(d\mathbf{y}') \underline{\mu}(dt'') \right\} \times \\ &\quad \underline{\mu}_{\mathbf{a}'}(d\mathbf{x}) \underline{\mu}_{\mathbf{b}'}(d\mathbf{y}) \underline{\nu}(d\tau). \end{aligned}$$

Splitting the space-time integrals in the last line will prove convenient shortly. Making the change of variable $t'' \rightarrow t' - t''$ and invoking the flip and shift-invariance of $\underline{\mu}$ yields

$$\begin{aligned} \underline{\mathbf{r}}_{\mathbf{a}', \mathbf{b}'}(\mathcal{X} \times \mathcal{Y} \times \mathcal{T}) &= \int_{\mathcal{T}} \int_{\mathcal{Y}} \int_{\mathcal{X}} \mathcal{E} \left\{ \int \int \int \int \underline{\mathbf{h}}(\mathbf{x}, t - t' - u; -\mathbf{x}') \underline{\mathbf{a}}(\mathbf{x}', t') \underline{\mathbf{b}}^H(\mathbf{y}', t' - t'') \times \right. \\ &\quad \left. \underline{\mathbf{g}}^H(\mathbf{y}, t - t' - u - \tau + t''; -\mathbf{y}') \underline{\mu}_{\mathbf{a}}(d\mathbf{x}') \underline{\mu}_{\mathbf{b}}(d\mathbf{y}') \underline{\mu}(dt') \underline{\mu}(dt'') \right\} \times \\ &\quad \underline{\mu}_{\mathbf{a}'}(d\mathbf{x}) \underline{\mu}_{\mathbf{b}'}(d\mathbf{y}) \underline{\nu}(d\tau). \end{aligned}$$

Now we assume that Fubini's theorem is satisfied, and we take the expectation inside the integrals and collapse the various spatial integrals and differentials:

$$\begin{aligned} \mathbf{r}_{a',b'}(\mathcal{X} \times \mathcal{Y} \times T) &= \int_T \iint \frac{1}{\int_{[\mathcal{V}/\mathcal{M}]} d\nu(u')} \int_{[\mathcal{V}/\mathcal{M}]} \int_{\mathbb{H}} \mathbf{h}(\mathcal{X}, t - t' - u; -\mathbf{x}') \times \\ &\quad \mathbf{r}_{ab}(d\mathbf{x}', d\mathbf{y}', t'') \underline{\mathbf{g}}^H(\mathcal{Y}, t - t' - u - \tau + t''; -\mathbf{y}') \nu(du) \mu(dt') \mu(dt'') \nu(d\tau). \end{aligned}$$

The integral over one period $[\mathcal{V}/\mathcal{M}]$ is the expectation over the delay u . Since $\underline{\mu} = \underline{\Sigma}_{\mathcal{M}}$, we can write this as

$$\begin{aligned} \mathbf{r}_{a',b'}(\mathcal{X} \times \mathcal{Y} \times T) &= \frac{1}{\int_{[\mathcal{V}/\mathcal{M}]} d\nu(u')} \int_T \int \sum_{t' \in \mathcal{M}} \int_{[\mathcal{V}/\mathcal{M}]} \int_{\mathbb{H}} \mathbf{h}(\mathcal{X}, t - t' - u; -\mathbf{x}') \times \\ &\quad \mathbf{r}_{ab}(d\mathbf{x}', d\mathbf{y}', t'') \underline{\mathbf{g}}^H(\mathcal{Y}, t - t' - u - \tau + t''; -\mathbf{y}') \nu(du) \mu(dt'') \nu(d\tau). \end{aligned}$$

We now recognize that within the innermost temporal integral $u \in [\mathcal{V}/\mathcal{M}]$, and thus $t' + u$ represents a coset decomposition of some $u'' \in \mathcal{V}$. The temporal integral and the summation can therefore be combined to form an integral with respect to $\nu(du'')$:

$$\begin{aligned} \mathbf{r}_{a',b'}(\mathcal{X} \times \mathcal{Y} \times T) &= \frac{1}{\int_{[\mathcal{V}/\mathcal{M}]} d\nu(u')} \int_T \iint \int_{\mathbb{H}} \mathbf{h}(\mathcal{X}, t - u''; -\mathbf{x}') \times \\ &\quad \mathbf{r}_{ab}(d\mathbf{x}', d\mathbf{y}', t'') \underline{\mathbf{g}}^H(\mathcal{Y}, t - u'' - \tau + t''; -\mathbf{y}') \nu(du'') \mu(dt'') \nu(d\tau). \end{aligned}$$

Now we invoke the flip invariance and shift invariance of ν with respect to \mathcal{V} to eliminate t :

$$\begin{aligned} \mathbf{r}_{a',b'}(\mathcal{X} \times \mathcal{Y} \times T) &= \frac{1}{\int_{[\mathcal{V}/\mathcal{M}]} d\nu(u')} \int_T \iint \int_{\mathbb{H}} \mathbf{h}(\mathcal{X}, u''; -\mathbf{x}') \times \\ &\quad \mathbf{r}_{ab}(d\mathbf{x}', d\mathbf{y}', t'') \underline{\mathbf{g}}^\dagger(\mathcal{Y}, \tau - t'' - u''; -\mathbf{y}') \nu(du'') \mu(dt'') \nu(d\tau). \end{aligned}$$

After factoring the cross-correlation differential on the right according to (2.29b) and applying (2.22) twice in the spirit of (2.20) and (2.21), this simplifies to

$$\boxed{\mathbf{r}_{a',b'}(\mathcal{X} \times \mathcal{Y} \times T) = \frac{1}{\int_{[\mathcal{V}/\mathcal{M}]} \nu(d\tau)} (\mathbf{h} \boxtimes \mathbf{r}_{ab} \boxtimes \mathbf{g}^\dagger)(\mathcal{X} \times \mathcal{Y} \times T),} \quad (\text{B.9})$$

which is just a scaled version of the previous result (B.8). For $\mathcal{V} = \mathbb{R}$ and $\mathcal{M} = T\mathbb{Z}$, the scale factor is $1/T$.

Appendix C.

The Wave Equation

Electromagnetic waves in free space obey the *homogeneous wave equation*

$$\nabla^2 \psi - \frac{1}{c^2} \frac{\partial^2}{\partial t^2} \psi = 0,$$

where $\psi(\mathbf{x}, t)$ is a component of the electric or magnetic field or a related quantity such as the vector potential. Fourier transforming both sides on the variable t results in the *Helmholtz equation*

$$\nabla^2 \Psi(\mathbf{x}, f) + (2\pi f/c)^2 \Psi(\mathbf{x}, f) = 0.$$

Two important solutions to the wave equation are the monochromatic *spherical wave*

$$\psi(\mathbf{x}, t) = \frac{1}{\|\mathbf{x}\|} e^{j2\pi(f_0 t - k\|\mathbf{x}\|)} \quad (\text{C.1})$$

and plane wave

$$\psi(\mathbf{x}, t) = e^{j2\pi(f_0 t - \mathbf{k} \cdot \mathbf{x})}. \quad (\text{C.2})$$

Applying the wave equation to the spherical wave yields scalar wavenumber $k = f_0/c = 1/\lambda_0$. Applying the wave equation to the plane wave yields

$$k_x^2 + k_y^2 + k_z^2 = (f_0/c)^2,$$

where complex wavenumber vector $\mathbf{k} = (k_x, k_y, k_z)$. For solutions where \mathbf{k} is purely real we have $\|\mathbf{k}\| = |f_0|/c$, and the resulting plane wave propagates in the direction $\hat{\mathbf{k}}$. However,

when $\mathbf{k} = \mathbf{k}_r + j\mathbf{k}_i$ is complex, the imaginary part turns the complex exponential into a real one:

$$\psi(\mathbf{x}, t) = e^{j2\pi(f_0 t - \mathbf{k}_r \cdot \mathbf{x})} e^{2\pi \mathbf{k}_i \cdot \mathbf{x}}$$

This is a decaying exponential in the $-\hat{\mathbf{k}}_i$ direction, and a growing exponential in the $\hat{\mathbf{k}}_i$ direction. Growing exponentials do not represent physically realizable fields, but decaying exponential or *evanescent* waves do exist in the near field of radiation sources and represent stored energy that does not propagate away from the source.

Polychromatic plane waves are formed by replacing the complex exponential with an arbitrary function. First, write the wavenumber vector as $\mathbf{k} = \hat{\mathbf{x}}_0 f_0 / c$ in terms of propagation direction $\hat{\mathbf{x}}_0$, and substitute into (C.2):

$$\psi(\mathbf{x}, t) = e^{j2\pi f_0 (t - \mathbf{x} \cdot \hat{\mathbf{x}}_0 / c)}.$$

Substituting arbitrary time function $a(t)$ for the complex exponential yields the polychromatic plane wave

$$\psi(\mathbf{x}, t) = a(t - \mathbf{x} \cdot \hat{\mathbf{x}}_0 / c)$$

with temporal Fourier transform

$$\Psi(\mathbf{x}, f) = A(f) e^{-j2\pi \mathbf{x} \cdot \hat{\mathbf{x}}_0 f / c}$$

which satisfy the wave and Helmholtz equations, respectively.

Appendix D.

Elevation-Azimuth Spherical Coordinate System

In describing the spatial dimensions of array patterns, it is customary to employ the spherical coordinate system shown in Figure D.1. Here a three-dimensional vector \mathbf{x} which might be defined in terms of Cartesian coordinates $(x, y, z)^T$ is instead described by the triple $(r, \phi, \theta)^T$, where r is the *range* (or radius), ϕ is the *elevation*, and θ is the *azimuth*. Far-field array patterns are not a function of range, and so only elevation and azimuth are used, describing a spherical shell. Those familiar with the spherical coordinate systems often used in math and physics should note some minor variations: here elevation angle ϕ is measured up from the x - y plane, while azimuth is measured clockwise from the y -axis, which is usually oriented to face due north. Conversion between Cartesian and spherical coordinates is as follows:

$$\begin{pmatrix} r \\ \phi \\ \theta \end{pmatrix} = \begin{pmatrix} \sqrt{x^2 + y^2 + z^2} \\ \sin^{-1}(z/r) = \cos^{-1}(\sqrt{x^2 + y^2}/r) \\ \tan^{-1}\left(\frac{x}{y}\right) \end{pmatrix}$$
$$\begin{pmatrix} x \\ y \\ z \end{pmatrix} = r \begin{pmatrix} \cos(\phi) \sin(\theta) \\ \cos(\phi) \cos(\theta) \\ \sin(\phi) \end{pmatrix}$$

We can also define a local Cartesian coordinate system at the point \boldsymbol{x} using orthogonal unit vectors $(\hat{\mathbf{r}}(\boldsymbol{x}), \hat{\boldsymbol{\phi}}(\boldsymbol{x}), \hat{\boldsymbol{\theta}}(\boldsymbol{x}))$. These indicate the directions of increasing range, elevation, and azimuth, respectively. This coordinate system simplifies discussions of polarization, as the far field electric and magnetic fields always point perpendicular to $\hat{\mathbf{r}}$ and are often described in terms of their $\hat{\boldsymbol{\phi}}$ (“vertical”) and $\hat{\boldsymbol{\theta}}$ (“horizontal”) components. These unit vectors can be computed as

$$\hat{\mathbf{r}} = \begin{pmatrix} \cos(\phi) \sin(\theta) \\ \cos(\phi) \cos(\theta) \\ \sin(\phi) \end{pmatrix} \quad (\text{D.1a})$$

$$\hat{\boldsymbol{\phi}} = \begin{pmatrix} -\sin(\phi) \sin(\theta) \\ -\sin(\phi) \cos(\theta) \\ \cos(\phi) \end{pmatrix} \quad (\text{D.1b})$$

$$\hat{\boldsymbol{\theta}} = \begin{pmatrix} \cos(\theta) \\ -\sin(\theta) \\ 0 \end{pmatrix}. \quad (\text{D.1c})$$

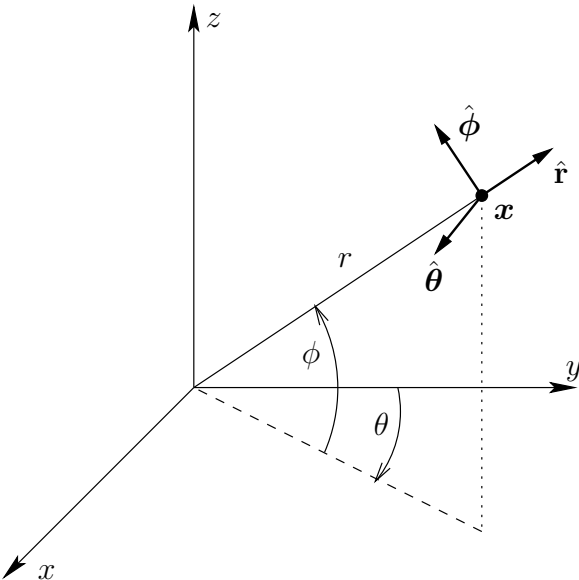


Figure D.1: A spherical coordinate system is used to describe antenna array patterns. Elevation angle ϕ is measured up from the horizon (the x - y plane), and azimuth angle θ is measured clockwise from due north (the y -axis). Range r is included for completeness but not used.

Appendix E.

The Element Pattern of a Short, Thin Dipole

We assume that an infinitely thin dipole antenna at the origin aligned with the z axis is driven by an ideal current signal with Fourier transform $I(f)$. We further assume that the total length L is much less than a wavelength for all frequencies of interest, so that the phase of the current at any point on the dipole is approximately constant. This *electrically small* assumption greatly simplifies analysis, as the terminal input current is essentially the radiating current. To avoid current discontinuity at the ends of the dipole, the magnitude of the current is assumed to slope linearly from its maximum at the center to zero at the ends. The resulting current density is

$$\vec{\mathbf{J}}(d\mathbf{x}, f) = I(f)\underline{\delta}(dx)\underline{\delta}(dy) \operatorname{tri}\left(\frac{2z}{L}\right) dz \hat{\mathbf{z}}$$

where $\mathbf{x} = x\hat{\mathbf{x}} + y\hat{\mathbf{y}} + z\hat{\mathbf{z}}$ and

$$\operatorname{tri}(t) \triangleq \begin{cases} 1 - |t|, & |t| \leq 1 \\ 0, & |t| > 1. \end{cases}$$

The spatial Fourier transform of the current density is

$$\vec{\mathbf{J}}(\mathbf{v}, f) = I(f)\frac{L}{2} \operatorname{sinc}^2\left(\frac{Lv_z}{2}\right) \hat{\mathbf{z}},$$

where $\mathbf{v} = v_x\hat{\mathbf{x}} + v_y\hat{\mathbf{y}} + v_z\hat{\mathbf{z}}$ and

$$\operatorname{sinc}(t) \triangleq \frac{\sin(\pi t)}{\pi t}.$$

The wideband element pattern is found from (3.24b) as

$$\vec{\mathbf{A}}_{\text{el}}(\mathbf{v}, f) = -\frac{\mu_0}{4\pi} j 2\pi f \frac{L}{2} \text{sinc}^2\left(\frac{Lv_z}{2}\right) \mathbf{\Gamma}_{\hat{\mathbf{v}}\hat{\mathbf{z}}}.$$

The visible pattern is found by substituting $\mathbf{v} = -\hat{\mathbf{x}}f/c$:

$$\vec{\mathbf{A}}_{\text{el}}(-\hat{\mathbf{x}}f/c, f) = -\frac{\mu_0}{4\pi} j 2\pi f \frac{L}{2} \text{sinc}^2\left(\frac{-L[\hat{\mathbf{x}}]_z f}{2c}\right) \mathbf{\Gamma}_{\hat{\mathbf{x}}\hat{\mathbf{z}}}.$$

In the spherical coordinate system of Appendix D, we have $[\hat{\mathbf{x}}]_z = \sin(\phi)$ and

$$\begin{aligned} \mathbf{\Gamma}_{\hat{\mathbf{x}}\hat{\mathbf{z}}} &= (\hat{\mathbf{z}} - \sin(\phi)\hat{\mathbf{x}}) \\ &= \cos(\phi)\hat{\phi}(\hat{\mathbf{x}}). \end{aligned}$$

Now the visible element pattern simplifies to

$$\vec{\mathbf{A}}_{\text{el}}(-\hat{\mathbf{x}}f/c, f) = -\frac{\mu_0}{4\pi} j 2\pi f \frac{L}{2} \text{sinc}^2\left(\frac{L \sin(\phi) f}{2c}\right) \cos(\phi)\hat{\phi}(\hat{\mathbf{x}}).$$

Finally, because of the short length assumption we have

$$\text{sinc}^2\left(\frac{L \sin(\phi) f}{2c}\right) \approx 1$$

for all frequencies of interest, and so

$$\vec{\mathbf{A}}_{\text{el}}(-\hat{\mathbf{x}}f/c, f) \approx -\frac{\mu_0}{4\pi} j 2\pi f \frac{L}{2} \cos(\phi)\hat{\phi}(\hat{\mathbf{x}}). \quad (\text{E.1})$$

The magnitude of the pattern is a separable function of ϕ and f only; the dipole is omnidirectional about the z axis. The magnitude is proportional to both temporal frequency f and dipole length L . Other dipole orientations can easily be handled by replacing $\hat{\mathbf{z}}$ with an arbitrary unit vector, although the simple form of (E.1) will be lost.

Figure E.1 shows several views of the element pattern for a short vertical ($\hat{\mathbf{z}}$ -oriented) dipole. In all plots the wideband directive gain (3.71) is plotted for the temporal frequency band $\mathcal{F} = [0.55f_s, 0.95f_s]$, which corresponds to the signal band of the example designs in Chapter 3. Reference frequency $f_s = 1/T$ here is arbitrary, as the directive gain of the dipole is invariant to frequency scaling. Figure E.1(a) shows the element pattern over one

hemisphere of directions, for three representative frequencies. The pattern on the opposite hemisphere is identical. The horizontal lines indicate constant elevation angle, while the vertical curved lines indicate constant azimuth angle, both in increments of 30° . Visually we can see the salient features of (E.1): the element pattern is constant across azimuth for a given elevation and frequency, the pattern has nulls at elevations $\phi = \pm 90^\circ$, and in any given direction the directive gain increases as the square of frequency. Figures E.1(b) and E.1(c) show principal-axis slices of the element pattern vs. frequency, Figures E.1(d) and E.1(e) show principal-axis patterns at selected frequencies in greater detail, and Figure E.1(f) shows the frequency response at boresite.

While the omni-directional pattern of the dipole is desirable in many applications, for planar arrays we usually wish to only radiate in directions that lie on the hemisphere from which the array face is visible. Radiation behind the face, the so-called *backlobes*, is to be suppressed. With an array of dipoles oriented perpendicular to array normal, the backlobes are actually the mirror image of the desired radiation pattern, and half the radiated power is sent in unwanted directions. If instead the dipoles are offset by some distance from an ideal ground plane, then backward-propagating radiation is reflected forward. Assume the dipole above is offset by a distance h along the y axis from an ideal ground plane in the x - z plane. The apparent current density is that of the physical dipole and its reflection:

$$\vec{\mathbf{J}}(d\mathbf{x}, f) = I(f)\delta(dx) \left[\delta(dy) - \delta(dy) \right] \text{tri}\left(\frac{2z}{L}\right) dz \hat{\mathbf{z}},$$

when viewed from in front of the array. The sign change on the reflection is a consequence of boundary conditions at the ground plane. From (3.24b), the resulting element pattern is

$$\vec{\mathbf{A}}_{\text{el}}(\mathbf{v}, f) = -\frac{\mu_0}{4\pi} j 2\pi f \left[e^{-j2\pi h v_y} - e^{j2\pi h v_y} \right] \frac{L}{2} \text{sinc}^2\left(\frac{L v_z}{2}\right) \Gamma_{\hat{\mathbf{v}}\hat{\mathbf{z}}},$$

where the quantity in the brackets is just the array factor of a two-element array with coefficients ± 1 . Applying the identities $e^{-ja} - e^{ja} = -j2 \sin(a)$ and $[\hat{\mathbf{x}}]_y = \cos(\phi) \cos(\theta)$ and

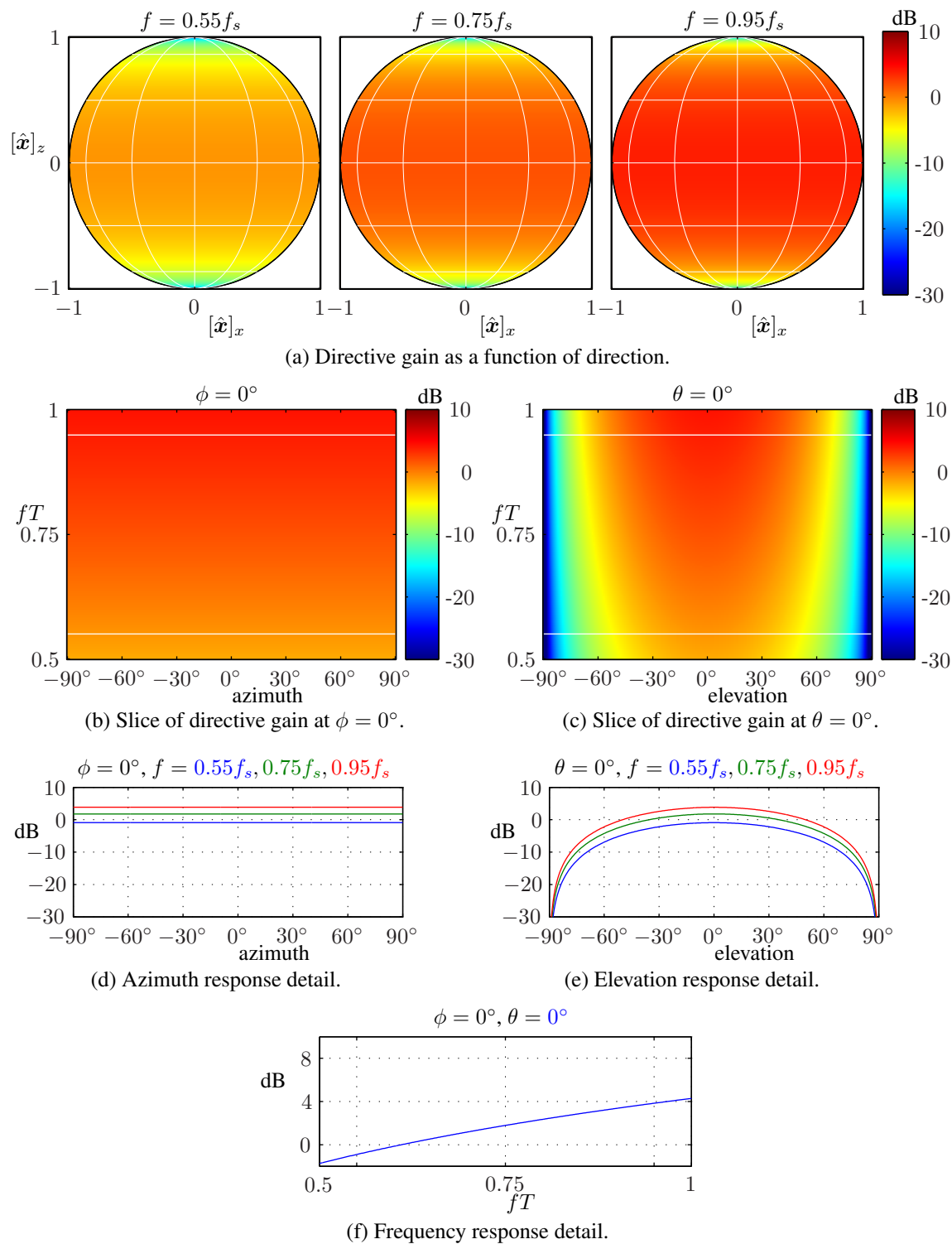


Figure E.1: Element pattern of a short vertical dipole.

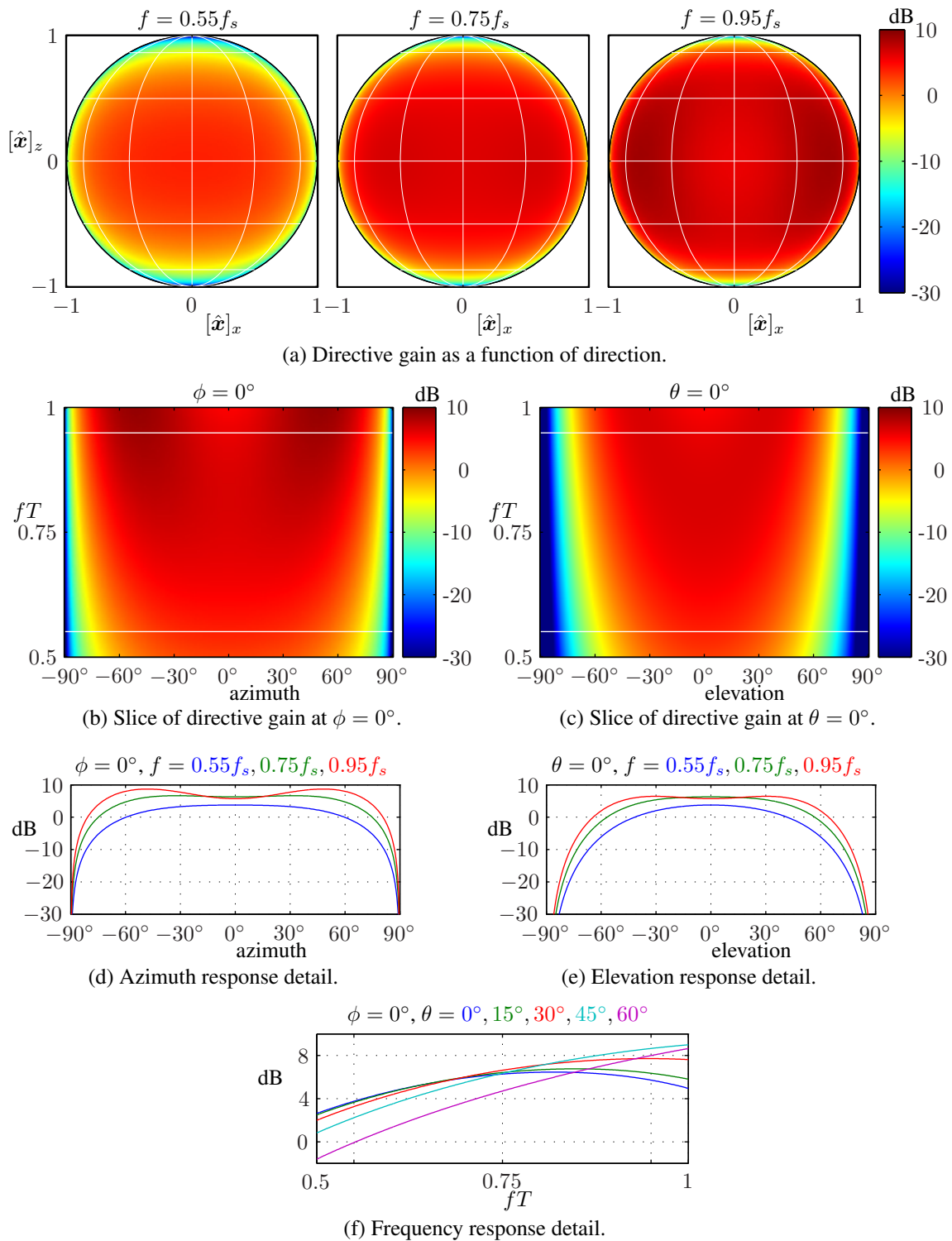


Figure E.2: Element pattern of a short vertical dipole in front of a ground plane.

the previous assumptions yields the approximate visible pattern

$$\vec{\mathbf{A}}_{\text{el}}(-\hat{\mathbf{x}}f/c, f) \approx \begin{cases} -\frac{\mu_0}{4\pi} 2\pi f \sin(2\pi h \cos(\phi) \cos(\theta) f/c) L \cos(\phi) \hat{\phi}(\hat{\mathbf{x}}), & |\theta| \leq 90^\circ \\ 0, & \text{otherwise} \end{cases} \quad (\text{E.2})$$

Since the vector direction of the element pattern (and the array pattern of any array made entirely from such elements) is always $\hat{\phi}(\hat{\mathbf{x}})$, the horizontal polarization component is zero, and we can factor the element pattern as

$$\vec{\mathbf{A}}_{\text{el}}(-\hat{\mathbf{x}}f/c, f) = A_{\text{elV}}(-\hat{\mathbf{x}}f/c, f) \hat{\phi}(\hat{\mathbf{x}}), \quad (\text{E.3})$$

the cascade of the vertical scalar element pattern and the elevation unit vector. This will simplify the notation in the examples.

A consequence of adding the ground plane is that the element pattern's shape is now frequency dependent. The most common choice for the offset is $h = \frac{\lambda_0}{4} = \frac{c}{4f_0}$, so that at boresite the element and its reflection are exactly in phase at nominal operating frequency f_0 . This choice, however, also means that at $f = 2f_0$ the element pattern has a null at boresite, limiting the useful bandwidth. Figure E.2 shows the same dipole as Figure E.1 with a quarter-wavelength offset of $h = c/4f_0$ from a ground plane in the x - z plane, where $f_0 = \sqrt{0.55f_s \times 0.95f_s} \approx 0.72f_s$ is the geometric band center. Comparing the two sets of plots shows that directive gain is improved by about 4 dB for most angles. The pattern is still very close to omnidirectional over the hemisphere, but does have a null in all directions parallel to the ground plane ($\theta = \pm 90^\circ$).

Appendix F.

Second-Order Cone Programming

A powerful special case of convex optimization is *second-order cone programming*, or SOCP [97]. SOCP allows the minimization of a linear objective, subject to second-order cone (SOC) constraints, which encompass linear and convex quadratic constraints. One standard formulation of a second-order cone program (also abbreviated SOCP) is

$$\min_{\mathbf{x}} \quad \mathbf{f}^T \mathbf{x} \quad (\text{F.1a})$$

$$\text{s.t.} \quad \|\mathbf{A}_k^T \mathbf{x} + \mathbf{b}_k\|_2 \leq \mathbf{c}_k^T \mathbf{x} + d_k, \quad k = 1, \dots, K. \quad (\text{F.1b})$$

The number of linearly independent columns in \mathbf{A}_k is R_k , the *rank* of the second-order cone. An equivalent notation for the SOC constraint of (F.1b) is the pair of constraints

$$\|\mathbf{A}\mathbf{x} + \mathbf{b}\|_2^2 \leq (\mathbf{c}^T \mathbf{x} + d)^2$$

$$0 \leq \mathbf{c}^T \mathbf{x} + d.$$

Although (F.1) tends to be the most convenient for filter design due to the explicit inequality constraints, for some applications its dual problem [97]

$$\max_{\mathbf{y}} \quad \sum_k (-d_k \mathbf{b}_k^T) \mathbf{y}_k$$

$$\text{s.t.} \quad (-\mathbf{c}_k, \mathbf{A}_k) \mathbf{y}_k = \mathbf{f}_k$$

$$\|([\mathbf{y}_k]_2, \dots, [\mathbf{y}_k]_{R_k})^T\|_2 \leq [\mathbf{y}_k]_1 \quad k = 1, \dots, K$$

is preferred. Here the full vector of dual variables

$$\mathbf{y} = \begin{pmatrix} \mathbf{y}_1 \\ \vdots \\ \mathbf{y}_K \end{pmatrix}$$

is formed by concatenating the dual variable vectors $\{\mathbf{y}_k\}$ corresponding to each of the K SOC constraints, and similarly the primal objective vector \mathbf{f} is split into K subvectors as

$$\mathbf{f} = \begin{pmatrix} \mathbf{f}_1 \\ \vdots \\ \mathbf{f}_K \end{pmatrix}.$$

The primal and dual problems are equivalent in that any problem that can be expressed in one form can be converted to the other via auxiliary variables. Most modern solvers iteratively solve both problems simultaneously, so the choice of problem formulation is generally based on convenience.

Although SOCP seems quite limited, with only one basic type of constraint, it can be used to solve a wide range of problems using creative combinations of multiple constraints. A linear constraint results as a special case when \mathbf{A}_k and \mathbf{b}_k are zero. Of specific interest here, SOCP can be used to exactly constrain l_1 , l_2 , and l_∞ norms of error vectors that are affine in the optimization variables. Using discretization SOCP can be used to approximately constrain L_1 , L_2 , and L_∞ norms of affine error functions [97, 109], as well as norms formed by combining these basic three in various ways [110, 111]. Exact L_2 formulations also exist [52] that do not require discretization. Any constraint can also be used as the objective via an auxiliary variable:

$$\begin{aligned} \min_{\mathbf{x}, \delta} \quad & \delta \\ \text{s.t.} \quad & \|\mathbf{A}_k^T \mathbf{x} + \mathbf{b}_k\|_2 \leq \delta. \end{aligned}$$

The following sections briefly summarize how SOCP can be used to constrain the various norms of an error function $E : [0, 1] \times \mathbb{R}^N \rightarrow \mathbb{C}$, where $E(f, \mathbf{x})$ represents a complex frequency response error at normalized frequency f that is affine in the N optimization variables \mathbf{x} . The dependence on the optimization variables is hereafter made implicit for

simplicity, and we will simply write $E(f)$. The extension to error functions of multiple dimensions is straightforward.

L_∞ -Norm Constraints

For a function E the L_∞ or Chebychev norm is defined as

$$\|E\|_\infty \triangleq \operatorname{ess\,sup}_f |E(f)|.$$

Since the functions of interest are continuous with compact support, this reduces to

$$\|E\|_\infty \triangleq \max_f |E(f)|.$$

For a function E that is affine in the optimization variables, the L_∞ -norm can be (approximately) constrained using SOCP [109] by discretizing the interval $[0, 1]$. Letting $\{0, f_1, \dots, f_{K_{\text{inf}}-1}, 1\}$ partition the interval $[0, 1]$ (choosing $f_k = k/K_{\text{inf}}$ is common), the set of rank-2 SOC constraints

$$\left\| \begin{array}{c} \operatorname{Re}\{E(f_k)\} \\ \operatorname{Im}\{E(f_k)\} \end{array} \right\|_2 \leq \delta, \quad k = 0, \dots, K_{\text{inf}}$$

bounds the maximum value of $|E(f_k)|$ on the grid by δ , which can be a constant or an auxiliary optimization variable [97]. This is usually written more compactly as

$$|E(f_k)| \leq \delta, \quad k = 0, \dots, K_{\text{inf}}.$$

The spacing between the grid points must be chosen to limit violations of the bound between constraints to acceptable levels. Errors between the discretized approximation and the true norm can be made arbitrarily small at the cost of an increased number of constraints. Often a looser grid is used in the initial stages of a design to obtain rapid solutions, while a tight grid is used for the final design. For a 1D FIR filter of length N an approximate rule of thumb for the minimum grid spacing is $1/(20N)$, although in multidimensional designs lesser linear densities are usually sufficient.

If E is a real-valued function, representing a linear-phase filter, then using SOC constraints as shown above results in a degenerate (rank-1) cone. Using cones here is inefficient; instead we use a pair of linear constraints per frequency:

$$-\delta \leq E(f_k) \leq \delta, \quad k = 0, \dots, K_{\text{inf}}.$$

L_2 -Norm Constraints

In contrast to the L_∞ norm, which requires one constraint per discrete frequency, the L_2 norm requires only a single SOC constraint. The L_2 norm of the error function is defined as

$$\|E\|_2 \triangleq \left(\int_0^1 |E(f)|^2 df \right)^{\frac{1}{2}}.$$

Since E was assumed affine in the optimization variables \mathbf{x} , the result can be written as a positive semidefinite quadratic form in the augmented vector $(1, \mathbf{x}^T)^T$:

$$\|E\|_2^2 = \begin{pmatrix} 1 & \mathbf{x}^T \end{pmatrix} \mathbf{Q} \begin{pmatrix} 1 \\ \mathbf{x} \end{pmatrix}.$$

The real, positive-semidefinite kernel \mathbf{Q} can be factored as

$$\mathbf{Q} = \mathbf{S}^T \mathbf{S} = \begin{pmatrix} \mathbf{S}_c^T \\ \mathbf{S}_l^T \end{pmatrix} \begin{pmatrix} \mathbf{S}_c & \mathbf{S}_l \end{pmatrix},$$

reducing the quadratic to the desired form:

$$\begin{aligned} \|E\|_2^2 &= (\mathbf{S}_l \mathbf{x} + \mathbf{S}_c)^T (\mathbf{S}_l \mathbf{x} + \mathbf{S}_c) \\ &= \|\mathbf{S}_l \mathbf{x} + \mathbf{S}_c\|_2^2. \end{aligned}$$

Thus an L_2 constraint can always be represented exactly with a SOC, provided the integral can be calculated exactly. In many cases this can be achieved using the random process formulation of [52]. If not, the integral must be evaluated using a numerical method, perhaps the simplest being a Riemann sum over a uniform partition $\{f_k\}$ of $[0, 1]$. The resulting SOC constraint can be written

$$\sum_k |E(f_k)|^2 \Delta f \leq \delta^2,$$

where δ is a nonnegative constant or auxiliary variable. Compared to the L_∞ norm it takes a tighter grid to get the same level of approximation error using a Riemann sum, a conservative rule of thumb in one dimension being $\Delta f \approx 1/(40N)$. The choice of a small spacing has less impact since it does not increase the size of the optimization problem itself, but just the amount of computation required to set up the problem.

L_1 -Norm Constraints

The L_1 norm is the trickiest of the norms to constrain using SOCP as well as the least common. One application is in the design of communication filters to control intersymbol interference [112]. The L_1 norm of the error function is defined as

$$\|E\|_1 \triangleq \int_0^1 |E(f)| df.$$

Approximating the integral directly as a Riemann sum does not result in a SOC. Instead, introduce the real, nonnegative auxiliary function $\beta : [0, 1] \rightarrow \mathbb{R}^+$ and consider the pair of constraints

$$\begin{aligned} |E(f)| &\leq \beta(f) \\ \int_0^1 \beta(f) df &\leq \delta. \end{aligned}$$

Due to the nonnegativity of β , this implies the desired constraint

$$\int_0^1 |E(f)| df \leq \delta. \quad (\text{F.2})$$

To discretize, choose a uniform partition $\{f_k\}$ of $[0, 1]$ and introduce the auxiliary optimization variables $\{\beta_k\}$. The following set of constraints then approximates the integral:

$$|E(f_k)| \leq \beta_k, \quad k = 0, \dots, K_1 \quad (\text{F.3a})$$

$$\sum_k \beta_k \Delta f \leq \delta. \quad (\text{F.3b})$$

At optimality the constraints (F.3a) are all necessarily satisfied with equality, and thus (F.3b) approximates (F.2) as desired [113, 112]. As with the L_∞ norm, when E is real-valued linear constraints rather than SOC constraints should be used in (F.3a). Although this method introduces many new variables as well as constraints, the resulting problem is quite sparse and can be efficiently handled by most available solvers. The L_1 norm is even more sensitive than the L_2 norm to small values in its argument, and as such an accurate approximation requires an even tighter grid of frequencies. A conservative rule of thumb in one dimension is $\Delta f \approx 1/(60N)$.

BIBLIOGRAPHY

- [1] G. C. Tavik, C. L. Hilterbrick, J. B. Evins, J. J. Alter, J. G. Crnkovich, J. W. de Graaf, W. H. II, G. P. Hrin, S. A. Lessin, D. C. Wu, and S. M. Hagewood, "The advanced multifunction RF concept," *IEEE Transactions on Microwave Theory and Techniques*, vol. 53, no. 3, pp. 1009–1020, Mar. 2005.
- [2] P. K. Hughes and J. Y. Choe, "Overview of advanced multifunction RF system (AMRFS)," in *IEEE Int'l Symp. on Phased Array Systems and Technology*, Dana Point, CA, May 2000.
- [3] G. M. Raz and B. D. van Veen, "Baseband volterra filters for implementing carrier based nonlinearities," *IEEE Transactions on Signal Processing*, vol. 46, no. 1, pp. 103–114, Jan. 1998.
- [4] H. Chiriex, "High power outphasing modulation," *Proc. IRE*, pp. 1370–1392, Nov. 1935.
- [5] F. Raab, "Efficiency of outphasing RF power-amplifier systems," *IEEE Transactions on Communications*, vol. 33, no. 10, pp. 1094–1099, Oct. 1985.
- [6] H. H. Faust, B. Connolly, T. M. Firestone, R. C. Chen, B. H. Cantrell, and E. L. Mokole, "A spectrally clean transmitting system for solid-state phased-array radars," in *Proc. IEEE Radar Conference*, Philadelphia, PA, Apr. 2004.

- [7] P. K. Bondyopadhyay, "The first application of array antenna," in *IEEE Int'l Symp. on Phased Array Systems and Technology*, Dana Point, CA, May 2000.
- [8] R. C. Hansen, *Phased Array Antenna*. New York: John Wiley & Sons, 1998.
- [9] E. Brookner, "Phased arrays around the world - progress and future trends," in *IEEE Int'l Symp. on Phased Array Systems and Technology*, Boston, MA, Oct. 2003.
- [10] A. C. Schell, "Antenna developments of the 1950s to the 1980s," in *IEEE Int'l Symp. of the Antennas and Propagation Society*, 2001.
- [11] G. Hyde, "Historical perspectives on commercial and nonmilitary government space applications of microwave systems in the baltimore/washington area," *IEEE Transactions on Microwave Theory and Techniques*, vol. 46, no. 12, pp. 2196–2201, Dec. 1998.
- [12] O. G. Vendik and Y. V. Yegorov, "The first phased-array antennas in russia: 1955-1960," *IEEE Antennas and Propagation Magazine*, vol. 42, no. 4, pp. 46–52, Aug. 2000.
- [13] E. Rai, S. Nishimoto, T. Katada, and H. Watanabe, "Historical overview of phased array antennas for defense application in japan," in *IEEE Int'l Symp. on Phased Array Systems and Technology*, 1996.
- [14] W. X. Zhang, "Antenna development in china," *IEEE Antennas and Propagation Magazine*, vol. 38, no. 6, pp. 49–63, Dec. 1996.
- [15] W. M. Waters and B. R. Jarrett, "Bandpass signal sampling and coherent detection," *IEEE Transactions on Aerospace and Electronic Systems*, vol. AES-18, no. 4, pp. 731–6, Nov. 1982.

- [16] D. W. Rice and K. H. Wu, "Quadrature sampling with high dynamic range," *IEEE Transactions on Aerospace and Electronic Systems*, vol. AES-18, no. 4, pp. 736–9, Nov. 1982.
- [17] R. L. Mitchell, "Creating complex signal samples from a band-limited real signal," *IEEE Transactions on Aerospace and Electronic Systems*, vol. 25, no. 3, pp. 425–427, May 1989.
- [18] C. M. Rader, "A simple method for sampling in-phase and quadrature components," *IEEE Transactions on Aerospace and Electronic Systems*, vol. AES-20, no. 6, pp. 821–824, Nov. 1984.
- [19] D. P. Scholnik and J. O. Coleman, "Simple, exact models of sample-interleaving demodulators/modulators for quadrature bandpass sampling/reconstruction," in *Proc. 1997 Conf. on Information Sciences and Systems (CISS '97)*, Baltimore, MD, Mar. 1997.
- [20] J. O. Coleman, "A measure-convolution approach to elementary signals and systems," in *Proc. Conf. on Information Sciences and Systems*, Baltimore, Mar. 1999.
- [21] —, "Measure signals and systems," in preparation.
- [22] D. P. Scholnik and J. O. Coleman, "Optimal design of wideband array patterns," in *Proc. IEEE Int'l Radar Conference (RADAR 2000)*, Alexandria VA, May 2000.
- [23] —, "Formulating wideband array-pattern optimizations," in *Proc. IEEE Int'l Symp. Phased Array Systems and Technology (ISPAST 2000)*, Dana Point, CA, May 2000.
- [24] —, "Superdirectivity and SNR constraints in wideband array-pattern design," in *IEEE Int'l Radar Conference*, Atlanta, GA, May 2001.

- [25] Y. Tamura, M. Okada, and O. Akasaka, "AD/DA conversion with multidimensional signal processing for acoustical sensor array," in *Proc. SICE'96*, 1996, pp. 831–832.
- [26] Y. Tamura, N. Kawakami, O. Akasaka, M. Okada, and K. Koyama, "Beam-forming using multidimensional sigma-delta modulation," in *Proc. IEEE Ultrasonics Symp.*, 1998, pp. 1077–1080.
- [27] D. P. Scholnik and J. O. Coleman, "Joint Spatial and Temporal Delta-Sigma Modulation for Wideband Antenna Arrays and Video Halftoning," in *Proc. IEEE Int. Conf. Acoustic, Speech, and Signal Processing (ICASSP 2001)*, Salt Lake City, UT, May 2001.
- [28] ———, "Space-Time Vector Delta-Sigma Modulation," in *Proc. 2002 Int'l Symp. on Circuits and Systems (ISCAS 2002)*, Scottsdale, AZ, May 2002.
- [29] ———, "Computability Constraints in Space-Time Delta-Sigma Arrays," in *Proc. Asilomar Conf. on Signals, Systems, and Computers*, Pacific Grove, CA, Nov. 2001.
- [30] D. P. Scholnik, J. O. Coleman, D. Bowling, and M. Neel, "Spatio-temporal delta-sigma modulation for shared wideband transmit arrays," in *Proc. IEEE Radar Conference*, Philadelphia, PA, Apr. 2004.
- [31] D. P. Scholnik, J. O. Coleman, J. Brandriss, D. Bowling, M. Neel, S. Rogala, and F. Schiavone, "Results of July 2003 space-time delta-sigma hardware experiments at China Lake," Naval Research Laboratory, Memo Report MR8877, Sept. 2005.
- [32] H. L. Royden, *Real Analysis*. Prentice Hall, 1988.
- [33] P. Billingsley, *Probability and Measure*, 2nd ed. John Wiley & Sons, 1987.
- [34] H. Bohr, *Almost Periodic Functions*. New York: Chelsea, 1947.
- [35] K. M. Mikkola, "Infinite-dimensional linear systems, optimal control and algebraic Riccati equations," Ph.D. dissertation, Helsinki University of Technology, 2002.

- [36] D. E. Dudgeon and R. M. Mersereau, *Multidimensional Digital Signal Processing*. Prentice-Hall, 1984.
- [37] J. O. Coleman, "Ping-pong sample times on a linear array halve the nyquist rate,," in *Proc. IEEE Int. Conf. Acoustic, Speech, and Signal Processing*, Montreal, Quebec, Canada, May 2004.
- [38] W. Rudin, *Real and Complex Analysis*, 3rd ed. McGraw-Hill, 1987.
- [39] S. Akkarakaran and P. P. Vaidyanathan, "Bifrequency and bispectrum maps: A new look at multirate systems with stochastic inputs," *IEEE Transactions on Signal Processing*, vol. 48, no. 3, pp. 723–736, Mar. 2000.
- [40] F. D. Neeser and J. L. Massey, "Proper complex random processes with applications to information theory," *IEEE Transactions on Information Theory*, vol. 39, no. 4, pp. 1293–1302, July 1993.
- [41] J. C. Candy and G. C. Temes, "Oversampling methods for A/D and D/A conversion," in *Oversampled Delta-Sigma Data Converters*. New York: IEEE Press, 1991.
- [42] *Delta-Sigma Data Converters : Theory, Design, and Simulation*. New York: IEEE Press, 1996.
- [43] J. O. Coleman, "The spectral products created by nonlinear intersymbol interference in NRZ data," in *Proc. Asilomar Conf. on Signals, Systems, and Computers*, Pacific Grove, CA, Nov. 2005.
- [44] D. P. Scholnik, "A Parallel Digital Architecture for Delta-Sigma Modulation," in *Proc. 2002 Midwest Symp. on Circuits and Systems (MWSCAS 2002)*, Tulsa, OK, Aug. 2002.

- [45] M. Iwamoto, A. Jayaraman, G. Hanington, P. Chen, A. Bellora, W. Thornton, L. Larson, and P. Asbeck, "Bandpass delta-sigma class-S amplifier," *Electronics Letters*, vol. 36, no. 12, pp. 1010–1012, June 2000.
- [46] A. Jayaraman, P. F. Chen, G. Hanington, L. Larson, and P. Asbeck, "Linear high-efficiency microwave power amplifiers using bandpass delta-sigma modulators," *IEEE Microwave and Guided Wave Letters*, vol. 8, no. 3, Mar. 1998.
- [47] R. M. White, B. H. Cantrell, J. P. McConnell, and J. J. Alter, "Delta-sigma waveform generation for digital radars," in *Proc. IEEE Radar Conference*, Philadelphia, PA, Apr. 2004.
- [48] B. Dufort and G. W. Roberts, "Increasing the performance of arbitrary waveform generators using periodic sigma-delta modulated streams," *IEEE Transactions on Instrumentation and Measurement*, vol. 49, no. 1, pp. 188–199, Feb. 2000.
- [49] R. M. Gray, "Quantization noise spectra," *IEEE Transactions on Information Theory*, vol. 36, no. 6, pp. 1220–1244, Nov. 1990.
- [50] S. H. Ardalan and J. J. Paulos, "An analysis of nonlinear behavior in delta-sigma modulators," *IEEE Transactions on Circuits and Systems*, vol. 34, no. 6, pp. 593–603, June 1987.
- [51] J. O. Coleman, "Embedded FIR generalized eigenfilters using test inputs," in *Proc. 1998 Int'l Conf. on Acoustics, Speech, and Signal Processing (ICASSP '98)*, May 1998.
- [52] ———, "Systematic mapping of quadratic constraints on embedded FIR filters to linear matrix inequalities," in *Proc. 1998 Conf. on Information Sciences and Systems (CISS '98)*, Princeton, NJ, Mar. 1998.

- [53] U. Horbach and M. Lang, "Design and implementation of sigma-delta D/A converters with optimized loop filters," in *Proc. IEEE Int. Symp. Circuits and Systems*, New York, NY, Apr. 1991.
- [54] S. R. Norsworthy, "Optimal nonrecursive noise shaping filters for oversampling data converters part 1: theory," in *Proc. IEEE Int. Symp. Circuits and Systems*, May 1993, pp. 1353–1356.
- [55] N. Fraser and B. Nowrouzian, "A novel technique for the estimation of stability in feedforward and multiple-feedback oversampled Σ - Δ A/D converter configurations," in *Proc. European Conf. on Circuit Theory and Design*, Espoo, Finland, Aug. 2001.
- [56] V. Mladenov, H. Hegt, and A. van Roermund, "On the stability of high order sigma-delta modulators," in *IEEE Conf. on Electronics, Circuits, and Systems*, Malta, Sept. 2001.
- [57] M. Vogels and G. Gielan, "Efficient analysis of the stability of sigma-delta modulators using wavelets," in *Proc. IEEE Int. Symp. Circuits and Systems*, vol. 3, Geneva, Switzerland, May 2000, pp. 758–764.
- [58] N. Thao, "Vector quantization analysis of $\Sigma\Delta$ modulation," *IEEE Transactions on Signal Processing*, vol. 44, no. 4, pp. 808–817, Apr. 1996.
- [59] R. J. van de Plassche, "Dynamic element matching for high-accuracy monolithic D/A converters," *IEEE Journal of Solid-State Circuits*, vol. 11, pp. 795–800, Dec. 1976.
- [60] R. Schreier and B. Zhang, "Noise-shaped multibit D/A converter employing unit elements," *Electronics Letters*, vol. 31, no. 20, pp. 1712–1713, Sept. 1995.

- [61] I. Galton, "Spectral shaping of circuit errors in digital-to-analog converters," *IEEE Transactions on Circuits and Systems—Part II: Analog and Digital Signal Processing*, vol. 44, no. 10, pp. 808–817, Oct. 1997.
- [62] D. P. Scholnik and J. O. Coleman, "Joint shaping of quantization and hardware-mismatch errors in a multibit delta-sigma DAC," in *Proc. 2000 Midwest Symp. on Circuits and Systems (MWSCAS 2000)*, Lansing MI, Aug. 2000.
- [63] R. T. Baird and T. S. Fiez, "Linearity enhancement of multi-bit $\Delta\Sigma$ A/D and D/A converters using data weighted averaging," *IEEE Transactions on Circuits and Systems—Part II: Analog and Digital Signal Processing*, vol. 42, pp. 753–762, Dec. 1995.
- [64] G. Luckjiff and I. Dobson, "Hexagonal sigma-delta modulation," *IEEE Transactions on Circuits and Systems—Part I: Fundamental Theory and Applications*, vol. 50, no. 8, pp. 991–1005, Aug. 2003.
- [65] D. P. Scholnik and J. O. Coleman, "Vector delta-sigma modulation with integral shaping of hardware-mismatch errors," in *IEEE 2000 Int'l Symp. on Circuits and Systems (ISCAS 2000)*, Geneva, Switzerland, May 2000.
- [66] J. Nieznanski, "Performance characterization of vector sigma-delta modulation," in *Proc. IEEE Industrial Electronics Conference*, 1998, pp. 531–536.
- [67] G. I. Bourdopoulos and T. L. Deliyannis, "High-order vector sigma-delta modulators," *IEEE Transactions on Circuits and Systems—Part II: Analog and Digital Signal Processing*, vol. 47, no. 6, pp. 493–503, June 2000.
- [68] T. N. Pappas, J. P. Allebach, and D. L. Neuhoff, "Model-based digital halftoning," *IEEE Signal Processing Magazine*, vol. 20, no. 4, pp. 14–27, July 2003.

- [69] M. Mese and P. P. Vaidyanathan, "Recent advances in digital halftoning and inverse halftoning methods," *IEEE Transactions on Circuits and Systems—Part I: Fundamental Theory and Applications*, vol. 49, no. 6, pp. 790–805, June 2002.
- [70] D. J. Lieberman and J. P. Allebach, "Efficient model based halftoning using direct binary search," in *Proc. Int'l. Conf. Image Processing*, vol. 1, Oct. 1997, pp. 775–778.
- [71] R. Floyd and L. Steinberg, "An adaptive algorithm for spatial grayscale," *Proc. Soc. Image Display*, vol. 17, no. 2, pp. 75–77, 1976.
- [72] T. D. Kite, B. L. Evans, A. C. Bovik, and T. L. Sculley, "Digital halftoning as 2-D delta-sigma modulation," in *Proc. IEEE Int. Conf. Image Processing*, 1997, pp. 799–802.
- [73] N. Damera-Venkata, B. L. Evans, and V. Monga, "Color error diffusion halftoning," *IEEE Signal Processing Magazine*, vol. 20, no. 4, pp. 51–58, July 2003.
- [74] J. O. Coleman, D. P. Scholnik, and J. J. Brandriss, "A specification language for the optimal design of exotic FIR filters with second-order cone programs," in *Proc. Asilomar Conf. on Signals, Systems, and Computers*, Pacific Grove, CA, Nov. 2002.
- [75] E. D. Andersen and K. D. Andersen, "The MOSEK interior point optimizer for linear programming: an implementation of the homogeneous algorithm," in *High Performance Optimization*. Kluwer Academic Publishers, 2000, pp. 197–232.
- [76] Jos F. Sturm, "Using SeDuMi 1.02, a MATLAB toolbox for optimization over symmetric cones," in *Optimization Methods and Software*, 1999, vol. 11–12, pp. 625–653, special issue on Interior Point Methods.

- [77] K. Toh, M. Todd, and R. Tutuncu, "SDPT3—a matlab software package for semidefinite programming," *Optimization Methods and Software*, vol. 11, pp. 545–581, 1999.
- [78] C. L. Dolph, "A current distribution for broadside arrays which optimizes the relationship between beam width and side-lobe level," *Proc. I.R.E.*, vol. 34, pp. 335–348, June 1946.
- [79] T. T. Taylor, "Design of line source antennas for narrow beamwidth and low side-lobes," *IRE Trans. Antennas Prop.*, vol. AP-3, p. 16, 1955.
- [80] S. A. Schelkunoff, "A mathematical theory of arrays," *Bell Sys. Tech. Jour.*, vol. 22, pp. 80–107, Jan. 1943.
- [81] C. J. Bouwkamp and N. G. deBruijn, "The problem of optimum antenna current distribution," *Philips Res. Rep.*, vol. 1, pp. 135–158, 1946.
- [82] H. J. Riblet, "Discussion on 'a current distribution for broadside arrays which optimizes the relationship between beam width and side-lobe level'," *Proc. I.R.E.*, vol. 35, pp. 489–492, May 1947.
- [83] E. N. Gilbert and S. P. Morgan, "Optimum design of directive antenna arrays subject to random variation," *Bell Sys. Tech. Jour.*, vol. 34, pp. 637–663, May 1955.
- [84] H. J. Riblet, "Note on the maximum directivity of an antenna," *Proc. I.R.E.*, vol. 36, pp. 620–624, May 1948.
- [85] Y. T. Lo, S. W. Lee, and Q. H. Lee, "Optimization of directivity and signal-to-noise ratio of an arbitrary antenna array," *Proc. IEEE*, vol. 54, no. 8, pp. 1033–1045, Aug. 1966.

- [86] M. M. Dawoud and A. Anderson, "Design of superdirective arrays with high radiation efficiencies," *IEEE Trans. Antennas and Propagation*, vol. 26, pp. 819–823, 1978.
- [87] E. H. Newman, J. H. Richmond, and C. H. Walter, "Superdirective receiving arrays," *IEEE Trans. Antennas and Propagation*, vol. AP-26, no. 5, pp. 629–635, Sept. 1978.
- [88] S. Haykin and J. Kessler, "Relation between the radiation pattern of an array and the two-dimensional discrete fourier transform," *IEEE Transactions on Antennas and Propagation*, pp. 419–420, May 1975.
- [89] H. Leuret and S. Boyd, "Antenna array pattern synthesis via convex optimization," *IEEE Trans. on Signal Processing*, vol. 45, no. 3, pp. 526–32, Mar. 1997.
- [90] F. Wang, V. Balakrishnan, P. Y. Zhou, J. J. N. Chen, R. Yang, and C. F. C, "Optimal array pattern synthesis using semidefinite programming," *IEEE Transactions on Signal Processing*, vol. 51, no. 5, pp. 1172–1183, May 2003.
- [91] C.-Y. Tseng and L. J. Griffiths, "A simple algorithm to achieve desired patterns for arbitrary arrays," *IEEE Transactions on Signal Processing*, vol. 40, no. 11, pp. 2737–2746, Nov. 1992.
- [92] L. I. Vaskelainen, "Iterative least-squares synthesis methods for conformal array antennas with optimized polarization and frequency properties," *IEEE Transactions on Antennas and Propagation*, vol. 45, no. 7, pp. 1179–1185, July 1997.
- [93] M. Dinnichert, "Full polarimetric pattern synthesis for an active conformal array," in *IEEE Int'l Symp. on Phased Array Systems and Technology*, Dana Point, CA, May 2000.

- [94] D. A. Shnidman, "An optimization technique for sum and difference array factors," *IEEE Transactions on Aerospace and Electronic Systems*, vol. 40, no. 1, pp. 360–370, Jan. 2004.
- [95] C. A. Balanis, *Antenna Theory*. John Wiley & Sons, Inc., 1982.
- [96] R. C. Jones, "New calculus for the treatment of optical systems," *J. Opt. Soc. Amer.*, vol. 31, pp. 488–493, 1941.
- [97] M. S. Lobo, L. Vandenberghe, S. Boyd, and H. Lebret, "Applications of second-order cone programming," *Linear Algebra and its Applications*, vol. 284, pp. 193–228, Nov. 1998.
- [98] R. Vanderbei, "LOQO: An interior point code for quadratic programming," *Optimization Methods and Software*, vol. 12, pp. 451–484, 1999.
- [99] M. M. Dawoud and M. A. Hassan, "Design of superdirective endfire antenna arrays," *IEEE Trans. Antennas and Propagation*, vol. 37, no. 6, pp. 796–800, June 1989.
- [100] A. Bloch, R. G. Medhurst, and S. D. Pool, "Note on the maximum directivity of an antenna," *Proc. I.R.E.*, vol. 48, p. 1164, June 1960.
- [101] M. Uzsoky and L. Solymar, "Theory of super-directive linear arrays," *Acta Phys., Acad. Sci. Hung.*, vol. 6, p. 195, 1956.
- [102] R. W. P. King, "Supergain antennas and the yagi and circular arrays," *IEEE Trans. Antennas and Propagation*, vol. 37, no. 2, pp. 178–186, Feb. 1989.
- [103] L. Solymar, "Maximum gain of a line source antenna of the distribution function is a finite fourier series," *IRE Trans. Antennas Prop.*, vol. AP-6, pp. 215–219, July 1958.
- [104] R. F. Harrington, "On the gain and beamwidth of directional antennas," *IRE Trans. Antennas Prop.*, vol. AP-6, pp. 219–225, July 1958.

- [105] N. Yaru, "A note on super-gain antenna arrays," *Proc. I.R.E.*, vol. 39, pp. 1081–1085, Sept. 1951.
- [106] R. C. Hansen, "Superconductive antennas," *IEEE Trans. Aerospace and Electronic Systems*, vol. 26, no. 2, pp. 345–355, Mar. 1990.
- [107] J. O. Coleman, D. P. Scholnik, and P. E. Cahill, "Synthesis of a polarization-controlled pattern for a wideband array by solving a second-order cone program," in *Proc. 2005 IEEE AP-S Int'l Symp.*, Washington, DC, July 2005.
- [108] J. O. Coleman, "Three-phase sample timing on a wideband triangular array of $4/3$ the usual density reduces the nyquist rate for far-field signals by two thirds," in *Proc. Asilomar Conf. on Signals, Systems, and Computers*, Pacific Grove, CA, Nov. 2004.
- [109] J. O. Coleman and D. P. Scholnik, "Design of nonlinear-phase FIR filters with second-order cone programming," in *Proc. 1999 Midwest Symp. on Circuits and Systems (MWSCAS '99)*, Las Cruces NM, Aug. 1999.
- [110] O. Burdakov and B. Merkulov, "On a new norm for data fitting and optimization problems," Linköping University, Linköping, Sweden, Tech. Rep. LiTH-MAT-R-2001-29, 2001.
- [111] D. P. Scholnik, "Mixed-norm FIR filter optimization using second-order cone programming," in *Proc. IEEE Int. Conf. Acoustic, Speech, and Signal Processing*, Orlando, FL, May 2002.
- [112] J. O. Coleman and D. W. Lytle, "Linear-programming techniques for the control of intersymbol interference with hybrid FIR/analog pulse shaping," in *Conf. Record, Int'l Conf. on Communications*, Chicago, June 1992, pp. 329.2.1–329.2.6.

- [113] J. O. Coleman, "The use of the FF design language for the linear-programming design of finite-impulse-response digital filters for digital-communication and other applications," Ph.D. dissertation, University of Washington, Seattle, WA, Dec. 1991.